LOCKHEED MARTIN ENERGY RESEARCH LIBRARIES
3 4456 0514428 8

CENTRAL RESEARCH LIBRARY
DOCUMENT COLLECTION

OAK RIDGE NATIONAL LABORATORY
operated by
UNION CARBIDE CORPORATION • NUCLEAR DIVISION
for the
U. S. ATOMIC ENERGY COMMISSION

ORNL-TM-3300

cy. 1

FUELS AND MATERIALS DEVELOPMENT PROGRAM QUARTERLY PROGRESS REPORT FOR PERIOD ENDING DECEMBER 31, 1970

OAK RIDGE NATIONAL LABORATORY
CENTRAL RESEARCH LIBRARY
DOCUMENT COLLECTION
LIBRARY LOAN COPY
DO NOT TRANSFER TO ANOTHER PERSON
If you wish someone else to see this document, send in name with document and the library will arrange a loan.
UCN-7969
(3 3-67)

NOTICE This document contains information of a preliminary nature and was prepared primarily for internal use at the Oak Ridge National Laboratory. It is subject to revision or correction and therefore does not represent a final report.

This report was prepared as an account of work sponsored by the United States Government. Neither the United States nor the United States Atomic Energy Commission, nor any of their employees, nor any of their contractors, subcontractors, or their employees, makes any warranty, express or implied, or assumes any legal liability or responsibility for the accuracy, completeness or usefulness of any information, apparatus, product or process disclosed, or represents that its use would not infringe privately owned rights.

ORNL-TM-3300

Contract No. W-7405-eng-26

METALS AND CERAMICS DIVISION

FUELS AND MATERIALS DEVELOPMENT PROGRAM QUARTERLY PROGRESS REPORT FOR PERIOD ENDING DECEMBER 31, 1970

Compiled by

P. Patriarca

Edited by

D. J. Rucker

JULY 1971

OAK RIDGE NATIONAL LABORATORY
Oak Ridge, Tennessee
operated by
UNION CARBIDE CORPORATION
for the
U.S. ATOMIC ENERGY COMMISSION

LOCKHEED MARTIN ENERGY RESEARCH LIBRARIES

3 4456 0514428 8

FOREWORD

This quarterly progress report describes research and development on nuclear fuels and materials at the Oak Ridge National Laboratory for the U.S. Atomic Energy Commission. This work is either sponsored by or of particular interest to the Fuels and Materials Branch of the Division of Reactor Development and Technology.

Progress on these programs is reported for the three major divisions of the work — Fast Reactor Technology, Space Power Technology, and General Reactor Technology — under the appropriate AEC activity titles listed below.

Chapter Number	AEC Activity Title	189a Number	AEC Activity Number
	PART I. FAST REACTOR TECHNOLOGY		
1	FBR OXIDE FUELS DEVELOPMENT	10090	04 40 02 01 1
2	DEVELOPMENT OF ADVANCED FBR FUEL	10092	04 40 02 01 1
3	FBR CLAD AND STRUCTURAL ALLOY DEVELOPMENT	10026	04 40 02 01 1
	MECH PROP OF ALLOYS IN REACTOR	10097	04 40 02 03 1
4	FAB DEV OF FBR CLADDING	10202	04 40 02 04 1
5	WELDING DEV — FBR SS COMPONENTS	10219	04 40 02 04 1
6	PROPERTIES OF FERRITIC STEEL WELDS	10241	04 40 02 05 1
7	NDT TECHNIQUES FOR FBR	10106	04 40 02 04 1
8	SODIUM CORROSION STUDIES	10096	04 40 02 02 1
9	SODIUM REMOVAL AND CAUSTIC EFFECTS	10248	04 40 02 02 1
10	DEV OF FBR NEUTRON-ABSORBER MATERIALS	10242	04 40 02 02 1
	PART II. SPACE POWER TECHNOLOGY		
11	DEVELOPMENT OF NITRIDE FUELS	10213	04 40 02 01 1
12	CLADDING MATERIALS FOR SPACE ISOTOPIC HEAT SOURCES*	10507	04 30 05 04 1
13	PHYSICAL AND MECHANICAL METALLURGY OF REFRACTORY ALLOYS	10110	04 40 02 05 1

*Sponsored by Division of Space Nuclear Systems.

Chapter Number	AEC Activity Title	189a Number	AEC Activity Number
14	TUNGSTEN METALLURGY	10104	04 40 02 04 1
15	FAST-NEUTRON IRRADIATION EFFECTS ON ELECTRICAL INSULATORS*	10068	04 30 02 02 1
	PART III. GENERAL REACTOR TECHNOLOGY		
16	FUEL ELEMENT FABRICATION DEVELOPMENT	10107	04 40 02 04 1
17	TRANSURANIUM ELEMENT PROCESSING — TARGET FABRICATION†	85	05 05 05 00 0
	HIGH FLUX ISOTOPE REACTOR†	88	05 05 05 00 0
	RADIATION DAMAGE†	103	05 06 01 03 0
18	JOINING RESEARCH ON NUCLEAR MATERIALS	10103	04 40 02 04 1
19	NONDESTRUCTIVE TESTING	10220	04 40 02 04 1
20	ADVANCED MATERIALS FOR STEAM GENERATORS	10217	04 40 02 02 1

*Sponsored by Division of Space Nuclear Systems.

†Sponsored by Division of Research.

CONTENTS

Page

SUMMARY xiii

PART I. FAST REACTOR TECHNOLOGY

FUELS

1. DEVELOPMENT OF FBR OXIDE FUELS 3
Development of Fabrication Processes 3
Series II Unencapsulated Fuel Pins for Irradiation in the Experimental Breeder Reactor-II 3
Fuel Pins for Studies of Fuel Reprocessing 4
Fuel Pin for Tests of Mechanical Interaction 5
Characterization of $(U,Pu)O_2$ Fuels 7
Moisture Analysis 8
Relocation of Alpha Facility 10
Behavior of Fission Products in Oxide Fuels 12
Thermal Expansion of Solid Solution of Rare-Earth Oxide and UO_2 12
Irradiation Testing of $(U,Pu)O_2$ Fuels 14
Fast-Flux Irradiation Tests 15
Transient Tests 19
Uninstrumented Thermal-Flux Irradiation Tests 19
Instrumented Tests in the ETR 20
Tests of Thermal Performance 23
Tests of Mechanical Interaction of Fuel and Cladding . . . 29
Analysis of Fuel Element Performance 33
Development of a Model for Fuel Restructuring 33
Round-Robin Exercise in Modeling 39
Microscopy of $(U,Pu)O_2$ Fuels 40
Redistribution of Actinides in Irradiated $(U,Pu)O_2$ 43
Migration of Fission Products in $(U,Pu)O_2$ Nuclear Fuels 45

Examinations of Chemical Interactions of Fuel and Cladding in Sphere-Pac $(U,Pu)O_2$ Fuel Pins 45

Notes 49

2. DEVELOPMENT OF ADVANCED FBR FUELS 53

Synthesis, Fabrication, and Characterization of Advanced FBR Fuels 53

Synthesis and Fabrication of Mixed Nitrides 53

Sintering Experiments on (U,Pu)N 65

Ball Milling and Sintering of Nitrides 69

Synthesis of Uranium Nitride 73

New Facilities 73

Characterization of Nitride Fuels 77

Development of the Dumas Technique for the Determination of Nitrogen in (U,Pu)N 79

Compatibility of Mixed Nitrides and Carbides with LMFBR Cladding Alloys 81

The Pu-Cr-N System 81

Thermodynamics of Plutonium Nitride 86

Irradiation Testing of Mixed Nitrides and Carbides 93

Thermal-Flux Tests 93

Fast-Flux Tests 94

Notes 96

CLADDING AND OTHER STRUCTURAL MATERIALS

3. MECHANICAL PROPERTIES OF ALLOYS IN REACTOR ENVIRONMENTS AND DEVELOPMENT OF LMFBR CLADDING AND STRUCTURAL MATERIALS 97

Status of Irradiation Experiments 97

Austenitic Stainless Steels 98

Mechanical Properties of Types 304 and Titanium-Modified 304 Stainless Steel 99

Effect of Composition on the Swelling of Austenitic Stainless Steels Irradiated in HFIR 106

Microstructural Studies of Unirradiated Standard and Titanium-Modified Type 316 Stainless Steel and Consequential Considerations 112

Studies of Phases Formed in Type 316 Stainless Steel . . . 120

Incoloy 800 122

Effect of Heat Treatment on the Mechanical Properties of Incoloy 800 122

Irradiation Damage to Refractory Metals 126

Formation of Voids in Niobium and Nb–1% Zr 126

Notes 132

4. FABRICATION DEVELOPMENT FOR FBR CLADDING 134

Effect of Fabrication Variables During Mandrel-Plug Drawing on the Quality and Properties of Type 316 Stainless Steel Tubing 134

Studies of Artificial Defects 134

Study of Discontinuities Introduced During Fabrication 134

Effects of Artificially Induced Defects on the Mechanical Properties of Unirradiated Annealed Type 316 Stainless Steel Tubing 135

Development of Type 316 Stainless Steel with Ultrafine Grain Size 140

Effect of Planetary Swaging on the Structure and Creep Properties of Type 316 Stainless Steel 143

Production of Type 316 Stainless Steel by Planetary Swaging 143

Notes 144

5. WELDING DEVELOPMENT FOR FBR STAINLESS STEEL COMPONENTS . . . 145

Study of Submerged-Arc Process 145

Investigations of Mechanical Properties 145

Tensile Tests 148

Study of Gas Metal-Arc Process 148

Preparation of Weldment Specimens 148

Study of Shielded Metal-Arc Process 149

Preparation of Weldment Specimens 149

Investigations of Mechanical Properties 150

Irradiation Studies 152

Heat-Treatment Studies 152

Corrosion Studies 156

Notes 157

6. PROPERTIES OF FERRITIC STEEL WELDS 159
Plain Carbon Steels 159
Preparation of Specimens 159
Conventional 2.25% Cr—1% Mo Low-Alloy Steel 160
Preparation of Specimens 160
Low-Carbon Low-Alloy Steels 160
Literature Search and Information Gathering 160
Procurement of Material and Preparation of Specimens 160
Stabilized Low-Alloy Steels 160
Literature Search 160
Procurement of Material 161
Preparation and Testing of Specimens 161
Notes 169
7. NONDESTRUCTIVE TESTING TECHNIQUES FOR LMFBR 170
Development of Advanced Techniques 170
Development of Eddy-Current Instrument 170
Ultrasonic Schlieren Techniques for Evaluation of Welds 170
Measurement of Cold Work in Stainless Steel Tubing 172
Instrument Development 172
Notes 173
8. SODIUM CORROSION STUDIES 174
Comparative Corrosion Tests on Refractory Alloys 174
Effect of Oxygen on the Compatibility of Vanadium and Vanadium Alloys with Sodium 174
Oxidation of Vanadium and Vanadium Alloys 176
Notes 180
9. SODIUM REMOVAL AND CAUSTIC EFFECTS 182
Examination of ALCO/BLH Steam Generator 182
Corrosion Effects of Sodium Leaks or Spills in Gases Containing Oxygen 185
Design of Oxidation Experiments 185
Notes 187
10. DEVELOPMENT OF FBR NEUTRON-ABSORBER MATERIALS 188
Characterization of Boron Carbide 188

Indexing of Powder X-Ray Diffraction Patterns 188
Irradiation Behavior of Boron Carbide 192
Thermal Reactor Tests 192
Fast Reactor Tests 195
X-Ray Diffraction Study of Irradiated Boron Carbide . . 195
Transmission Electron Microscopy of Irradiated Boron Carbide 202
Notes 208

PART II. SPACE POWER TECHNOLOGY

FUELS

11. DEVELOPMENT OF URANIUM MONONITRIDE FUELS 211
Irradiation Testing 211
Postirradiation Examination of Capsule UN-3 211
Intergranular Fractures in T-111 in Capsule UN-3 215
Fabrication of Irradiation Capsules 219
Proposed Irradiation Tests of UN in the EBR-II 220
Notes 222

CLADDING AND OTHER STRUCTURAL MATERIALS

12. CLADDING MATERIALS FOR SPACE ISOTOPIC HEAT SOURCES 224
Development of Improved Alloys 224
Platinum-Base Alloys 224
Notes 226
13. PHYSICAL AND MECHANICAL METALLURGY OF REFRACTORY ALLOYS . . . 227
Physical Metallurgy 227
Effect of Nitrogen on Mechanical Properties of T-111 . . 227
Effect of Oxygen on Mechanical Properties of T-111 . . . 227
Development of Age-Hardening Refractory Alloys 230
Mechanical Properties 234
Mechanical Properties of Welds 234
Long-Time Creep Properties of Refractory Alloys 235

Joining 235

Analysis of Cracking During Welding of TZM and Molybdenum 235

Analysis of Cracking in Molybdenum Tubing 237

Fabrication of Refractory Metal Components 237

Investigation of Remelting Temperature in Brazes 241

Physical Properties 243

Thermal Conductivity of Molybdenum Alloys 243

Notes 243

14. TUNGSTEN METALLURGY 245

Primary and Secondary Working of Tungsten Alloys 245

Extrusion of Tungsten Alloys 245

Chemical Vapor Deposition 246

Deposition of Tungsten with a Dispersion of Fine Particles 246

Deposition of Tungsten-Rhenium Alloys 247

Evaluation of Methods for Joining Tungsten Alloys 250

Development of Filler Metals 250

Creep Behavior of Tungsten and Tungsten Alloys 252

Creep Properties of Chemically Vapor Deposited Tungsten 252

Creep Properties of Advanced Tungsten Alloys 252

New Equipment 254

Effect of Low-Pressure Oxygen on the Creep Properties of W—25% Re 254

Behavior of Tungsten Alloys Under Fast-Neutron Irradiation 257

Irradiation Damage to Tungsten Alloys 257

Design of Experiment 258

Electrical Resistivity of Tungsten 260

Notes 261

15. FAST-NEUTRON IRRADIATION EFFECTS ON ELECTRICAL INSULATORS . . 263

General Survey of Fast-Neutron Effects on Electrical Insulators 263

Irradiation of High-Density Commercial Al_2O_3 Products Considered for Thermionic Insulators 264

Metal-Clad Al_2O_3 Specimens 265
Notes 265

PART III. GENERAL REACTOR TECHNOLOGY

FUELS

16. DEVELOPMENT OF FUEL ELEMENT FABRICATION 269
Irradiation Studies 269
Design and Fabrication of HFIR Irradiation Experiments 269
Development of HFIR Core with Increased Fuel Loading 272
Establishment of Standards for Burned U_3O_8 and High-Fired U_3O_8 HFIR Plates 272
Fabrication Development 273
Deformation Behavior of Fuel Cores During Rolling . . . 273
Notes 274

CLADDING AND OTHER STRUCTURAL MATERIALS

17. IRRADIATION DAMAGE TO ALUMINUM AND ALUMINUM ALLOYS 276
Material and Irradiation History 277
Measurements of Density and Dimensional Change 280
Measurements of Mechanical Properties 282
Notes 294
18. JOINING RESEARCH ON NUCLEAR MATERIALS 295
The Effect of Minor Variations in Chemical Composition on Weldability 295
Weldability of Incoloy 800 295
Weldability of Stainless Steels 297
Notes 303
19. NONDESTRUCTIVE TESTING 304
Electromagnetic Inspection Methods (Eddy Currents) 304
Solutions for Electromagnetic Induction Problems 304
Ultrasonic Inspection Methods 306
Ultrasonic Frequency Analysis 306

Penetrating Radiation 310

Radiation Scattering 310

Closed-Circuit Television for Radiographic Evaluation 311

Notes 312

20. ADVANCED MATERIALS FOR STEAM GENERATORS 313

General Corrosion at 595 and 650°C 313

Studies of Weldments Between Similar and Dissimilar Metals 313

Studies on Simulated Root Pass Compositions 318

Stress-Corrosion Cracking in a Chloride Environment . . 320

Notes 321

SUMMARY

PART I. FAST REACTOR TECHNOLOGY

FUELS

1. DEVELOPMENT OF FBR OXIDE FUELS

We fabricated and inspected 20 unencapsulated fuel pins for irradiation in the EBR-II. These pins, which contain sol-gel Sphere-Pac fuel and pellets clad in type 316 stainless steel, were shipped to the reactor. We fabricated 12 fuel pins of mechanically blended $(U,Pu)O_2$ pellets. After irradiation in the ETR, these pins will be used for studies of fuel reprocessing. Mechanically blended mixed oxide pellets were received from WADCO for use in the first irradiation test of mechanical interaction of fuel and cladding. Since the gas release and moisture content of the pellets as received from WADCO did not meet specifications, we heat treated them by our standard method to reduce these values. They are now ready for loading into the fuel pin.

Our irradiation program on mixed oxide fuels includes thermal-flux experiments that permit use of instrumented capsules and continuously controlled heat rates and fast-flux experiments in which the fission-rate distribution and irradiation effects on the cladding are more typical of operating conditions for an LMFBR. Our series I encapsulated tests in the EBR-II contained mixed oxide Sphere-Pac fuels. Two of these capsules were returned to ORNL after attaining a peak burnup of 6% FIMA at a peak linear heat rate of 14 kW/ft. The peak fluence to which both pins were exposed was approximately 4×10^{22} neutrons/cm^2. The maximum diametral change for pin S-1-A, which had type 304 stainless steel cladding, was 0.0018 in.; the comparable change for pin S-1-E, which had type 316 stainless steel cladding, was 0.0010 in. This difference in diametral expansion seems consistent with measured changes in density due to void formation. The fission gas released from the only pin yet examined was about twice that found in similar fuel irradiated in a thermal-flux environment. We attribute this difference in behavior to

(1) the high percentage of the fuel that operated above 1750°C and (2) the depression of the thermal-neutron flux in the tests in the thermal reactor causing more fissions to occur in cooler regions of the fuel. Two transverse metallographic sections of the pin with type 316 stainless steel cladding revealed no evidence of chemical interactions of fuel and cladding even though the temperature of the inner surface of the cladding is calculated to have been 550°C. The subassembly data package for the EBR-II series II unencapsulated fuel pins was submitted to the EBR-II project for review. We have begun the assembly and inspection of hardware components for the fabrication of replacement pins to be installed in the second and third subassembly loadings for the series II experiment.

We previously reported the design and operating conditions, post-irradiation metallographic examinations, and initial evaluation of the results of the transient tests of six fuel pins. A multiple regression analysis correlating the calculated transient temperature distributions with measured temperature and the observed and predicted extent of fuel melting for the pin that operated at peak power indicates an average coefficient of heat transfer from fuel to cladding of about 2 W cm^{-2} $°C^{-1}$ gives the best fit. This result agrees with the gap conductance calculated for Sphere-Pac fuel from instrumented capsules operated in the ORR.

One capsule containing Sphere-Pac mixed oxide fuel being irradiated in the ETR has attained a burnup level of 9.9% FIMA and will soon be removed for examination. Two capsules that have cladding thermocouple instrumentation are being irradiated to investigate the fuel swelling and chemical interaction of Sphere-Pac and pelletized fuels and their cladding. These capsules have been irradiated to a peak burnup of about 2.3% FIMA. The performance of these capsules to date closely matches the design conditions. The design and fabrication of capsule components for two additional capsules in this series are under way. Each of these capsules will contain one fuel pin with a 20-in.-long column of fuel. The purpose will be to compare U-Fine Sphere-Pac fuel with pellets.

Further analysis of data from the instrumented tests in the ORR showed that, at least at low burnups, the degree of restructuring, the

amount of fission gas released, and the operating temperatures in particulate (Sphere-Pac) and pellet fuels are essentially the same for initial fuel densities of 82% of theoretical. Microscopic examination of the Ti-modified type 304 stainless steel used in capsule SG-3 indicated that the cladding exposed to the fuel pellets had undergone localized grain boundary attack to a depth of 0.003 to 0.004 in. during operation to peak temperatures of about 600°C. Shielded electron microprobe analysis of this structure is continuing.

The first in-reactor power cycling capsule (MINT-1) will contain a prototype fast reactor fuel pin. The test will be conducted with programmed power cycles and an occasional overpower cycle. All parts for the fuel pin and capsule were procured, and assembly is in progress. In addition, reliability testing of the instrumentation is almost complete.

In our analysis of fuel element performance, special emphasis is being given to modeling mechanical interaction of fuel and cladding and to characterizing irradiated $(U,Pu)O_2$ fuels. Our first effort to mathematically describe the phenomenon of fuel restructuring during irradiation was empirical in nature; and while this approach is useful in some applications, we have found it limited by its inability to consider those aspects of fuel restructuring that are dependent on time. We attempted to use various models proposed for fuel restructuring but found that these have deficiencies in some respects. More efficient methods of calculating the kinetics of fuel restructuring must be developed.

At the 1970 meeting of the Working Group on Analytical Techniques for Predicting Fuel Pin Behavior and Design, eight fuel pins were selected for detailed study by means of models for fuel performance available to the members of the working group. We have completely analyzed two of the pins, and the data on the remaining six are now ready to be analyzed. In support of our modeling effort, we have made a more detailed examination of irradiated microstructures to define porosity as a function of radial position, in-reactor redistribution of U and Pu, and migration of fission products in mixed oxide fuels. We are also attempting to model these phenomena mathematically.

2. DEVELOPMENT OF ADVANCED FBR FUELS

The sintering of $(U_{0.8},Pu_{0.2})N$ compacts made from powders derived from U-Pu alloy or from mechanical mixtures of UN and PuN is improved by heat treating the compacts while maintaining a N_2 pressure slightly above the value that will lead to decomposition of the mononitride phase. The enhanced sintering effect is more pronounced at lower temperatures, such as 1800°C, than at 2200°C. Mechanical mixtures of UN and PuN are difficult to sinter to greater than 85% of theoretical density because of the difficulty of obtaining uniform diffusion of one compound into the other.

The Dumas method for analysis of N in nitrides shows great promise for use with (U,Pu)N since it allows rapid collection of the N and does not require a dissolution procedure before the analysis. Essentially identical results were obtained for the N content of UN by the Dumas method and by the Kjeldahl method after dissolution in H_3PO_4.

Uranium-plutonium alloys were received for use in producing (U,Pu)N fuel for irradiation experiments in the EBR-II, and the nitride powders are now being synthesized.

Two capsules containing (U,Pu)N clad with type 316 stainless steel were inserted into the ETR in December.

CLADDING AND OTHER STRUCTURAL MATERIALS

3. MECHANICAL PROPERTIES OF ALLOYS IN REACTOR ENVIRONMENTS AND DEVELOPMENT OF LMFBR CLADDING AND STRUCTURAL MATERIALS

Irradiation experiments are in progress on types 304, 316, and 318 stainless steel, Ti-modified types 304 and 316 stainless steel, Sandvik 12R72HV, 19-9-DL, and Incoloy 800. These materials have been worked and annealed to obtain various microstructures and are being irradiated at 350 to 800°C to fast fluences of at least 3.5×10^{22} neutrons/cm^2. Some samples of these materials were removed and are in various states of examination.

The irradiation of annealed type 304 stainless steel to fast fluences of 1.5 to 3.5×10^{22} neutrons/cm^2 at 535 and 590°C causes modest changes in the rupture life and minimum creep rate at 550 and 600°C. Irradiation at 800°C reduces the rupture life and increases the minimum creep rate.

The change in the fracture strain was the most significant; values as low as 0.5% were observed. Tensile and creep-rupture tests of the irradiated Ti-modified alloy showed that this material had higher fracture strains than standard type 304 stainless steel. The Mo and Ti concentrations in several alloys of type 316 stainless steel were varied over small ranges. The swelling measured after exposure in the High Flux Isotope Reactor (HFIR) to a fast fluence of 1.5 to 2.9 $\times 10^{22}$ neutrons/cm^2 at 575 to 600°C was increased slightly with increasing Mo and decreased drastically with increasing Ti. The recrystallization and precipitation that occur in the standard and Ti-modified steel after solution annealing and cold working were characterized as a function of annealing temperature. Further studies were made of the precipitates that formed in several heats. The phases present under certain conditions were $M_{23}C_6$, TiN, TiC, $Ti_2(S,C)$, X, Laves, and σ.

Studies on aged Incoloy 800 showed that aging at 550°C was reduced markedly by following the solution anneal of 0.5 hr at 1150°C with a 100 hr anneal at 800°C. These heats contained 0.03 to 0.1% C and 0.1 to 0.27% Ti; the aging response decreased with decreasing C content and was unaffected by Ti concentration.

Samples of Nb and Nb–1% Zr were irradiated in the Experimental Breeder Reactor-II (EBR-II) at 790±25°C to a fluence of 2.5 $\times 10^{22}$ neutrons/cm^2. The voids were small and uniformly distributed in the Nb sample, but were generally larger and very inhomogeneously distributed in the alloy. However, the bulk swelling of the two materials under those conditions was not significantly different. A capsule is being designed for irradiation of W and W-base alloys in the EBR-II at 900 to 1800°C.

4. FABRICATION DEVELOPMENT FOR FBR CLADDING

Our study of the relationships between the size of defects in stainless steel tubing and its stress-rupture properties is continuing. An improved type of artificial defect with depths equal to 10% of the wall thickness reduces the properties of the tubing at 650°C. All failures in defected tubes were at the site of the artificial defect.

We completed a bench test that showed that surface defects can be introduced into the cladding during fuel loading; long scratches 0.0002 to 0.0003 in. deep were documented.

5. WELDING DEVELOPMENT FOR FBR STAINLESS STEEL COMPONENTS

Creep-rupture tests of submerged-arc weldment specimens showed that ductility (total elongation) decreased with longer rupture lives. A weldment prepared with Hobart HS-300 flux showed atypical results compared with other submerged-arc welds. Heat treatment of 75 tensile specimens was completed except for the 1000-hr aging. An additional gas metal-arc weld was prepared with a 98% Ar–2% O_2 gas mixture. A section of weld made in 2-in. plate with 1/4-in. electrodes containing controlled amounts of minor elements was procured from Combustion Engineering, Inc. Creep-rupture tests were performed on heat-treated shielded metal-arc welds containing B; in general, the heat treatments studied reduced the rupture lives but did not adversely affect ductilities. A lot of 232 weldment specimens was delivered to WADCO for irradiation testing. Further studies were conducted to determine the effects of various heat treatments on microstructure. Solution anneals up to 1190°C (2175°F) had varying effects on the amount of ferrite taken into solution in several different welds.

6. PROPERTIES OF FERRITIC STEEL WELDS

We completed our search of the literature for the stabilized low-alloy steels and located and ordered commercial material.

We observed cracking in TIGAMAJIG weldments in stabilized low-alloy steel; however, backfilling of these cracks by a low-melting phase makes them difficult to observe. An extensive electron-beam microprobe analysis showed these liquated regions to be rich in Nb. This Nb enrichment can result in the formation of a low-melting eutectic Fe_2Nb δ-phase. The enrichment in Nb is derived from the NbC precipitates which, at elevated temperatures, decompose and thereby provide the high level of Nb necessary to produce the eutectic structure.

7. NONDESTRUCTIVE TESTING TECHNIQUES FOR LMFBR

New components were designed and assembled for the eddy-current instrument to measure both size and depth of flaws. Several ultrasonic techniques and the schlieren system are being used to evaluate sample welds that contain intentional flaws. Several improvements with multiple sensors and diffraction techniques are being studied.

We improved the stability of the eddy-current instrument that is being developed to measure cold work in stainless steel tubing. We are now measuring the cold work in rods prepared by Argonne National Laboratory. A new configuration of coils is being studied to reduce the effect of some of the variables.

8. SODIUM CORROSION STUDIES

We compared microhardness profiles for V and V alloy specimens that had acquired O from Na at 600°C. The profiles corroborated conclusions concerning O distribution that had previously been deduced from measurements of weight gain, O analyses, and metallography. Metallographic studies of V–20% Ti oxidized in low-pressure O_2 showed that the oxidation front representing internal precipitation of Ti was followed by a second front, presumably caused by transformation of α-phase V to β-phase V. The microstructures of V–20% Ti exposed to the gaseous environment were identical to those previously observed in Na tests.

9. SODIUM REMOVAL AND CAUSTIC EFFECTS

The ALCO/BLH steam generator, which experienced leakage of water into Na while under test at the Liquid Metal Engineering Center, was shipped to ORNL for destructive examination to determine the mechanism of failure and the metallurgical integrity of the unit.

We began studies of the corrosion effects of Na leaks on metal surfaces in contact with mixtures of N_2 and air. An apparatus is being constructed to permit the controlled leakage of Na through a stainless steel specimen under ambient conditions that simulate those surrounding the primary containment vessel of the FFTF Reactor.

10. DEVELOPMENT OF FBR NEUTRON-ABSORBER MATERIALS

Boron carbide with a high B:C ratio of 4.5 may contain free B, depending upon the fabrication schedule. When free B was present, the rate of He release from the (n,α) reaction during irradiation at 350 to 500°C were higher than when no free B was present. The rate of He release from powders that had B:C ratios of 3.6 and 4.5 did not vary significantly with irradiation temperature from 350 to 500°C.

Annealing boron carbide with a B:C ratio of about 3.6 at temperatures as high as 2000°C did not lead to the solution of all the graphite C into the boron carbide structure. However, after irradiation at 350°C to 9% burnup of ^{10}B, the graphite was no longer present.

Transmission electron microscopy revealed irradiation damage in boron carbide that appeared very similar to that observed in metal after very high fluence. A high density of black spots was observed, which was probably due to lattice strains from both displacement damage and the (n,α) reaction products. The damage appeared to be uniform, and no bubbles of He have yet been positively identified.

PART II. SPACE POWER TECHNOLOGY

FUELS

11. DEVELOPMENT OF URANIUM MONONITRIDE FUELS

Examination of capsule UN-3 after irradiation showed that the T-111 cladding was unsatisfactory for use at a temperature of 1400°C at the outside surface of the cladding. The W-Re cladding performed satisfactorily in the same test at 1300°C. Fabrication of capsules UN-4 and UN-5 is nearing completion, and they are scheduled to be inserted into the reactor in February 1971. A proposal is being prepared for a program of irradiation testing of UN in the fast-neutron flux of the EBR-II.

CLADDING AND OTHER STRUCTURAL MATERIALS

12. CLADDING MATERIALS FOR SPACE ISOTOPIC HEAT SOURCES

New cladding materials are being developed for containment of radioisotopes in power systems for use in space. We found that adding 1% Hf to the Pt–5% Mo alloy improved tensile strength at both room temperature and elevated temperatures without impairing the ductility. Alloys in the Pt-Rh-W and Pt-Rh-Re systems and modifications of those that contain additions of Hf, Zr, or Ti are also being investigated for fabricability, melting point, air oxidation, compatibility, mechanical properties, and weldability.

13. PHYSICAL AND MECHANICAL METALLURGY OF REFRACTORY ALLOYS

The time required to produce 1% creep strain in T-111 in a 1×10^{-6} torr pressure of N_2 at 1400°C was found to be about one-third of that required to produce the same strain in ultrahigh vacuum, and the rupture life was about one-eighth of that in vacuum. A method was devised for determining the solubility limit of O in T-111, and equipment was set up to prepare specimens. The development of age-hardening refractory alloys continued. The aging responses of Ta-Hf and Ta-Zr alloys were determined by both hardness and tensile testing. Yield strengths over 300,000 psi were obtained with the Ta–65% Hf alloy. Stress-rupture tests on T-222 welds showed rupture times to be equal to those of unwelded material at low stresses but shorter at high stresses. Long-time stress-rupture data were also obtained on the Nb alloy SU-16. This is the strongest Nb-based alloy we have tested. Welding activities included the completion of a thermal convection loop of Mo and studies into the morphology of fractures in Mo tubing and welds in Mo alloys. In addition, studies on brazes of refractory alloys were continued in an attempt to understand the mechanisms controlling the remelting temperature. Attempts to verify the exceptionally low lattice thermal conductivity of Mo are awaiting improvements to the sensitivity of the longitudinal heat flow apparatus.

14. TUNGSTEN METALLURGY

Preliminary experiments on dispersion strengthening of W by gas entrainment of particles during chemical vapor deposition (CVD) was encouraging even though the desired volume fraction of particles was not obtained. Studies of the effect of the ratio of H_2 to metal fluoride on the quality of CVD W–25% Re alloys showed that the best deposits were formed from nearly stoichiometric ratios.

The initial results of bend tests of gas tungsten-arc welds in W–25% Re sheet showed that the addition of W–25 at. % Re–30 at. % Mo and Mo–50% Re filler metals were detrimental to the bend ductility.

Data for the time to 1% creep for CVD W are presented as a function of stress at 1400, 1650, and 2200°C. Specimens from several deposits of CVD W were tested at 1650°C; the data are in good agreement. The initial creep-rupture tests of W–3.8% ThO_2 at 1400 to 2200°C showed the material to be about twice as strong as unalloyed W. Six ultrahigh-vacuum creep machines were procured and installed for long-time creep tests at low strains. Additional creep tests on W–25% Re in low-pressure O_2 showed that the formation of a surface layer of σ-phase significantly strengthens the material.

A new task on fast-neutron irradiation damage in W alloys was begun. Existing data are summarized, and preliminary design of an irradiation experiment is reported. Base-line data for electrical resistivity are being determined.

15. FAST-NEUTRON IRRADIATION EFFECTS ON ELECTRICAL INSULATORS

The following advanced materials are being evaluated as possible electrical insulators in thermionic converters: (1) synthetic sapphire Al_2O_3, (2) single-crystal MgO, (3) transparent, polycrystalline Y_2O_3, and (4) Si_2ON_2. Preliminary visual inspections of solid cylindrical specimens of these advanced materials that had been irradiated at 400 and 800°C in the EBR-II revealed almost no gross fracture. The results suggest that further investigation of these materials may be warranted as possible alternatives to polycrystalline Al_2O_3, which has the

disadvantage of separating at the grain boundaries after receiving moderately high fast-neutron fluences.

PART III. GENERAL REACTOR TECHNOLOGY

FUELS

16. DEVELOPMENT OF FUEL ELEMENT FABRICATION

The irradiation experiment, designated PM capsule 1, was built and will be inserted into the HFIR to evaluate several properties that are believed to influence the performance of both ATR and HFIR fuel elements at high fission densities.

CLADDING AND OTHER STRUCTURAL MATERIALS

17. IRRADIATION DAMAGE TO ALUMINUM AND ALUMINUM ALLOYS

Density measurements and tensile tests were performed on specimens cut from the 6061 Al target basket, a component irradiated at 60°C in the HFIR. The maximum change in density was −1.06% for a specimen that had received a neutron fluence of 5.4×10^{22} neutrons/cm^2 (> 0.8 MeV) and 1.2×10^{23} neutrons/cm^2 (thermal). This Mg_2Si precipitate-hardened alloy swells considerably less than solid-solution alloys or high-purity Al under similar conditions.

We investigated the effects of neutron fluence, deformation rate, and deformation temperature on mechanical properties. Strengthening was induced by irradiation, but the tensile strength tended to increase with increasing deformation rate. The ductility of the irradiated alloy was reduced below that of control specimens over the entire range of test temperatures (25 to 500°C), but a set of conditions leading to particularly low ductilities was high neutron fluences [above 3×10^{22} neutrons/cm^2 (> 0.8 MeV)] at temperatures near 200°C for slow deformation rates. This information is of particular value in determining the service life of certain Al components for use in-reactor.

18. JOINING RESEARCH ON NUCLEAR MATERIALS

Only two of the experimental Incoloy 800 alloys used as filler metal in weldments in 1/2-in.-thick Incoloy 800 plate failed to pass bend tests; one of these contained additions of S and P, and the other was high in C content. Three filler-metal alloys cracked during welding.

Metallographic studies of autogeneous electron-beam and gas tungsten-arc welds on annealed and on 50% cold-worked experimental stainless steel drop castings showed a band of what appeared to be tempered martensite in the heat-affected zones of those alloys that underwent a strain-induced transformation to martensite during welding. This band was not seen in the more stable alloys.

Electron microscopy of the alloys that contained martensite indicated that the microstructures of these alloys consisted of austenite with a high density of dislocations and bands of ϵ phase; the martensitic needles occurred within these bands.

19. NONDESTRUCTIVE TESTING

We are analyzing the variations in electromagnetic induction caused by several second-order effects in an attempt to improve the absolute accuracy of measurements of impedance. A new computer program shows promise of being able to calculate both electrical conductivity and lift-off from a single value of impedance. In our studies of the measurement of thickness by means of phase-sensing, we discovered that we could design a coil that will exhibit minimum effect due to variations in life-off at the same operating conditions that produce maximum response to changes in thickness.

Measurements of flaw size and orientation by ultrasonic frequency analysis of a specimen containing machined flaws were shown to be far superior to those made with conventional amplitude techniques.

Measurement of induced fluorescent x rays from the U dispersed in the core of a fuel plate showed a relationship between detected radiation and thickness of the Al cladding.

We are attempting to reduce the noise problem in the closed-circuit television system being studied as part of a high-speed high-resolution densitometer. Neutral density filters will be used as part of the calibration.

20. ADVANCED MATERIALS FOR STEAM GENERATORS

Specimens of weldments of alloys for use in steam generators recently accumulated a total exposure of 16,000 hr in superheated steam at 595 and 650°C (1100 and 1200°F) and were evaluated. The calculated penetrations of base metals in 20 years were all below 0.0005 in. for the Inconel 625, Hastelloy X, and IN 102 similar-metal weldments. Inconel 600 welded to itself with Inconel 82 filler metal was attacked about 0.002 in. for the exposure at 595°C and about 0.003 in. for the exposure at 650°C. The amounts of corrosion for the various dissimilar-metal weldments was also low and interpretable in terms of the corrosion of the alloys of which they were made.

The synthesized root pass specimens reached exposure times at 595 and 650°C ranging from 2000 to 9000 hr. Whereas the amounts and rates of corrosion usually were, as expected, significantly higher at 650°C than at 595°C for the respective alloys, temperature did not appear to be nearly so important an experimental variable as surface preparation. The order of the amounts of corrosion for the individual surface conditions continued, but for few exceptions, to be (1) as welded, (2) electropolished, (3) belt ground, and (4) sandblasted.

PART I

FAST REACTOR TECHNOLOGY

FUELS

1. DEVELOPMENT OF FBR OXIDE FUELS

P. Patriarca A. L. Lotts C. M. Cox

The purpose of this program is to advance the technology of $(U,Pu)O_2$ as a fuel for the LMFBR. The oxide fuels studied in this program are derived from coprecipitation, mechanical blending, and sol-gel processes and are fabricated by cold pressing and sintering and Sphere-Pac. We emphasize determination of the properties and performance of oxide fuels derived from the sol-gel process and fabricated by Sphere-Pac techniques, but we also compare these fuels with those fabricated by other processes. The main objectives of the program are (1) to establish the performance characteristics and limitations of $(U,Pu)O_2$ fuel fabricated by the different processes, (2) to obtain a fundamental understanding of the mechanisms that are involved in the behavior of fuel elements under irradiation, (3) to develop fabrication techniques that provide both economy and a product with optimized performance, and (4) to develop analytical methods sufficiently accurate to optimize experimental design and to predict the response of fuel elements to LMFBR service conditions.

Development of Fabrication Processes

J. D. Sease

Series II Unencapsulated Fuel Pins for Irradiation in the Experimental Breeder Reactor-II (R. A. Bradley, W. J. Leonard, M. K. Preston[1])

We fabricated 20 unencapsulated fuel pins, 19 of which are scheduled for incorporation into a 37-pin subassembly of the EBR-II that we shall share with the Babcock & Wilcox Company.[2] The pins contain sol-gel Sphere-Pac fuel and pellet fuel in type 316 stainless steel cladding. The fabrication of the pins was described previously.[3,4]

The 20 fuel pins were inspected visually, marked, cleaned, and packaged in individual containers. The individual containers were placed in DOT-6M shipping containers (ten in each container) and shipped to the reactor site.

We began manufacturing component parts for 21 replacement pins for the series II irradiations in the EBR-II. The requirements for these pins were described previously.[2]

Fuel Pins for Studies of Fuel Reprocessing (R. A. Bradley)

We fabricated 12 fuel pins for capsules to be irradiated in the ETR. After irradiation, these fuel pins will be used by the Chemical Technology Division for studies of fuel reprocessing. Each fuel pin contains about 3 in. of $(U_{0.75},Pu_{0.25})O_{1.98}$ pellets.

The pellets were fabricated at WADCO (ref. 5) to FFTF specifications from mechanically blended powders. They were fully characterized at WADCO and at ORNL. Only the gas release and moisture content did not meet specifications.

We heat treated three batches, a total of 250 pellets, to reduce the gas release to the specified limit. The pellets were heated in flowing Ar at 300°C/hr to 1450°C. Then the gas was changed to Ar–4% H_2, and the pellets were held at 1450°C for 1 to 2 hr, as indicated below:

Heat Treatment	Number of Pellets	Time at 1450°C in Ar–4% H_2 (hr)
H160	50	1.25
H161	100	1.5
H163	100	2.2

The pellets were cooled to 850°C in Ar–4% H_2 and from 850°C to room temperature in Ar.

The ratio of O:metal, gas release, and moisture content were determined after heat treatment. The results of these analyses are summarized in Table 1.1. The data indicated that the values for O:metal and gas release were within specifications. Results of initial moisture analyses were highly variable. The variability of these results was probably due

Table 1.1. Summary of Analyses for Ratio of Oxygen to Metal, Gas Release, and Moisture for $(U,Pu)O_2$ Pellets After Heat Treatment

Heat Treatment Number	Ratio O:Metal	Gas Release (cm^3/g)	Moisture Content (ppm)
H160	1.988	0.027	20
H161	1.986	0.03	17
H163	1.981	0.04	17
Average	1.985±0.004[a]	0.034±0.010[a]	

[a]Range indicates 95% confidence limit on average.

to the introduction of moisture-laden air into the sample tube as the sample was loaded.[6] We believe the moisture content of this fuel was about 20±5 ppm.

Pellets with densities of 89.0±1.5% of theoretical were loaded into 12 fuel pins and 1 archive pin. Fuel column heights, weights, and fuel densities of these pins are listed in Table 1.2. The closure welds were inspected by He leak detector, dye penetration, and x-ray radiography. Four welds did not have sufficient penetration but were satisfactorily repaired.

Fuel Pin for Tests of Mechanical Interaction (R. A. Bradley)

We received the fuel for the MINT-1 test of the mechanical interaction of fuel and cladding during irradiation, characterized it, and are ready to insert it into the capsule as soon as it is delivered.[7]

The capsule will contain about 9.6 in. of $(U_{0.75},Pu_{0.25})O_2$ pellets prepared at WADCO to FFTF specifications. The pellets were fully characterized at WADCO and at ORNL. Only the gas release and moisture content did not meet specifications.

We heat treated about 100 pellets to reduce the gas release to the specified limit. The pellets were heated at 300°C/hr to 1450°C in flowing Ar–4% H_2 (2.5 scfh), held at 1450°C for 42 hr (until the moisture in the effluent reached 30 ppm), cooled to 850°C in Ar–4% H_2, and cooled from 850°C to room temperature in Ar.

Table 1.2. Data for Fuel Pins for Studies of Fuel Reprocessing

Fuel Pin Identification	Cladding Identification	Fuel Data					
		Heat Treatment	Height (in.)	Weight (g)	Average Pellet Density[a] (% of theoretical)	Average Planar Smear Density[a] (% of theoretical)	Average Smear Density of Bed (% of theoretical)
43-117-1	22-004-5	H161	3.13	14.412	88.46±0.48	84.34±0.46	82.27
43-117-2	22-004-17	H161	3.14	14.585	88.53±0.52	84.23±0.50	82.27
43-117-3	22-004-12	H163	3.10	14.414	88.26±0.35	84.14±0.33	82.09
43-117-4	22-004-9	H161 (9 pellets) H163 (5 pellets)	3.12	14.510	88.26±0.45	84.06±0.43	82.10
43-118-1	22-022-9	H160 (1 pellet) H163 (13 pellets)	3.13	14.510	88.07±0.37	83.80±0.35	81.83
43-118-2	22-004-10	H161	3.12	14.583	88.66±0.41	84.36±0.39	82.31
43-118-3	22-022-1	H163	3.13	14.592	88.27±0.39	84.07±0.37	82.07
43-118-4	22-004-1	H160	3.12	14.362	88.51±0.50	84.13±0.48	82.13
43-119-1	22-022-3	H161	3.14	14.445	88.29±0.49	84.01±0.47	81.98
43-119-2	22-014-6	H161	3.15	14.571	88.48±0.36	84.27±0.34	82.24
43-119-3	22-022-6	H163	3.12	14.438	88.24±0.39	84.13±0.37	82.14
43-119-4	22-004-16	H160	3.13	14.440	88.36±0.41	84.07±0.39	82.05
Archive	22-022-4	H160 (3 pellets) H161 (3 pellets) H163 (3 pellets)					

[a]Range indicates 95% confidence limit on average.

The ratio of O:metal, gas release, and moisture content were determined after heat treatment. The results of these analyses, summarized in Table 1.3, indicate that the ratio of O:metal and gas release are within specifications. As with a previous batch of fuel, the results of moisture analyses were highly variable due to the analytical technique used.[6,8] We believe the best value to use for the moisture content is 20±4 ppm.

Table 1.3. Results of Triplicate Analyses of Ratio of Oxygen to Metal, Gas Release, and Moisture Content of $(U,Pu)O_2$ Pellets for MINT-1 after Heat Treatment H194

Analysis Number	Ratio O:Metal	Gas Release (cm^3/g)	Moisture Content (ppm)
1	1.951	0.04	18
2	1.954	0.02	21
3	1.953	0.03	21
Average	1.953±0.004[a]	0.03±0.01	20±4.2

[a]Range indicates 95% confidence interval on average.

The pellets were dimensionally inspected, and the densities were calculated. We have sufficient pellets in the range of 89.5±1.0% of theoretical density for a 10-in. fuel stack with archive pellets.

Characterization of $(U,Pu)O_2$ Fuels

C. M. Cox J. D. Sease J. M. Leitnaker

The development of sol-gel fuel fabrication requires characterization of both the chemical composition and physical properties of the material to control the process and to interpret meaningfully the irradiation behavior. In many cases the analytical technique itself must be developed or modified to meet the requirements of mixed oxide fuels. In this section we report both the development or improvement of analytical techniques and the results of analyses on mixed oxide fuels.

Moisture Analysis (R. A. Bradley, W. H. Pechin)

The specifications for $(U,Pu)O_2$ fuel require less than 30 ppm moisture.[9] At ORNL, moisture content is determined by passing dry N_2 over the specimen as it is heated to 1000°C and measuring with a P_2O_5 electrolytic cell the amount of H_2O released.

We found that the moisture content for one batch of fuel ranged from 7.5 to 30 ppm after heat treatment, from 35 to 59 ppm after storage for several weeks in an Ar atmosphere, and from 17 to 20 ppm after vacuum outgassing (10^{-2} torr) at 25°C (ref. 8). The results indicated that the moisture content increased when the fuel was exposed to the glove-box atmosphere, but that it could be reduced by vacuum outgassing at room temperature.

To determine whether this was true, we conducted a statistically designed experiment to investigate the effect of storage and outgassing on the moisture content of mixed oxide pellets. The experiment was also designed to study possible sources of variation in the technique for moisture analysis.

The results of moisture analyses on nine pellets included in the experimental design and three pellets analyzed immediately after heat treatment are summarized in Table 1.4. An analysis of variance on these data indicated no significant difference between the moisture contents of stored, exposed, or outgassed pellets.

Probably the most important conclusion that we drew from this experiment was that the standard deviation due to unexplained variation was unacceptably high. With the observed standard deviation, the 95% confidence interval on the average of three analyses was ±18 ppm. The standard deviation was so great that small effects on moisture content caused by the various treatments would not have been detected.

After reviewing the equipment and technique used for moisture analysis, we decided that the large, unexplained variation was caused by air introduced into the analyzer when the sample was loaded. We subsequently analyzed eight pellets in such a manner that very little or no air was introduced into the moisture analyzer when the samples were loaded; we attached a plastic glove bag to the moisture analyzer

Table 1.4. Moisture Content Determined for $(U,Pu)O_2$ Pellets When Analyzer Exposed to Air During Loading

Sample Number	Moisture Content, ppm			
	As Sintered	Stored[a]	Exposed[b]	Outgassed[c]
1	10	37	21	37
2	10	23	27	28
3	13	64	31	31
Average	11±4[d]	41±18[d]	26±18[d]	32±18[d]
Standard Deviation	1.7	12.6[e]	12.6[e]	12.6[e]

[a]Pellets stored in desiccator containing molecular sieve for 3 to 6 days.

[b]Pellets removed from desiccator and exposed to glove box atmosphere (Ar) for 24 hr.

[c]Previously exposed pellets outgassed (2×10^{-2} torr) at 25°C for about 20 hr.

[d]Range indicates 95% confidence limit on average.

[e]Determined by analysis of variance.

and purged the glove box with Ar before opening the sample container and loading the sample. The moisture contents of pellets analyzed in this manner are shown in Table 1.5.

The standard deviation due to unexplained error was reduced by a factor of 4, and the 95% confidence interval was reduced to ±4.5 ppm. An analysis of variance indicated no significant difference in the moisture contents of pellets given the following treatments:

1. sealed in a metal can in the Ar atmosphere of the glove box immediately after unloaded from the furnace and then stored in the can in air for 1 day;
2. stored in a desiccator in the Ar atmosphere of the glove box for 2 days;
3. stored in a desiccator for 10 days and then exposed to the Ar atmosphere of the glove box for 1 day;
4. stored in a desiccator for 11 days.

Table 1.5. Moisture Content Determined for $(U,Pu)O_2$ Pellets When Analyzer Protected From Air During Loading

Sample Number	Moisture Content After Designated Treatment,[a] ppm			
	1	2	3	4
1	24.4	20.7	17.9	18.8
2	15.7	20.9	14.6	13.1
3	18.7	19.1		
Average	19.6±4.6[b]	20.2±4.6[b]	16.2±5.6[b]	15.9±5.6[b]
Standard Deviation[c]	3.23	3.23	3.23	3.23

[a]Treatment 1: sealed in a metal can in the Ar atmosphere of a glove box immediately after unloaded from furnace, stored in can in air for 1 day.
Treatment 2: stored in a desiccator in the Ar atmosphere of a glove box for 2 days.
Treatment 3: stored in a desiccator for 10 days, then exposed to the Ar atmosphere of a glove box for 1 day.
Treatment 4: stored in a desiccator for 11 days.

[b]Range indicates 95% confidence limit on average.

[c]Determined from analysis of variance.

We believe that, for all future moisture analyses, some arrangement should be made to prevent introduction of air into the system when the sample is loaded. We are designing an "air lock" device, but, until it is fabricated, we are using plastic glove bags.

Relocation of Alpha Facility (R. A. Bradley, J. D. Sease)

The Fuel Cycle Alpha Facility was constructed to replace the Interim Alpha Facility, which has been operated by the Metals and Ceramics and the Chemical Technology Divisions since 1964. The new facility consists of two 24 × 48-ft alpha laboratories and a 24 × 24-ft laboratory for the prototype coating furnace. The laboratories and the arrangement of equipment are shown in Fig. 1.1. The laboratory that contains the coating furnace is designated laboratory 1; the two alpha laboratories are designated laboratories 2 and 3. Operations in

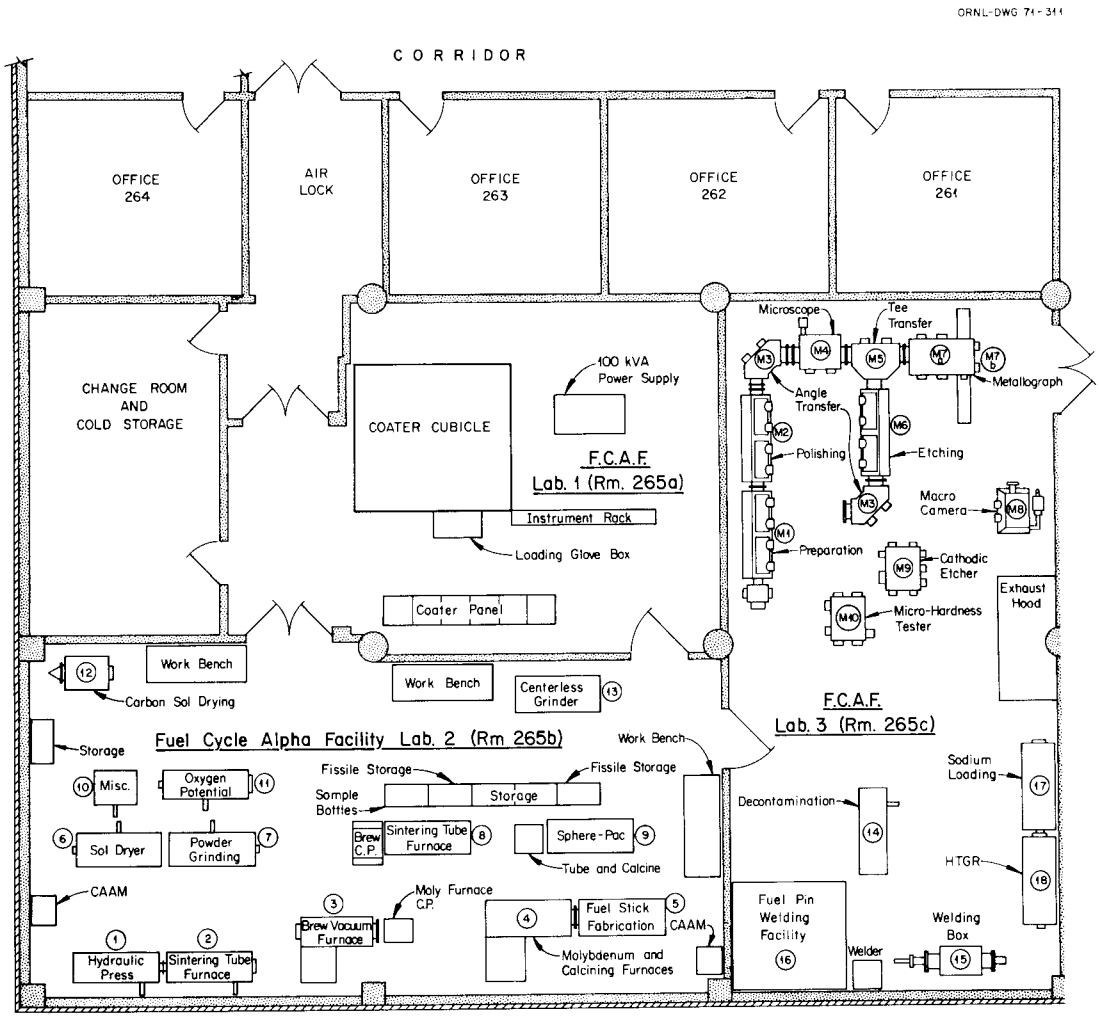

Fig. 1.1. Layout of Fuel Cycle Alpha Facility and Capsule Assembly Laboratory.

laboratory 1 will not involve work with highly alpha-active materials. Initially, the principal operations in laboratory 2 will be

1. preparation of $(U,Pu)O_2$ powder,
2. fabrication of $(U,Pu)O_2$ fuels,
3. heat treatment of oxide, carbides, or nitrides that contain Pu,
4. centerless grinding of ceramic fuel bodies,
5. loading of fuel rods, and
6. storage of fissile material.

Laboratory 3 will initially be used for

1. metallography of alpha-active materials,
2. welding of fuel rods,

3. decontamination of fuel rods,
4. Na and/or NaK bonding of fuels, and
5. storage of fissile materials.

Construction was completed. An operational safety analysis was written, and that portion that pertained to air-handling systems was reviewed by the Radioactive Operations Committee. The room-air and glove-box exhaust systems were put into operation and tested thoroughly. Approval to move Pu-contaminated glove boxes into the Fuel Cycle Alpha Facility was received from the Radioactive Operations Committee and the Metals and Ceramics Division Radiation Control Officer.

All of the glove boxes were moved from the Interim Alpha Facility to the Fuel Cycle Alpha Facility and connected to the glove-box exhaust system. We are now installing equipment in glove boxes and connecting utilities.

Behavior of Fission Products in Oxide Fuels (J. M. Leitnaker)

Fission products in mixed oxides may cause several important effects. They may interact directly with the cladding material, affect the O potential of the fuel so that O will react with the cladding material, or, by their volume, cause the cladding to swell.

We are beginning to investigate these effects. Initially, we are studying the Eu-U-O system. We intend to broaden this study to the Nd-U-O system as soon as possible and, finally, to extrapolate the work on these systems to predict the behavior of all rare-earth fission products.

Studies of $EuO_{1.5}$ in UO_2. — Modifications to equipment described previously[10] were nearly completed. A high-temperature furnace with Pt-Rh windings was obtained and is being installed. Experimental work on the actual system can now proceed.

Thermal Expansion of Solid Solution of Rare-Earth Oxide and UO_2 (L. A. Harris)

The objective of our x-ray study is to obtain the lattice constants for a series of mixed oxides of U and Eu as a function of temperature and O pressure so that quantitative data can be obtained on which we

may base extrapolations of the behavior of all fission products. The method of investigation involves the use of a high-temperature x-ray diffractometer attachment and various mixtures of CO and CO_2 as well as H_2.

We investigated solid-solution mixtures of U and Eu oxides containing 0, 10, 15, 30, and 40 mole % Eu. We mixed these samples with equal weights of ThO_2, which we used as an internal standard. The mixtures were formed into slurries by wetting them with alcohol and then deposited upon the Pt sample holder by means of an eye dropper. Temperatures were read by means of a Pt vs Pt–10% Rh thermocouple spot welded to the bottom of the sample holder.

The first set of experiments was carried out in a flowing gas mixture of 90.65 vol % CO to 9.35 vol % CO_2. The adjusted lattice constants are listed below as a function of temperature:

Temperature (°C)	Lattice Constant (Å)
UO_2	
Room	5.468
322	5.482
632	5.501
944	5.519
$(U_{0.9},Eu_{0.1})O_{2\pm y}$	
Room	5.459
400	5.482
820	5.505
1170	5.524
$(U_{0.85},Eu_{0.15})O_{2\pm x}$	
Room	5.438
330	5.460
606	5.477
944	5.497
$(U_{0.7},Eu_{0.3})O_{2\pm x}$	
Room	5.423
216	5.431
411	5.451
610	5.462
965	5.485
$(U_{0.6},Eu_{0.4})O_{2\pm x}$	
Room	5.415
356	5.435
614	5.453
912	5.476

A plot of these lattice constants against temperature appears to be linear.

A plot of the data for thermal expansion versus temperature for the UO_2 specimen (Fig. 1.2) is in good agreement with that for similar data reported by Smith,[11] who used an identical high-temperature x-ray diffractometer attachment.

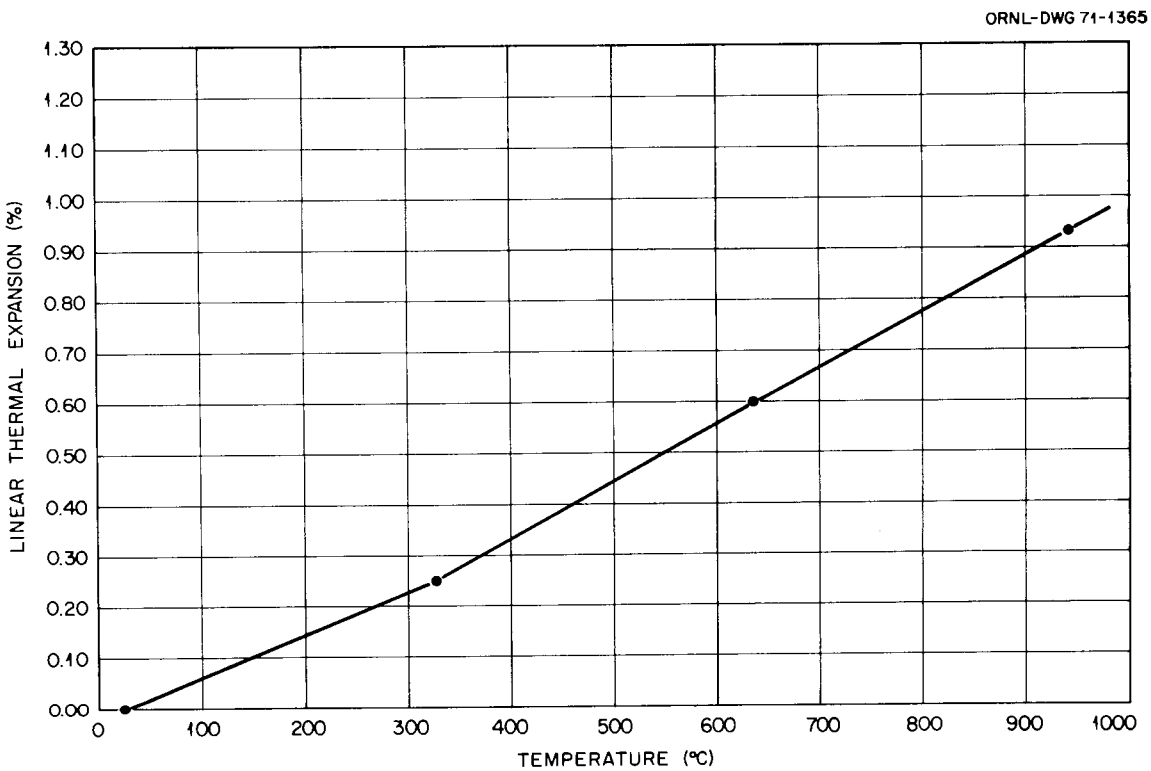

Fig. 1.2. Thermal Expansion of UO_2 ($CO:CO_2$ = 90.65/9.35).

Irradiation Testing of $(U,Pu)O_2$ Fuels

C. M. Cox T. N. Washburn

The performance characteristics of mixed $(U,Pu)O_2$ fuels are being evaluated in a variety of irradiation tests for potential application in an LMFBR. We are now concentrating on comparative tests of fuel fabricated as pellets or as microspheres loaded by the Sphere-Pac technique. The program includes thermal-flux experiments, which permit

use of instrumented capsules and continuously controlled heat rates, and fast-flux experiments, in which the fission-rate distribution and radiation effects on the cladding are more typical of those for operating conditions anticipated in an LMFBR.

Fast-Flux Irradiation Tests (A. R. Olsen)

The fast-flux irradiation tests in the EBR-II are designed to approximate conditions to be encountered in a commercial-scale LMFBR. The objective of these tests is to establish the effects of fuel fabrication form (Sphere-Pac or pellet), void distribution, and stoichiometry on the swelling of the fuel, mechanical and chemical interactions of fuel and cladding, release of fission gas, and distribution of fission products in a $(U,Pu)O_2$ fuel operating at typical heat rates to design levels of burnup.

The five series I encapsulated tests all contain Sphere-Pac fuels. Two of the capsules, S-1-A and S-1-E, were returned to ORNL after the initial period of irradiation in subassembly X 050, which was discharged from the EBR-II at the end of run 42 on May 18, 1970. The other three capsules are scheduled for continued irradiation in a new subassembly. Table 1.6 shows the recently revised estimates of peak burnup for each of the five capsules. These estimates are based on the advertised EBR-II fission rates.

Only capsule S-1-E was originally scheduled for destructive examination; capsule S-1-A was to be held for a transient test at a later date. However, since both fuel pins were removed from their capsules, complete dimensional data were obtained on both. These data are currently being analyzed statistically. The peak fluence (> 0.1 MeV) for both pins was about 4×10^{22} neutrons/cm^2. The maximum diametral change for the S-1-A pin, which had type 304 stainless steel cladding, was 0.0018 in.; the comparable change for the S-1-E pin, which had type 316 stainless steel cladding, was 0.0010 in. These values are the largest changes derived from averaging four diametral measurements at each of 45 selected axial locations both before and after irradiation. This difference between the two types of stainless steels seems consistent with measured density changes due to void formation reported by Claudson et al.[12]

Table 1.6. Series I Sphere-Pac $(U_{0.8},Pu_{0.2})O_{1.98}$ Capsules Irradiated in EBR-II

Capsule Identification	Type Stainless Steel Cladding Material	Fuel Smear Density (% of theoretical)	Peak Linear[a] Heat Rate (kW/ft)	Peak Temperature at Inside Surface of Cladding (°C)	Peak Burnup, % FIMA	
					Current[b]	Target
S-1-A	304	83	14	570	5.9	5.9
S-1-B	304	86	14	600	6.0	11.8
S-1-C	316	83	14	590	6.2	11.8
S-1-D	316	80	13	580	6.1	11.8
S-1-E	316	82	14	590	6.0	6.0

[a]Calculated with EBR-II fission rates.

[b]Calculated through EBR-II run 42.

Based on the calculated average burnup level of 5.4% FIMA for pin S-1-E, 78% of the ^{85}Kr and 74% of all of the Xe isotope fission gases were released. This release is about twice that found in similar fuel irradiated in a thermal flux to similar burnup levels.[13,14] We anticipated this difference for two reasons: (1) a higher percentage of the fuel in pin S-1-E operated at temperatures above 1750°C (about 75% for the fast-flux case and as low as 20% for the thermal-flux cases), and (2), due to depression of the thermal-neutron flux, more fissions occurred in the cooler regions of the fuel in the thermal-flux tests.

Selected sections of pin S-1-E were removed for burnup analysis and metallographic examination. Although neither examination is complete, the two transverse metallographic sections removed from the bottom and center of the fuel pin were examined by optical microscopy. Photographic composites of these sections at low magnification are shown in Fig. 1.3.

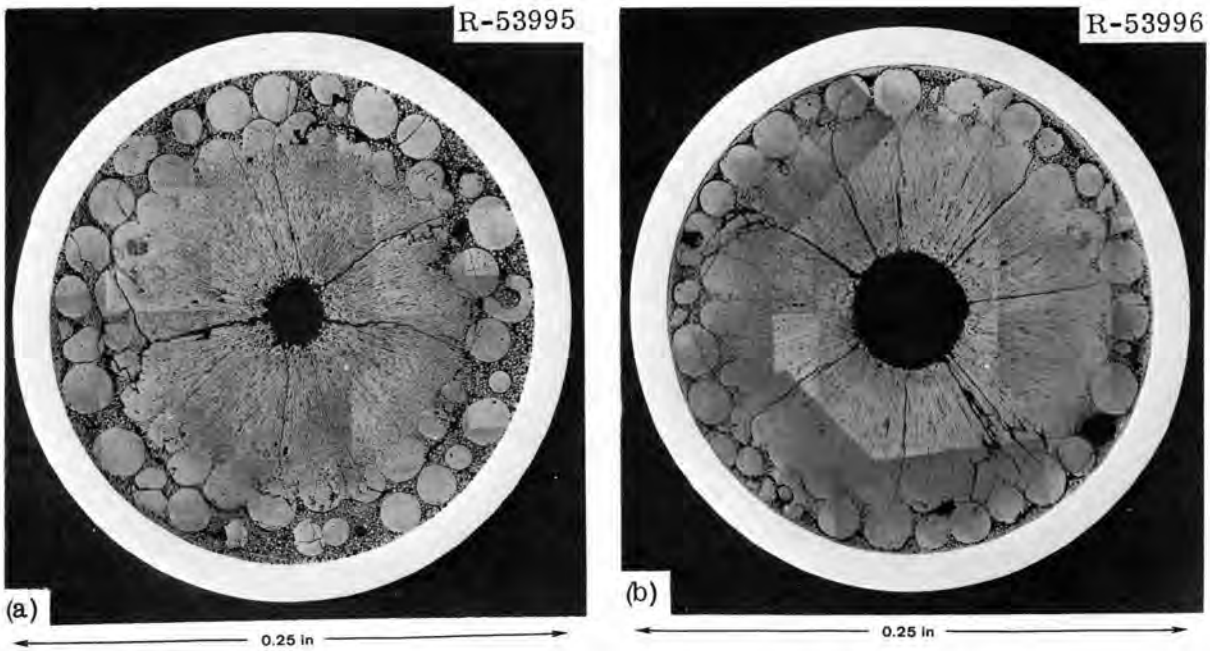

Fig. 1.3. Transverse Metallographic Sections from the Fuel Pin in EBR-II Capsule S-1-E. (a) Section from bottom of pin operated at 11 kW/ft with a calculated temperature of 490°C at the inside surface of the cladding; (b) section from center of pin operated at 13 kW/ft with a calculated temperature of 550°C at the inside surface of the cladding.

The extent of fuel restructuring and the diameter of the central void increased with increasing fission rate from the bottom to the center section. There is no evidence of chemical interaction between fuel and cladding in either section.

We plan additional examinations for these sections and sections from the top of the fuel column. These include measurements of grain growth, analysis of porosity distribution, and electron microprobe analysis for fuel components and fission products.

The series II unencapsulated pin tests were described previously.[2] These tests will be run in subassembly X-112 together with similar fuel pins fabricated by the Babcock & Wilcox Company. The data package for the subassembly was submitted to the EBR-II project for review; approval was granted for shipment of the ORNL pins to the site. Although only 19 ORNL pins are scheduled for insertion in the first subassembly, we shipped 20 pins so that a spare would be available.

The base composition for all fuel in both the ORNL and Babcock & Wilcox pins is $(U_{0.8},Pu_{0.2})O_2$. All ORNL pins contain sol-gel-derived fuel, while the Babcock & Wilcox pellets and Vi-Pac shards were made by coprecipitation. The two programs have been coordinated to obtain data for (1) the qualification of vibratorily compacted $(U,Pu)O_2$ particulate fuel (spheres and shards) for LMFBR use and (2) the comparison of performance characteristics of pellets fabricated from coprecipitated or sol-gel-derived powders. The emphasis in these tests is on the effects of fuel form and void distribution on the release of fission gas, redistribution of fission products, and mechanical and chemical interactions of fuel and cladding at linear heat rates of about 14 kW/ft to burnup levels greater than 50,000 MWd/metric ton of U plus Pu with cladding temperatures of 550 to 650°C.

The pins are scheduled for irradiation in an N-37 subassembly, but they can be installed in a J-37-A or an E-37 subassembly. The initial subassembly loading is scheduled for irradiation to an average burnup of 50,000 MWd/metric ton of U plus Pu. Table 1.7 shows the planned burnup levels for the various fuel forms.

Table 1.7. Summary Sheet for Babcock & Wilcox and ORNL Programs

Burnup (MWd/metric ton)	Number of Pins Removed at Scheduled Withdrawals of Subassembly	Number of Pins Achieving Indicated Burnup				
		Sphere-Pac		Vi-Pac	Pellets	
		ORNL	B & W	B & W	ORNL	B & W
$\times 10^3$						
25		2	3	2	0	2
50	12	10	2	2	8	2
75	9	2	3	2	0	2
100	37	5	3	3	3	2
TOTAL		19	11	9	11	8

We began assembling and inspecting the hardware components for the fabrication of the replacement pins to be installed in the second and third subassembly loadings.

Transient Tests (C. M. Cox, D. R. Cuneo[15])

Examinations of the six fuel pins in capsules TR-1 and TR-2 were completed. These fuel pins contained unirradiated pellet and Sphere-Pac $(U_{0.80},Pu_{0.20})O_{1.98}$ and were subjected to severe power transients at the TREAT that melted up to 50% of the fuel. None of the pins failed. Design and operating conditions, metallographic examinations after irradiation, and our initial evaluation of the results were reported.[16,17]

A multiple regression analysis correlating the observed and predicted extent of fuel melting for the pin that operated at peak power, TR-2B, indicates that the coefficient for heat transfer from fuel to cladding is about twice that inferred from Fitts'[18] steady-state data.

Uninstrumented Thermal-Flux Irradiation Tests (A. R. Olsen, D. R. Cuneo,[15] R. A. Bradley)

A series of uninstrumented capsules is being irradiated in the X-basket facilities of the ETR. Each capsule contains four test pins

arranged in tandem. The initial objective of these tests was to investigate the effects of fabrication form and extended burnup on release of fission gas, migration of fission products, and swelling of the fuel. Some capsules are now being irradiated specifically to provide short-cooled irradiated fuel for LMFBR reprocessing studies. The current status of these tests is given in Table 1.8.

The accumulation of the final small amount of burnup on capsule 43-113 was delayed by operational difficulties at the ETR, but this capsule is now scheduled for discharge in February at the end of ETR cycle 110.

Capsules 43-117, -118, and -119 were assembled and shipped to the reactor. All three capsules are being irradiated for reprocessing studies and have operated in the reactor without incident. Details of the fuel processing and capsule loadings are described elsewhere in this report.[8]

Instrumented Tests in the ETR (T. N. Washburn, M. K. Preston[1])

The instrumented tests in the ETR are designed to determine the performance of sol-gel-derived fuel under simulated LMFBR design operating conditions. The first two capsules (43-120 and -121) are being irradiated to investigate fuel swelling and the chemical interactions of fuel and cladding for Sphere-Pac and pellet fuels. These capsules were irradiated through cycle 109E or about 104 effective days at full power (about 2.3% FIMA peak) as of December 3, 1970. The thermal performance of these capsules to date closely matches the design conditions. Table 1.9 summarizes the properties of the fuel and the latest operating conditions. The ETR fuel loading was changed during November, and the peak fuel pin is operating with a temperature of 630°C at the inside surface of the cladding. Therefore, these capsules will not be moved to positions of higher flux until March or April 1971.

During ETR cycle 109A, the neutron flux was measured in positions C-11-SE and C-10-SE, and the gamma heating was measured for several

Table 1.8. Noninstrumented Thermal-Flux Tests of $(U,Pu)O_2$ Fuels

Experiment Number	Fuel		Number of Pins	Peak Burnup (% FIMA)	Peak Linear Heat Rate (W/cm)	Peak Temperature at Inner Surface of Cladding (°C)	Status December 1970
	Form	Composition					
43-99	Sphere-Pac	$(^{235}U_{0.80},Pu_{0.20})O_{2.00}$	2	1.5[a]	1640[a]	1000	Examined
43-100	Sphere-Pac	$(^{235}U_{0.80},Pu_{0.20})O_{2.00}$	2	1.4[a]	1470[a]	900	Examined
43-103	Sphere-Pac Pellet	$UO_{2.02}$ (20% ^{235}U) $UO_{2.00}$ (20% ^{235}U)	3 1	5	690	530	Examined
43-112	Sphere-Pac	$(^{238}U_{0.85},Pu_{0.15})O_{1.97}$ $UO_{2.02}$ (20% ^{235}U)	3 1	0.7	500	360	Examined
43-113	Sphere-Pac	$^{238}U_{0.85},Pu_{0.15})O_{1.97}$ $UO_{2.02}$ (20% ^{235}U)	3 1	10[b]	500[b]	380[b]	In-reactor, ≅ 9.9% FIMA
43-115	Sphere-Pac	$(^{238}U_{0.85},Pu_{0.15})O_{1.97}$ $UO_{2.02}$ (20% ^{235}U)	3 1	6.5	600	460	Examined
43-116	Sphere-Pac	$(^{238}U_{0.85},Pu_{0.15})O_{1.97}$	4	1.5[b]	600[b]	460[b]	Processed
43-117	FTR Pellets	$(^{238}U_{0.75},Pu_{0.25})O_{1.98}$	4	1.5	430[b]	360[b]	In-reactor
43-118	FTR Pellets	$(^{238}U_{0.75},Pu_{0.25})O_{1.98}$	4	4.0	430[b]	360[b]	In-reactor
43-119	FTR Pellets	$(^{238}U_{0.75},Pu_{0.25})O_{1.98}$	4	8.0	430[b]	360[b]	In-reactor
43-123	FTR Pellets	$(^{238}U_{0.75},Pu_{0.25})O_{1.98}$	4	4.0	350[b]	310[b]	In preparation

[a]Pins failed in reactor from overpowering.

[b]These are target design values.

Table 1.9. Operating Conditions for ETR Instrumented Test Capsules 43-120 and 43-121, December 3, 1970

Fuel Pin Number	Type of Fuel[a]	Smear Density (% of theoretical)	Gas Release (cm^3/g)	Heat Rate (kW/ft)	Peak Temperature at Inside Surface of Cladding[b] (°C)	Approximate Peak Burnup (% FIMA)
120-1	Pellet	81.1	0.04	16.2	600	2.1
120-2	Pellet	81.5	0.04	16.6	610	2.3
120-3	Sphere-Pac	84.8	0.10	16.0	590	2.1
120-4	Sphere-Pac	84.6	0.10	10.7	430	1.4
121-1	Pellet	81.0	0.04	15.0	560	1.8
121-2	Pellet	81.2	0.04	17.3	630	2.3
121-3	Sphere-Pac	83.9	0.10	13.7	520	1.8
121-4	Sphere-Pac	85.5	0.10	10.4	420	1.4

[a]Ratio O:metal = 1.985±0.005; ratio Pu:(U + Pu) = 20%.

[b]Outside diameter of cladding = 0.250 in.; wall thickness = 0.016 in.

positions during the shutdown at midcycle 109. These data will permit better correlation between the thermocouple readings and the rate of heat generation.

Each of the second two capsules in this series will contain one fuel pin that has a 20-in.-long column of fuel. One capsule[18] will contain U-Fine Sphere-Pac fuel, and the other capsule will contain pellets to permit a direct comparison of these two forms of fuel. The purposes of this test are (1) to investigate the chemical interaction between fuel and cladding over a wide range of cladding temperatures to a maximum of 650°C, (2) to determine the release of fission gas as a function of burnup and load cycling, (3) to determine the performance of a long fuel column of Sphere-Pac fuel, and (4) to check the U-Fine fabrication process. The design was completed, and the capsule components are being fabricated.

Tests of Thermal Performance (R. B. Fitts, E. L. Long, Jr., J. L Miller, Jr.)

These irradiation tests are designed[19] to monitor the thermal performance of fuel pins in the ORR poolside facility.[20] The temperatures of the cladding and fuel center and the rates of heat generation are continuously measured and recorded. These data are being used to evaluate the thermal characteristics of various fuels in-reactor and the effects of irradiation conditions upon the temperatures and rates of structural change within the operating fuels.

The third capsule irradiated in this series, capsule SG-3, is being examined. This capsule contained one fuel pin of $(U_{0.8},Pu_{0.2})O_{1.99}$ Sphere-Pac[21] fuel at a smear density of 82% of theoretical and a second fuel pin of 83.5% dense sol-gel pellet[22] fuel of the same composition and smear density. This experiment provided a direct comparison of these fuels to fuel-center temperatures near 2000°C.

The structures of these two fuels are shown in Fig. 1.4 after irradiation to a burnup of about 4500 MWd/metric ton, including about 40 hr at the peak central temperature of 2000°C. The extent of restructuring is virtually identical, although there are differences in the microstructural details. The temperature scales indicated on the figure were

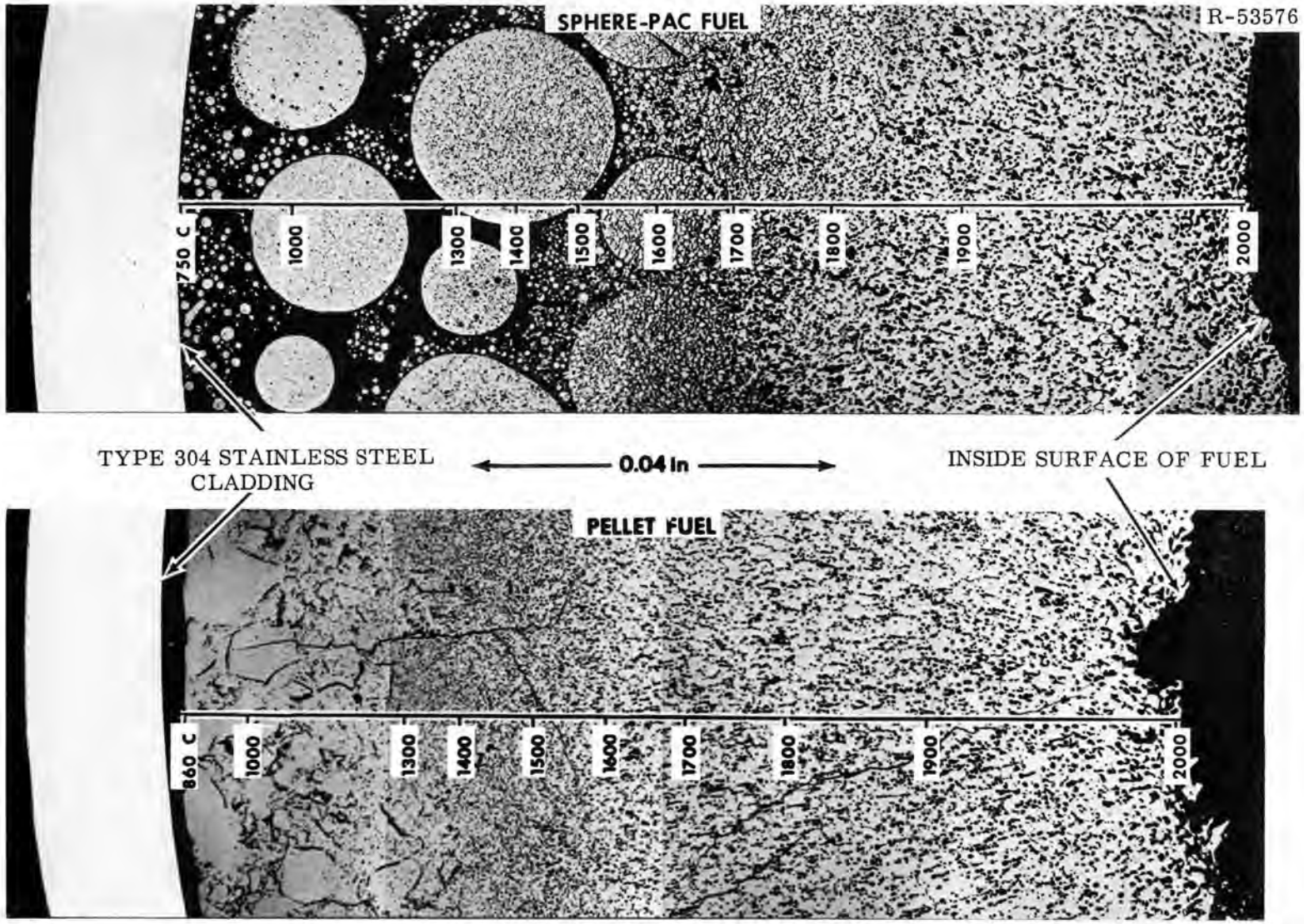

Fig. 1.4. Transverse Sections of $(U_{0.8},Pu_{0.2})O_{1.99}$ Fuel Irradiated at a Maximum Heat Rating of 16 kW/ft and Central Temperature of 2000°C.

computed[23] from the temperatures measured at the fuel center and the surface of the cladding, the measured rates of heat generation, and reported data[24] on the thermal conductivity of 82% dense $(U,Pu)O_2$ fuel. The calculation, therefore, assumes only that the fuel conductivity is the same for pellet and Sphere-Pac fuel.

The temperatures indicated at the surface of the fuel permit the evaluation of the coefficient for heat transfer between fuel and cladding for these two fuel forms. The gap conductance for the pellet fuel was 0.73 W cm^{-2} $°C^{-1}$, which is consistent with data from similar analyses made at other sites.[25] The gap conductance for the Sphere-Pac fuel pin was 1.93 W cm^{-2} $°C^{-1}$. Recent analyses of results from transient irradiations of Sphere-Pac fuel indicate a value about a factor of 2 greater during the transients.[26]

The first discernible outlining of grain boundaries (porosity concentration in the grain boundaries) was observed in both fuels at about 1300°C. The occurrence of this phenomenon at the same calculated temperature in both fuel forms leads to confidence in our method of calculation and in the assumption of identical thermal conductivities for the two fuels. The microsphere structure completely disappears from the Sphere-Pac fuel at 1700°C. These two observations provide valuable correlations between temperature and structure for use in the analysis of uninstrumented tests.

The temperatures of the cladding, coolant, and fuel center are shown in Fig. 1.5 for the two pins; the calculated fuel temperature is shown for comparison. The fuel temperatures are within ±8% of the calculated temperatures; we believe these temperature differences to be within experimental accuracy. The release of fission gases was essentially the same in both fuel pins (about 13%).

This experiment showed that, at least at low burnup, the degree of restructuring, the release of fission gas, and the operating temperatures in particulate (Sphere-Pac) and pellet fuels are essentially the same for initial fuel densities of 82% of theoretical.

Microprobe Analysis of SG-3 Fuel Pins. — Metallographic samples from the pellet and Sphere-Pac fuel pins in capsule SG-3 were examined by means of a shielded electron microprobe. The pellet fuel pin showed

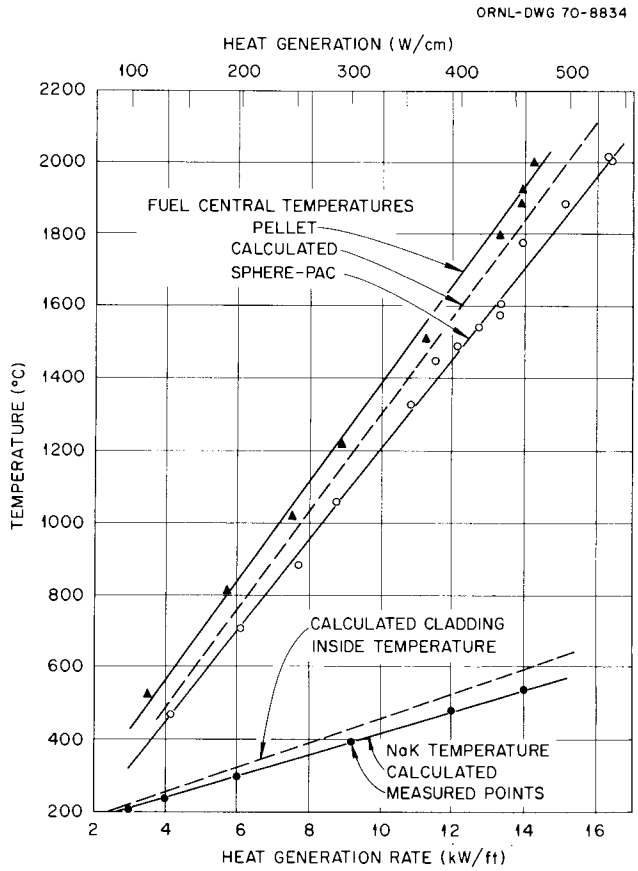

Fig. 1.5. Variation of Calculated and Measured Temperatures for Fuel and Capsule with Rate of Heat Generation in Capsule SG-3.

metallic particles in cracks near the fuel surface, some metal in the grain boundaries of the fuel adjacent to the thermocouple well, and some attack of the grain boundaries in the Ti-modified type 304 stainless steel cladding. The Sphere-Pac fuel pin showed no evidence of attack in the cladding but did show evidence of some attack on the W–3% Re thermocouple wires and the inside of the W–26% Re thermocouple sheath.

The grain boundaries of the Ti-modified type 304 stainless steel on the pellet fuel pin were attacked to a depth of 0.003 to 0.004 in. (see Fig. 1.6) during operation to peak temperatures of about 600°C. The microprobe showed only the normal constituents of type 304 stainless steel plus Ti in the body of the grains. The attacked grain boundaries were depleted of Fe and Cr. No material was detected that might have

Fig. 1.6. Attack of Grain Boundaries in Titanium-Modified Type 304 Stainless Steel Cladding from Pellet Fuel Pin in Capsule SG-3. 500×.

contributed to this attack. Since the sample was prepared with a water-base polishing medium, some materials (Cs compounds for instance) could have been lost during sample preparation.

The material deposited in the cracks at the surface of the fuel extended as much as 0.020 in. into the fuel. In some places this material was predominantly Fe and, in others, predominantly Cr. In addition, there was a discontinuous metallic layer rich in Cr on the surface of the fuel, and, where fuel adhered to the cladding, a layer rich in Fe on the inside edge of adherent fuel particles. There was no evidence of a uniform reaction layer between fuel and cladding, although there were areas in which such a layer might have been beginning to form. The metallic material shown in Fig. 1.7 was adjacent to the thermocouple sheath near the center of the fuel and in the fuel. This material was W–26% Re, which, undoubtedly, came from the thermocouple sheath. A cross section of the thermocouple in the Sphere-Pac fuel pin is shown in Fig. 1.8. Other thermocouple areas show circumferentially uniform porosity

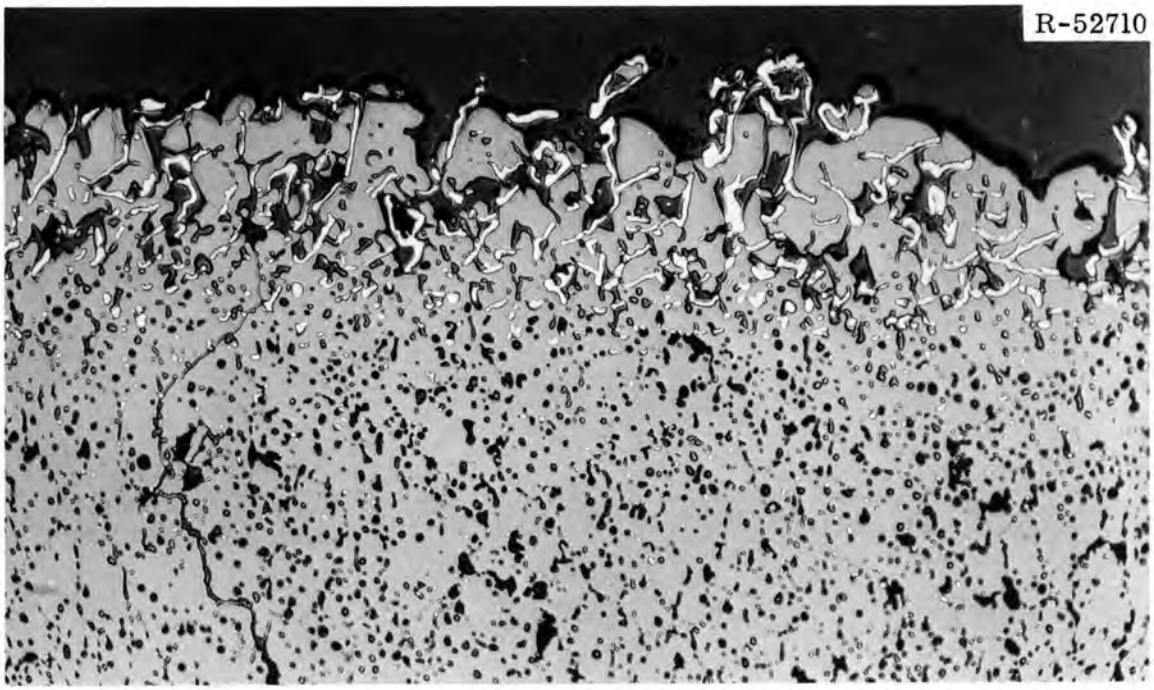

Fig. 1.7. Fuel From Pellet Fuel Pin in Capsule SG-3 Showing Metallic Deposit Adjacent to Thermowell. 100×.

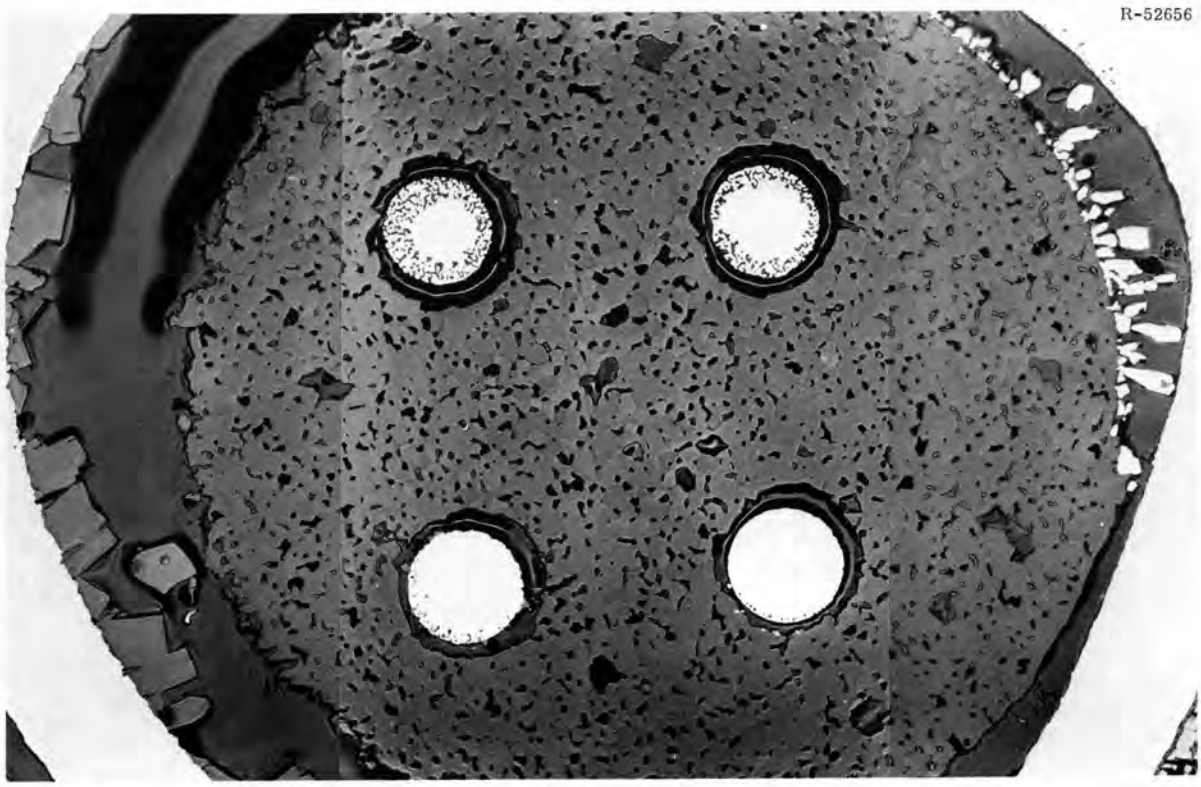

Fig. 1.8. Cross Section of W–3% Re vs W–25% Re Thermocouple From Sphere-Pac Fuel Pin in Capsule SG-3. 100×. Reduced 38%.

penetrating radially 25 to 50% of the way through the W–3% Re wire and slight loss of material from the W–25% Re wires. There was no evidence of selective loss of W or Re. The thermocouple sheath contained a small amount of porosity adjacent to the location where crystals of W–26% Re sheath material were deposited on the BeO thermocouple-insulator pellet. Directly opposite this location, ceramic crystals, probably BeO, were deposited on the inside of the thermocouple sheath. The thermocouple operated successfully throughout the test, but reactions took place that, if they had not ceased, could have caused its eventual failure.

Tests of Mechanical Interaction of Fuel and Cladding (R. B. Fitts, R. L. Senn[27])

The intent of our program is to measure in-reactor the axial extension of both the fuel column and cladding and also the internal gas pressure in a fuel pin during operation of prototypic LMFBR fuel pins under carefully controlled conditions. These include programmed power cycles and an occasional overpower cycle. The irradiation capsules are designed so that the fuel pin operates in the ORR poolside irradiation facility[20] at power and temperature conditions typical of those expected in early LMFBR's. The irradiation tests will last 1 to 2 years and will give burnup levels of 5 to 9%.

As described previously,[28] the first in-reactor power-cycling capsule (MINT-1) will contain a prototype FTR fuel pin. All of the parts for the fuel pin and capsule were procured and are being assembled. Insertion of the capsule into the reactor was delayed until February because of difficulties in the development of the in-test calibration system for the displacement transducers. This delay was considered worthwhile, since the calibration system will greatly increase our confidence in the test results.

A one-dimensional analysis of the temperature distribution in the MINT-1 capsule as a function of heat generation in the test fuel pin, made with the GENGTC computer code,[29] is shown in Fig. 1.9. The previously reported[28] operating schedule for the MINT-1 capsule will be revised to reflect these calculated operating temperatures.

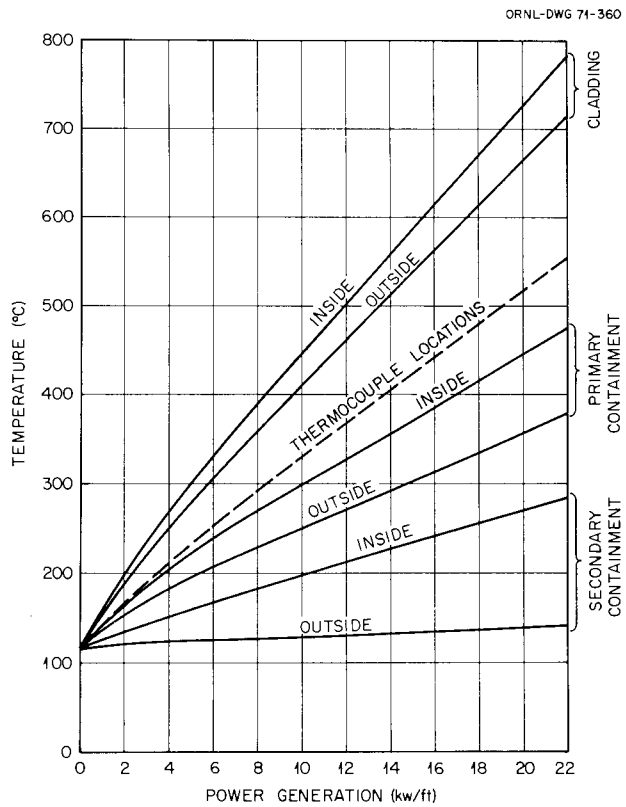

Fig. 1.9. Temperature Profiles for the MINT Capsules.

A two-dimensional (R,θ) analysis of the effects of cladding thermocouples on the temperature distribution within the capsule was made by H. C. Roland[30] with the HEATING code[31] and temperature-dependent thermal conductivities for the capsule materials. Axially symmetric heat generation in the fuel and circumferentially uniform temperatures at the outer surface of the capsule were assumed. The analysis indicated that, for three adjacent thermocouples in the NaK annulus at 19 kW/ft heat generation in the fuel, the maximum temperature difference between cold and hot spots at circumferential intervals of 90 deg on the outer surface of the cladding would be 45°C. Since there are three adjacent thermocouples only in the lower 2 in. of the fuel pin, where the heat generation is usually less than the maximum, and since 19 kW/ft is the peak overpower heat-generation rate, this difference of 45°C is an upper limit for the temperature perturbation induced by thermocouples. For the normal midplane conditions, where there are two thermocouples and

a heat-generation rate of 16 kW/ft, the temperature differential around the cladding was calculated to be only 20°C. These are considered to be acceptable variations. The temperatures calculated for various positions in the capsule agree well with the one-dimensional analysis of heat transfer. We plan further calculations to evaluate the effects of the off-center condition of heat generation that will actually exist in these tests.

The in-test calibration system for the MINT capsules provides for movement of the measuring train to two known positions to permit checking and, if necessary, partial recalibration of the displacement transducers during in-reactor operation of the capsules. An electromagnet lifts the measuring train to the test positions, which are above the normal measuring range employed in the experiment. These positions are fixed by a cam-and-pin arrangement, as illustrated in Fig. 1.10. This design has progressed through several bench tests. We have shown that the concept works, but early units were inconsistent and short-lived. Bench testing showed that the cams and drive pins were worn after about 100 cycles, although some units continued to operate intermittently to about 300 cycles. Improvements made to provide longer life have included use of hardened, high-speed steel for the cams and the drive pin. Careful assembly and alignment are required for these small devices.

The sixth bench-test assembly of the calibrating device, which provides two calibration points 0.051 in. apart, has operated successfully

ORNL-DWG 71-910

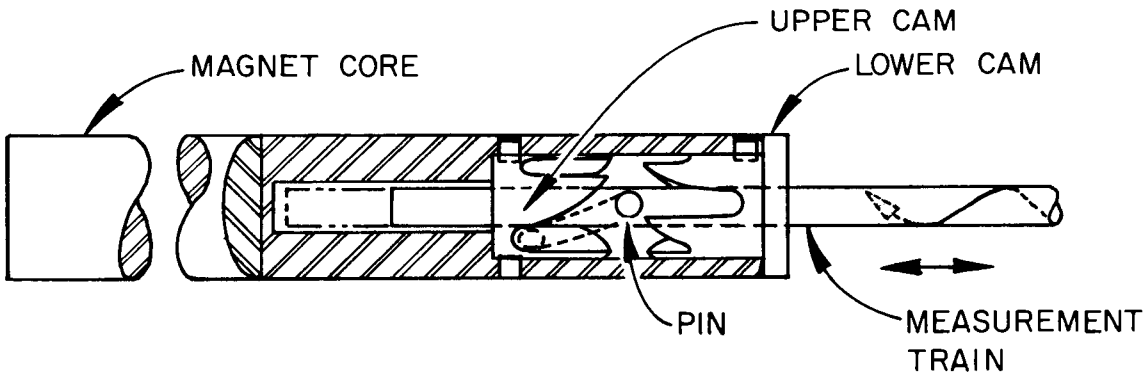

Fig. 1.10. In-Test Calibration Assembly.

for about 130 cycles. The displacement transducer and readout device reproduce the 0.051-in. distance between these calibration points to within about ±0.002 in., as measured with a micrometer. The core for this test is built with 17-4 PH stainless steel cams hardened to a Rockwell C-scale hardness of 40, and with a hardened drill rod actuating pin. The previous bench tests of these materials showed excessive wear on the cams. Parts now on order for the next test include cams made of high-speed steel hardened to a Rockwell C-scale hardness of 60.

We are also trying to reduce the impact of the push rod on the top of the fuel element as the magnet releases the core. It should be possible to release the magnet in such a way that the core will drop slowly rather than suddenly. We added a thin disk of stainless steel between the core and the magnet to prevent the core from reaching the point of maximum magnetic flux so that less energy change will be required to break contact. By externally programming the power supply with a timed step-function and/or ramp-function power reduction, we expect to be able to drop the core and push rod slowly and eliminate the impact problem. We have not yet developed the programming device, and, although we have a fair estimate of the sequence of power level and timing required, more bench testing is needed to establish the exact requirements.

The variable-permeance displacement transducers specified for the capsule were used for the last four bench tests and are operating satisfactorily. Signal-conditioning equipment for the transducers was received. Initial testing showed good response and linearity. The variable-permeance pressure transducer, coupled with the signal-conditioning equipment, is being tested and appears to be satisfactory. We are imposing about 100 pressure cycles (15 to 500 psig) per week plus continuous stable operation at 300 psig between cycles and looking for any changes in the calibration of the transducer due to pressure cycles or long-term operation.

The thermocouples that monitor the temperature of the cladding in the MINT-1 capsule are brazed to the inside wall of the primary containment tube. This locates the thermocouples on the outside of the NaK annulus that surrounds the fuel pin. The brazing alloy is preplaced by

plating layers of electrolessly deposited Ni and Cr on the thermocouple sheaths. The first test of this approach was successful, and a full mockup of the assembly is being prepared for a final proof test. In addition a dummy capsule is being prepared for testing in the Materials Compatibility Laboratory to verify the compatibility of this braze with NaK.

Analysis of Fuel Element Performance

C. M. Cox

The objectives of this work are a fundamental understanding of the behavior of LMFBR fuel elements and the development of analytical models to describe their performance and the probability of their failure under various operating conditions. Special emphasis is given to modeling mechanical interactions of fuel and cladding and to characterizing irradiated $(U,Pu)O_2$ fuels. This work is an integral part of the program of irradiation testing and provides design methods and evaluation of the tests.

Development of a Model for Fuel Restructuring (F. J. Homan)

It is well known that ceramic fuels are restructured during irradiation at elevated temperatures; the fabricated porosity apparently moves up the temperature gradient toward the thermal center. Our first efforts to describe this phenomenon mathematically were empirical in nature, as described in the PRØFIL code.[23] This approach, while useful for some applications, is clearly limited by its inability to consider the aspects of fuel restructuring that are dependent on time. Time dependence is important in the modeling of mechanical interactions of fuel and cladding (due to differential thermal expansion between fuel and cladding) that occur on startup of the fuel pin. Restructuring reduces fuel temperatures and thermal expansion; but unless the rate of restructuring is known, it is not possible to determine how quickly the mechanical interaction will diminish with decreasing fuel temperatures. We consider the restructuring process to include hot pressing,

sintering, and migration of pores to the thermal center. There are insufficient data on the sintering of potential LMFBR fuels at high temperatures to permit development of a quantitative model, and our primitive model for hot pressing[32] does not predict sufficiently rapid densification to be in agreement with what is observed experimentally. Accordingly, we recently added a model for pore migration to our FMØDEL code. The model is that proposed by Nichols;[33] the velocity of a pore is

$$v \cong \frac{9P_o\ \Omega\ \Delta H_v\ [N(M_1 + M_2)]^{1/2}\ \exp\left(\frac{-\Delta H_v^*}{RT}\right)\frac{dT}{dx}}{16P\sigma^2 T^{3/2}\ (2\pi k M_1 M_2)^{1/2}}\ , \qquad (1.1)$$

where

v = pore velocity (cm/sec),
P_o = a constant (dyne/cm^2),
Ω = fuel molecular volume (cm^3/molecule),
ΔH_v = molar heat of vaporization (erg/mole),
ΔH_v^* = molar heat of vaporization (cal/mole),
P = total pressure in pore (dyne/cm^2),
N = R/k = Avogadro's number (atoms/mole),
k = Boltzmann's constant = 1.38047×10^{-16} erg/°K,
R = gas constant = 1.986 cal/mole °K,
$\frac{dT}{dx}$ = temperature gradient (°C/cm^2),
M_1 = molecular weight of fuel (g/mole),
M_2 = molecular weight of primary vapor constituent (g/mole), and
$\pi\sigma^2$ = cross section for collisions between fuel and vapor species (cm^2).

Note that the pore velocity as given in Eq. (1.1) is independent of the size and shape of the pores. Therefore, according to this model, all pores at a given position within the fuel will move with the same velocity.

In order to calculate the time-dependent change in the porosity distribution in an operating fuel pin due to pores moving up the temperature gradient with the velocities described by Eq. (1.1), consider the physical situation associated with one radial increment of an axial

segment of unit length. The increment is bounded by R_i and R_{i+1} (the inner and outer radii, respectively), and characterized by temperatures T_i and T_{i+1} and temperature gradients $(dT/dx)_i$ and $(dT/dx)_{i+1}$. The pore velocities at R_i and R_{i+1} are v_i and v_{i+1}, respectively. Assume that initially there are N pores each with volume V in the axial fuel segment under consideration. The number of pores in the ith radial increment is then given by

$$N_i = A_i \, N/A_T \quad , \tag{1.2}$$

where

A_i = cross sectional area of the ith radial increment, and

A_T = cross sectional area of the entire fuel segment.

In t seconds, all pores in the annulus bounded by R_i and $R_i + v_i t$ will leave the ith radial increment, and all pores in the annulus bounded by R_{i+1} and $R_{i+1} + v_{i+1} t$ will enter the increment. The number of pores entering will, therefore, be

$$N_i' = \frac{N_i \pi}{A_i} \left[(R_i + v_i t)^2 - R_i^2 \right] \quad , \tag{1.3}$$

and the number of pores leaving the increment will be

$$N_{i+1}' = \frac{N_{i+1} \pi}{A_{i+1}} \left[(R_{i+1} + v_{i+1} t)^2 - R_{i+1}^2 \right] \quad . \tag{1.4}$$

Thus, the ith increment will have gained $N_{i+1}' - N_i'$ pores. The total number of pores now in the increment will be

$$N_i'' = N_i + N_{i+1}' - N_i' \quad . \tag{1.5}$$

The fractional porosity in the ith increment will then be

$$P_i = \frac{N_i'' \, (V)}{A_i} \quad , \tag{1.6}$$

whereas the initial porosity fraction was

$$(P_i)_o = \frac{NV}{A_t} \quad . \tag{1.7}$$

The ratio

$$\frac{P_i}{(P_i)_o} = \frac{A_t}{A_i}\left(\frac{N_i''}{N}\right) \tag{1.8}$$

reduces to

$$\frac{P_i}{(P_i)_o} = 1 + \frac{\pi}{A_i}\left[(R_{i+1} + v_{i+1}t)^2 - R_{i+1}^2 - (R_i + v_i t)^2 + R_i^2\right] , \tag{1.9}$$

which is dependent only upon geometry, the bubble velocities at R_i and R_{i+1}, and the time step considered. The initial number of pores (N) and volume of a single pore (V) cancelled out of the expression.

Note that this approach depends upon the assumption that the pore velocity v_i is described by the temperature T_i and temperature gradient $(dT/dx)_i$, not just at the radial node R_i but throughout the entire neighborhood of this node. This is only approximately correct. In the FMØDEL code, temperature and temperature gradients are calculated only at radial nodes and assumed to vary linearly between nodes. To prevent large errors from being introduced into the calculations of porosity, the time step t is restricted so that the distance $v_i t$ can never exceed $(R_{i+1} - R_i)/3$. Temperature distributions are recalculated after every t-sec period, and the new temperatures and temperature gradients are used in the subsequent calculation of porosity distribution. This sequence is repeated until the entire time period of interest has been considered.

Some quantitative results obtained with this method are presented in Figs. 1.11 and 1.12. In making these calculations, we used data representative of the central axial region of General Electric pin F2H and UO_2 data[33] for the constants in Eq. (1.1). In Fig. 1.11, the local heat rate, central fuel temperature, and void radius are plotted against elapsed time. Note the change in the time scale at about 6 hr. The

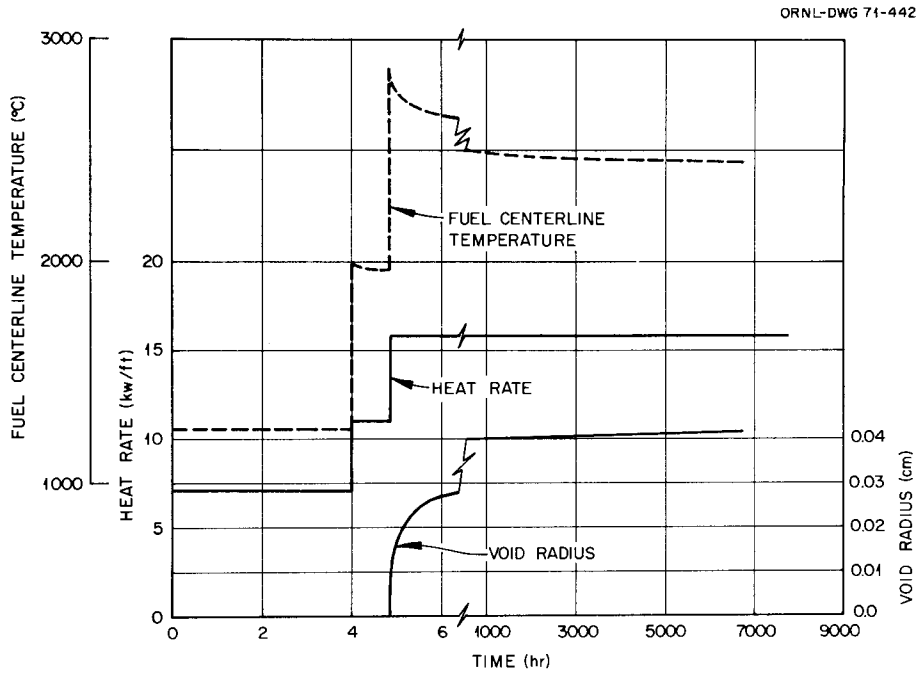

Fig. 1.11. Calculated Heat Rate, Temperature at Fuel Center, and Void Radius as Functions of Time.

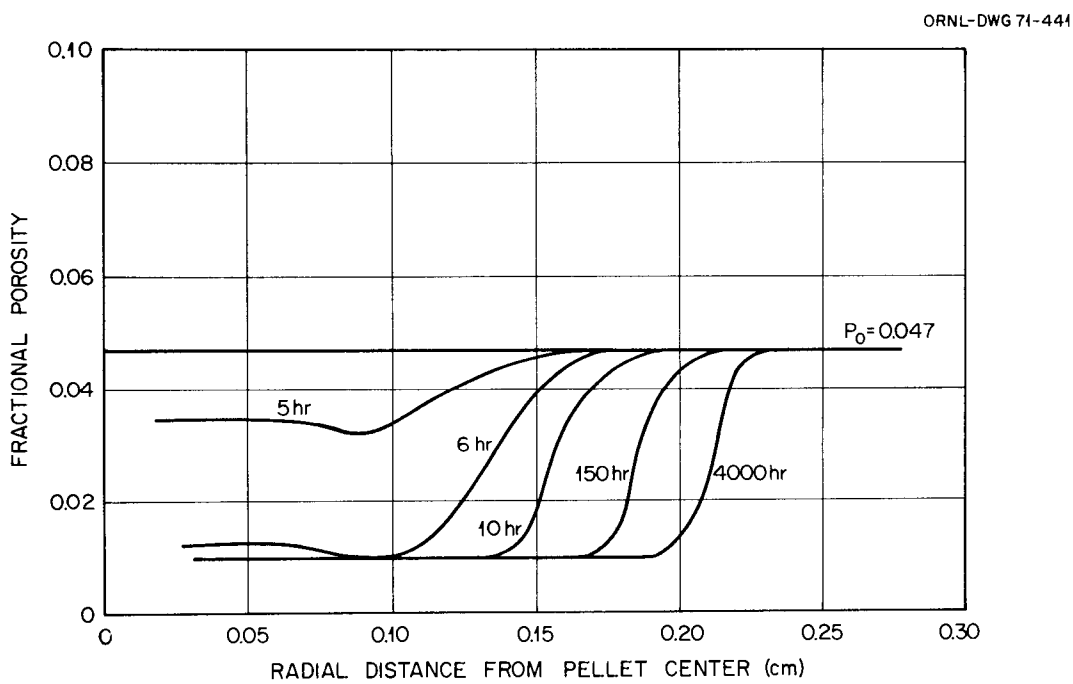

Fig. 1.12. Calculated Variation of Porosity with Radial Position as Influenced by Exposure Time.

model predicts rapid restructuring immediately after the pin achieves full power and continuing restructuring at a decreasing rate throughout the irradiation lifetime of the pin. This is shown by the still decreasing temperature at the fuel center and increasing radius of the central void even at the end of life. However, pins irradiated to higher burnup would be expected to experience a reversal of this trend as accumulation of fission products in the fuel lattice reduces thermal conductivity and the central void begins to close due to fuel swelling. Figure 1.12 shows the porosity distribution after increasing periods of irradiation. This representation supports the statement made earlier that restructuring continues throughout the operating lifetime of the fuel pin. The calculations presented in Figs. 1.11 and 1.12 are in good qualitative agreement with the work of Rim and French,[34] who also used Nichols' model for pore velocity in their calculations.

The temperature gradients calculated with the FMØDEL code are quite high in the fuel region adjacent to the cladding and diminish to zero at the thermal center. Strict application of Eq. (1.1) would result in a pore velocity going to zero as the pores approach the thermal center and subsequent pileup of pores in the inner radial increment. One can assume that pores will become part of the central void when they have moved to within one diameter of that void, with the temperature gradient one pore diameter away from the thermal center as the final driving force to push pores into the void. But even when this refinement of the code is used, the predicted pileup of pores in the inner radial increment is much too large to be physically meaningful. Lackey[35] observed pileups of pores near the thermal center during examination of irradiated Sphere-Pac fuel pins, but not nearly to the extent predicted by strict application of Eq. (1.1). We concluded, therefore, that Nichols' model for pore velocity is of marginal usefulness in the fuel region immediately adjacent to the central void. Another driving force in addition to the temperature gradient must be in operation there. In order to apply the Nichols' model, we arbitrarily set the temperature gradient at the inner radial node equal to the gradient at the second node. We expect that further refinement of the model will be needed for this region.

Application of Nichols' model for pore velocity, as described here. gave us the time-dependent representation of fuel restructuring we needed. A price was paid for this added sophistication, however, in the form of increased running time needed for the FMØDEL code. This is primarily due to the high pore velocities associated with fuel operating near its melting point and the requirement imposed earlier that the neighborhood around the ith radial node be no larger than a third of the thickness of the ith increment. Very short time periods are required under these conditions. In the calculations presented in Figs. 1.11 and 1.12, the lower limit of porosity was arbitrarily set at 1% to reduce the calculational burden; but even this modification did not prevent excessive running times for low-density fuel operating at high temperatures. We anticipate that more efficient methods of calculating the kinetics of fuel restructuring will have to be developed and implemented.

Round-Robin Exercise in Modeling (F. J. Homan, W. H. Bridges)

A working group on Analytical Techniques for Predicting Fuel Pin Behavior and Design was established in 1969 by the USAEC Division of Reactor Development and Technology. The working group consists of representatives from three industrial sites and three national laboratories, all of whom have AEC-sponsored irradiation programs for the development of LMFBR fuel pins. This group has met twice, first in March 1969 and again in April 1970. At the 1970 meeting, eight fuel pins were selected for detailed study by means of models for fuel performance and other analytical techniques available to the members of the working group. The purpose of this round-robin exercise is to compare the predictions and capabilities of the various codes so as to define a suitable direction for future development of analytical methods for predicting the performance of fuel pins.

The fabrication data and operating conditions to be used in the study of the eight pins were mailed to participants in September and October 1970. We have translated the data for all eight pins into useful form and punched it into computer cards for use with the FMØDEL code. Two of the pins were completely analyzed; the cards for the remaining

six pins are ready to be run. We estimate that the entire job is 70% complete.

Microscopy of $(U,Pu)O_2$ Fuels (W. J. Lackey, T. M. Kegley, Jr.)

Our efforts to model $(U,Pu)O_2$ irradiation behavior more accurately are primarily directed toward fuel swelling, release of fission gas, and various aspects of restructuring. Recent reports have described in-reactor grain growth, porosity, and behavior of bubbles of fission gas as determined by light and electron microscopy,[36,37] and Pu distribution as determined by electron microprobe.[38] We now report the amount of porosity at various known radii in an irradiated $(U,Pu)O_2$ fuel pin. This fuel pin operated long enough (28 days) for appreciable restructuring to occur but not long enough for significant fuel swelling. Consequently, knowledge of the relationship between porosity and radial position can be used to estimate the void volume available for accommodating fuel swelling, which occurs throughout the life of a fuel pin.

The fuel pin examined (43-112-3C) was described earlier.[36–38] Briefly, it consisted of $(U_{0.85},Pu_{0.15})O_2$ microspheres clad in a 0.252-in.-OD × 0.010-in.-wall-thickness stainless steel tube. The fuel was 3 in. long, and the initial smear density was 81.4% of theoretical. The pin was irradiated in the ETR at a linear heat rate of 13.6 kW/ft to a burnup of 0.7% FIMA. The amount of porosity present was determined with a Quantimet image-analyzing computer from 500× photomicrographs taken along three radii of an unetched transverse section. As a check on the Quantimet, the amount of porosity apparent in several of the photomicrographs was determined by manual point counting with the aid of a grid with 30 lines per inch. No attempt was made to distinguish fabrication porosity from bubbles of fission gas; all observable voids were included. Replica electron microscopy of this fuel pin showed that the quantity of porosity not observable at 500× was insignificant for the region of the fuel pin examined in this study.

The results are presented in Fig. 1.13 as percent porosity versus fractional fuel radius. We believe that radial fuel relocation occurred predominantly via vapor transport along the channels between spheres and by vapor transport across voids. Both processes result in outward

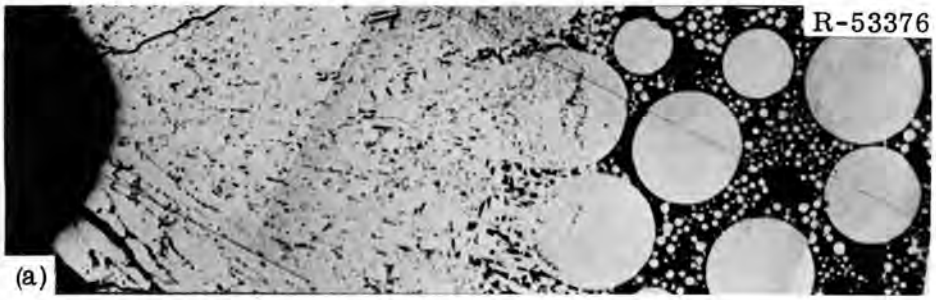

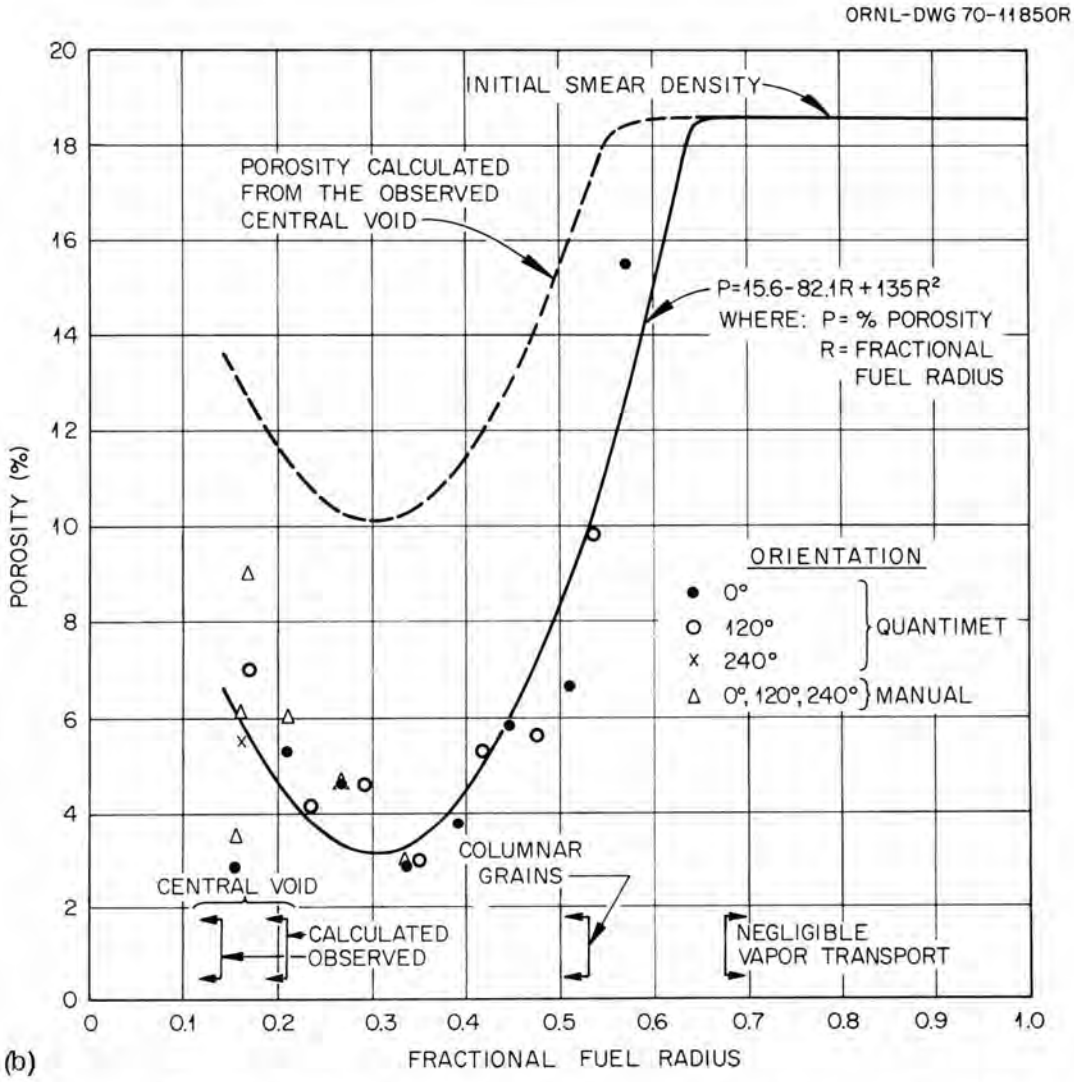

Fig. 1.13. Radial Variation in Porosity for $(U_{0.85},Pu_{0.15})O_2$ Irradiated at 13.6 kW/ft to 0.7% FIMA. (a) Microstructure of radius of irradiated fuel pin, and (b) calculated and observed porosity distributions.

movement of the fuel. Microscopic examination revealed that no fuel was transported beyond a fractional fuel radius of about 0.68. Consequently, we assumed the porosity in the region between fractional fuel radii of 0.68 and 1.0 to be the same as that before irradiation (18.6%). Over the remainder of the cross section, the porosity distribution was approximated by a parabola with a minimum of 3% porosity at about the midradius of the columnar grains. The equation of the parabola was determined from a least-squares analysis of the Quantimet data:

$$P = 15.6 - 82.1R + 135R^2 , \qquad (1.10)$$

where

P = % porosity and

R = fractional fuel radius.

The porosity increased as the central void was approached, perhaps because the smaller thermal gradient reduced the velocity of void migration and consequently led to a pileup of voids. Porosity distributions similar in shape to our experimental results were calculated[34,39] by means of Nichols'[33] model for void movement by evaporation and condensation up a thermal gradient.

Equation (1.10) was integrated to determine the total quantity of porosity present, and the result was used to calculate the size of the central void. The calculated size was larger than the observed size, as shown in Fig. 1.13. The dashed curve of Fig. 1.13 shows the extent to which the parabola fitted to the data would have to be raised to make the size calculated for the central void agree with the observed size. The agreement of the porosity determined with the Quantimet analyzer with that determined manually shows that the experimental data are not in error to the extent indicated by the dashed curve.

Another factor that could have caused the observed and predicted sizes of the central void to differ is the uncertainty in the initial smear density at this cross section. However, reasonable axial variations in the initial density are not as large as the difference in smear density (87.3 vs 81.4% of theoretical) required to account for the variation in observed void size if smear density alone is responsible for the discrepancy. Therefore, we believe that these data indicate some axial

movement of the fuel. Although the cross section examined was located toward the end of the fuel pin that had the highest heat rating, the section was 1/2 in. from the end of the fuel column. Consequently, some fuel operated at a higher temperature than that of the section examined, and this higher temperature quite possibly caused a small amount of vapor to move axially from the hotter fuel and condense in the region of columnar grains in the section examined. This explanation requires an increase in the amount of fuel at this cross section of only 3.0%.

Redistribution of Actinides in Irradiated $(U,Pu)O_2$ (W. J. Lackey, A. R. Olsen, D. K. Bates[40])

The in-reactor redistribution of U and Pu is being studied by electron microprobe analysis[38] and alpha autoradiography[41] because of its potential influence on the performance of $(U,Pu)O_2$ fuel pins. We are attempting to develop theoretical models for comparison with radial profiles for Pu:(U+Pu) observed after irradiation. Our first attempt was to write a computer program, VAPUR, for calculating the radial variation in Pu content of the solid according to the method proposed by Aitken and Evans.[42] This model assumes that at steady-state neither the ratio of $H_2O:H_2$ (ref. 43) nor the ratio of Pu:U (ref. 42) in the gas phase varies with radial position. We used the thermodynamic data summarized by Rand and Markin.[43]

After verifying that our computer program was correct by duplicating some of Rand and Markin's calculations, we unsuccessfully attempted to reproduce the results of Aitken and Evans' calculations. We suspect an error in their calculations. Contrary to their results for the gas phase, our calculations (Fig. 1.14) for hypostoichiometric $(U_{0.8},Pu_{0.2})O_2$ show the ratio of Pu:U in the gas phase to increase with increasing temperature for any given ratio of $H_2O:H_2$ in the range $10^{-1.93}$ to $10^{-3.00}$ over the temperature range 1400 to 3000°K. When we used Raoult's law in the manner suggested by Aitken and Evans to calculate the Pu profile in the solid-phase composition from the previously calculated gas-phase compositions, the result was opposite that observed in irradiated fuel pins. That is, the model predicted that the hotter fuel would have a

lower Pu content than the colder fuel even for ratios of O:metal approaching 2.00 where, according to our calculations and recent studies by mass spectrometry,[44] the vapor phase is rich in U compared to the solid at all temperatures of interest. Consequently, if the slope of the curve resulting from a plot of the ratio of Pu:U in the gas phase versus temperature for a given ratio of $H_2O:H_2$ is actually positive, as our calculations indicate (Fig. 1.14), then we suspect some aspect of the model to be in error, since the model would predict a lower Pu content for the hotter fuel than for the colder fuel. The U-rich vapor over the hottest fuel simply could move down the temperature and pressure gradients and leave a Pu-enriched solid at the higher temperatures. Thus, a kinetic model might be appropriate. It is also possible that the model

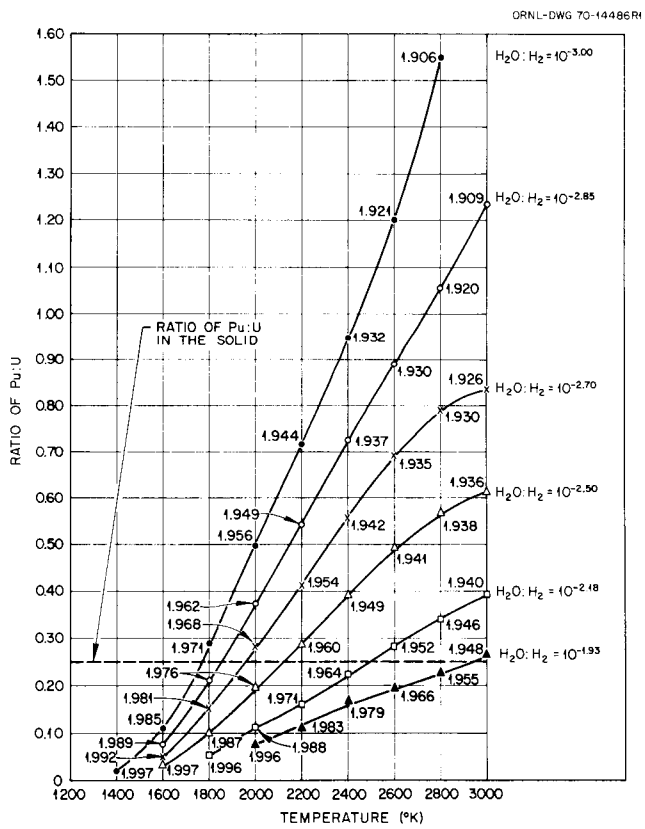

Fig. 1.14. Ratio of Plutonium to Uranium in the Gas Phase over $(U_{0.8},Pu_{0.2})O_{2-x}$ as a Function of Temperature. The number at each point is the ratio of oxygen to metal for $(U_{0.8},Pu_{0.2})O_2$.

developed by Aitken and Evans is correct, but that the thermodynamic data used were not sufficiently accurate. We are currently examining the mass spectrometric data[44] in an attempt to determine the source of the discrepancy.

Migration of Fission Products in $(U,Pu)O_2$ Nuclear Fuels (P. T. Carlson)

The purpose of this investigation is to develop both theoretical and experimental understanding of the redistribution of fission products in mixed oxide fuels subjected to large temperature gradients.

Of current interest is the examination of a Sphere-Pac $(U,Pu)O_2$ fuel pin (S-1-E) irradiated in the EBR-II. Two sampling techniques are being considered for analyzing the distribution of fission products. The first procedure involves microsampling of a small area of the oxide fuel matrix by laser-beam vaporization; the second technique consists of drilling radially into the pin and removing the drilled plug for examination. In the laser-vaporization technique, a cover glass is placed about 1 mm above a cross section of the fuel, and the laser beam is focused through the slide onto the surface of the sample. When the laser is fired, the resultant vaporized fuel material condenses on the glass slide. The slide is then scanned by gamma-ray spectroscopy to determine the concentration of fission products at the particular point of vaporization. A step-wise laser-sampling of the cross section in this manner will yield the concentration of each fission product as a function of radial distance from the center of the fuel pin. A similar procedure is followed in the second sampling technique. The thin rod of fuel material removed by drilling is made into thin sections that are similarly analyzed by gamma-ray spectroscopy. The profiles resulting from either technique will be examined in relation to theoretical expressions.

Examinations of Chemical Interactions of Fuel and Cladding in Sphere-Pac $(U,Pu)O_2$ Fuel Pins (C. M. Cox)

We summarized the limited ORNL data that might be pertinent to chemical interactions of fuel and cladding in Sphere-Pac pins with operating conditions similar to those proposed for our series II subassembly for the EBR-II. Table 1.10 summarizes the fabrication and

Table 1.10. Fabrication and Irradiation Conditions for Selected ORNL Sphere-Pac $(U,Pu)O_2$ Fuel Pins

Pin	Reactor	Ratio		Uranium Enrichment (%)	Smear Density (% of theoretical)	Cladding			Peak Heating Rate (kW/ft)	Peak Temperature at Inside Surface of Cladding (°C)	Peak Burnup, %		Maximum Temperature at Fuel Center (°C)	Maximum Cladding Penetration[a] (in.)	Status (January 1, 1971)
		Pu:(U+Pu)	O:Metal			Type Stainless Steel	Outside Diameter (in.)	Wall Thickness (in.)			Design	Current			
														$\times 10^{-4}$	
99-1	ETR	0.20	2.00	93	76	304	0.252	0.010	34.6	730	1.4	1.4	Molten	< 2.5	Examination completed.
99-3	ETR	0.20	2.00	93	76	304	0.252	0.010	49.9	1000	2.8	2.8	Molten	< 2.5	Examination completed.
100-1	ETR	0.20	2.00	93	76	304	0.252	0.010	29.3	650	1.2	1.2	Molten	c	Examination completed.
100-3	ETR	0.20	2.00	93	76	304	0.252	0.010	44.9	900	2.5	2.5	Molten	c	Examination completed.
115-3	ETR	0.15	1.97	0.6	82	304	0.252	0.010	20.6[b]	460	6.5	6.5	2400	< 2.5	Mount being prepared for electron microprobe.
S-1-A	EBR-II	0.20	1.99	93	83	304	0.254	0.016	13.7	570	5.9	5.9	2240		Dimensional inspection completed.
S-1-B	EBR-II	0.20	1.99	93	86	304	0.254	0.016	14.3	600	12	6.0	2330		At EBR-II awaiting reinsertion.
S-1-C	EBR-II	0.20	1.99	93	83	316	0.250	0.015	14.1	590	12	6.3	2300		At EBR-II awaiting reinsertion.
S-1-D	EBR-II	0.20	1.98	93	80	316	0.250	0.015	13.4	580	12	6.0	2190		At EBR-II awaiting reinsertion.
S-1-E	EBR-II	0.20	1.99	93	82	316	0.250	0.015	13.5	590	6.1	6.1	2200	< 2.5	Destructive examination in progress.
120-3	ETR	0.20	1.98	0.6	85	316	0.250	0.015	17	650	12	1.4	2500		In-reactor.
121-3	ETR	0.20	1.98	0.6	84	316	0.250	0.015	17	650	12	1.2	2500		In-reactor.

[a] Determined by optical metallography.

[b] Time-averaged.

[c] Pins failed, and reaction of fuel and NaK precluded this measurement.

operating conditions for $(U,Pu)O_2$ Sphere-Pac pins that were irradiated to burnups greater than 1% FIMA and to peak cladding temperatures greater than 400°C. Information describing the thermal performance,[45] transient performance,[17] and steady-state irradiation performance[46,47] of other Sphere-Pac pins was reported.

We irradiated four $(U_{0.8},Pu_{0.2})O_{2.00}$ fuel pins clad with type 304 stainless steel in the ETR at severe overpower conditions ranging from 29 to 50 kW/ft to burnups of 1 to 3% FIMA. Pins 99-3 and 100-3 failed by molten fuel penetrating the cladding. Fuel from pin 100-3 fell beside pin 100-1 and caused its failure. Pin 99-1 successfully operated with a peak cladding temperature of 730°C to 1.4% FIMA. These pins are of interest in this context since they were clad with type 304 stainless steel and had quite high cladding temperatures. Optical metallography [Fig. 1.15(a) and (b)] revealed that precipitation of carbides at grain boundaries increased with temperature but indicated no significant chemical interactions. Figure 1.15(a) shows the typical interface (as polished) between fuel and cladding in pin 99-1. Figure 1.15(b) is a similar photomicrograph for pin 99-3.

Pin 115-3, also described in Table 1.10, operated to 6.5% FIMA at a time-averaged peak heating rate of 21 kW/ft with type 304 stainless steel cladding at 460°C. Optical metallography, as shown in Fig. 1.15(c), indicated no intergranular penetration of the cladding and little or no precipitation of carbides at the grain boundaries.

The fabrication and operating conditions of our Sphere-Pac pins from EBR-II subassembly X 050 are also summarized in Table 1.10. We began destructive examination of pin S-1-E and completed dimensional inspection of pin S-1-A. As shown in Fig. 1.15(d), optical metallography at the midplane of pin S-1-E revealed neither grain-boundary attack nor any other chemical interactions of fuel and cladding. Microprobe examinations will soon be initiated.

Our data have shown the performance of the Sphere-Pac fuel to be excellent. Two Sphere-Pac and two pellet pins are operating in instrumented capsules in the ETR with peak cladding temperatures of 620 to 650°C and at burnups of about 3% FIMA (ref. 48). These will continue

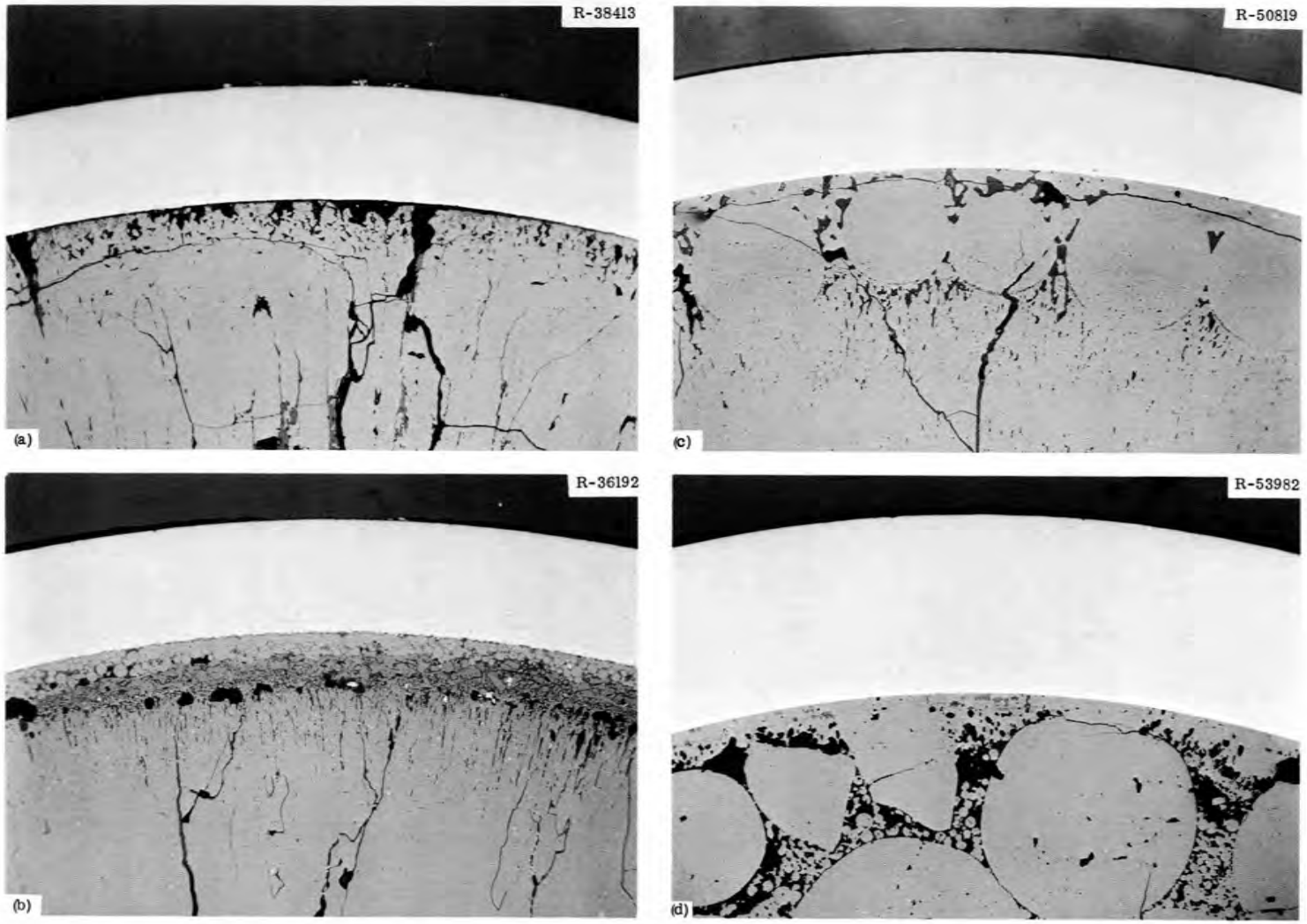

Fig. 1.15. Irradiated Sphere-Pac $(U,Pu)O_2$ Fuel. (a) Irradiated in ETR to 1.4% FIMA at 35 kW/ft, type 304 stainless steel cladding at 730°C. (b) Irradiated in ETR to 2.8% FIMA at 50 kW/ft, type 304 stainless steel cladding at 1000°C. (c) Irradiated in ETR to 6.5% FIMA at 21 kW/ft, type 304 stainless steel cladding at 460°C. (d) Irradiated in EBR-II to 6.1% FIMA at 13.5 kW/ft, type 316 stainless steel cladding at 550°C. As polished.

operation to a burnup in excess of 10% FIMA. The pins are clad with the same type 316 stainless steel cladding used in the series II bundle[49] in the EBR-II and will be examined before the series II pins have reached 5% FIMA; they will provide, therefore, an early check on these operating conditions.

Notes

1. On loan from General Engineering Division.

2. A. R. Olsen, Fuels and Materials Development Program Quart. Progr. Rept. Sept. 30, 1969, ORNL-4480, pp. 29–33.

3. R. A. Bradley, W. J. Leonard, T. B. Lindemer, R. B. Pratt, and W. H. Pechin, Fuels and Materials Development Program Quart. Progr. Rept. June 30, 1970, ORNL-4600, pp. 7–10.

4. R. A. Bradley, W. J. Leonard, T. B. Lindemer, and W. H. Pechin, Fuels and Materials Development Program Quart. Progr. Rept. Sept. 30, 1970, ORNL-4630, pp. 13–15.

5. Formerly Battelle Memorial Institute Pacific Northwest Laboratory.

6. R. A. Bradley and W. H. Pechin, "Moisture Analysis," pp. 8–10, this report.

7. R. B. Fitts and R. L. Senn, "Tests of Mechanical Interaction of Fuel and Cladding," pp. 29–33, this report.

8. R. A. Bradley, "Fuel Pins for Studies of Fuel Reprocessing," pp. 4–5, this report.

9. C. A. Strand, WADCO, personal communication, December 3, 1970.

10. J. M. Leitnaker, Fuels and Materials Development Program Quart. Progr. Rept. Sept. 30, 1970, ORNL-4630, pp. 21–26.

11. D. K. Smith, Norelco Reporter 10(1), 19 (1963).

12. T. T. Claudson et al., Nucl. Appl. Technol. 9(1), 10–23 (July 1970).

13. A. R. Olsen, D. R. Cuneo, and J. H. Goode, Fuels and Materials Development Program Quart. Progr. Rept. March 31, 1970, ORNL-4560, pp. 24–27.

14. A. R. Olsen, Trans. Am. Nucl. Soc. 13(1), 32–33 (June 1970).

15. On loan from Reactor Chemistry Division.

16. C. M. Cox, E. J. Manthos, D. R. Cuneo, and R. E. Adams, Metals and Ceramics Div. Ann. Progr. Rept. June 30, 1970, ORNL-4570, pp. 58–59.

17. C. M. Cox, E. J. Manthos, and D. R. Cuneo, Trans. Am. Nucl. Soc. 13(2), 653–654 (1970).

18. R. B. Fitts, E. L. Long, Jr., and J. L Miller, Jr., "Tests of Thermal Performance," pp. 23–29, this report.

19. R. B. Fitts and V. A. DeCarlo, Fuels and Materials Development Program Quart. Progr. Rept. June 30, 1968, ORNL-4330, pp. 20–23.

20. D. B. Trauger, Some Major Fuel Irradiation Test Facilities of the Oak Ridge National Laboratory, ORNL-3574 (April 1964).

21. F. G. Kitts, R. B. Fitts, and A. R. Olsen, "Sol-Gel Urania-Plutonia Microsphere Preparation and Fabrication into Fuel Rods," pp. 195–210 in Plutonium Fuels Technology, ed. by K. E. Horton, R. E. Macherey, and R. J. Allio, Vol 13 in the series Nuclear Metallurgy, American Institute of Mining, Metallurgical and Petroleum Engineers, New York, 1968.

22. R. A. Bradley, Fuels and Materials Development Program Quart. Progr. Rept. Sept. 30, 1969, ORNL-4480, pp. 7–8.

23. C. M. Cox and F. J. Homan, PRØFIL – A One-Dimensional FØRTRAN IV Program for Computing Steady-State Temperature Distributions in Cylindrical Ceramic Fuels, ORNL-TM-2443 (March 1969); Addendum (August 1969).

24. W. E. Baily et al., "Thermal Conductivity of Uranium-Plutonium Oxide Fuels," pp. 293–308 in Plutonium Fuels Technology, ed. by K. E. Horton, R. E. Macherey, and R. J. Allio, Vol 13 in the series Nuclear Metallurgy, American Institute of Mining, Metallurgical and Petroleum Engineers, New York, 1968.

25. C. N. Craig et al., Heat Transfer Coefficients Between Fuel and Cladding in Oxide Fuel Rods, GEAP-5748 (January 1969).

26. C. M. Cox and D. R. Cuneo, "Transient Tests," p. 19, this report.

27. Reactor Division.

28. R. B. Fitts, R. L. Senn, J. G. Morgan, and J. D. Jenkins, Fuels and Materials Development Program Quart. Progr. Rept. June 30, 1970, ORNL-4600, pp. 58–63.

29. H. C. Roland, GENGTC, A One Dimensional CEIR Computer Program for Capsule Temperature Calculations in Cylinder Geometry, ORNL-TM-1942 (December 1967).

30. Consultant from the University of Tennessee.

31. W. D. Turner and J. S. Crowell, Notes on Heating; An IBM-360 Heat Conduction Program, CTC-INF-980 (November 1969).

32. F. J. Homan, LMFBR Fuel Cycle Studies Progr. Rept. June 1970, No. 16, ORNL-TM-3072, pp. 76–80.

33. F. A. Nichols, J. Nucl. Mater. 22, 214–222 (1967).

34. Chang Saeng Rim and Henri French, Trans. Am. Nucl. Soc. 12(1), 103 (June 1969).

35. W. J. Lackey and T. M. Kegley, Jr., LMFBR Fuel Cycle Studies Progr. Rept. October 1970, No. 20, ORNL-TM-3217, pp. 79–82.

36. W. J. Lackey, Fuels and Materials Development Program Quart. Progr. Rept. Sept. 30, 1970, ORNL-4630, pp. 47–54.

37. W. J. Lackey, Fuels and Materials Development Program Quart. Progr. Rept. March 31, 1970, ORNL-4560, pp. 71–74.

38. W. J. Lackey and J. L Miller, Fuels and Materials Development Program Quart. Progr. Rept. June 30, 1970, ORNL-4600, pp. 69–71.

39. F. J. Homan, LMFBR Fuel Cycle Studies Progr. Rept. December 1970, No. 22, ORNL-TM-3281, pp. 56–62.

40. Summer employee sponsored by Oak Ridge Associated Universities.

41. A. R. Olsen and D. R. Cuneo, Metals and Ceramics Div. Ann. Progr. Rept. June 30, 1970, ORNL-4570, pp. 53–55.

42. E. A. Aitken and S. K. Evans, Thermodynamic Data Program Involving Plutonia and Urania at High Temperatures, Quart. Rept. No. 7, February 1 to May 1, 1969, GEAP-12027.

43. M. H. Rand and T. L. Markin, "Some Thermodynamic Aspects of $(U,Pu)O_2$ Solid Solutions and Their Use as Nuclear Fuels," pp. 637–650 in Thermodynamics of Nuclear Materials, International Atomic Energy Agency, Vienna, 1968.

44. A. D. Tevebaugh and P. E. Blackburn, Reactor Development Program Progr. Rept. July 1970, ANL-7726, pp. 142–144.

45. R. B. Fitts, Trans. Am. Nucl. Soc. 13(2), 549–551 (1970).

46. A. R. Olsen, C. M. Cox, and R. B. Fitts, Trans. Am. Nucl. Soc. 12(2), 605–606 (1969).

47. A. R. Olsen, Trans. Am. Nucl. Soc. 13(2), 549–551 (1970).

48. T. N. Washburn and M. K. Preston, "Instrumented Tests in the ETR," pp. 20–23, this report.

49. A. R. Olsen, "Fast-Flux Irradiation Tests," pp. 15–19, this report.

2. DEVELOPMENT OF ADVANCED FBR FUELS

P. Patriarca J. L. Scott

The carbides and nitrides of U and Pu, which have thermal conductivities about five times that of $(U,Pu)O_2$, have the potential for significantly reducing power costs for the LMFBR because of higher specific power, higher linear heat ratings, shorter doubling times, and reduced capital costs. Improved nuclear safety is also possible through their use.

The main question regarding the use of carbides or nitrides is whether they will perform satisfactorily under LMFBR core conditions to burnups above 100,000 MWd/metric ton. The goal of our program is to answer this question for (U,Pu)N; other laboratories have been assigned to evaluate (U,Pu)C. The ORNL program consists of irradiation tests in a thermal reactor, the ETR, and in a fast reactor, the EBR-II. It includes fabrication and characterization of the fuel; design, fabrication, and characterization of the fuel pins; and examination of the fuel pins after irradiation. Finally, a small study is included to define quality standards of fuel and cladding to avoid compatibility problems during irradiation.

Synthesis, Fabrication, and Characterization of Advanced FBR Fuels

V. J. Tennery

Synthesis and Fabrication of Mixed Nitrides (E. S. Bomar, V. J. Tennery)

Sintering work with UN showed that sintered density is higher for a given temperature and time if the overpressure of N_2 over the nitride during sintering is reduced.[1] We designed a number of experiments that will allow us to determine the effect of reduced N_2 pressure, the ratio of N:metal in the starting nitride powders, and the possible benefit of additions of U and/or Pu hydride the sintered densities of mechanical mixtures of UN and PuN. Our first

step, however, was to establish a base line for behavior by preparing nitride from prealloyed U and Pu. Figure 2.1 compares the sintering behavior of the mononitride, $(U_{0.8},Pu_{0.2})N$, with a starting powder high in sesquinitride content when sintered at two levels of N_2 pressure and with two and three levels of hydride addition, respectively. The mononitride powder was prepared by the hydride-dehydride-nitride process with final treatment at 1050°C under a vacuum of 10^{-5} torr, whereas the sesquinitride material was made by heating the sesquinitride powder to only 800°C under 630 torr N_2. The sintering temperature was reduced to 1800°C for these experiments to ensure the safety of the

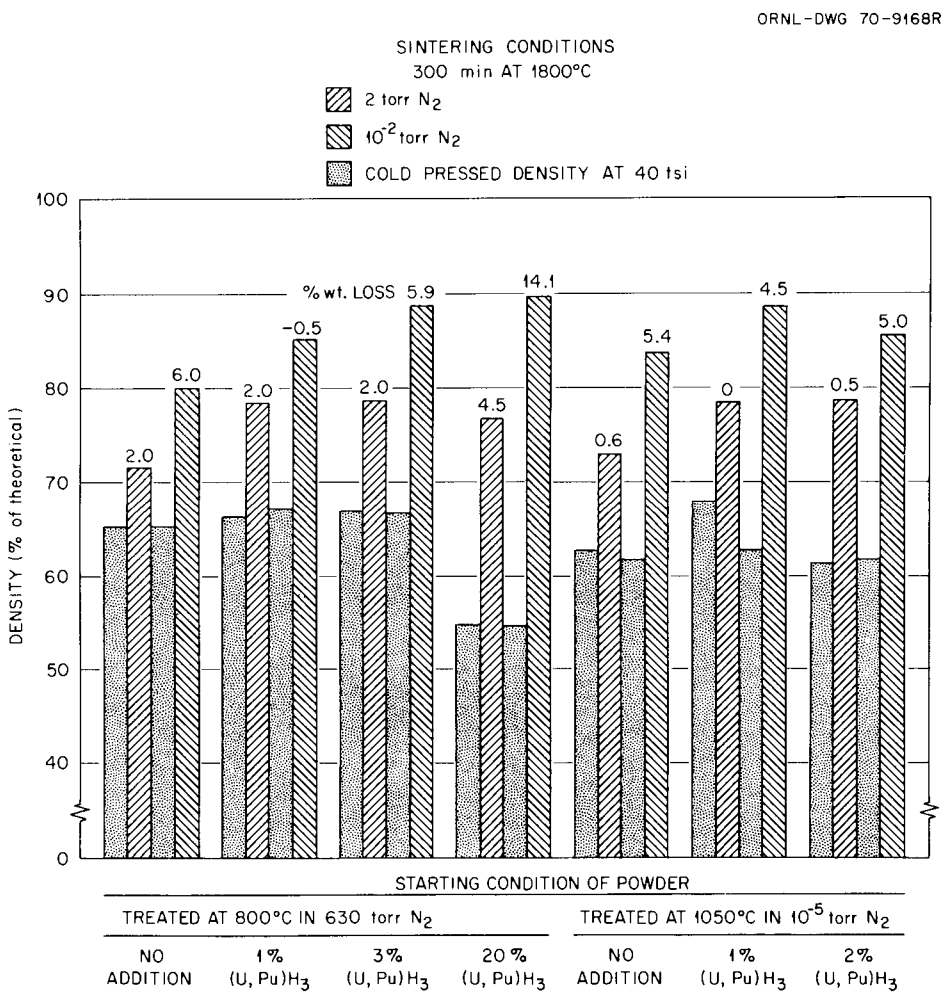

Fig. 2.1. Sintering Behavior of $(U_{0.8},Pu_{0.2})N$ Prepared from Prealloyed Uranium and Plutonium Metals.

furnace equipment in the event a sizeable quantity of U-Pu metal was produced during the experiment.

Comparable samples of sesquinitride and mononitride behaved similarly. The addition of 1 or 3% $(U_{0.8},Pu_{0.2})H_3$ to each of the nitride powders increased the resulting densities by about 7%. Lowering the N_2 overpressure to 10^{-2} torr increased the sintered densities an additional 7 to 10%. For an overpressure of 2 torr N_2, the mononitride samples lost 0.5% of their weight and the sesquinitride powders lost 2%, an amount attributable to the decomposition of the sesquinitride phase. When 20% hydride was added to the sesquinitride powder, the final density was not significantly greater than that obtained when 3% hydride was added, but the weight loss for an overpressure of 2 torr N_2 rose to 4.5% instead of falling, as had been expected, due to formation of nitride by the metal from the hydride. At an overpressure of 10^{-2} torr, the density rose to 89%, but the weight loss increased to 14%.

Three pellets whose appearance is representative of those obtained from this sintering series are shown in Fig. 2.2. From left to right, they were prepared from mononitride plus 1% hydride, mononitride plus 3% hydride, and sesquinitride-rich nitride plus 20% hydride.

Metallographic examination showed that the measured increase in density that resulted from a decrease in the N_2 overpressure was not due to the formation of metal but to improved sintering that was accompanied by enhanced grain growth. Similarly, no free metal was found in the pellet that originally contained 20% $(U_{0.8},Pu_{0.2})H_3$.

The effect of reduced partial pressure of N_2 on the microstructure of $(U_{0.8},Pu_{0.2})N$ pellets prepared from prealloyed metal is shown in Fig. 2.3. A reduction in porosity and an increase in grain size (to about ASTM 8) is apparent. The addition of 20% of the pellet weight as $(U_{0.8},Pu_{0.2})H_3$ further decreased porosity but produced about the same amount of grain growth.

Experiments similar to those described above were also performed on mechanical mixtures that contained 80% UN and 20% PuN by weight plus, in some instances, other reference materials. The results for the first

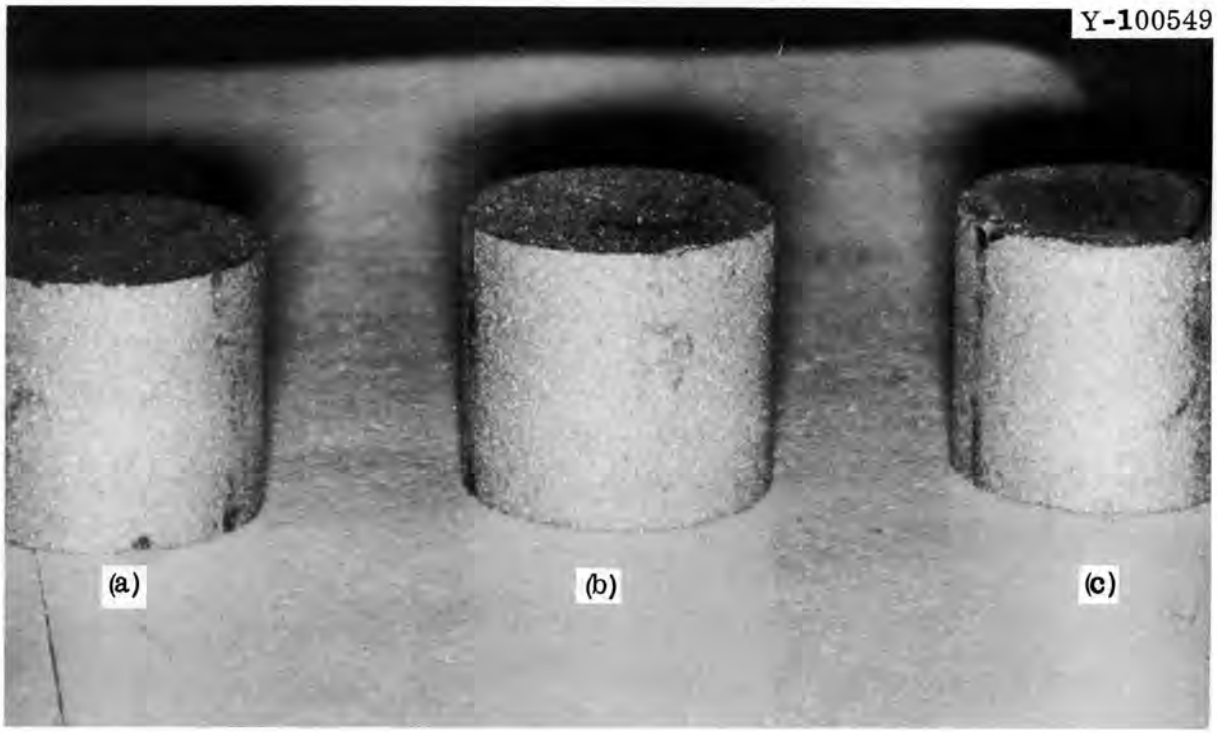

Fig. 2.2. Pellets of $(U_{0.8},Pu_{0.2})N$ Fabricated by Cold Pressing at 40 tsi and Sintering at 1800°C in Nitrogen at a Pressure of 10^{-2} torr. Nitride powder prepared from prealloyed uranium plus plutonium metal. Condition of starting powders, from left to right, (a) heated at 1050°C in vacuum of 10^{-5} torr, then 1% $(U_{0.8},Pu_{0.2})H_3$ added. (b) Heated at 1050°C in vacuum of 10^{-5} torr, then 3% $(U_{0.8},Pu_{0.2})H_3$ added. (c) Heated at 800°C under 630 torr N_2, then 20% $(U_{0.8},Pu_{0.2})H_3$ added.

set of samples, which were sintered at 1800°C, are shown in Fig. 2.4. The trends reported previously for mixed nitride prepared from prealloyed U-Pu are found in this experiment; namely, both the addition of 1 and 3% hydride as UH_3 and the reduction of N_2 overpressure to 0.01 torr improved sinterability of powder with a high ratio of N:metal, but the resulting pellet densities were less than those obtained with prealloyed powder. Nonetheless, the maximum value of 81% of theoretical density which resulted from the addition of 3% UH_3 and a 0.01 torr N_2 pressure, was much higher than previously observed for mechanical mixtures of UN and PuN. Loss of weight during sintering was slightly higher than found for nitride prepared for prealloyed U and Pu.

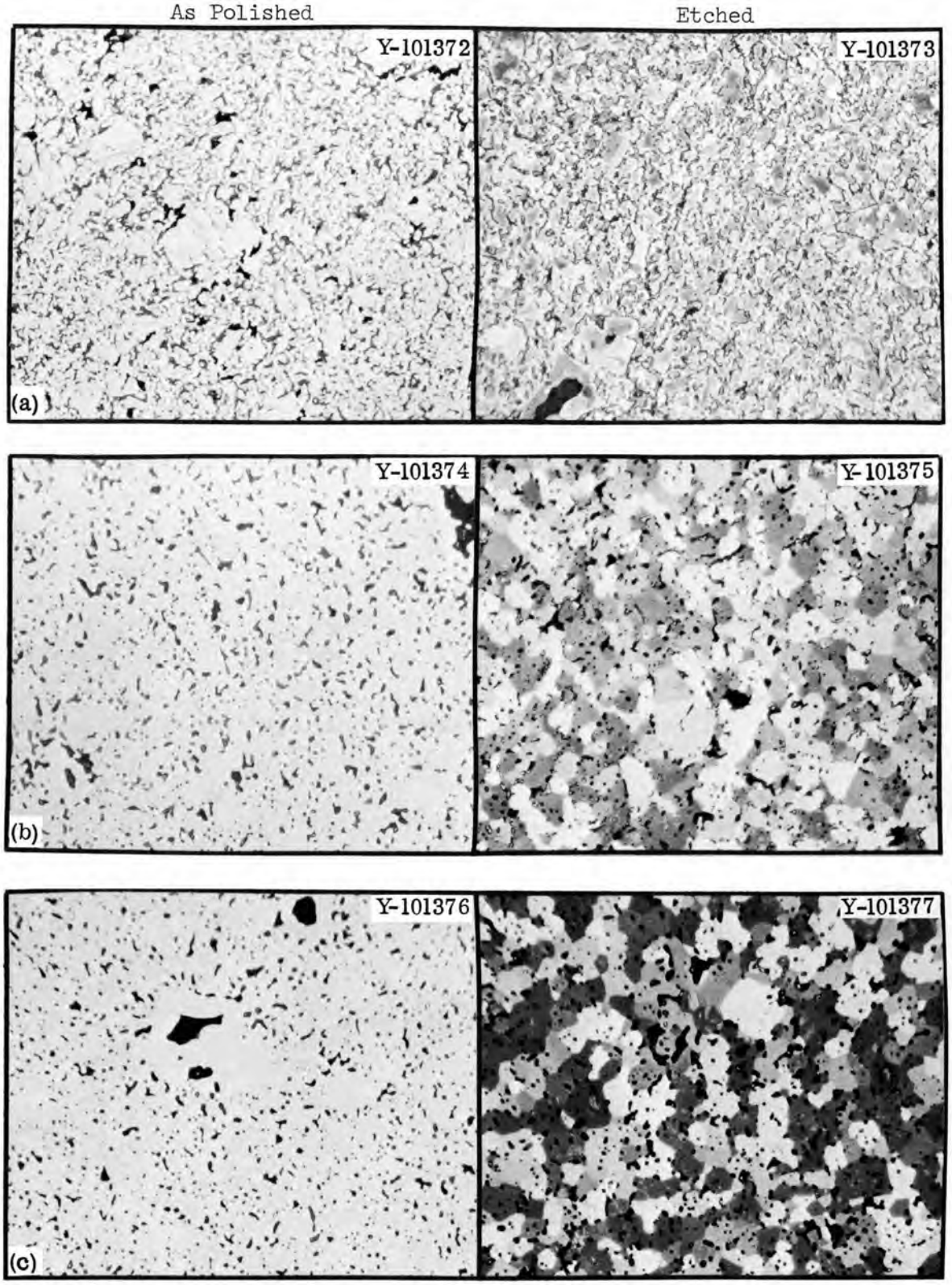

Fig. 2.3. Microstructures of $(U_{0.8},Pu_{0.2})N$ Pellets Sintered 300 min at 1800°C. Each sample heated to 1400°C under vacuum of 10^{-5} torr; furnace then backfilled with nitrogen to (a) 2 torr, (b) 10^{-2} torr, and (c) 10^{-2} torr. Pellet shown in (c) originally contained 20% $(U_{0.8},Pu_{0.2})H_3$. Pellets etched with 30 parts lactic, 10 parts HNO_3, and 1 part HF. 200×.

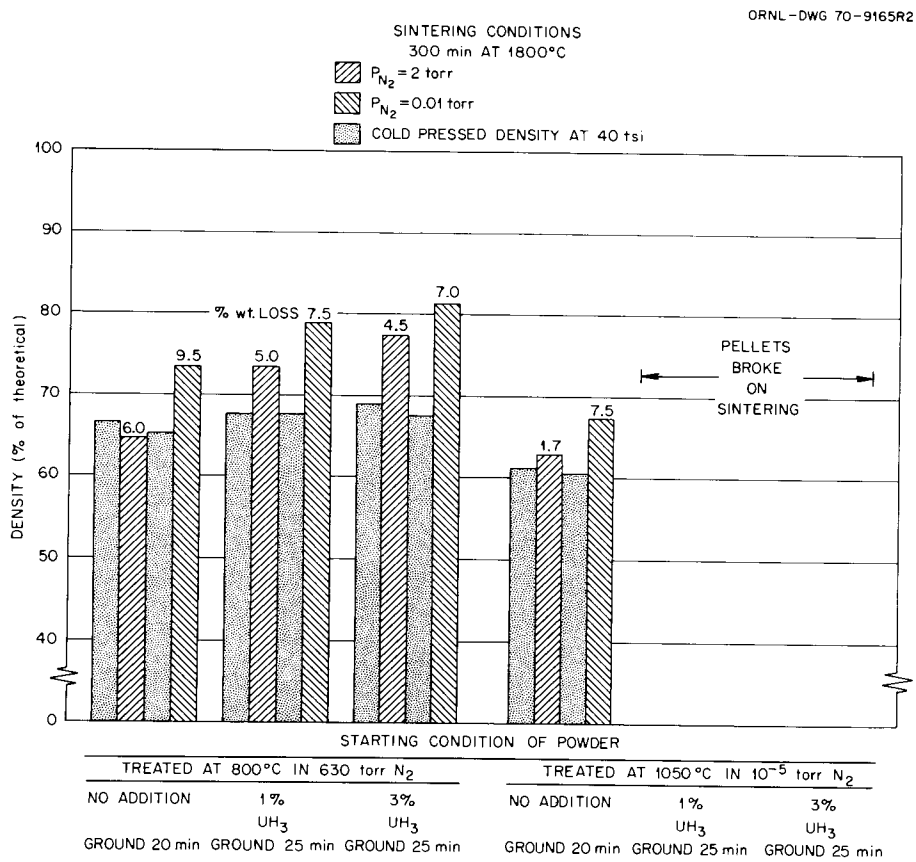

Fig. 2.4. Sintering Behavior of Mechanical Mixtures of 80% Uranium Nitrides Plus 20% Plutonium Nitride.

A macrophotograph of the pellet from the sesquinitride-rich series to which 3% UH_3 was added is shown in Fig. 2.5. The broken companion pellet from the mononitride series is shown in Fig. 2.6.

The microstructure of the pellet in Fig. 2.5 contains distributions of both coarse and fine porosity, as shown in Fig. 2.7. The coarse porosity, which is distributed in a dense matrix, we assumed to be the original site of PuN particles. The PuN preferentially dissolved in the UN; the small amount of UN that diffused into the PuN was lost during sectioning and polishing of the sample. As with the prealloyed nitrides, reduction of N_2 pressure from 2 to 0.01 torr caused additional grain growth and a 4% increase in sintered density.

Fig. 2.5. Pellet with a Composition of $(U_{0.8},Pu_{0.2})N$ Prepared From a Mechanical Mixture of Sesquinitride-Rich Uranium Nitride, Plutonium Nitride, and 3 wt % Uranium Hydride. Pellet sintered 5 hr at 1800°C with a N_2 overpressure of 0.01 torr. Bottom portion of picture is due to reflection from tungsten setter plate.

Fig. 2.6. Pellet Prepared and Treated as Above Except Uranium Mononitride Substituted for Sesquinitride-Rich Uranium Nitride.

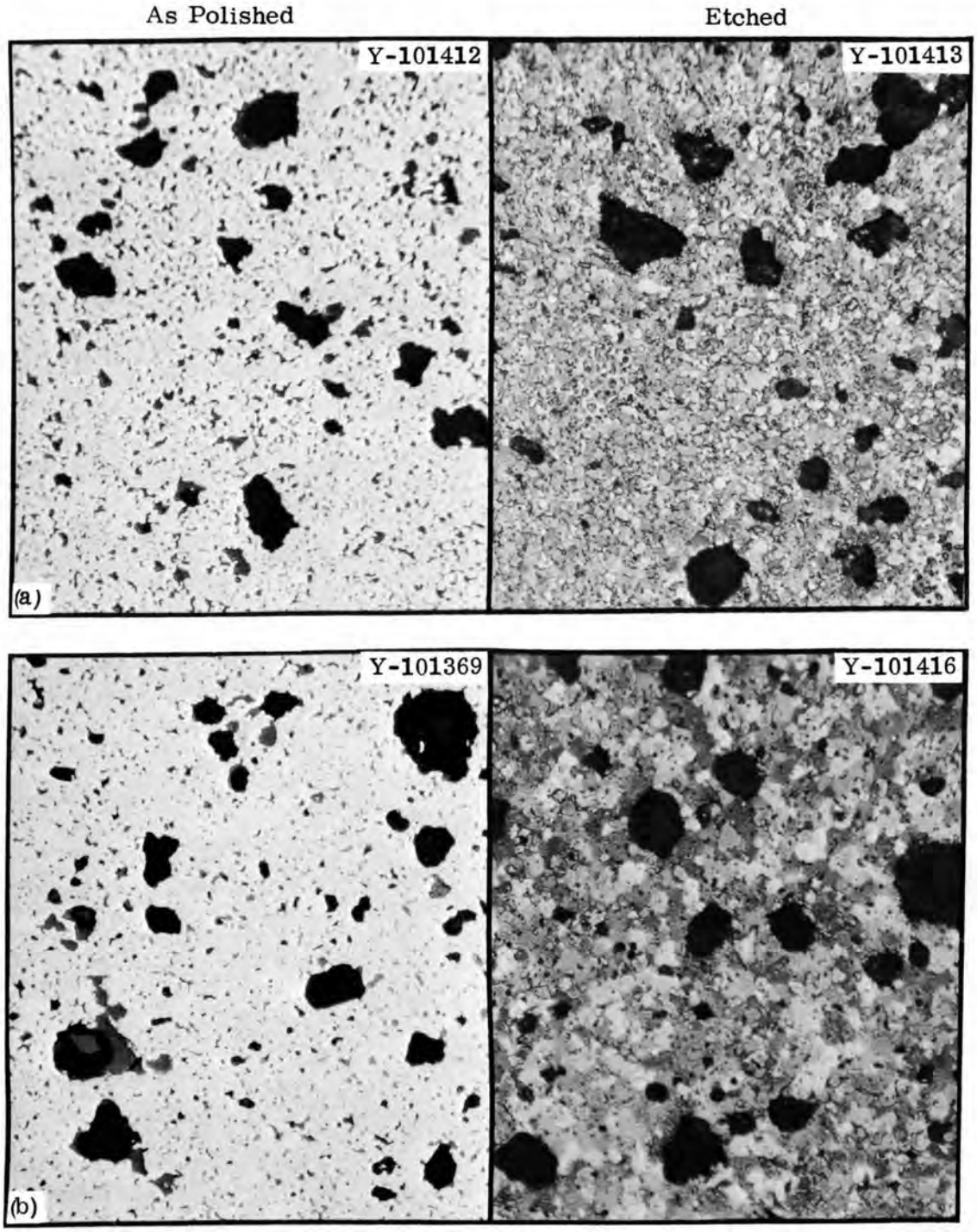

Fig. 2.7. Microstructure of $(U_{0.8},Pu_{0.2})N$ Pellets Prepared From Mechanical Mixture of Sesquinitride-Rich Uranium Nitride, Plutonium Nitride, and 3 wt % Uranium Hydride. Pellets sintered 5 hr at 1800 °C at nitrogen overpressures of (a) 2 torr to 77% of theoretical density and (b) 0.01 torr to 81% of theoretical density. 200×.

A second series of pellets was prepared and sintered in which four factors were changed: UN (designated 3S3) prepared with a large number of hydride-dehydride-nitride process cycles was substituted for the mononitride previously used, the sintering temperature was increased to 2000°C, overpressures of 0.1 and 0.5 torr N_2 were used, and the sintering furnace was backfilled to 630 torr with Ar after the addition of N_2. The method of preparing the 3S3 powder resulted in a finer particle size than that obtained in our previous powders. Data for density and weight loss are given in Fig. 2.8 for this set of pellets.

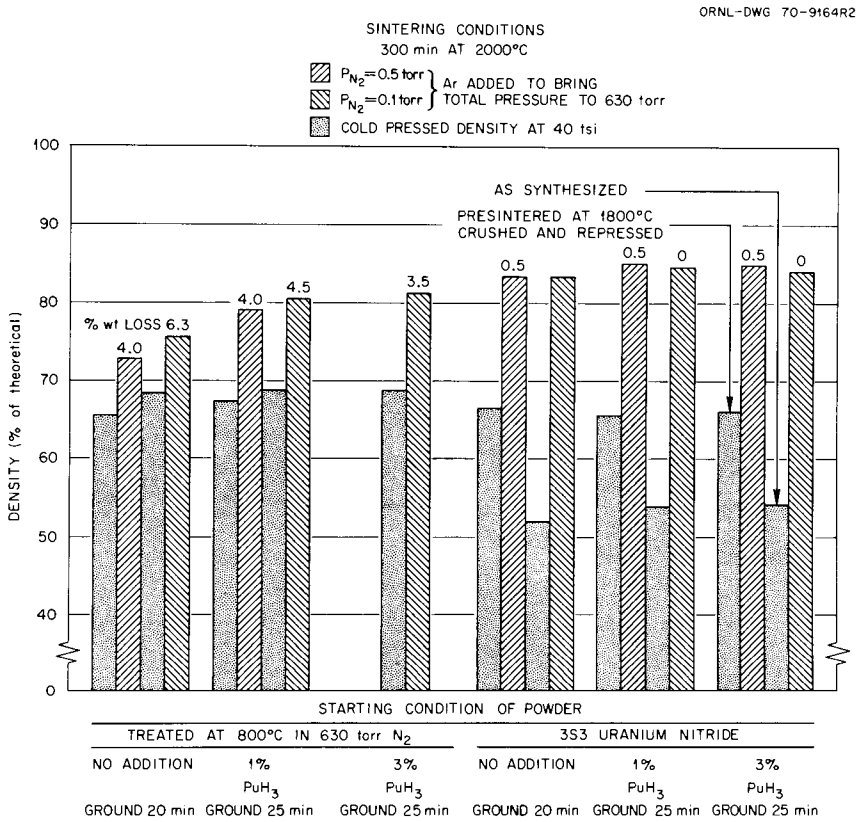

Fig. 2.8. Sintering Behavior of Mechanical Mixtures of 80% Uranium Nitrides Plus 20% Plutonium Nitride.

The weight loss by the pellets prepared from sesquinitride-rich powder was reduced by about 50% as a result of using an Ar cover gas during sintering. The pellets prepared from 3S3 powder lost virtually no weight during sintering.

The hydride addition, in this case as PuH_3, again increased density by a few percent for the sesquinitride-rich powders; however, the maximum density obtained was again 81%. The lower partial pressure of N_2 resulted in higher densities, but the differential was smaller than that observed in the experiment at 1800°C. The general appearance of the sintered pellets from this series is shown in Fig. 2.9. A product

Fig. 2.9. Appearance of $(U_{0.8},Pu_{0.2})N$ Pellet Prepared From the Same Mechanical Mixture Used for Pellet Shown in Fig. 2.2, Except That Plutonium Hydride was Substituted for Uranium Hydride and the Sintering Conditions were Changed to 5 hr at 2000°C and an Overpressure of 0.01 torr N_2 with Argon Added to 630 torr.

of uniformly good appearance was obtained for the pellets prepared from UN powder 3S3 (Fig. 2.10); there was no indication of cracking or spalling, as resulted for the mononitride feed in the set of pellets sintered at 1800°C. There was no benefit from either the addition of PuH_3 or reducing the partial pressure of N_2 from 0.5 to 0.1 torr. The density of all of the pellets ranged between 83 and 85% of theoretical.

Fig. 2.10. Pellet of $(U_{0.8},Pu_{0.2})N$ Sintered Same as Pellet in Fig. 2.9 Except Uranium Mononitride (Designated 3S3) Substituted for Sesquinitride-Rich Uranium Nitrides.

Since we interpreted the coarse porosity in the microstructure of the pellets sintered at 1800°C to be the original sites of PuN particles, we assumed that a treatment consisting of presintering followed by crushing and grinding would reduce or eliminate the coarse porosity. The feed for the pellets made from the 3S3 powder and sintered at an N_2 pressure of 0.5 torr was conditioned in this manner. Figure 2.11 shows that pretreatment reduced but did not eliminate the coarse porosity. The densities after sintering were the same. Any benefit from the solid-solutioning treatment appears to have been counterbalanced by the failure of the grinding step to restore the powder to a sinterability comparable to that of the fine 3S3 starting powder.

The use of an Ar backfill in the furnace in these two sintering experiments greatly reduced weight loss for all pellets, but the effect on the series that contained the 3S3 powder was greatest – it essentially reduced it to zero.

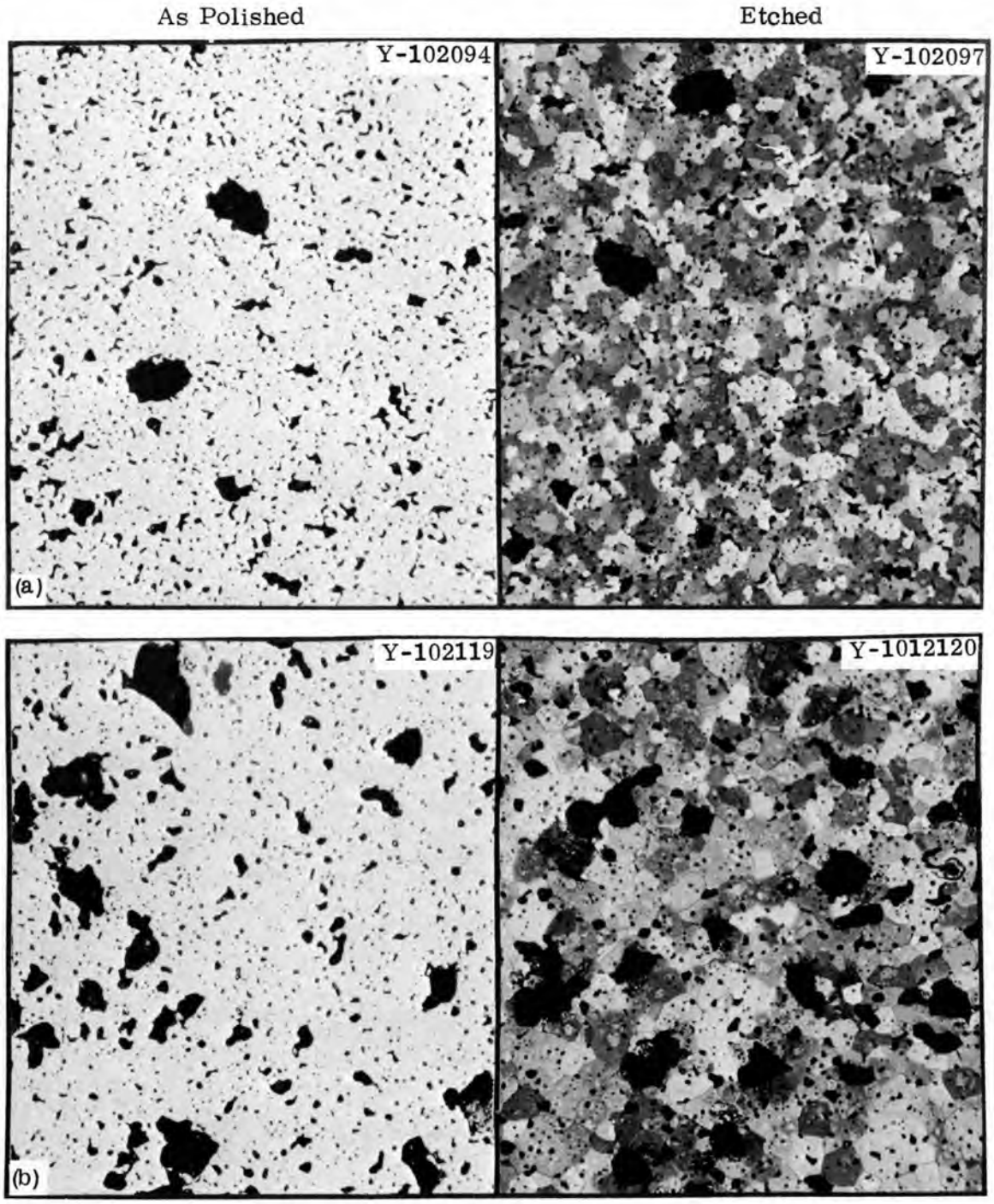

Fig. 2.11. Microstructure of $(U_{0.8},Pu_{0.2})N$ Pellets Prepared From a Mechanical Mixture Containing 3S3 Uranium Mononitride. (a) Powder was pretreated at 1800°C for 3 hr in N_2, ground 65 min, and then sintered again at 2000°C and an overpressure of 0.5 torr N_2. The number of large pores was reduced. Density was 84% of theoretical. (b) No pretreatment was given. Pellet was sintered at 2000°C and an overpressure of 0.1 torr N_2. Density was 83% of theoretical. 200×.

We also checked the behavior of several powders at 2250°C and a pressure of 0.1 torr N_2 but found limited improvement over the results obtained at lower temperatures and smaller N_2 overpressures. Weight loss was less than 1% for all samples at 2250°C.

Several conclusions can be drawn from the work done to date:

1. Conditions have been found both for the synthesis of U and Pu nitrides and the subsequent sintering of pellets pressed from mechanical mixtures of these powders to yield densities up to 85% of theoretical.

2. Loss of weight during sintering is reduced to less than 1% by use of an Ar cover gas at 630 torr.

3. As was found in other work on UN, a reduction in N_2 pressure to a level short of what would result in formation of free metal increases the sintered density.

Sintering Experiments on (U,Pu)N (V. J. Tennery)

We conducted experiments to confirm the role of N_2 pressure in the sintering of compacts of (U,Pu)N made from powders derived from U-Pu alloy or from mechanically blended UN and PuN powders. For the nitride powders prepared from the alloy, we selected sintering conditions corresponding to points A, B, C, and A′, B′, and C′ on the phase diagram shown in Fig. 2.12. The samples were heated to the temperatures corresponding to the indicated points while the N_2 pressure was maintained at the value shown on the diagram. The $(U_{0.81},Pu_{0.19})N$ samples were maintained at temperature for 300 min and then cooled quickly to 1400°C; the furnace was evacuated before further cooling to room temperature. The densities of the specimens after sintering are shown in Fig. 2.13; the enhanced sintering in $(U_{0.81},Pu_{0.19})N$ due to the reduced N_2 pressure is clearly indicated.

We conducted similar experiments on compacts made from mechanically mixed UN and PuN powders. The conditions chosen for the sintering runs are shown on the phase diagram in Fig. 2.14; those at low N_2 pressure correspond roughly to line Y, and those at higher pressure

ORNL-DWG 70-12933

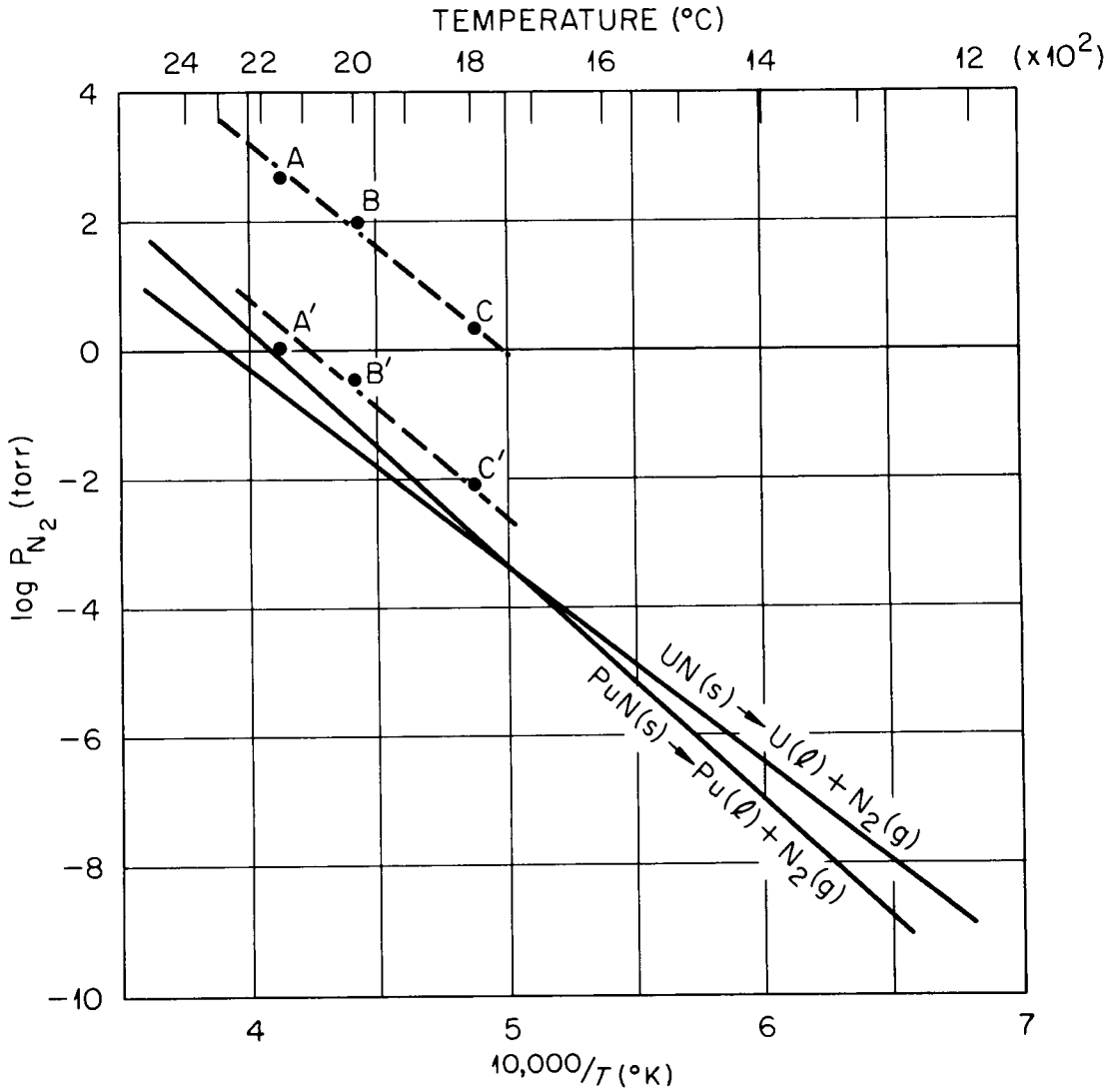

Fig. 2.12. Temperature and Pressure Conditions Used for Sintering $(U_{0.81},Pu_{0.19})N$ Specimens Derived From Alloy Powders.

correspond to line X. Two different UN powders were used in order to determine whether variations in the sinterability of the UN powder had a significant effect upon the densification of the blend of UN and PuN. The PuN powder used was designated PuN (4), and the UN powders used were designated 3S3 and 4+5. The 3S3 powder had a smaller particle size than did 4+5.

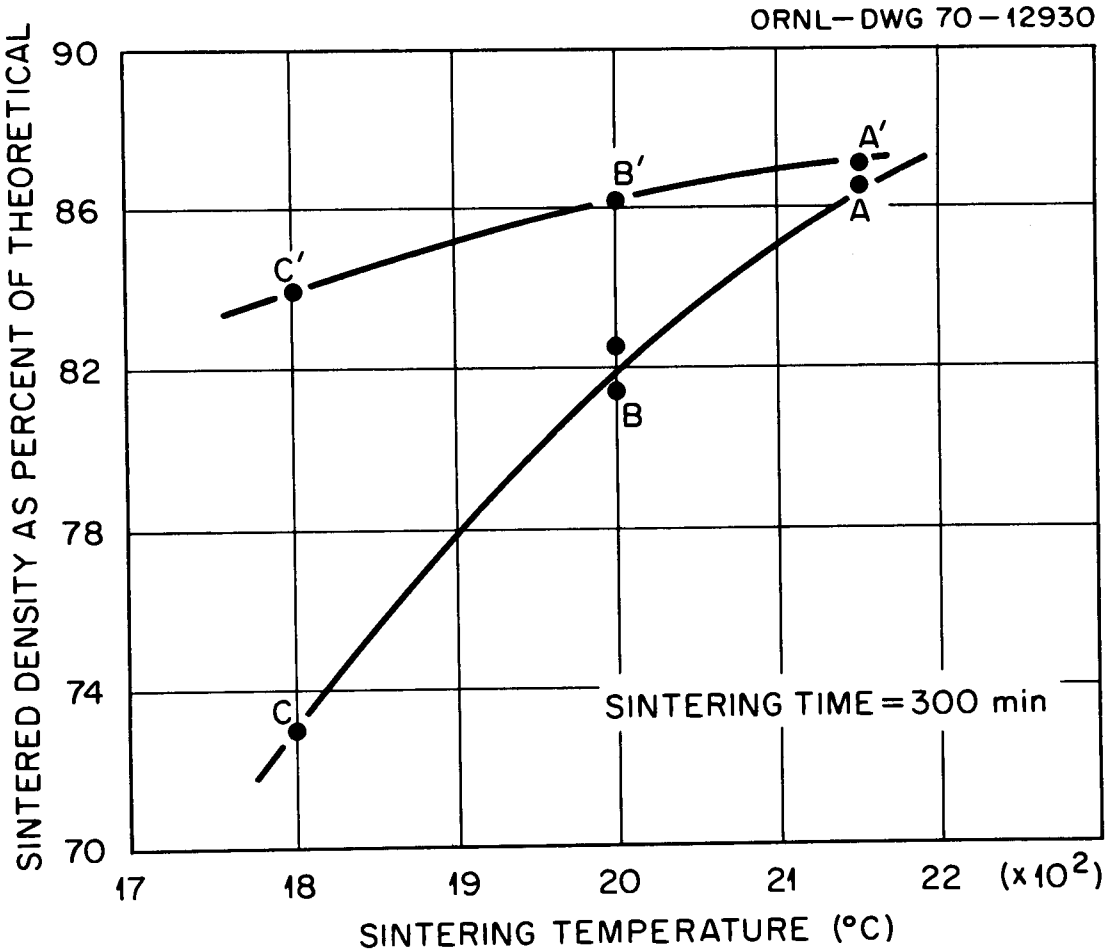

Fig. 2.13. Sintered Densities of $(U_{0.81},Pu_{0.19})N$ Specimens Sintered Under Conditions Shown in Fig. 2.12.

The data for the densification of these mechanical mixtures are shown in Fig. 2.15. In the case of the blend of UN (4+5) and PuN (4) sintered along lines X or Y, the sintered density was essentially a linear function of the sintering temperature. The use of lower N_2 pressures during sintering improved densification. In the case of the mechanical mixture of UN (3S3) and PuN (4), the densification was a nonlinear function of the sintering temperature and achieved a limit of about 84% of theoretical. In fact, all of the mechanical mixtures approached a density of about 84% of theoretical at the highest practical sintering temperatures (i.e., 2300°C or lower). The reason for these relatively low densities is evident in the microstructure of a sintered,

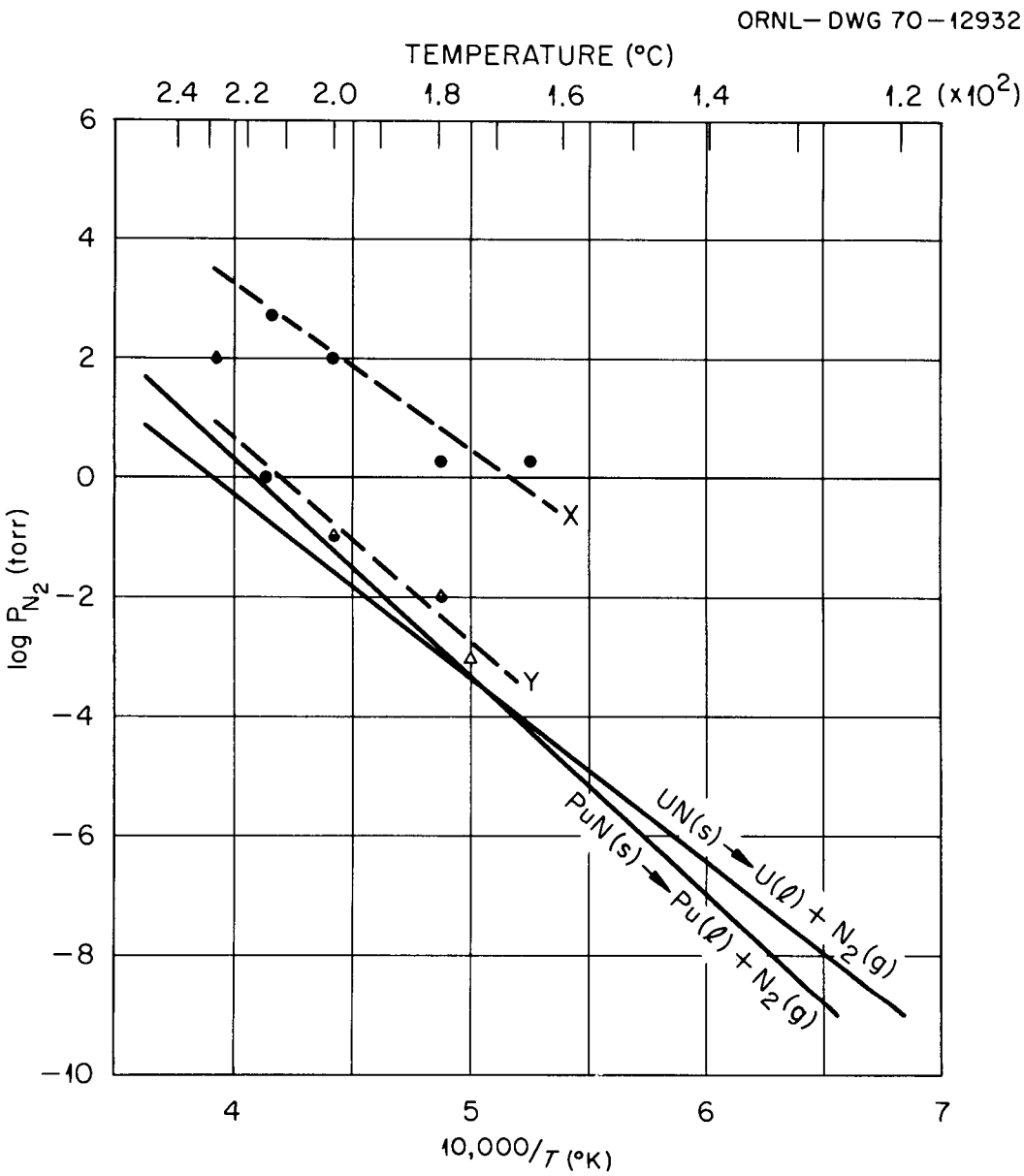

Fig. 2.14. Temperature and Pressure Conditions Used for Sintering $(U_{0.8},Pu_{0.2})N$ Specimens Derived From Mechanical Mixtures of Uranium Nitride and Plutonium Nitride.

mechanically blended sample (Fig. 2.11). There are numerous large voids in the microstructure that are apparently the sites of the original PuN particles. The presence of these voids effectively limited the ultimate density that could be achieved in the sintered compacts.

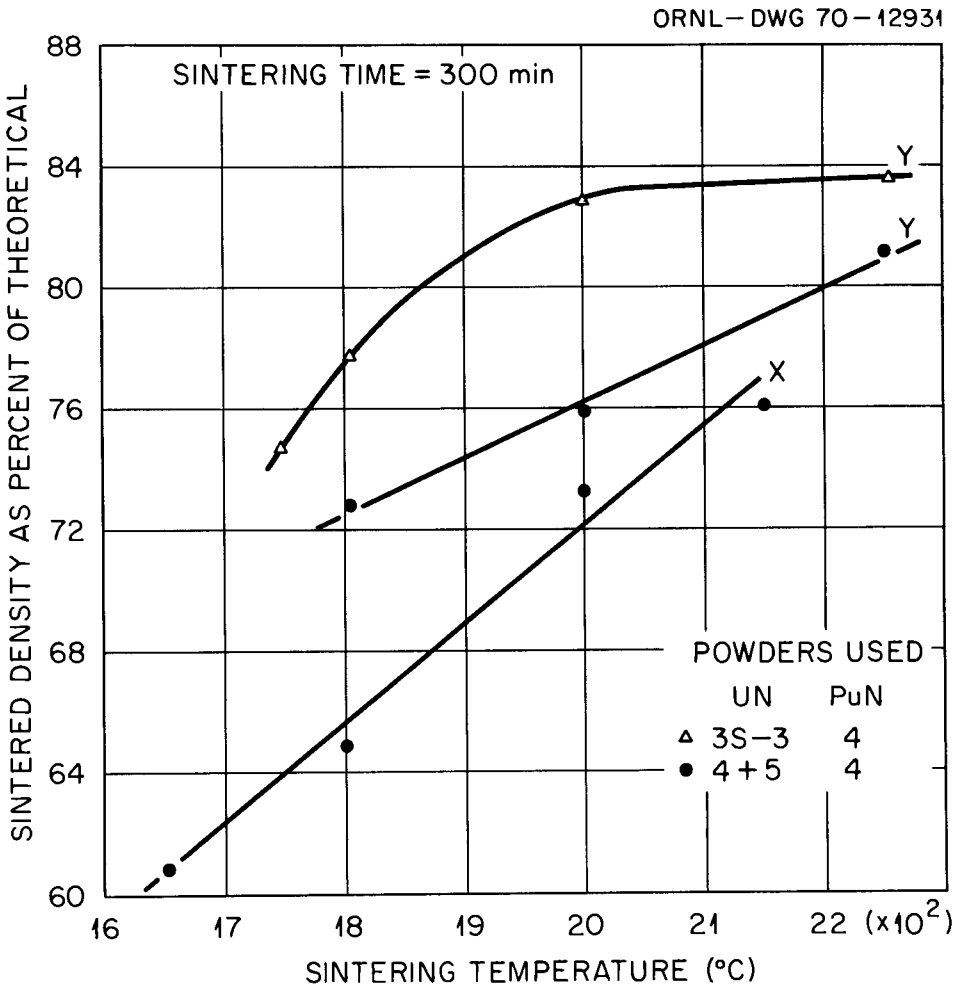

Fig. 2.15. Sintered Densities of $(U_{0.8},Pu_{0.2})N$ From Mechanical Mixtures of Uranium Nitride and Plutonium Nitride Powders.

Ball Milling and Sintering of Nitrides (E. S. Bomar)

Pellets prepared for irradiation tests in the ETR had a maximum density of about 90% of theoretical.[2] The next irradiation tests in the program will be conducted in the EBR-II; in these experiments a higher density is preferred. Workers at Battelle Memorial Institute (Columbus) reported[3] improved sinterability after ball milling (U,Pu)N powders in Mallinckrodt's Nanograde hexane.[4] In the manufacture of hexane, the Nanograde is given a final distillation treatment in glass equipment to remove trace impurities that would interfere with the use

of hexane as a carrier in a test for the presence of pesticides. Since the Mallinckrodt product was not readily available to us, we substituted hexane supplied by Fisher Scientific Company with a certification that it met the standards of purity of the American Chemical Society.

To reduce the O impurity content due to possible reaction with moisture, we dried the hexane by adding about 200 cm^3 of Type 13 Molecular Sieve to 800 cm^3 of the hexane. This treatment reduced the moisture content from 8 to less than 0.5 ppm.

We modified a stainless steel ball mill by adding a 1/8-in.-thick liner of depleted U metal to avoid pickup of steel in the powders during milling. We tested the performance of the mill with a charge made of 205 g of UN, 2029 g of 5/16-in.-diam WC balls, and 250 cm^3 of hexane, which was sufficient to cover the balls. We milled the nitride for a total of 32 hr but removed samples after 1, 2 1/2, 16, and 32 hr. We separated the WC balls from the mixture of UN and hexane by passing the charge through a 64-mesh screen and rinsing it with additional hexane. Most of the hexane was removed by decanting and the balance by evaporation at a reduced pressure created by a small diaphragm pump.

Pellets were pressed from the UN powders extracted at different times during milling. All of the powders exhibited good fabrication properties. We sintered them at 1800°C for 5 hr at 10^{-3} torr N_2. The sintered density depended directly on milling time and ranged from 89 to 97% of theoretical.

We repeated the same milling and sintering procedure with (U,Pu)N that contained about 18% Pu. The mixed nitride powder responded to milling satisfactorily but showed evidence of free metal during sintering, since several of the pellets stuck to the W setter plate. When we repeated the sintering experiment at 2150°C and 630 torr N_2, the results were similar. Since the latter conditions had previously proved satisfactory for preparation of mixed nitride pellets for irradiation in the ETR, the free metal apparently was present in the milled powder rather than formed during the sintering. Further, the absence of free metal in the UN powder discounts the U liner as a source. We shall

process the mixed nitride through another nitriding cycle to remove the metal content before we perform additional sintering experiments.

Samples from both the UN and (U,Pu)N sintered pellets were examined metallographically. The UN, as shown in Fig. 2.16, had a clean, dense structure with no evidence of free metal. The mixed nitride had a continuous, intergranular network of metal, which can be seen in Fig. 2.17.

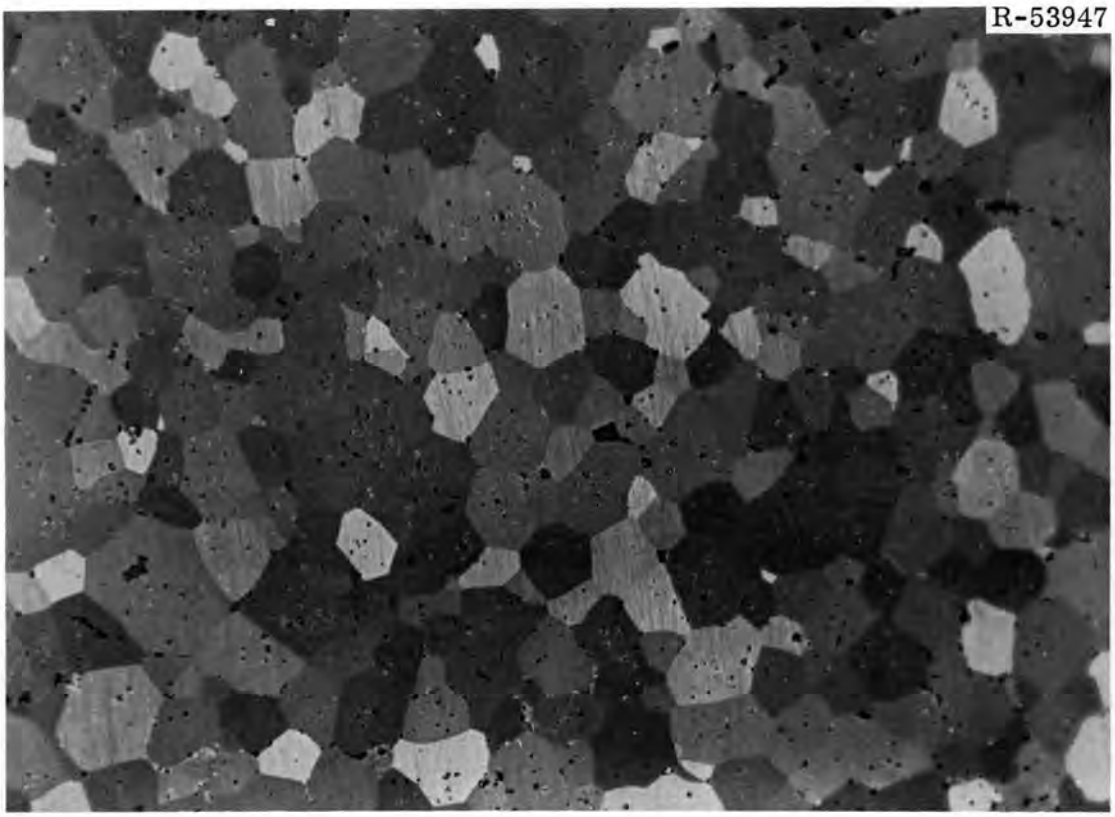

Fig. 2.16. Microstructure of Uranium Mononitride Pellet Sintered for 5 hr at 1800°C with an Overpressure of 10^{-2} torr N_2. Uranium mononitride powder preconditioned by ball milling for 32 hr in hexane. Etched with solution of HNO_3, HF, and lactic acids. 500×.

Some increase in O impurity accompanied milling of the nitride powders. The mixed nitride initially contained 825 ppm O; the samples analyzed after 16 and 32 hr contained 1500 and 1450 ppm O, respectively.

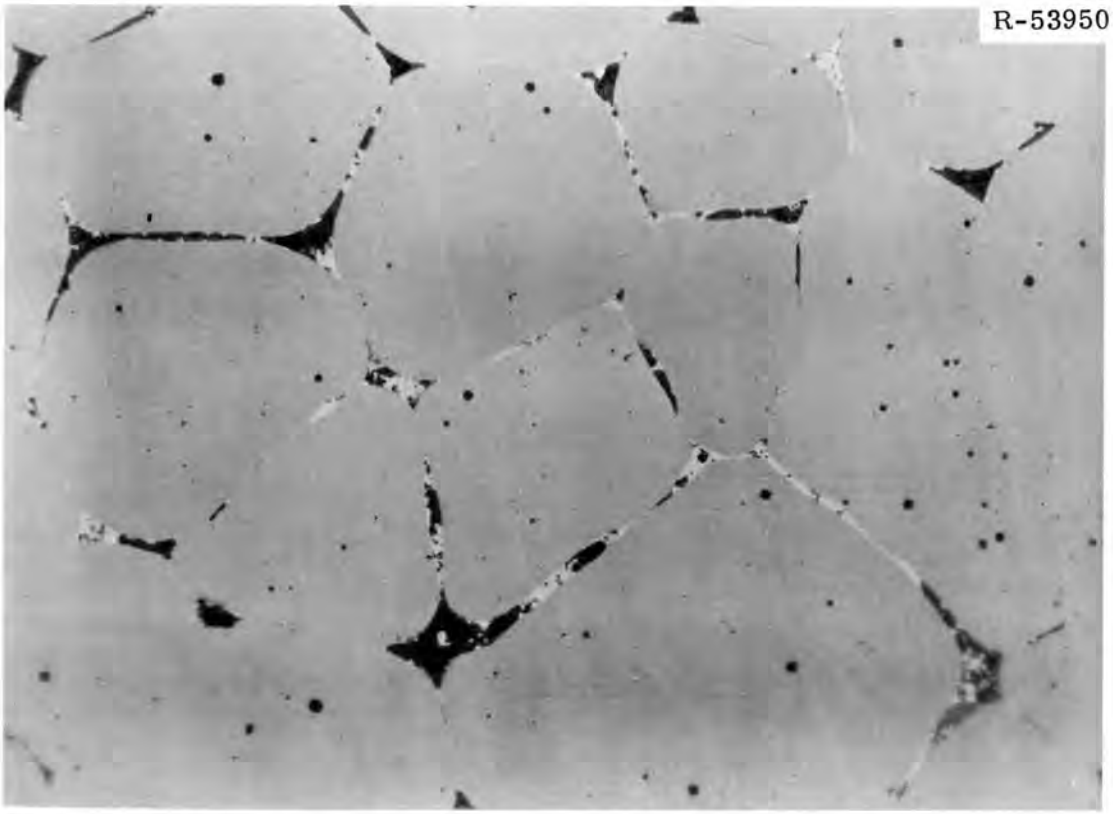

Fig. 2.17. Microstructure of (U,Pu)N Pellet Sintered 5 hr at 1800 to 1900°C with an Overpressure of 10^{-2} torr N_2. Free metal at grain boundaries is due to incomplete conversion of uranium-plutonium alloy to nitride. A portion of the free metal has reacted with the cell atmosphere to form a dark reaction product. As polished. 500×.

A much larger change was found, however, in the C content. The mixed nitride initially contained about 300 ppm C; but after milling for 16 hr it contained 3000 ppm C, and after 32 hr it contained 4650 ppm C.

Abnormal wear of the WC balls was first suspected, but no W was found by spectrographic examination of the nitride powder. To avoid the hazards of broken glass in the Pu glove boxes, after we dried the hexane, we transferred it to a polyethylene bottle before putting it into the glove-box line. We had checked the stability of polyethylene in contact with hexane by storing some of the liquid in a polyethylene bottle for a few days. There were no visible effects on the polyethylene.

After finding the increase in C impurity in the milled powders, we placed samples of hexane from the original glass bottle and from a polyethylene bottle in which the hexane had been tumbled for 24 hr into two watch glasses. That from the glass container evaporated to dryness with only a trace of residue, but that from the polyethylene bottle left a substantial deposit. The polyethylene was, undoubtedly, the source of a portion of the C picked up by the milled powder. Another milling experiment is now in progress with UN to verify this suspected source of C contamination in the ball-milled nitride powders.

Synthesis of Uranium Nitride (V. J. Tennery)

We produced about 1.8 kg of UN powder that contained 100 ppm O. The powder will be used to fabricate end pellets for pins for irradiations in both the EBR-II and ETR. This powder will also provide about 270 dense UN pellets for use in development of a suitable Na bonding technology and of a nondestructive testing procedure for the relatively long Na-bonded pins that contain (U,Pu)N for irradiation in the EBR-II.

New Facilities (V. J. Tennery)

Several new facilities are being prepared for operation in our inert-atmosphere Pu facility. The general purposes and status of these are briefly described below.

Helium Purifier and Recirculator for Plutonium Glove-Box Atmospheres (E. S. Bomar). — The CVI Corporation completed fabrication of a low-pressure He purifier and recirculation unit that will provide the inert atmosphere required by a number of our glove boxes and will serve the needs of both the Interim Plutonium Laboratory and the Fuel Cycle Alpha Facility. The purifier functions on the principle of adsorption at cryogenic temperature on a bed of activated C and was designed to reduce each of a broad range of impurities to levels less than 5 ppm by volume.

The purifier is mounted on skids and consists of two parallel purification sections and two independent and parallel enclosed blowers. The system is piped and valved to allow either blower to be used selectively with either purification section to allow continuous operation. Switchover from one purification section to the other is automatic and is dictated by analyzers for O and hydrocarbons at the purifier discharge. Selection and switchover of the blowers, however, must be made manually. The use of the analyzer signal to indicate adsorber-bed breakthrough and to automatically switch to the standby carbon bed will allow use of the full capacity of the bed before recycle is necessary and will, therefore, reduce the frequency of regeneration and its attendant costs.

Each purification section consists of a vacuum-insulated cold box that contains a counterflow Giauque-Hampson type of heat exchanger, evaporator coil, and cryogenic adsorber. The coil and adsorber are immersed in liquid N, which provides the refrigeration for the process. Each cold box incorporates an O-ring-sealed bell jar that may be lifted vertically to expose the cryogenic portions of the system. The whole purifier assembly is mounted on a welded skid framework. Those portions of the skid that support the cold boxes are bolted, however, to allow horizontal removal of the cold boxes from the main skid for transportation to an area where suitable headroom exists for removing the bell jars.

Each blower assembly consists of a single-stage rotary lobe-type blower and 15 hp 1800-rpm induction motor with special class H insulation suitable for 125 °C ambient temperature. The blower and motor are seal welded into a leak-tight enclosure with all piping penetrations welded and electrical leads "potted." The access plate sealed with an O-ring provided on the top of each blower enclosure is large enough to allow removal of either the blower or motor. A control panel is located on one end of the purification skid. All startup and manual control operations must be performed at this panel. A remote console is also provided from which alarms, equipment status, and several pertinent process functions can be monitored.

The manufacturer proof tested the purifier before shipment to demonstrate satisfactory performance of the adsorber beds and of the automatic switchover feature of the unit. We spent about 8 hr removing internal impurities that were either adsorbed on pipe surfaces or trapped in several sections of dead-end piping connected to instruments such as pressure gages. The level of O_2 impurity in the discharge from the purifier gradually decreased from an initial level of more than 1000 to 3 ppm O. When the level reached 3 ppm O, air was injected into the return line to the purifier at the rate of 3 scfh, which is equivalent to a rate of loading of about 63% of the design level. This addition had no detectable adverse effect on the level of impurities in the discharge He, which fell to as low as 0.3 ppm during an overnight run. After 12 1/2 hr, the rate at which air was added was increased to 5 scfh and, 2 1/2 hr later, increased again to 7 scfh without a change in the level of O_2 impurity in the discharge He.

Next we sampled the purified gas at a level two-thirds of the way through the C bed. After 2 1/2 hr, we noted a slight rise to 0.8 ppm. The rate at which the O_2 content rose in the discharge stream of the purifier was slow enough to provide the 31-min period necessary for cooling and testing the standby adsorber bed before the O_2 content reached an excessive level. From an original level of 0.8 ppm, the O content increased to 9 ppm after 3 hr and to 50 ppm after 6 hr. The breakthrough profile is shown in Fig. 2.18. The integrated volume of air adsorbed by the bed before breakthrough occurred was 176% of the design capacity.

The purifier was delivered to ORNL on a pneumatically cushioned trailer and positioned without undue difficulty. We are proceeding with the balance of the installation.

Mercury Pycnometer Facility (J. P. De Luca). — We are installing an Hg pycnometer and an analytical balance in a glove box for determining the bulk density of sintered fuel pellets of (U,Pu)N and other Pu-bearing ceramics. The installation of the equipment is 90% complete. The glove box was received from the vendor in satisfactory condition. A

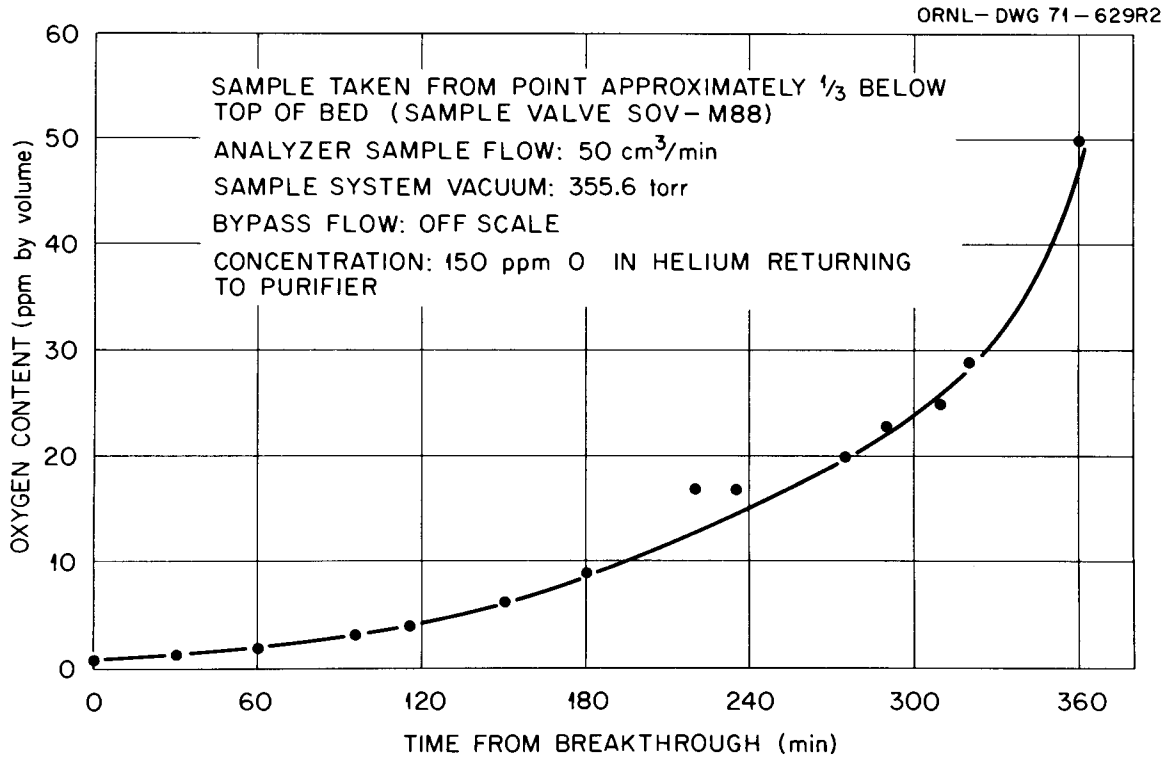

Fig. 2.18. Oxygen Content of Helium From Bed A of CVI Purifier Following Breakthrough.

system of Hg vapor filters was designed, fabricated, and installed on the glove box off-gas system to remove any Hg vapor that might result from the Hg pycnometer so that the off-gas header, valves, and He purifier soon to be installed would not be attacked by traces of Hg vapor. A detector for Hg vapors was also installed on the glove box to determine the amount of vapor in the glove box and in the off-gas line after the atmosphere from the glove box passes through the Hg filters. Thus, the efficiency of the Hg filters is monitored continuously.

The control system for the glove-box atmosphere was fabricated and installed. The glove box was installed in the Interim Plutonium Facility. The mechanical vacuum pump and analytical balance that are to be used in conjunction with the pycnometer were received and installed. The

pycnometer, which is being fabricated at ORNL, is nearly completed. It will be checked for operational performance and then installed. We expect the pycnometer system to be operational by February 1971.

Oscillatory Grinder (V. J. Tennery). — The ability to grind ceramic powders to increase their sintering activity is basic to the development of experimental fuels for irradiation experiments. The experimental difficulties are increased for (U,Pu)N powders because of the extreme tendency of these materials to become contaminated with O. The high hardness of these materials also leads to contamination by the grinding medium itself unless the grinding method and medium are chosen very carefully.

The observed experimental difficulty of achieving sintered densities greater than 90% of theoretical for (U,Pu)N led us to examine the use of ball milling in hexane and dry grinding in an oscillatory mill. We previously used this latter method successfully on very pure oxides, and others have used it for (U,Pu) carbides.[5]

Accordingly we ordered and received an oscillatory mill. The glove box for this grinder was designed and ordered; if it is delivered, as expected, by March 30, 1971, the grinder should be operational by April 30, 1971. The control panel for the glove-box atmosphere for this facility is being assembled.

Characterization of Nitride Fuels (V. J. Tennery)

X-Ray Diffraction Studies of Uranium-Plutonium Nitrides. — We measured by x-ray diffraction methods the lattice constant of various UN-PuN solid solutions as a function of self-damage by irradiation at 25°C. The lattice constant of a sample of $(U_{0.8},Pu_{0.2})N$ increased by 0.0018 Å in 210 days from the time the sample was last annealed at high temperature. A sample of pure PuN showed about 2.9 times as much self-damage in the same time. The self-damage observed in $(U_{0.6},Pu_{0.4})N$ and $(U_{0.4},Pu_{0.6})N$ was very similar; it was about 60% of that observed in PuN in about 250 days. Self-damage in $(U_{0.2},Pu_{0.8})N$, on the other hand, was about 86% of that observed in PuN in 200 days.

Analytical Characterization. — Two shipments of U-Pu alloy were received; 2 kg of ^{235}U-Pu alloy and 1 kg of ^{238}U-Pu alloy were cast into ingots of about 500 g each and shipped to this laboratory under an Ar atmosphere. The ingots were relatively bright as received except for some minor surface contamination from the original casting molds.

The ingots were cleaned, and samples were analyzed for U and Pu isotopic contents before the metal was synthesized into nitride powder. The results of the isotopic analyses are given in Table 2.1. Alloy A will be used for producing about 120 nitride pellets for use in fuel pins for irradiation in the ETR, and alloy B will be used for producing about 500 nitride pellets for fuel pins for irradiation in the EBR-II.

Considerably less gamma radiation was emitted from either of these alloys than from another lot of alloy[6] from WADCO. We established that the level of residual gamma radiation in the earlier alloy originated from ^{241}Am, which had been produced from the ^{241}Pu. The ^{241}Pu contents

Table 2.1. Isotopic Contents of U-Pu Alloys

Isotope	Concentration, %	
	Alloy A	Alloy B
^{238}Pu	< 0.2	a
^{239}Pu	92.24	93.21
^{240}Pu	6.19	6.21
^{241}Pu	0.55	0.55
^{242}Pu	0.022	0.023
^{244}Pu	< 0.001	< 0.001
^{233}U	< 0.0004	< 0.0005
^{234}U	0.0006	0.914
^{235}U	0.159	92.56
^{236}U	0.003	0.451
^{238}U	99.84	6.08

[a]Not determined due to ^{238}U interference.

of alloys A and B were essentially equal to that observed in the earlier alloy. We concluded that the alloys we recently received contained Pu from reasonably recent processing and that the level of ^{241}Am had not had time to reach its equilibrium concentration in the material. As noted previously,[7] a level of about 0.5% isotopic ^{241}Pu in the alloy leads to significant doses to the hands of people who work with it in the glove box once appreciable ^{241}Am is produced.

Development of the Dumas Technique for the Determination of Nitrogen in (U,Pu)N (V. J. Tennery, J. L. Botts[8])

The Dumas technique has several potential advantages over the Kjeldahl method for determining N in compounds such as UN and (U,Pu)N as well as in powders that contain U_2N_3. Samples that contain a sesquinitride phase are especially difficult to analyze by the Kjeldahl technique because total dissolution of the sample by any simple acid is very difficult and sometimes requires several days for a 100-mg sample in heated, sealed, glass tubes. Rather than requiring sometimes laborious dissolution of the sample in acid under carefully controlled conditions followed by a titration, the Dumas method consists of oxidizing the sample in an orderly fashion so that the evolved N_2 can be collected and measured. No acids are used in the Dumas method, and once the analysis is started it requires only a minimum amount of attention while the N_2 is collected in the nitrometer. We have successfully oxidized UN samples in our Dumas apparatus by using the CO_2 sweep gas alone as the oxidant. This step avoids the need and potential danger of mixing a solid oxidant with the nitride sample before inserting it into the oxidizing furnace. When the Dumas sample consisted of one or two chunks fractured from the dense, sintered piece of UN, 0.060-g samples have been totally oxidized in 30 min at 1100°C in CO_2.

We compared the two techniques by analyzing Kjeldahl samples (mass about 0.50 g) and Dumas samples (mass about 0.050 to 0.060 g) of the same UN specimen (V-19), which analyses had shown contained 300 ppm O and 200 ppm C:

Nitrogen Content, wt %	
Kjeldahl	Dumas
5.38	5.48
5.41	5.48
5.46	5.47
5.49	5.49
5.48	5.47
5.52	5.46
5.53	5.47
5.52	5.47
5.49	5.45
5.47	5.45
5.53	5.46
5.45	5.46
5.54	
5.49	
5.47	
5.49	
5.51	
5.51	
Average = 5.49%	Average = 5.47%

This technique, when adapted to the analysis of (U,Pu)N, could require far less sample than has been required heretofore for the Kjeldahl analyses. The averaged results of the two procedures differed by only 0.02% N, and the precision of the Dumas method was superior to that of the Kjeldahl method. We are now placing a water jacket around the nitrometer to maintain constant temperature in order to reduce errors due to variations in room temperature and are trying to improve the precision of the nitrometer. The total nonmetal content of UN sample V-19 was determined as 5.54% using the Kjeldahl results and 5.52% using the Dumas nitrogen values, whereas 5.56% is the theoretical value for $^{238}U^{14}N$.

Compatibility of Mixed Nitrides and Carbides with LMFBR Cladding Alloys (J. M. Leitnaker)

Our approach to compatibility in high-performance fuel systems is to characterize interactions that can occur between the fuel and cladding material. A basic understanding of these reactions may point to methods for tailoring the fuel so that the reactions cannot occur and perhaps to methods for reducing reaction rates.

The Pu-Cr-N System (J. P. De Luca)

We continued investigation of the Pu-Cr-N system by heat treating five additional mixtures of Pu, Cr, and N. Table 2.2 lists all of the experiments run to date and the results. Enough information has been acquired to allow us to present the tentative ternary phase diagram of the Pu-Cr-N system between 800 and 1700°C.

The experiments can be most clearly discussed if they are divided into two groups: experiments in which the same phases were present before and after the anneal, and experiments in which different phases were present before and after the anneal.

Samples Pu-Cr-N-5, -7, and -8 make up the first group. In all three of these experiments the appropriate proportions of PuN (−325 mesh) and Cr_2N (−325 mesh) were mixed together and formed into 1/4-in.-diam pellets about 1/16 in. high. The Cr_2N had been prepared previously by heating Cr powder under 200 torr of N_2 at 1300°C for 720 min. An x-ray pattern showed it to be single-phase Cr_2N. The single-phase PuN was prepared by hydriding, dehydriding, and nitriding Pu metal.[9]

Sample Pu-Cr-N-5, which contained 50 at. % Cr (Cr + Pu = 100%). was heated to a dull red heat (700 to 800°C) under a vacuum; then N_2 was introduced, the temperature was raised, and it was heated 506 min at 1440°C. After the anneal, the sample was cooled to a dull red, the N_2 was removed, and the sample was cooled to room temperature under high vacuum. This same procedure was used with all the other samples

Table 2.2. Summary of Experimental Data for Pu-Cr-N System

Sample Designation	Phases Present Before Anneal	Time at Temperature (min)	Temperature (°C)	Nitrogen Pressure[a] (torr)	Chromium Content[b] (mole %)	Lattice Constant of PuN (Å)	Phases Present After Anneal[c]
Pu-Cr-N-2	PuN Cr	202	1705±5	200	65.51	4.90684±0.00016	PuN Cr_2N Cr
Pu-Cr-N-5	PuN Cr_2N	506	1440±5	200	50.00	4.90747±0.00011	PuN CrN [Camera lines, PuO_2, PuN beta radiation]
Pu-Cr-N-7	PuN Cr_2N	716	1315±5	400	50.85	4.90596±0.00012	PuN Cr_2N
Pu-Cr-N-8	PuN Cr_2N	731	1305±5	400	66.89	4.90603±0.00019	PuN Cr_2N
Pu-Cr-N-9	PuN Cr_2N	1262	790±20	400	32.05	4.90553±0.00009	PuN Cr_2N [CrN]
Pu-Cr-N-10	d	1437	1210±5	Dynamic Vacuum 2.0×10^{-7}	50.85	4.90744±0.00007	PuN Cr

[a]See text for details of when N_2 was introduced and removed.

[b]Calculated from starting material, assuming Cr + Pu = 100%.

[c]Phases shown in brackets were only tentatively identified.

[d]The starting material for sample Pu-Cr-N-10 was taken from the two-phase (PuN and Cr_2N) material that resulted from the annealing of sample Pu-Cr-N-7.

heated in N_2. The x-ray pattern made from sample Pu-Cr-N-5 showed that the primary phases that resulted were PuN and Cr_2N.

Table 2.2 shows the conditions under which samples Pu-Cr-N-7 and -8 were run and the results. Note that in each case the phases present before and after annealing were identical. The average lattice constants of PuN calculated from these samples ($\underline{a}$ = 4.90599) are identical, for all practical purposes, to that for pure PuN. Thus, it appears that Cr is not very soluble in PuN at room temperature. We have reason to believe that at high temperatures Cr or Cr_2N is slightly soluble in PuN.

From the results for samples Pu-Cr-N-5, -7, and -8 it appears that PuN did not enter into any type of reaction with Cr_2N. Therefore, one would expect that the phases present would depend only on the stability range of the Cr nitrides. This is, indeed, what is seen. According to Schwerdtfeger,[10] Cr_2N is the stable Cr nitride at temperatures and pressures under which these samples were run. A partial phase diagram at 760 torr total pressure for the Pu-Cr-N system is proposed in Fig. 2.19. The numbered solid lines in the two-phase region of Cr_2N and PuN represent the composition range of Cr_2N. According to Smith,[11] the homogeneity range of Cr_2N at the temperature of interest here is 27.6 to 33.3 at. % N.

Samples Pu-Cr-N-2, -5, and -10 make up the second group of experiments in this system. In each case, the initial and final compositions were different.

Table 2.2 shows that sample Pu-Cr-N-2 started as a mechanical mixture of PuN and fine Cr metal powder. After heat treatment three phases resulted: PuN, Cr_2N, and Cr (the microstructure is shown in Fig. 2.20). Since PuN, Cr_2N, Cr, and N_2 cannot all be in equilibrium unless by chance the N_2 pressure of 200 torr corresponds to the N_2 activity in the PuN-Cr_2N-Cr three-phase region the sample is probably not in equilibrium. A second explanation for the existence of the three condensed phases in sample Pu-Cr-N-2 is that Cr_2N is not stable at 1700°C and 200 torr N_2. A third possible explanation — and the most probable — for the existence of three condensed phases in

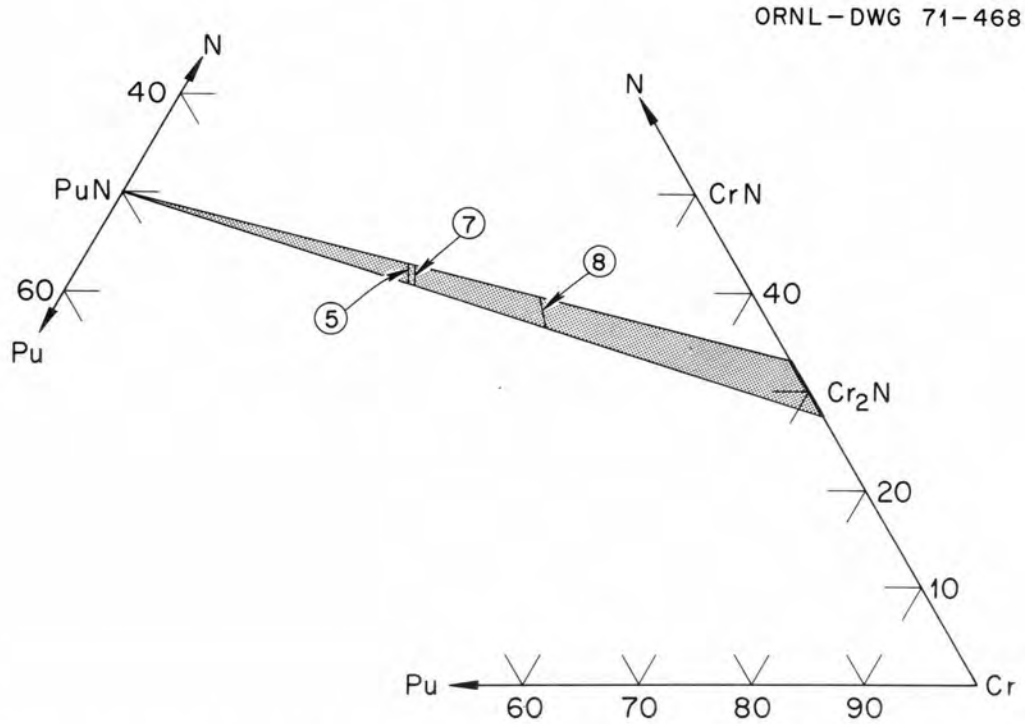

Fig. 2.19. Partial Phase Diagram of the Plutonium-Chromium-Nitrogen System.

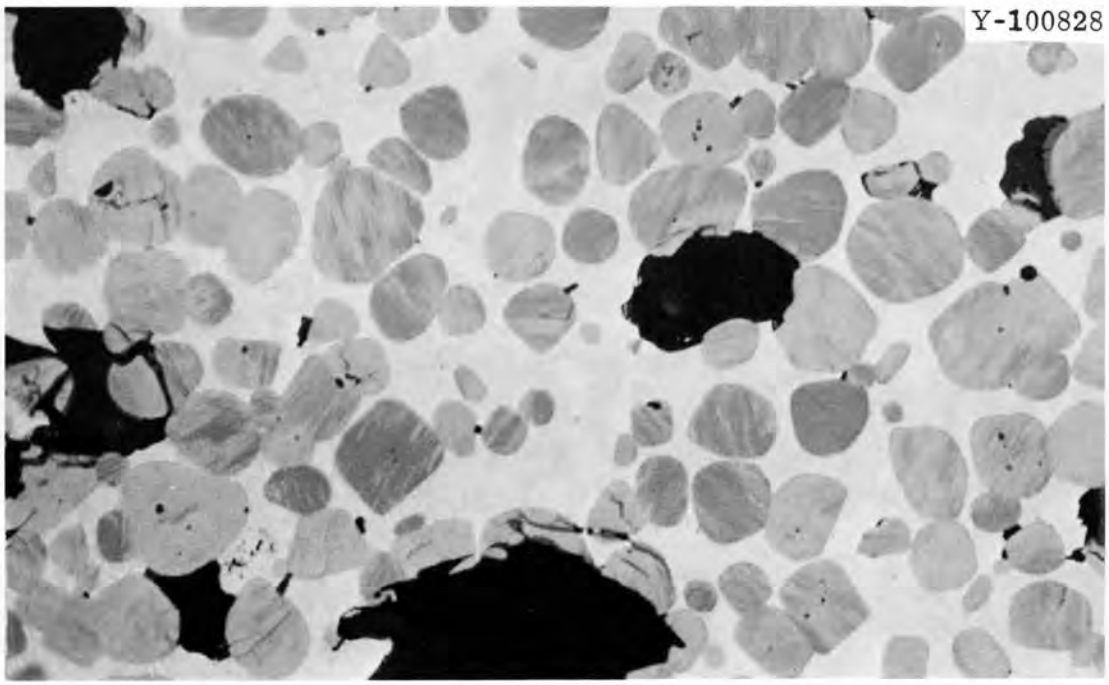

Fig. 2.20. Microstructure of Plutonium Nitride and Chromium Heated at 1705°C for 202 min Under 200 torr N_2. 500×.

sample Pu-Cr-N-2 is that as the sample was cooled in about 60 sec from 1700 to 800°C (at which temperature the N_2 is removed) the Cr_2N formed. Caplan et al.[12] showed "massive islands" of Cr_2N formed upon cooling Cr liquid containing dissolved N. Figure 2.20 shows that two precipitation reactions took place during cooling. Either Cr or a Cr compound did dissolve in the PuN (large, rounded, dark areas) but then precipitated during cooling so that the lattice constant of PuN at room temperature was identical to that of the pure phase. The second precipitation reaction was the formation of Cr_2N from the liquid phase. This is shown in Fig. 2.20 as islands of Cr_2N surrounded by the highly reflective Cr metal phase. Figure 2.20 also shows that the liquid dissolved some of the PuN, as indicated by the rounded corners on the PuN particles. Thus, it does appear that the PuN and Cr or PuN and Cr_2N do interact slightly at 1700°C. Thus at present it appears that all of the Cr_2N in sample Pu-Cr-N-2 formed during cooling and that PuN and Cr interacted only slightly at 1700°C under 200 torr N_2.

Sample Pu-Cr-N-9, a mixture of Cr_2N and PuN, was heated 1262 min at 790°C. X-ray analysis positively identified PuN and Cr_2N, and the two strong lines of CrN were also observed. Two lines are not enough to give a positive identification, but these lines did not match any other compound likely to have been in the system. At 400 torr N_2 and 790°C, CrN is the stable nitride phase. Since, as noted above, it is very unlikely that three condensed phases would be in equilibrium, it appears that the Cr_2N was being slowly converted to CrN. It is possible that CrN formed from Cr_2N during cooling; but in several investigations[10,11] of the Cr-N system, CrN has never been observed to form in this way.

Sample Pu-Cr-N-10 did not reach equilibrium. The starting mixture was Cr_2N and PuN. After 1380 min of heat treatment under vacuum, all of the Cr_2N was converted to Cr. No reaction was observed between PuN and Cr_2N or Cr.

Figure 2.21 is the proposed partial phase diagram for the Pu-Cr-N system. This figure was constructed from Fig. 2.19 and the information obtained from samples Pu-Cr-N-2, -9, and -10. Sample Pu-Cr-N-2 is

ORNL-DWG 71-467

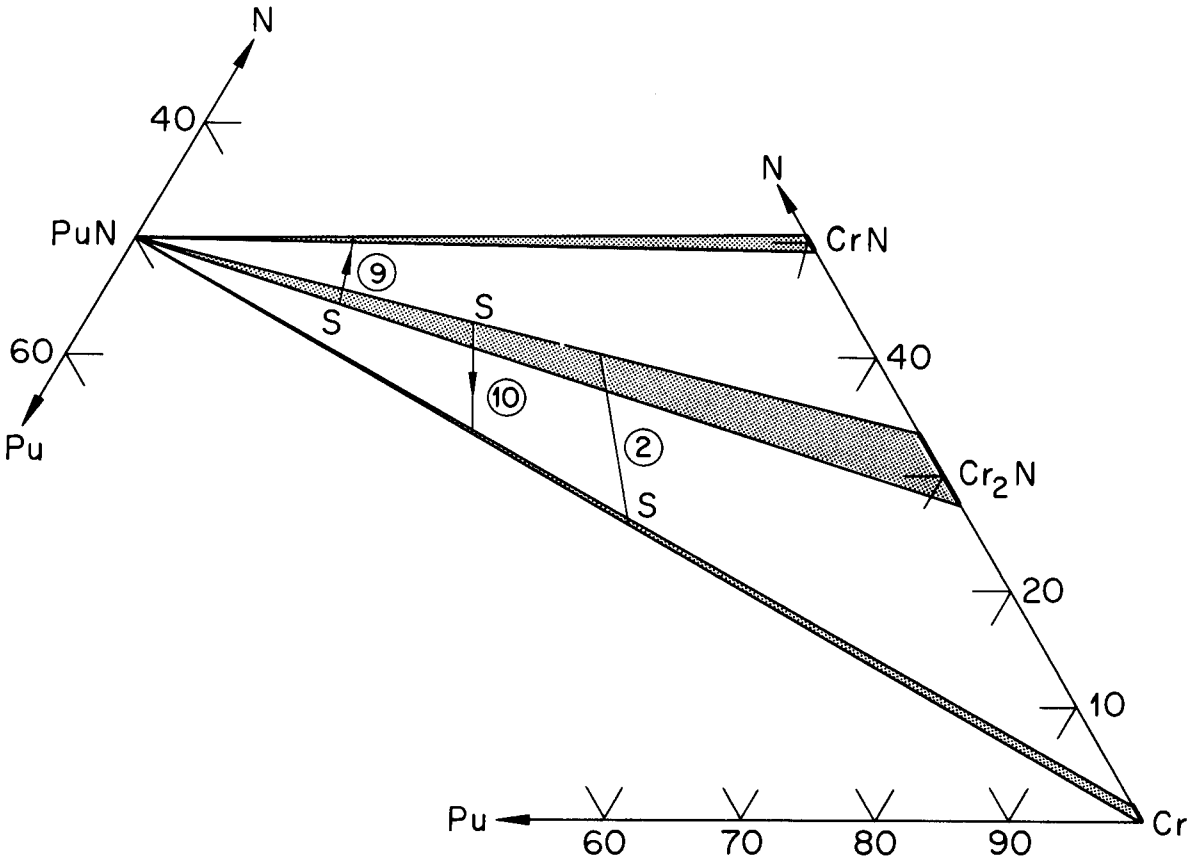

Fig. 2.21. Partial Phase Diagram of the Plutonium-Chromium-Nitrogen System.

represented in Fig. 2.21 by a solid line over a range of N_2 activities that includes all the possibilities mentioned above. Samples Pu-Cr-N-9 and -10 are represented as arrows pointing in the direction of equilibrium for each sample.

Thermodynamics of Plutonium Nitride (J. P. De Luca)

As part of our program on compatbility and thermodynamic characterization of advanced fuels systems for the second generation LMFBR's, we have built a sophisticated vapor-pressure apparatus. The apparatus can be used in investigating a variety of problems of great interest to the advanced fuels program. The equilibrium N_2 pressure of PuN and

(U,Pu)N can be determined and, as a result, (1) the thermodynamic compatibility of the fuels with stainless steel can be assessed quantitatively, (2) the homogeneity range (if it exists) of the nitride fuels can be determined, and (3) results will be produced that can aid in understanding the sintering process in the nitride fuels. Similar studies could be made of oxide fuels that contain Pu.

Another very important problem, which was pointed out previously,[13] is the effect of impurities, such as O and C, on the thermodynamic properties of the fuel. Investigation of this problem with the vapor-pressure apparatus can provide answers to many important questions: (1) the effect of a known amount of O on the compatibility of the advanced fuel system, (2) the effect of C on the reaction between the fuel and cladding, and (3) the effect of O on the interaction between fuel and cladding.

The apparatus can also be helpful for fuel synthesis since, with it, (1) the rate of hydriding can be determined as a function of temperature, hydrogen pressure, and microstructural condition of the alloy, and (2) the rate of dehydriding and nitriding can be determined as a function of the process variables to minimize the time required for these various steps.

General Function of Apparatus. — The system can be divided into six basic parts on the basis of component functions:

1. The vacuum equipment (three oil diffusion pumps and three mechanical pumps) provides and maintains a high to ultrahigh vacuum.

2. The system for control and measurement of gases (two variable leak valves, a capacitance manometer, a McLeod gage, and three hot-cathode ionization gases) allows introduction of known, small quantities of various gases and measurement of the accompanying change in pressure.

3. The weighing mechanism (a recording electrobalance) is used to measure the weight of samples at elevated temperatures.

4. The heating station (a split W-mesh resistance heater) is used to control the temperature of the sample.

5. A gas analysis system (a single-pole mass spectrometer) is used to determine the composition of the noncondensable vapors above the sample.

6. An inert-atmosphere glove box is used to load and unload the sample safely.

Figure 2.22, a schematic diagram of the apparatus, shows all the major parts except the glove box. In Fig. 2.23, an overall photograph of the equipment, the glove box is to the rear of the two large vacuum chambers, which house the furnace and electrobalance. Figure 2.24, a photograph of the inside of the glove box, shows the sample crucible and top heat shields being held by the rack-and-pinion mechanism used to load the sample. The large vacuum flange at the lower right in Fig. 2.24 is the opening through which the sample is loaded; the smaller flange at the upper left is the opening through which tare weights

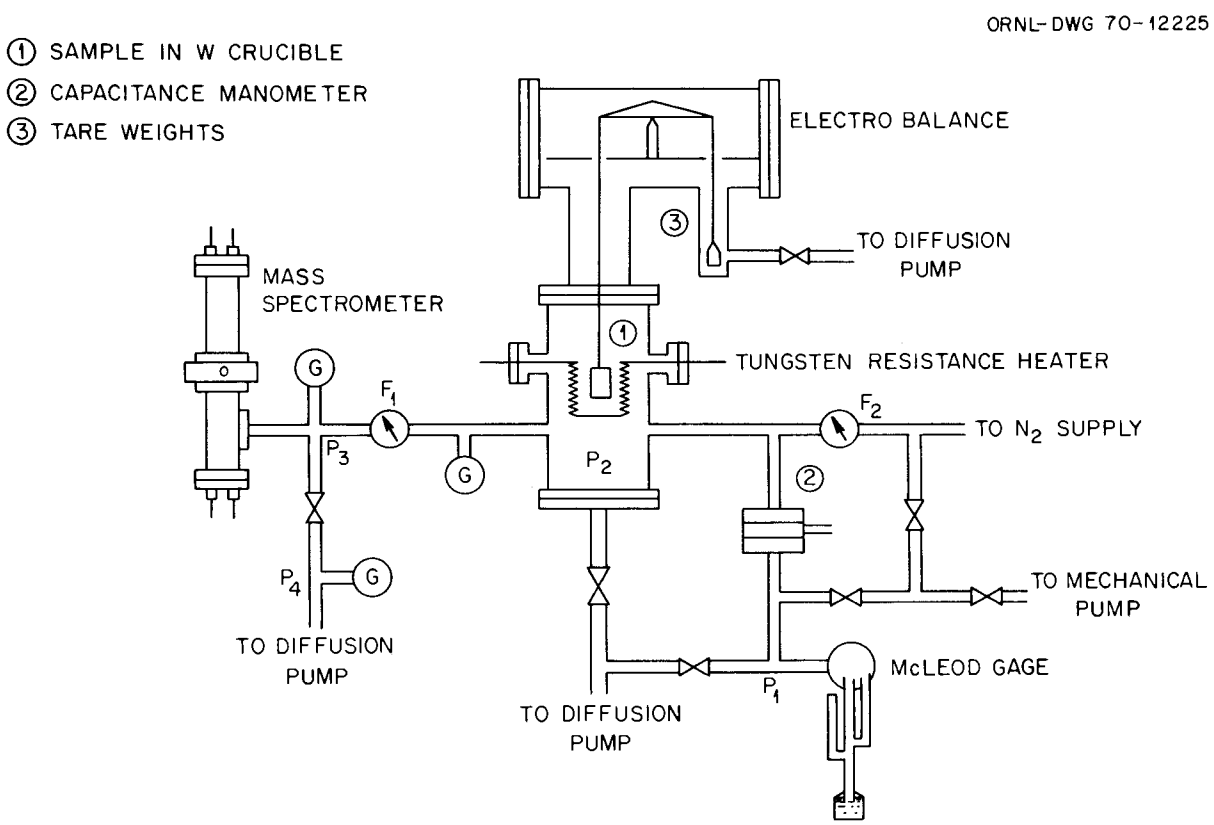

Fig. 2.22. Schematic Diagram of Vapor-Pressure Apparatus.

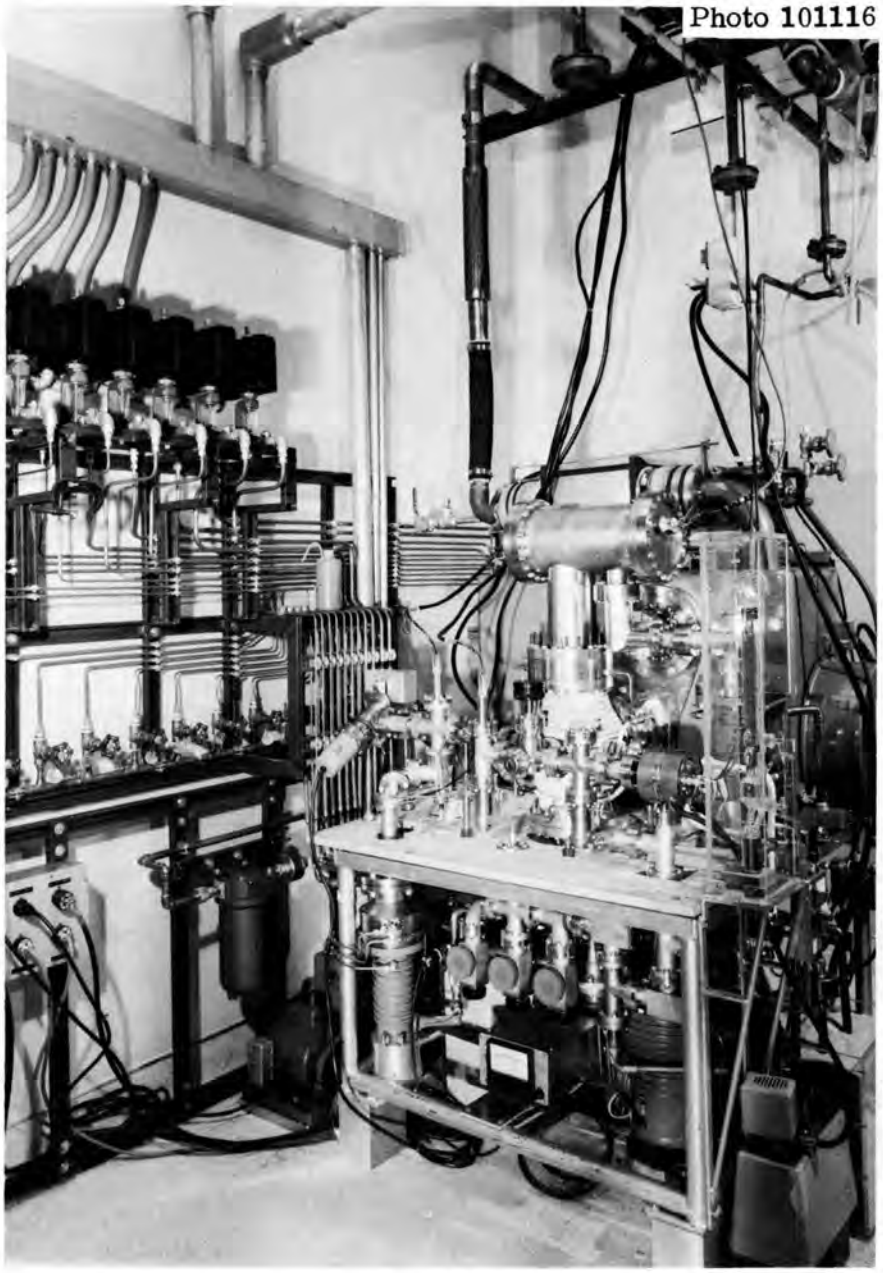

Fig. 2.23. Overall View of the Vapor-Pressure Apparatus.

are added or removed from the balance. Figure 2.25 shows the instrumentation for the vapor-pressure apparatus. Starting at the top on the left rack is the recorder for the electrobalance, the power supply for the balance, the controls for the vacuum system, the power supply for

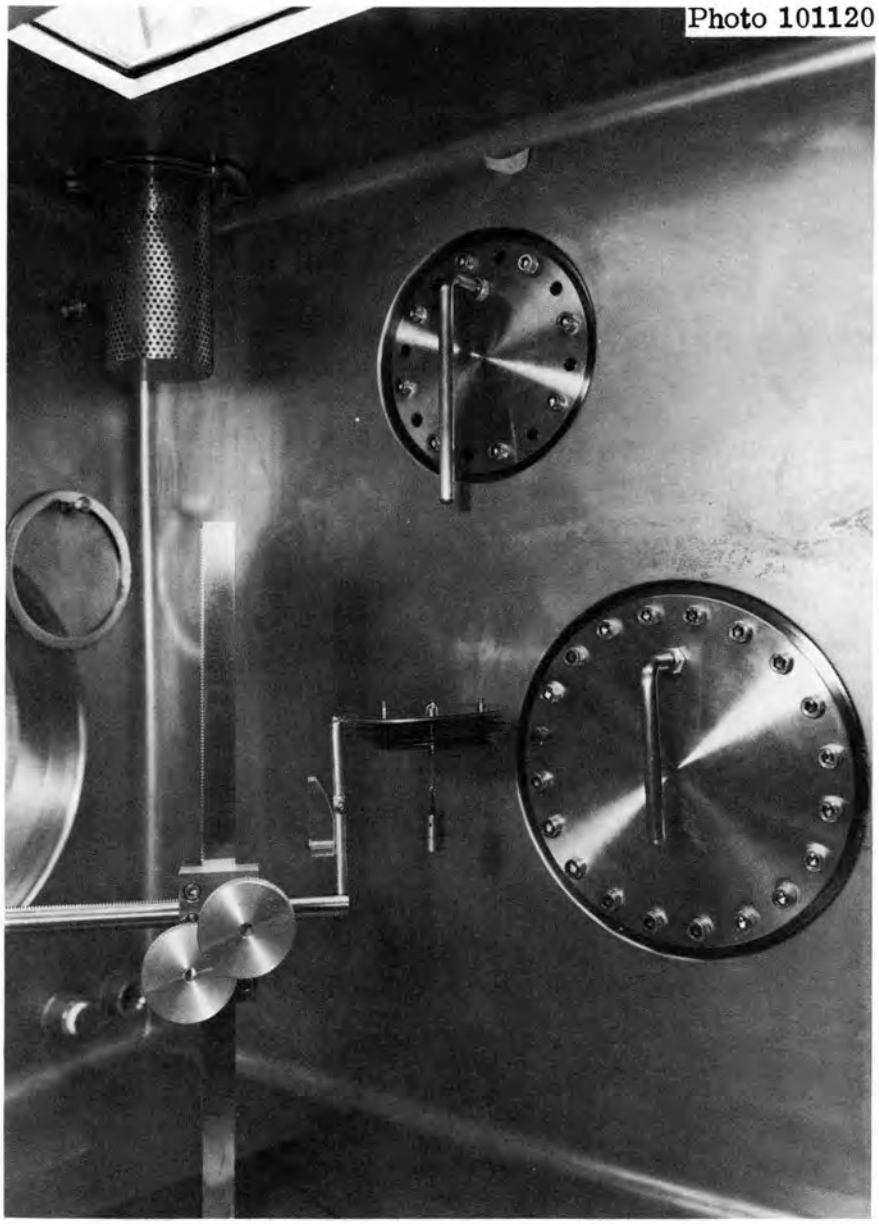

Fig. 2.24. View of the Two Loading Ports and Sample Crucible for the Vapor-Pressure Apparatus.

the capacitance manometer, and two controls for the ionization gage. The center cabinet is the power supply and control system for the furnace. The instrument on the right is the control console for analyses of residual gas.

Fig. 2.25. Instrumentation of the Vapor-Pressure Apparatus.

The basic mode of operation for this apparatus is rather straightforward. A sample of known weight [i.e., Pu, PuN, (U,Pu)N, etc.] is placed in a W crucible and suspended from one arm of the electrobalance in the center of the heating element. After the proper adjustments are

made on the balance, the system is closed by bolting down the two flanges shown in Fig. 2.24. The entire system is then evacuated to remove the unwanted gas species from the system (enclosed volume and inside surfaces after bakeout). Then, depending on the specific experiment, the temperature and pressure are changed in a controlled and specific manner. The desired atmosphere is introduced through the variable leak valve (F_2 in Fig. 2.22). The weight changes during these changes of temperature and pressure are continuously noted. The vapor above the sample can be analyzed by opening leak valve F_1.

Electrobalance. — A Cahn HR Recording Electrobalance adapted to function in ultrahigh vacuum is used in the vapor-pressure apparatus. This balance was mounted on a Varian flange for effective incorporation into the high-vacuum requirements of the system. The balance has a capacity of 100 g and is capable of detecting changes in sample weight of 2 μg.

Furnace. — The heating element is a split W-mesh resistance heater 1 in. in inside diameter and 2 in. high. The furnace is capable of attaining 2500°C. The furnace is controlled by a Leeds and Northrup three-function control unit, a saturable-core reactor, and a feedback system that detects absolute power input to the furnace.

On the runs made to date, the furnace temperature has been held so constant that no changes could be detected with the optical pyrometer. The temperature is read through a calibrated window with a calibrated Leeds and Northrup disappearing-filament optical pyrometer.

Mass Spectrometer. — A Veeco Residual Gas Analyzer is used to determine the composition of the gas over the sample. The system uses a magnetic-sector type of mass spectrometer tube for ionizing, accelerating, defluting, and analyzing the gases that diffuse into the spectrometer tube. The sensitivity, or minimum detectable particle pressure, is 1×10^{-13} torr N_2. The resolution of the system is one atomic mass unit at mass 75 (two adjacent mass peaks are said to be resolved if the distance from the base line to the valley between them is equal to or less than 10% of the sum of their heights). The mass range is from 2 to 300 atomic mass units.

Variable Leak Valve. — The two variable leak valves used in this system were manufactured by Varian Associates. These valves are bakeable, and the leak through them can be controlled to 1×10^{-10} torr liter/sec.

Irradiation Testing of Mixed Nitrides and Carbides

T. N. Washburn

Thermal-Flux Tests (E. J. Manthos, T. N. Washburn, M. K. Preston[14])

The initial irradiation tests consist of two capsules, each of which contains four uninstrumented fuel pins that are being irradiated in the ETR. These tests are of the "screening" type to evaluate the performance of nitride fuel synthesized from metal. The $(U_{0.8},Pu_{0.2})N$ pellets are fabricated by cold pressing and sintering to about 90% of theoretical density and a diameter of 0.245 in. The 2.5-in.-long fuel column is contained in a type 316 stainless steel sheath that is 0.300 in. in outside diameter and 0.0175 in. in wall thickness. A 0.010-in. radial gap between the pellet and cladding is filled with Na—19 wt % K (NaK-19) to enhance heat transfer. The peak design linear heat rating of these pins is 30 kW/ft with 60,000 MWd/metric ton for capsules 43-N1 and 43-N2, respectively.

Fabrication of these capsules (43-N1 and 43-N2) was completed during this report period. While the closure weld on capsule 43-N1 was being made, the welding machine malfunctioned and produced excessive penetration. The fuel pin was removed and the capsule repaired. During the final inspection of this capsule (43-N1), we detected a broken pellet (second from the bottom) in fuel pin 43-N1-1. We decided to irradiate it with the broken pellet because (1) the peak heat rate for this pin will be low (about 20 kW/ft), (2) the peak burnup for this pin will be low (about 2% FIMA), (3) we do not see any reason why this would endanger the performance of the other pins, (4) we think this

will be a good test for determining the mechanical interaction between the cladding and a broken pellet in the fuel column, and (5) if the pin does fail, it will not endanger the reactor because we have a secondary containment, the capsule.

Capsules 43-N1 and 43-N2 were neutron radiographed at the TREAT before they were inserted into the ETR. The neutron radiography showed the same thing as the x radiography taken before the capsules were shipped to Idaho. We cannot determine the NaK-19 level with either method. The capsules were inserted into the ETR during the midcycle 110 shutdown. The reactor went to full power on December 9, 1970.

Fast-Flux Tests (T. N. Washburn, E. J. Manthos, M. K. Preston[14])

Seven unencapsulated fuel pins, five for testing and two for spares, will be fabricated for testing in an EBR-II E-19 subassembly. The 19-pin subassembly will be shared with Battelle Memorial Institute. The request for approval-in-principle for these irradiations in EBR-II was approved by the USAEC. The characteristics and irradiation conditions for these fuel pins are given below:

Fuel	
Composition	$(U_{0.82},Pu_{0.18})N$
Enrichment, % ^{235}U	93
Diameter of pellet, in.	0.260
Density of pellet, % of theoretical	~ 90
Cladding	
Material, type stainless steel	316
Outside diameter, in.	0.310
Wall thickness, in.	0.015
Condition, % cold work	20
Fuel Pin	
Smear density, % of theoretical	78
Thickness of Na bond, in.	0.010
Length of fuel column, in.	13.5
Overall length, in.	40

Operating Conditions

Linear heat rating, kW/ft	30
Specific power, W/g	220
Peak cladding temperature, °C	~ 650
Temperature at fuel center, °C	~ 1050

A purchase requisition was issued for the type 316 stainless steel tubing to be used as cladding. We expect delivery February 1, 1971. The 0.310±0.001-in.-OD × 0.280±0.001-in.-ID tubing is being fabricated according to FFTF specification A-0086 from vacuum-melted material. We are sharing the tubing order with Battelle Memorial Institute; WADCO will inspect the tubing.

A purchase requisition was also issued for type 316 stainless steel bar stock to be used in the fabrication of end fittings. It is being fabricated from fully inspected, vacuum-melted, 1 3/16-in.-diam bar stock, heat 88229. The finished 13/32-in.-diam round bar stock will be fabricated in accordance with ASTM specifications A-276 and A-484. We expect delivery early in January 1971.

We have not yet decided what method of Na bonding will be used. We are investigating two different methods: ultrasonic vibration of the molten Na or centrifuging of the fuel pin while the Na is molten. We fabricated 500 dummy stainless steel pellets for tests to determine the better of two methods of adding Na to a fuel pin. We shall try to determine if the solid Na should be added to a pin before or after it is loaded with pellets. Depending on the results of these tests, we shall then attempt to repeat the results with depleted UN pellets in dummy fuel pins of the same configuration as the test pins.

The experimental plan was written and issued. An outline of the fabrication and quality assurance plan was written and will be revised and issued as soon as the Na loading and bonding method and Xe tagging procedures are determined.

Notes

1. V. J. Tennery, R. A. Potter, and T. G. Godfrey, "Synthesis and Characterization of Uranium Nitride," paper presented at 72nd Annual Meeting of the American Ceramic Society, Philadelphia, May 2–7, 1970. Abstract to be published in the Bulletin of the American Ceramic Society.

2. E. S. Bomar, Fuels and Materials Development Program Quart. Progr. Rept. March 31, 1970, ORNL-4560, pp. 40–45.

3. R. A. Smith et al., Annual Report. Progress on Development of Materials and Technology for Advanced Reactors During July 1968 through June 1969, BMI-1868, pp. A-1–A-3.

4. W. T. Langendorfer, Battelle Memorial Institute, Columbus, personal communication.

5. A. L. Nutt, Los Alamos Scientific Laboratory, personal communication.

6. V. J. Tennery, J. L. Botts, and J. P. De Luca, Fuels and Materials Development Program Quart. Progr. Rept. March 31, 1970, ORNL-4560, pp. 49–55.

7. Analytical Chemistry Division.

8. E. S. Bomar, Fuels and Materials Development Program Quart. Progr. Rept. March 31, 1969, ORNL-4420, pp. 43–45.

9. F. Anselin, J. Nucl. Mater. 10(4) 301–320 (1963).

10. K. Schwardtfeger, Trans. Met. Soc. AIME, 239(9), 1432 (1967).

11. W. H. Smith, Thermo-Dynamics and Phase Relations in the Systems Chromium-Nitrogen and Iron-Chromium-Nitrogen, Ph.D. Dissertation, Rensselaer Polytechnic Institute, Troy, N.Y., 1958.

12. D. Caplan et al., "Solubility of Nitrogen and Oxygen in Solid Chromium," pp. 196–215 in Ductile Chromium, American Society for Metals, Metals Park, Novelty, Ohio, 1957.

13. J. P. De Luca, Fuels and Materials Development Program Quart. Progr. Rept. Sept. 30, 1970, ORNL-4630, pp. 66–69.

14. On loan from General Engineering Division.

CLADDING AND OTHER STRUCTURAL MATERIALS

3. MECHANICAL PROPERTIES OF ALLOYS IN REACTOR ENVIRONMENTS AND DEVELOPMENT OF LMFBR CLADDING AND STRUCTURAL MATERIALS

J. R. Weir, Jr. H. E. McCoy, Jr.

The main emphasis of this program is on austenitic stainless steels. Included in our work are types 304 and 316 stainless steel and Ti-modified types 304 and 316 stainless steel. Types 318, 19-9-DL, and 12R72HV stainless steel have also been included in recent experiments inserted into the Experimental Breeder Reactor-II (EBR-II). The irradiation effects are determined by measurements of swelling and mechanical properties after irradiation. Experiments are run in three reactors: the EBR-II, the Oak Ridge Research Reactor (ORR), and the High-Flux Isotope Reactor (HFIR). Comparative results should reveal any effects of flux and reactor spectrum. Specimens of each material are irradiated in a variety of conditions so that the effects of irradiation temperature, fluence, and metallurgical condition can be evaluated.

Several specimens of Nb and Nb–1% Zr from the General Electric Nuclear Systems Programs experiments were examined. Microscopy studies were performed.

Status of Irradiation Experiments

E. E. Bloom

Subassembly X 034A was removed from row 2 of the EBR-II at the end of run 44B (August 4, 1970). Four elements of this subassembly (B, D, E, and F) accumulated 19,536 MWd, and three elements (O-A-2, O-C-2, and O-G-2) accumulated 8501 MWd. Diameters of each of the seven elements were measured by EBR-II personnel. Measurements were made at two orientations (0 and 90°) at 1-in. intervals over the core region and 2-in. intervals outside the core region. The four elements that had received the highest exposure increased significantly in diameter (the maximum value was about 1.7%). These elements were also distorted in such a way

that the tubes within the core region were elliptical rather than circular in cross section. Average diametral changes were used in an analysis of the specimen temperatures at end of life. This analysis indicated that the irradiation temperature within the core at end of life was significantly higher than the initial design temperature, and we decided to stop the experiment. The elements were shipped to ORNL, and we removed the specimen holders from all seven elements. The length and diameter of each holder are being measured, and then the specimen holders are being disassembled. Final analysis of heat transfer will be based upon these dimensions. A number of holders have been disassembled, and density measurements are in progress.

Subassembly X 035 was removed from row 7 of the EBR-II at the time the reactor power was increased to 62.5 MW(t). This subassembly was also shipped to ORNL. Measurements and disassembly will be started soon.

Subassembly X 100 is a Mark B-7 subassembly designed for the irradiation of test specimens of cladding and structural materials in a row 2 position of the EBR-II at a reactor power of 62.5 MW(t). The subassembly was installed in grid position 2-D-1 on October 7, 1970. This report summarizes the objectives of the irradiation experiment, the design of the irradiation subassembly, and the plan for evaluation after irradiation.

The main objective of this experiment is to establish the effects of heat treatment before irradiation (i.e., microstructure) on resistance to swelling and on mechanical properties after irradiation for type 316 stainless steel, which is the reference cladding material for the Fast Flux Test Facility (FFTF) Reactor, and Ti-modified type 316 stainless steel, an alloy that exhibits significant improvements in strength and resistance to embrittlement caused at elevated temperatures by the He produced by transmutation.

A second objective of the experiment is to investigate the effects of certain variations in the composition of type 316 stainless steel on swelling and mechanical properties after irradiation. The compositional variations include (1) 0.2 to 5.0% Mo, (2) 0.0 to 0.6% Ti, and (3) 0.2 and 0.6% C.

A third objective is to evaluate the effects of fast-neutron irradiation on the swelling and mechanical properties after irradiation of a number of alloys that are of interest to the overall liquid-metal-cooled fast breeder reactor (LMFBR) program: Sandvik 12R72HV, 19-9-DL type 318 stainless steel, and Ti-modified type 304 stainless steel.

A fourth objective is to evaluate the effects of irradiation on the mechanical properties of weldments.

An experiment (HFIR experiment 4) designed to investigate the effect of composition on the swelling of austenitic stainless steels was removed from the HFIR after receiving a peak fluence of about 2.9×10^{22} neutrons/cm^2 (> 0.1 MeV). Experiments designed to determine the effects of irradiation on the properties of type 316 and Ti-modified type 316 stainless steel after irradiation in the HFIR at 350 to 750°C to fluences to 1×10^{23} neutrons/cm^2 (> 0.1 MeV) (HFIR experiments 2, 3, 5, and 6) remain in the reactor.

The status of irradiation experiments sponsored by ORNL in the EBR-II and HFIR is summarized in Table 3.1.

Austenitic Stainless Steels

Mechanical Properties of Types 304 and Titanium-Modified 304 Stainless Steel (E. E. Bloom, J. O. Stiegler)

Types 304 and Ti-modified 304 stainless steel irradiated in EBR-II subassembly X 034 are being evaluated. The changes in density, irradiated microstructures, and tensile properties after irradiation were described previously.[1] The rupture lives of specimens irradiated at 500 to 800°C are compared with those of unirradiated specimens (with compensation for temperature) in Fig. 3.1. Specimens irradiated at 535°C to 1.5×10^{22} neutrons/cm^2 (> 0.1 MeV) and at 590°C to 2.5 to 3.5×10^{22} neutrons/cm^2 (> 0.1 MeV) had slightly shorter rupture lives than unirradiated specimens. Specimens irradiated at 800°C and tested at 704°C had rupture lives about one-tenth as long as those of unirradiated specimens. Creep rate, compensated for temperature, is shown as a function of stress in Fig. 3.2. There is a definite trend for specimens irradiated at 535 and 590°C and tested at 550 and 600°C, respectively, to have a

Table 3.1. Status of ORNL Irradiation Experiments

Experiment	Main Object of Investigation	Irradiation Temperature (°C)	Present Peak Fluence [neutrons/cm^2 (> 0.1 MeV)]	Status
			$\times 10^{22}$	
X 034 (elements A, C, and G)	Irradiation damage to types 304 and Ti-modified 304 stainless steel and Incoloy 800	370–800	3.5 (row 2)	Removed from reactor; evaluation about 85% complete
X 034A	Irradiation damage to types 304, Ti-modified 304, 316, and Ti-modified 316 stainless steel and Incoloy 800	370–800	6 (row 2)	Removed from reactor; disassembly about 45% complete
X 035	Irradiation damage to types 304 and Ti-modified 304 stainless steel and Incoloy 800	370–800	4 (row 7)	Removed from reactor
X 100	Effects of heat treatment before irradiation on irradiation damage to types 316, Ti-modified 316, 318, and Ti-modified 304 stainless steels, Sandvik 12R72HV, and 19-9-DL	370–750	0.2 (row 2)	Installed in reactor Oct. 7, 1970; elements A, B, and G to be removed at ~3.3 × 10^{22}, elements C and D at 6.7 × 10^{22}, and elements E and F at 1.3 × 10^{23} neutrons/cm^2 (> 0.1 MeV)
HFIR experiment 4	Effects of variations in composition of type 316 stainless steel on irradiation damage	575–600	2.9	Removed from reactor; evaluation about 50% complete
HFIR experiments 2 and 3	Effects of irradiation on properties of annealed and cold-worked types 316 and Ti-modified 316 stainless steel	350–650	4.9	To be removed from reactor at ~6 × 10^{22} neutrons/cm^2 (> 0.1 MeV)
HFIR experiment SANDL	Effects of irradiation on properties of annealed and cold-worked types 316 and Ti-modified 316 stainless steel	350–750	3.4	To be removed from reactor at ~1 × 10^{23} neutrons/cm^2 (> 0.1 MeV)

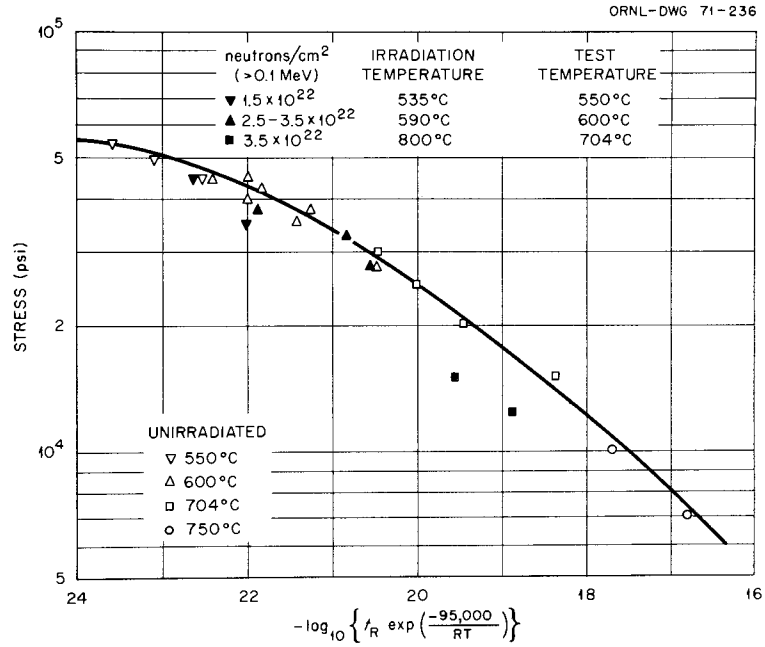

Fig. 3.1. Effect of Irradiation on the Temperature-Compensated Rupture Life of Annealed Type 304 Stainless Steel.

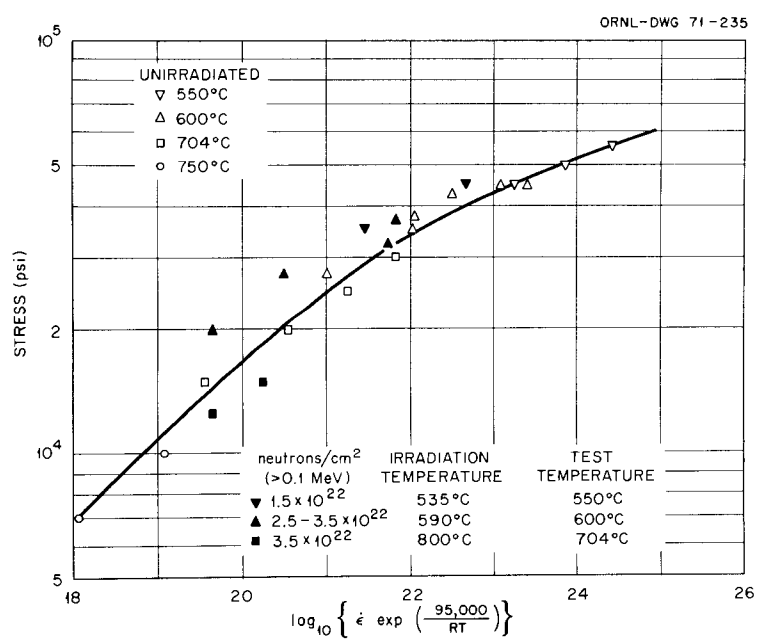

Fig. 3.2. Effect of Fast-Neutron Irradiation on the Temperature-Compensated Creep Rate of Annealed Type 304 Stainless Steel.

lower minimum creep rate than unirradiated specimens. Specimens irradiated at 800°C and tested at 704°C had a slightly higher minimum creep rate. The most significant effect of the irradiation was reduction of ductility, as shown in Fig. 3.3. The specimens irradiated and tested at 600°C and lower exhibited less than 3% total elongation compared to 20 to 30% for the unirradiated material.

Results of transmission and scanning electron microscopy of a specimen irradiated at 535°C to 1.5×10^{22} neutrons/cm^2 (> 0.1 MeV) and tested at 550°C and 35,000 psi stress are summarized in Fig. 3.4. This specimen had a total elongation of 0.5% and was at temperature for 1030 hr. Before the test, the specimen contained 2.3×10^{14} voids, with a mean diameter of 240 Å, and about 2×10^{15} faulted dislocation loops per cubic centimeter. After the test, the unstressed shoulder of the specimen contained faulted dislocation loops and dislocation lines that presumably resulted from the unfaulting of some of the loops. The density

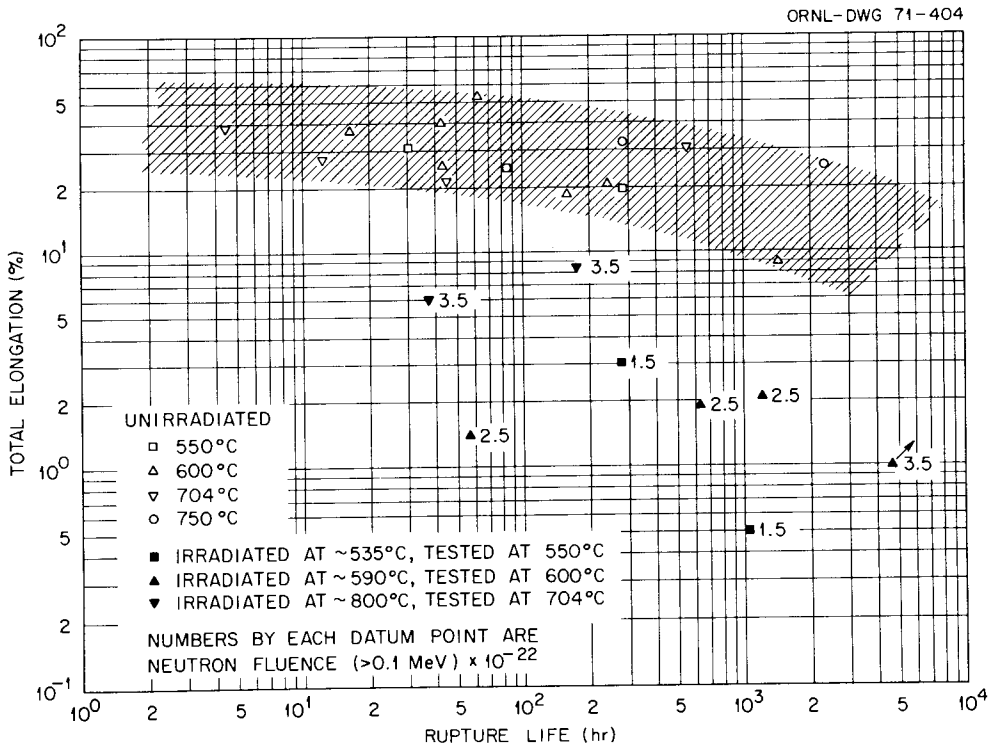

Fig. 3.3. Effect of Fast-Neutron Irradiation on the Creep-Rupture Ductility of Annealed Type 304 Stainless Steel.

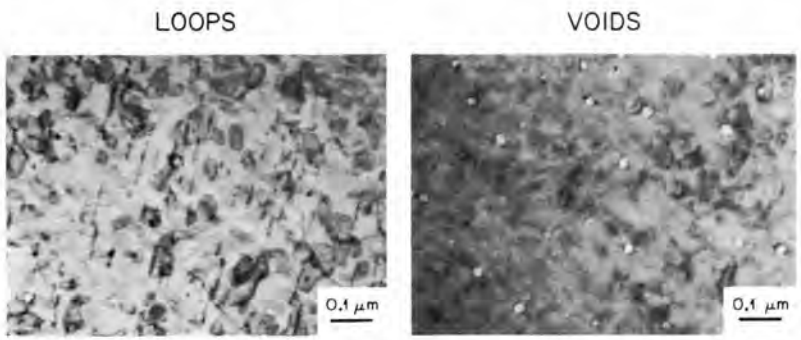

MICROSTRUCTURE OF SPECIMEN IRRADIATED AT 535°C TO 1.5×10^{22} neutrons/cm^2 (>0.1 MeV)

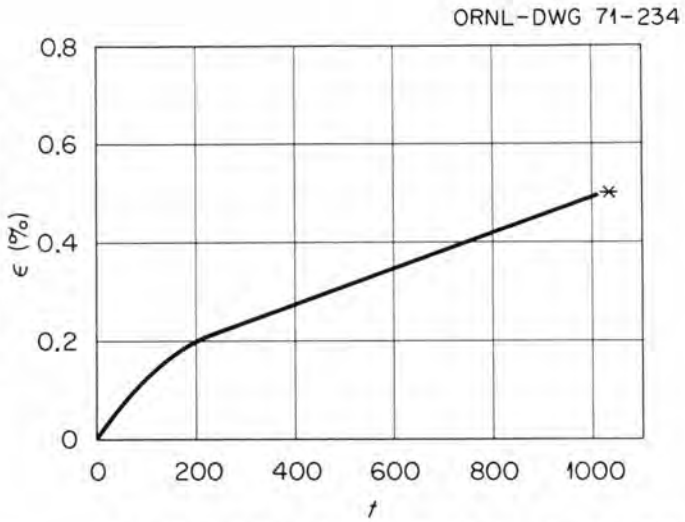

STRAIN-TIME CURVE FOR SPECIMEN TESTED AT 550°C AND 35,000 psi STRESS

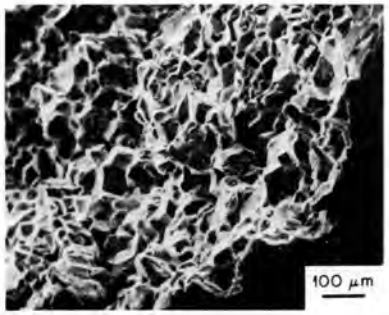

INTERGRANULAR FRACTURE OF TESTED SPECIMEN

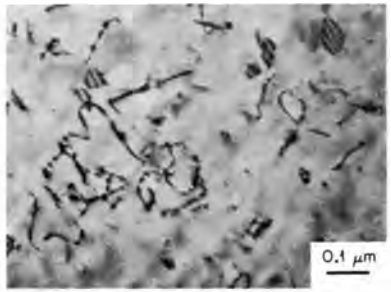

MICROSTRUCTURE IN UNSTRESSED SHOULDER REGION

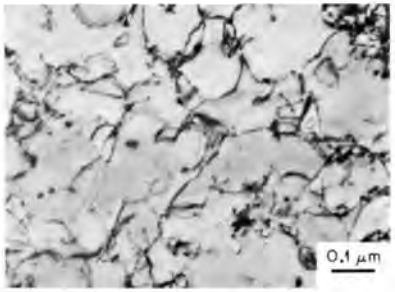

MICROSTRUCTURE IN STRESSED GAUGE SECTION

Fig. 3.4. Summary of the Creep-Rupture Behavior of Type 304 Stainless Steel After Irradiation in the Experimental Breeder Reactor-II.

of dislocations was higher in the stressed gage section of the specimen than in the shoulder, and very few faulted loops were present. It appears that the unfaulting of a dislocation loop is assisted by the applied stress, possibly through interaction with glide dislocations. It is possible that when stainless steels are irradiated at a temperature slightly below that at which the loops unfault, the final dislocation structure may be dependent on the stress state during irradiation. As we previously observed[2] for type 304 stainless steel irradiated and tested under similar conditions, the fracture was intergranular.

The tensile properties of Ti-modified type 304 stainless steel after irradiation are listed in Table 3.2. The strength properties do not differ significantly from those of standard type 304 stainless steel irradiated and tested under similar conditions.[3] Ductility, as measured by uniform strain, total elongation, or reduction in area, is higher for irradiation and test temperatures above about 450°C. Figure 3.5 compares the total elongation of standard and Ti-modified type 304 stainless steel after irradiation in the EBR-II. The modified alloy had much greater elongation at test temperatures above 450°C.

The results of creep-rupture tests after irradiation are listed in Table 3.3. At 600°C, the rupture life of modified type 304 stainless

Table 3.2. Tensile Properties[a] of Titanium-Modified Type 304 Stainless Steel After Irradiation in the Experimental Breeder Reactor-II[b]

Fast-Neutron Fluence [neutrons/cm^2 (> 0.1 MeV)]	Temperature, °C		Stress, psi		Elongation, %		Reduction in Area (%)
	Irradiation	Test	Yield	Ultimate Tensile	Uniform	Total	
$\times 10^{22}$			$\times 10^3$	$\times 10^3$			
2.0	550–610	550	39.6	53.9	19.1	24.6	37.7
2.0	550–610	650	35.8	40.7	8.8	30.4	34.9
3.0	750–820	750	15.5	17.4	10.0	44.2	47.0

[a]Tensile tested at 0.002 min^{-1}.

[b]Row 2, subassembly X 034.

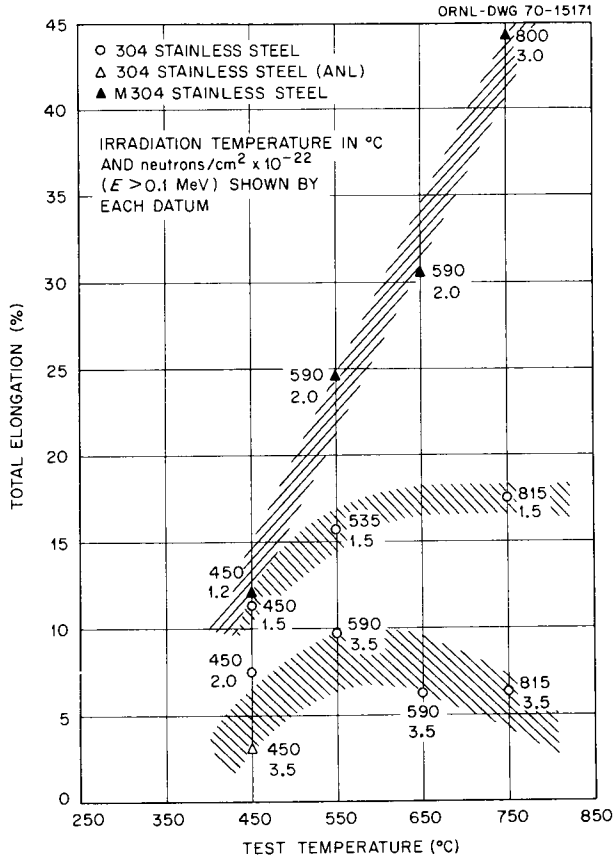

Fig. 3.5. Tensile Ductility of Standard Type 304 and Titanium-Modified Type 304 Stainless Steel After Irradiation in the Experimental Breeder Reactor-II (R. Carlander, Argonne National Laboratory, personal communication).

Table 3.3. Creep-Rupture Properties of Titanium-Modified Type 304 Stainless Steel After Irradiation[a]

Fast-Neutron Fluence [neutrons/cm² (> 0.1 MeV)]	Temperature, °C		Stress (psi)	Rupture Life (hr)	Minimum Creep Rate (%/hr)	Elongation, %		Reduction in Area (%)
	Irradiation	Test				At End of Second Stage	Total	
$\times 10^{22}$								
2.0	590	600	32,500	146.1			21.1	
3.0	590	600	27,500	220.1	0.054	11	17.0	22
3.0	590	600	20,000	3046.7	0.0019	9	9.9	16
3.0	800	704	15,000	49.9	0.49	20	35.1	24.5
3.0	800	704	12,500	287.4			29.8	

[a]Specimens were annealed 1 hr at 925°C before irradiation in the Experimental Breeder Reactor-II subassembly X 034.

steel was only one-tenth that of the standard type 304 stainless steel irradiated in the same experiment at the same temperatures; its minimum creep rate, however, was about ten times higher. These differences in strength properties were a result of the finer grain size in the Ti-modified type 304 stainless steel (annealed 1 hr at 925°C before irradiation) as compared to the standard type 304 stainless steel (annealed 1 hr at 1050°C before irradiation). The ductility of the modified alloy after irradiation, in terms of elongation at the end of second-stage creep, total elongation, or reduction in area, was significantly higher than that of the standard type 304 stainless steel (Fig. 3.3).

Metallographic examination of a specimen of Ti-modified type 304 stainless steel, annealed 1 hr at 925°C, irradiated at about 590°C to 3.0×10^{22} neutrons/cm^2 (> 0.1 MeV), and then tested at 600°C and 27,500 psi stress, was completed and is summarized in Fig. 3.6. Note from the curve for strain versus time that the material underwent about 11% strain before going into third-stage creep. Transmission electron microscopy of specimens removed from the stressed gage section revealed that a dislocation cell structure had formed with the voids and that precipitate particles acted as pinning points. Most significant was the observation by means of scanning electron microscopy that the specimen had failed in a very ductile, predominantly transgranular mode. This can be compared to the fracture of standard type 304 stainless steel, which is shown in Fig. 3.4. It was demonstrated[4] that irradiated Ti-modified type 304 stainless steel is significantly more ductile at temperatures where the He embrittlement phenomena predominates. The present results demonstrated that the improved ductility was retained under irradiation and test conditions where both displacement damage (voids and dislocation structure) and He affect mechanical properties, particularly ductility.[2]

Effect of Composition on the Swelling of Austenitic Stainless Steels Irradiated in HFIR (E. E. Bloom, J. O. Stiegler)

Specimens with the basic composition of either type 304 or type 316 stainless steel but containing various amounts of Ti, Mo, and C

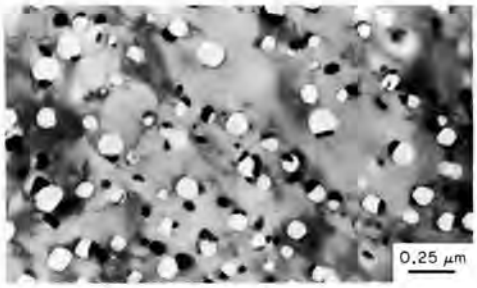

MICROSTRUCTURE OF M304 STAINLESS STEEL IRRADIATED AT 590°C TO 3.0×10^{22} neutrons/cm^2 (>0.1 MeV)

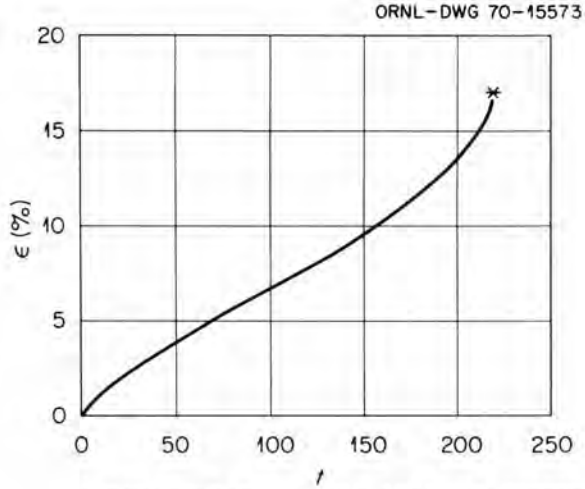

STRAIN-TIME CURVE FOR SPECIMEN TESTED AT 600°C AND 27,500 psi STRESS

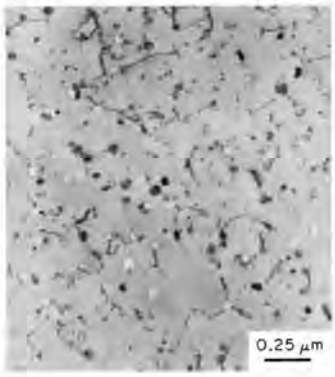

DISLOCATION STRUCTURE IN UNSTRESSED SHOULDER OF TESTED SPECIMEN

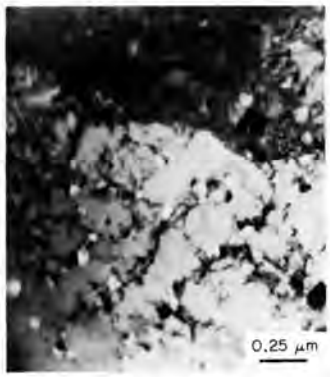

DISLOCATION STRUCTURE IN GAUGE SECTION OF TESTED SPECIMEN

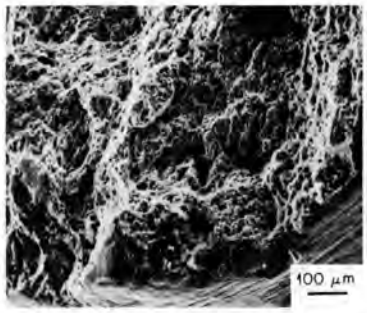

FRACTURE SURFACE

Fig. 3.6. Summary of the Creep-Rupture Behavior of Titanium-Modified Type 304 Stainless Steel After Irradiation in the Experimental Breeder Reactor-II.

were irradiated in the HFIR to fluences of 1.5 to 2.9×10^{22} neutrons/cm^2 (> 0.1 MeV). Figure 3.7 shows the specimen holder and SiC temperature monitor used in the HFIR irradiation experiments. The tensile specimen is centered in the Al specimen holder by thin (about 0.005 in. thick) stainless steel disks. The desired irradiation temperatures are obtained by means of a gas gap between the surface of the specimen and the inner surface of the specimen holder. The gas gap at the shoulder of the specimen and the thickness of the centering disks are adjusted to obtain a

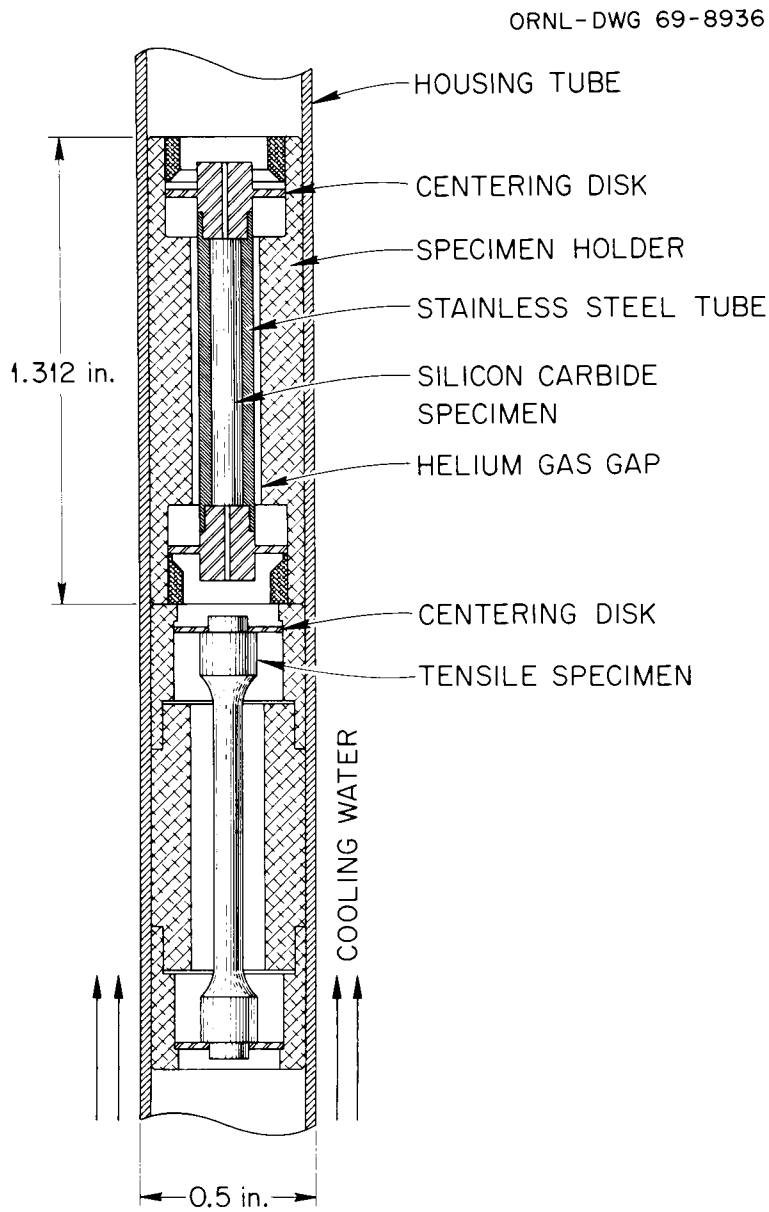

Fig. 3.7. Tensile Specimen and Silicon Carbide Specimen Holders Used in Irradiation Experiments in the High Flux Isotope Reactor.

nearly uniform temperature along the length of the specimen. Irradiation temperatures are monitored by the response of the SiC to annealing after irradiation.[5]

In the present experiment, specimens of austenitic stainless steel with variations in composition were irradiated at temperatures calculated to be 575 to 600°C. During disassembly of the experiment, we noted that

the specimens were discolored compared to their appearance before irradiation. The gage section appeared to have a thin film of oxide that was quite uniform along its length. The shoulders (or buttonheads) were somewhat brighter, which indicated that they operated at a different temperature. The densities of the irradiated specimens and unirradiated control specimens were determined in the same apparatus by the immersion technique. The reported changes in density are the average of five determinations, and the available results are tabulated in Table 3.4.

Table 3.4. Change in Immersion Density for Austenitic Stainless Steels Irradiated in the High-Flux Isotope Reactor at 575 to 600°C

Type Stainless Steel	Condition	Neutron Fluence (neutrons/cm^2)		Density Decrease (%)
		Thermal	Fast (> 0.1 MeV)	
		$\times 10^{22}$	$\times 10^{22}$	
316L (0.02% C)	a	4.4	1.9	1.6
316	b	5.0	2.2	2.2
316	c	5.6	2.5	2.1
High-purity 316	a	6.0	2.7	2.3
316 + 0.6% Ti	a	6.4	2.8	1.0
316 + 0.33% Ti	a	6.6	2.9	0.9
316	a	6.7	2.9	3.9
316 + 0.23% Ti	a	6.6	2.9	2.5
316 + 0.46% Ti	a	6.4	2.8	0.8
316 (0.2% Mo)	a	6.0	2.7	3.8
316 (2.4% Mo)	a	5.6	2.5	4.7
316 (4.8% Mo)	a	5.0	2.2	4.6
304L + 0.2% Ti	a	4.4	1.9	2.4
304 + 0.2% Ti	a	3.7	1.5	1.1

[a]Annealed 1 hr at 1050°C.

[b]Cold worked 50%, annealed 1 hr at 1300°C and 100 hr at 800°C.

[c]Cold worked 50%, annealed 1 hr at 1300°C.

These preliminary results indicate that the change in density produced by irradiation to a given fast-neutron fluence (> 0.1 MeV) in the HFIR was significantly larger than what occurs for an equivalent fast-neutron exposure in the EBR-II. For example, the specimen of annealed type 316 stainless steel irradiated at about 575°C to 2.9×10^{22} neutrons/cm^2 (> 0.1 MeV) in the HFIR decreased 3.9% in density. In comparison, annealed type 316 stainless steel irradiated at about 575°C to 2.7×10^{22} neutrons/cm^2 (> 0.1 MeV) in the EBR-II decreased only 0.68% in density.[6] The larger decrease in density for specimens irradiated in the HFIR was not unexpected. Recent results[7] indicate that a specimen irradiated to 2.9×10^{22} neutrons/cm^2 (> 0.1 MeV) in the HFIR may contain in excess of 10^3 ppm He. A specimen irradiated to an equivalent fast-neutron fluence in the EBR-II would contain less than 10 ppm He. Since He is effective in promoting void nucleation,[8] the void concentration in specimens irradiated in the HFIR may be higher than that in a specimen irradiated in the EBR-II. This would account for at least a portion of the greater change in density.

Two specimens of type 316 stainless steel (annealed 1 hr at 1050°C and 1 hr at 1300°C before irradiation) were included in the experiment. Irradiation at different axial positions resulted in neutron fluences of 2.9 and 2.5×10^{22} neutrons/cm^2 (> 0.1 MeV); density decreased 3.9 and 2.1%, respectively. The density decrease was, therefore, proportional to the fluence raised to the fourth power. This great dependence on fluence is consistent with recent observations on type 304 stainless steel irradiated at about 600°C (ref. 9).

Composition strongly influenced the amount of swelling under these irradiation conditions. Type 316 stainless steel with 0.33 or 0.46% Ti decreased 0.9 and 0.8% in density as compared to a decrease of 3.9% for the standard type 316 stainless steel. The series of specimens that contained Ti additions were from 100-lb vacuum-melted heats of the compositions listed in Table 3.5. The concentrations of elements such as B and Ni were about the same in each alloy. Therefore we assume the amount of He in the irradiated samples to be nearly constant. The different amounts of swelling thus appear to be a direct effect of the

Table 3.5. Compositions of Titanium-Modified Type 316 Stainless Steels

Titanium Addition to Type 316 Stainless Steel (%)	Composition, %										
	C	Cr	Ni	Mo	Ti	B	Mn	Si	P	S	N
None	0.06	17.2	12.5	2.1		0.0005	1.9	0.5	0.39	0.004	0.018
0.23	0.06	17.0	12.0	2.4	0.23	0.0007	0.5	0.4			
0.33	0.05	17.0	12.0	2.4	0.33	0.0007	0.4	0.4			
0.46	0.05	17.0	12.0	2.4	0.46	0.0005	0.3	0.4			
0.60	0.05	17.0	13.0	2.5	0.60	0.0005	0.2	0.4			

variation in Ti content and not a secondary effect of the concentration of He.

The specimens of type 316 stainless steel that contained 0.2, 2.4, and 4.8% Mo were each from small, 5-lb laboratory melts. Complete chemical analyses are not available. As can be seen from Table 3.4, these alloys swelled more than the specimens of standard type 316 stainless steel from the large, commercial melt. For the three alloys with common histories, it appears that increasing the Mo content from 0.2 to 4.8% caused a small increase in the amount of swelling.

The alloys irradiated in this experiment are being examined. Samples were submitted for He analyses. Samples removed from various positions along the length of the standard type 316 stainless steel specimen irradiated to 2.9×10^{22} neutrons/cm^2 will be examined by electron microscopy to establish the temperature distribution during irradiation. Tests of mechanical properties and electron microscopy are in progress.

Microstructural Studies of Unirradiated Standard and Titanium-Modified Type 316 Stainless Steel and Consequential Considerations (Dieter Fahr)

In order to study the effect of microstructure upon mechanical properties of stainless steels after irradiation, every effort should be made to obtain a structure that is as stable as possible under controlled conditions; otherwise, any change of the microstructure due to neutron irradiation alone cannot be determined.

Studies of type 316 stainless steel by electron microscopy revealed that specimens annealed 1 hr at 1050°C and cold worked 20% were recrystallized (up to 20%) as a result of a 4000-hr anneal at 650°C. Type 316 stainless steel modified with 0.23% Ti did not recrystallize under the same conditions. Figures 3.8 and 3.9 show the microstructures of the partially recrystallized standard type 316 stainless steel and the recovered, but not recrystallized, Ti-modified type 316 stainless steel. The heavy precipitates were identified as σ phase. Although precipitation preceded recrystallization, it did not prevent it in the standard type 316 stainless steel.

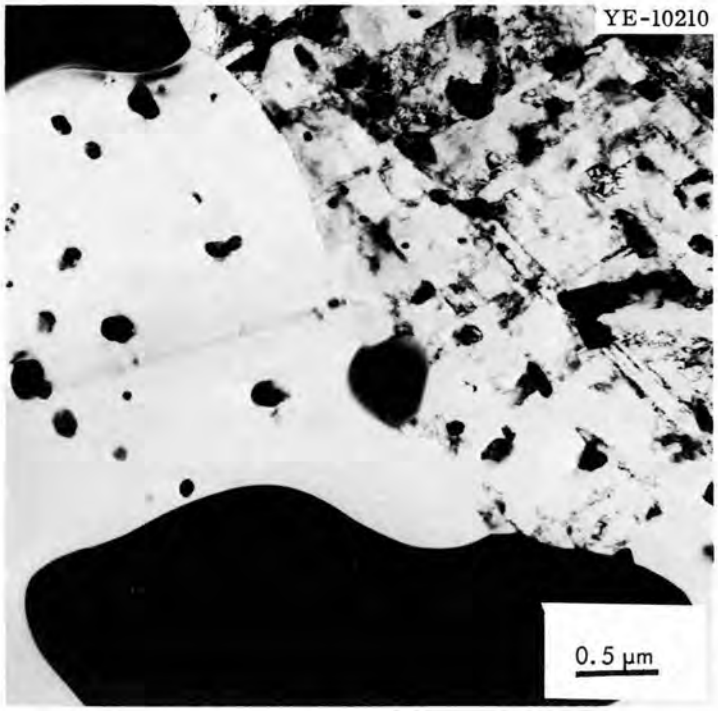

Fig. 3.8. Effect of 4000-hr Anneal at 650°C on the Microstructure of 20% Cold-Worked Standard Type 316 Stainless Steel.

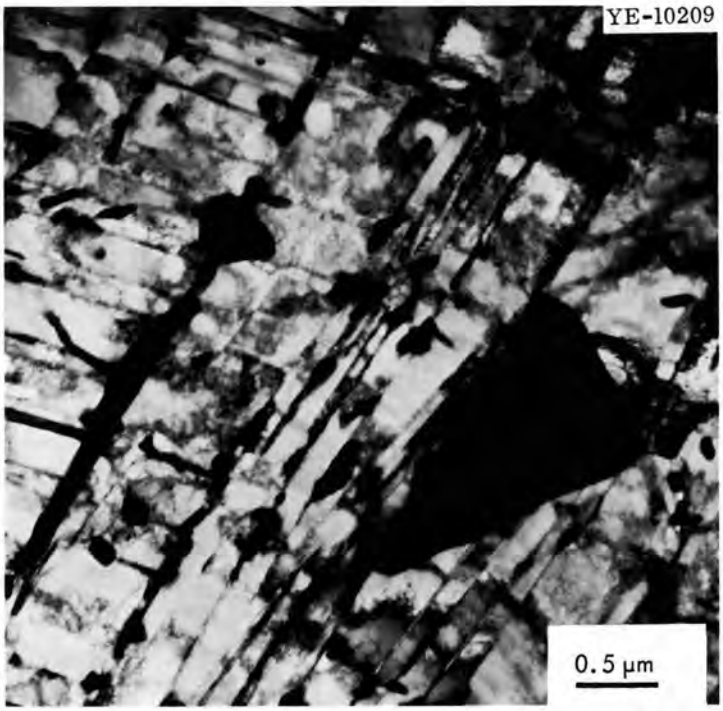

Fig. 3.9. Effect of 4000-hr Anneal at 650°C on the Microstructure of 20% Cold-Worked 0.23% Ti-Modified Type 316 Stainless Steel.

Figure 3.10 shows the effect of different annealing times at 750°C on the microstructure of 20% cold-worked standard and Ti-modified type 316 stainless steel. After 1 hr at 750°C, about 20% of the cold-worked structure of the standard type 316 stainless steel was recrystallized, while no recrystallization had taken place in the Ti-modified steel. Annealing 10 hr at 750°C led to a fully recrystallized microstructure in the standard type 316 stainless steel, while only about 5% of the structure was recrystallized in the Ti-modified steel.

Figure 3.11 shows the change in yield strength at room temperature with increasing annealing temperature for standard type 316 stainless steel cold worked 20% and annealed for 10 hr. The yield strength began to drop rapidly at annealing temperatures above 550°C.

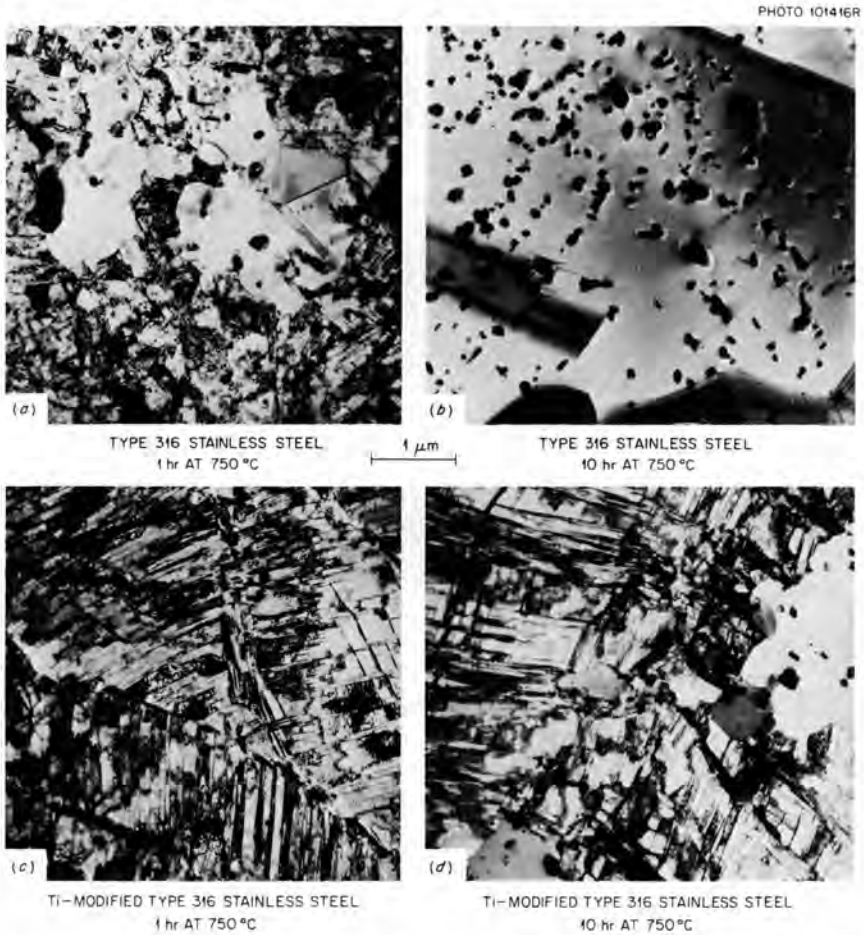

Fig. 3.10. Effect of Annealing on the Microstructure of 20% Cold-Worked Standard and 0.23% Ti-Modified Type 316 Stainless Steel.

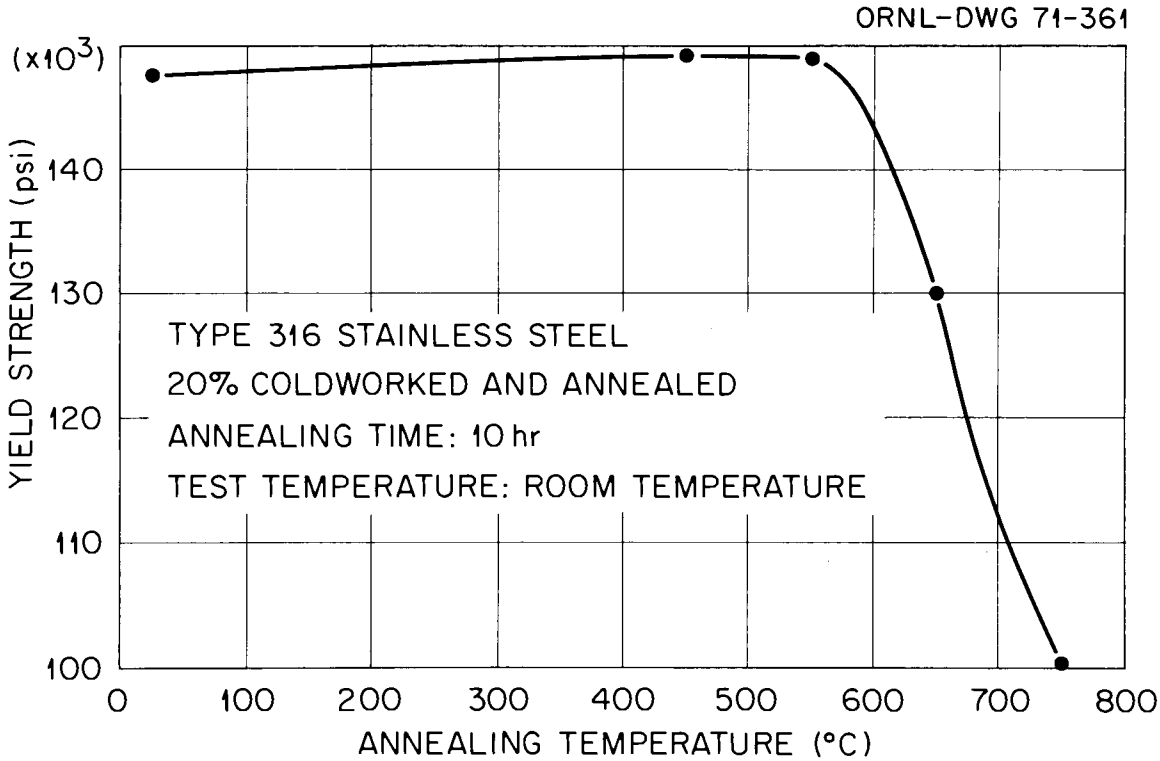

Fig. 3.11. Yield Strength Versus Annealing Temperature for Standard Type 316 Stainless Steel.

Studies by Leslie et al.[10] indicate that recrystallization can be strongly inhibited by finely dispersed precipitates that are present before cold working. The closely spaced precipitate particles reduce the tendency for cells to form during deformation and prevent the rearrangement of dislocations into cell walls and the development of new high-angle boundaries. This inhibition of cell formation by precipitates present during the cold-working process is almost certainly the reason for the great stability of the cold-worked structure in sintered Al products.

We were able to produce the required distribution of precipitate in type 316 stainless steel. The microstructure of an annealed (1 hr at 1050°C) standard type 316 stainless steel aged 4000 hr at 650°C is shown in Fig. 3.12. The extent of the increase in recrystallization temperature due to cold working such a structure as compared to that resulting from working the steel in the solution-annealed condition has not yet been determined.

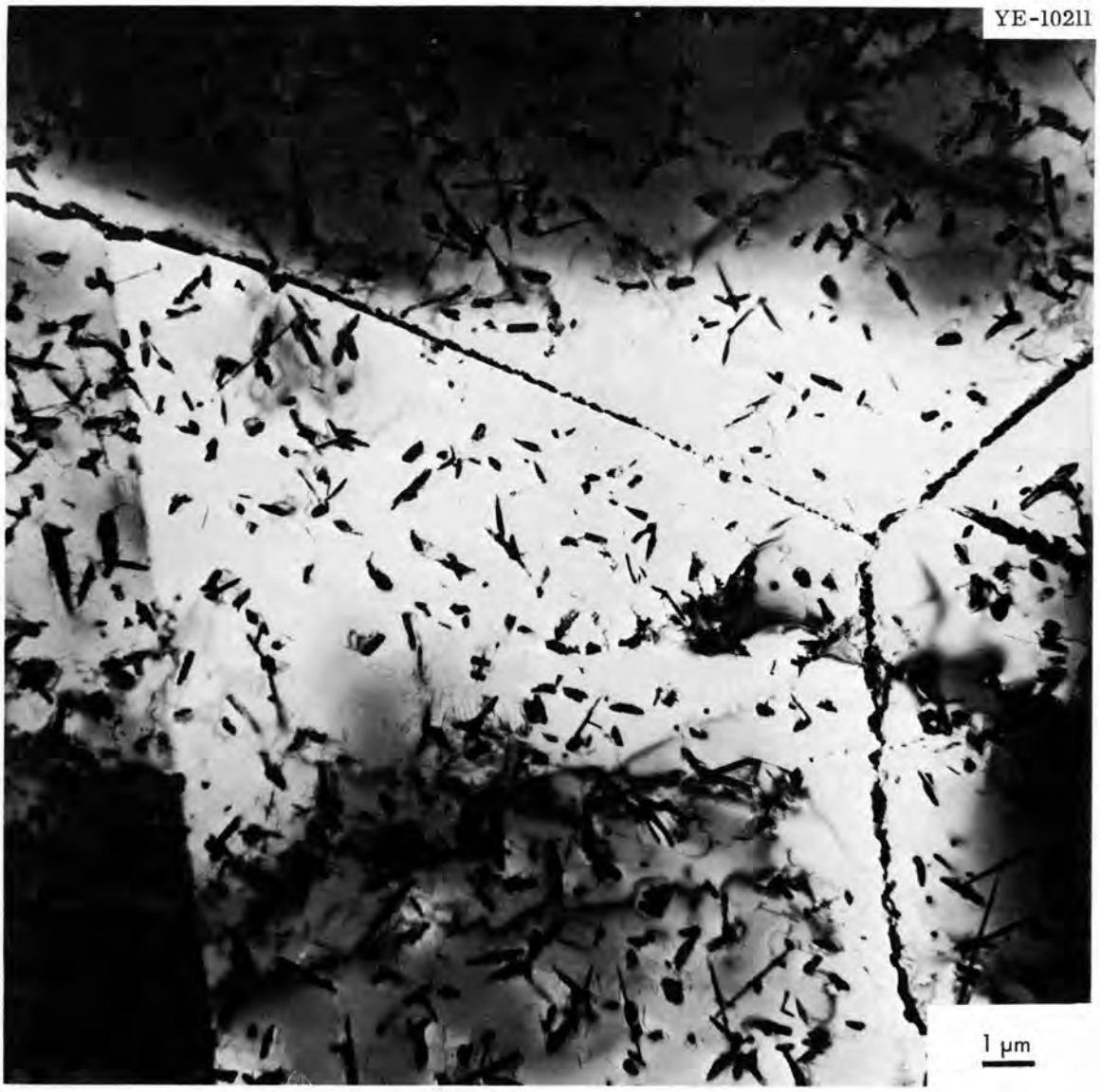

Fig. 3.12. Effect of 4000-hr Anneal at 650°C on the Microstructure of Solution-Annealed (1 hr at 1050°C) Standard Type 316 Stainless Steel.

A much more convenient way of stabilizing the microstructure by raising the recrystallization temperature is to add small amounts of Ti. This is also preferable in view of the improved mechanical properties of irradiated Ti-modified type 316 stainless steel.[11]

In investigations of the effect of solute elements on the recrystallization of Fe or low-C steels, it has been found that the rate of high-angle boundary migration drops very rapidly with the first small addition of one solute element. An extensive survey of the effects of additions

of binary transition elements on the recrystallization of Fe was conducted by Abrahamson and Blakeney.[12] They obtained very good correlations between the logarithms of rates of change of recrystallization temperature with atomic percent added element and the number of ground-state outer d-shell electrons in the solute. The change of recrystallization temperature was a linear function of solute concentration at low solute concentrations, and the limit of this linearity was also found to be a function of the ground-state electron configuration of the solute. Although no satisfactory explanation of these correlations is available, the following may be involved. Extending the proposals of Seeger and Schottky,[13] Feltham[14] suggests that at dislocations, subboundaries, and grain boundaries the atoms are less closely packed than in an ideal crystal. A redistribution of the conduction electrons is necessary to screen the displaced atom cores. The increase in energy due to this redistribution contributes to the energy of the defect. The energy of the defect can be reduced with the effectiveness with which the conduction electrons of the solute atoms aid in the screening process.

Figure 3.13 shows the effect of additions of elements of the first transition series on the recrystallization temperature of Fe. Titanium has the strongest effect. In the majority of cases, the maximum initial effect occurs at 0.10 at. % or less, within the region of solid solubility. Abrahamson and Blakeney[12] also found that atoms that have similar configurations of outer electrons (Ti, Zr, Hf) exhibit effects of the same order of magnitude. However, the greater the difference in energy level between solvent atom (Fe 3d) and solute atom (Ti 3d, Zr 4d, Hf 5d), the greater the rate of change in recrystallization temperature. Thus, the effectiveness of these elements in raising the recrystallization temperature of Fe increases in the order Ti, Zr, Hf.

Although Abrahamson and Blakeney[12] stated that there was no correlation between the atom sizes of the added elements and changes in recrystallization temperature, the size difference between solvent and solute atom certainly will affect the motion and rearrangement of dislocations. In fact, Ti, with the largest atomic radius of the added elements of the

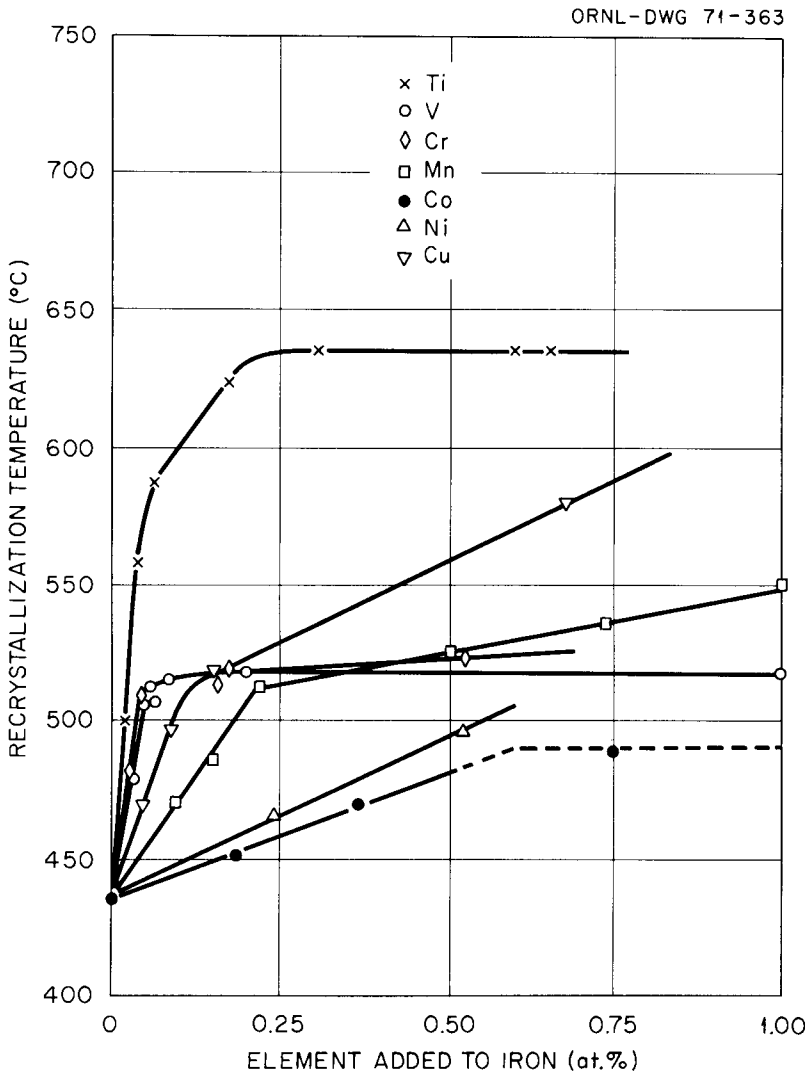

Fig. 3.13. Recrystallization Temperature of Iron Versus Atomic Percent Added Element of the First Transition Series. [Ref. E. P. Abrahamson, II and B. S. Blakeney, Jr., Trans. Met. Soc. AIME 218, 1101 (December 1960).]

first transition series, also causes the largest increase in recrystallization temperature (Fig. 3.13). The rate of change of recrystallization temperature with atomic percent solute is lower for V and Cr, as could have been predicted on the basis of their respective radii.

Although neither the lattice spacings nor the volume of the unit cell is related to the actual size of any particular atom, studies by Sutton and Hume-Rothery[15] show (Fig. 3.14) that for a constant atomic percentage of solute of the first transition series, Ti causes the

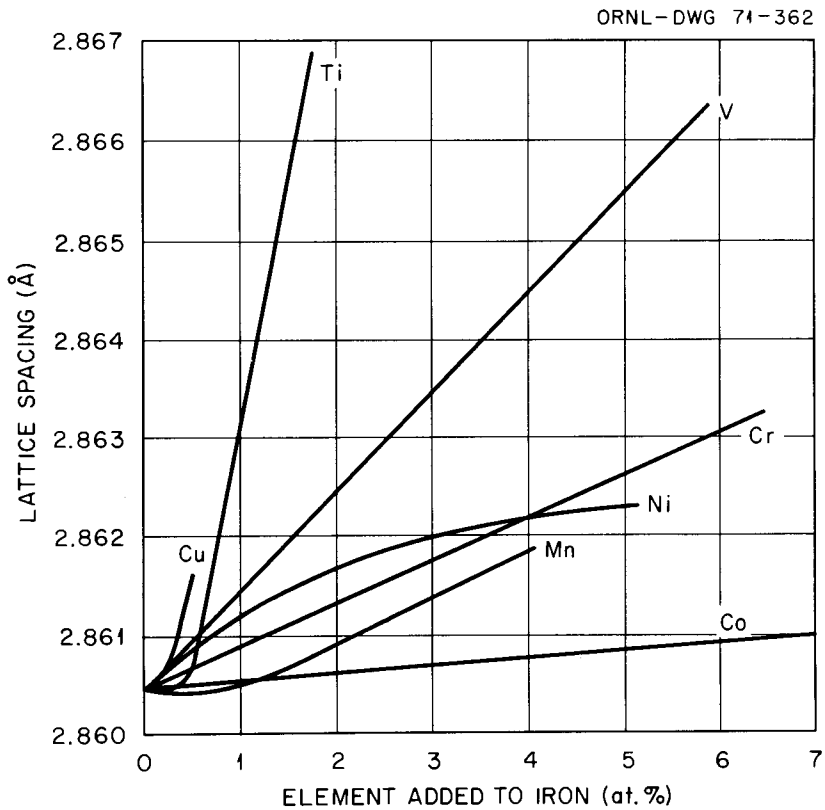

Fig. 3.14. Lattice Spacings of Solid Solutions of Different Elements in Iron. [Ref. A. L. Sutton and W. Hume-Rothery, Phil. Mag. 46, 1295 (1955).]

greatest lattice expansion. The elements V, Cr, and Mn cause progressively less expansion, in that order. On the other hand, Co, Ni, and Cu cause progressively more expansion. The lattice dilatations caused by these elements are clearly related to the group numbers of the periodic table and, hence, to the atomic radius of the solute atom.

It was noted above that Hf and Zr raise the recrystallization temperature of Fe even more than does Ti (they also have larger atomic radii than Ti). Moreover, their heats of formation for their respective oxides, nitrides, and carbides are higher (more negative) than the ones for the corresponding Ti compounds and increase (become more negative) in the order Ti, Zr, Hf. Values in the literature also indicate that Hf and especially Zr produce less He than does Ti based on their respective cross section for the (n,α) reaction. Although this may be insignificant considering the small additions necessary, the fact that Hf and Zr seem

to be at least as effective as Ti in regard to most effects and reactions that made Ti a desirable modifier for stainless steels suggests that Hf and Zr might be used to modify type 316 and other stainless steels. Moreover, the studies by Leslie et al.[10] indicate that recrystallization can be inhibited not only by elements in solid solution, but also by precipitates that are present before cold working. The dislocation substructure is more stable and different from that obtained by cold working the steel in the solution-annealed condition. Such a microstructure may not only raise the recrystallization temperature further but may also have beneficial effects on the formation of voids and swelling in general. By properly adjusting the amount of the modifying element to be added, one should be able to utilize its beneficial effects both in solid solution and in precipitate form.

Studies of Phases Formed in Type 316 Stainless Steel (R. E. Gehlbach)

Studies of the microstructures formed in type 316 stainless steel show a large amount of precipitation during exposure to elevated temperatures. It is necessary to identify these precipitates to understand the relationship between microstructure and mechanical properties. Our initial work on phase analysis was performed on four heats of type 316 stainless steel: two of the standard alloy (heats L and DO), one of type 316L (heat EO), and one modified alloy containing 0.23% Ti (heat R1).

We analyzed by x-ray diffraction precipitates electrolytically extracted from specimens aged 2000 or 4000 hr at 350 to 750°C and also from specimens cold worked 20% before aging at 650°C. All materials were annealed at 1050°C before cold working or aging. The specific conditions studied and the precipitates detected for each condition are listed in Table 3.6 according to heat.

In the aged standard type 316 stainless steel, the precipitate was the $M_{23}C_6$ (where M is metal) type of carbide. The metallic component was primarily Cr, but Mo and Fe were also present, as determined by electron microprobe analysis. Concentrations of X phase increased with respect to carbide in the L heat with increasing temperature, although the carbide exhibited stronger x-ray peak intensities at all temperatures.

Table 3.6. Precipitates Detected by X-Ray Diffraction After Electrolytic Extraction from Type 316 Stainless Steel

Cold[a] Work (%)	Aging[a] Time (hr)	Aging Temperature (°C)	Phases Present						
			$M_{23}C_6$	TiN	TiC	$Ti_2(S,C)$	X	Laves	σ
		Type 316 Stainless Steel, Heat L							
	2000	550	✓				✓		
	2000	650	✓				✓		
	2000	750	✓				✓	?	
		Type 316 Stainless Steel, Heat DO							
	0			✓					
	4000	350	✓	✓					
	4000	450	✓	✓					
	4000	550	✓	✓					
	4000	650	✓			✓	✓	✓	
20	4000	650						✓	✓
		Type 316L Stainless Steel, Heat EO							
	2000	650	✓				✓	✓	
		Type 316 Stainless Steel, Heat R1							
	4000	350		✓	✓	✓			
	4000	450		✓	✓	✓			
	4000	550		✓	✓	✓	✓		
	4000	650		✓	✓	✓			
20	4000	650						✓	✓

[a]All samples annealed 1 hr at 1050°C before cold working or aging.

A trace of Laves phase may have been present at 750°C. In the other heat, TiN, resulting from trace levels of Ti in the alloy, was present in all samples in addition to the carbide. (At 650°C this nitride was not detectable due to the large amount of other precipitates.) Titanium carbosulfide was detected at 650°C, as well as some Laves phase. Very little precipitation occurred at 550°C and below in the standard alloys. In the case of the DO heat, there was more TiN than carbide at 550°C and below. Both $M_{23}C_6$ and X phase precipitated profusely at 650°C.

In type 316L stainless steel at 650°C, $M_{23}C_6$, X phase, and a trace of Laves phase precipitated.

The carbide that precipitated in the Ti-modified type 316 stainless steel was TiC rather than $M_{23}C_6$. Again, very little precipitation occurred below 650°C. Large quantities of the titanium carbosulfide were present for all four aging temperatures as well as some primary TiN. A trace of X phase was detected at 550°C but not at 650°C. Chi phase may have been present at the higher temperature but masked by the presence of large quantities of the carbide and carbosulfide.

The effect of 20% cold work on precipitation was quite marked in the standard and modified alloys. Large amounts of σ phase precipitated in both alloys during aging of the cold-worked material for 4000 hr at 650°C. Some Laves phase appeared to be present but was not positively identified. Chi phase and carbides were not detected in x-ray patterns although they may have been present in very low concentrations.

Our goal is to relate these phase changes to the changes in mechanical properties observed for samples given similar anneals. These changes, in the absence of irradiation, must then be factored into the mechanical properties that we measure after irradiation.

Incoloy 800

Effect of Heat Treatment on the Mechanical Properties of Incoloy 800 (C. E. Sessions)

Previous studies[16] showed that heats of Incoloy 800 that contain 0.1% Ti and 0.1% C have improved creep ductility after irradiation at elevated temperatures (e.g., 700°C). However, for certain heat treatments and for certain irradiation conditions[17] [such as solution annealing 0.5 hr at 1150°C followed by irradiation at 550°C to 1.6×10^{21} neutrons/cm^2 (thermal and > 0.1 MeV)], the creep properties of the same alloy can be relatively poor. The deterioration in properties is in part caused by an aging reaction that is aggravated by irradiation and that is absent for heats with low C contents.[18] It was shown[17] that a heat treatment of 100 hr at 800°C before irradiation can produce microstructures that are less susceptible to this embrittling

aging reaction at 550°C, but the strength levels even before irradiation are lower in this case.

We are concerned with the influence of minor variations in composition on this aging reaction and are studying the aging of five heats of Incoloy 800 in which the ratio of Ti to C varies while the other alloying elements are maintained constant. The effect of aging times of 0, 1000, and 2000 hr at 500°C on the tensile properties at 650°C of two alloy compositions (0.1 and 0.26% Ti with 0.1% C) was discussed previously.[19] The results indicated no severe embrittlement for either composition. Also, creep results after 2000 hr of aging at 500°C indicated that the heat treatment of 0.5 hr at 1150°C and 100 hr at 800°C to agglomerate carbides produced a more stable structure than that of the solution-annealed material. As compared to aging at 500°C after only a solution anneal at 1150°C this treatment to agglomerate carbides, when given before aging, increased both the ductility and the creep rate while it reduced the rupture life by a factor of 5 to 10; when given after aging 2000 hr at 500°C, it increased creep rate by a factor of 20 and ductility by a factor of 2 (29 vs 57% elongation) at 30,000 psi and 650°C (ref. 19).

We completed additional creep tests for three different Incoloy 800 compositions; the compositions and creep results are tabulated in Table 3.7. These tests compared the influences of different compositions and heat treatments on the creep-rupture properties at 650°C after 1000 hr aging at 500°C. We measured the creep properties at 650°C so that we could compare the results with those from previous work at that temperature; however, we are switching our test temperature to 550°C, the temperature used in commercial steam generators, so that future results will be more germane to current reactor applications, in which Incoloy 800 components operate at 500 to 600°C. The current results for 650°C indicate, generally, that the effects of aging are similar for heats that contain 0.1% C and either 0.1 or 0.27% Ti. However, the heat with low C (0.03% C) and 0.1% Ti did not show any influence of the heat treatment for carbide agglomeration on the aging response.

The creep rate at a given stress varied by a factor of more than 100 for the tests reported in Table 3.7. For both heats with high C

Table 3.7. Creep-Rupture Properties of Experimental Heats of Incoloy 800 at 650°C

Test	Treatment Before Aging[a] Time (hr)	Treatment Before Aging[a] Temperature (°C)	Stress (psi)	Rupture Life (hr)	Minimum Creep Rate (%/hr)	Fracture Strain (%)
			× 10^3			
		Heat H; 0.1% Ti, 0.12% C[b]				
A10	0.5	1150	30	220.8	0.033	24.3
A16	0.5	1150	30	329.1	0.016	21.6
A24	0.5	1150	28	176.7	0.048	21.8
A23	0.5	1150	35	121.1	0.01	~ 12.8
A26}	0.5 100	1150 800	35	23.8	1.08	53.0
A17}	0.5 100	1150 800	30	48.5	0.60	55.3
A25}	0.5 100	1150 800	25	175.4	0.162	60.5
		Heat J; 0.27% Ti, 0.12% C[b]				
A27	0.5	1150	40	91.2	0.016	24.9
A18	0.5	1150	35	537.6	0.004	15.3
A29}	0.5 100	1150 800	40	5.9	4.00	48.1
A19}	0.5 100	1150 800	30	69.3	0.43	61.6
A28}	0.5 100	1150 800	25	595.5	0.028	44.0
		Heat A; 0.1% Ti, 0.03% C[b]				
A13	0.5	1038	25	114.8	0.249	63.5
A22	0.5	1038	30	43.0	0.61	61.2
A21	0.5	1038	22	300.2	0.136	69.1
A20	0.5	1038	30	37.4	0.84	62.6
A14}	0.5 100	1038 800	25	132.5	0.254	58.5
A40}	0.5 100	1038 800	22	246.9	0.144	64.0

[a]Aging treatment: 1000 hr at 500°C.

[b]The average concentrations of the other alloying elements were 48% Fe–30% Ni–21% Cr–0.7% Mn–0.21% Al.

(H and J) the heat treatment for carbide agglomeration resulted in the highest creep rates. The creep rate for the heat with 0.26% Ti varied by a factor of 100, depending on whether or not the aged samples were heat treated to agglomerate carbides before aging at 500°C; that for the heat with 0.1% Ti and 0.1% C varied by a factor of only 10, and that for the heat with 0.1% Ti and 0.03% C did not vary.

The rupture life at a given stress varied by a factor of 10 for the tests reported in Table 3.7, as shown in Fig. 3.15. The longest lives were for heat J, which was not heat treated to agglomerate carbides; the

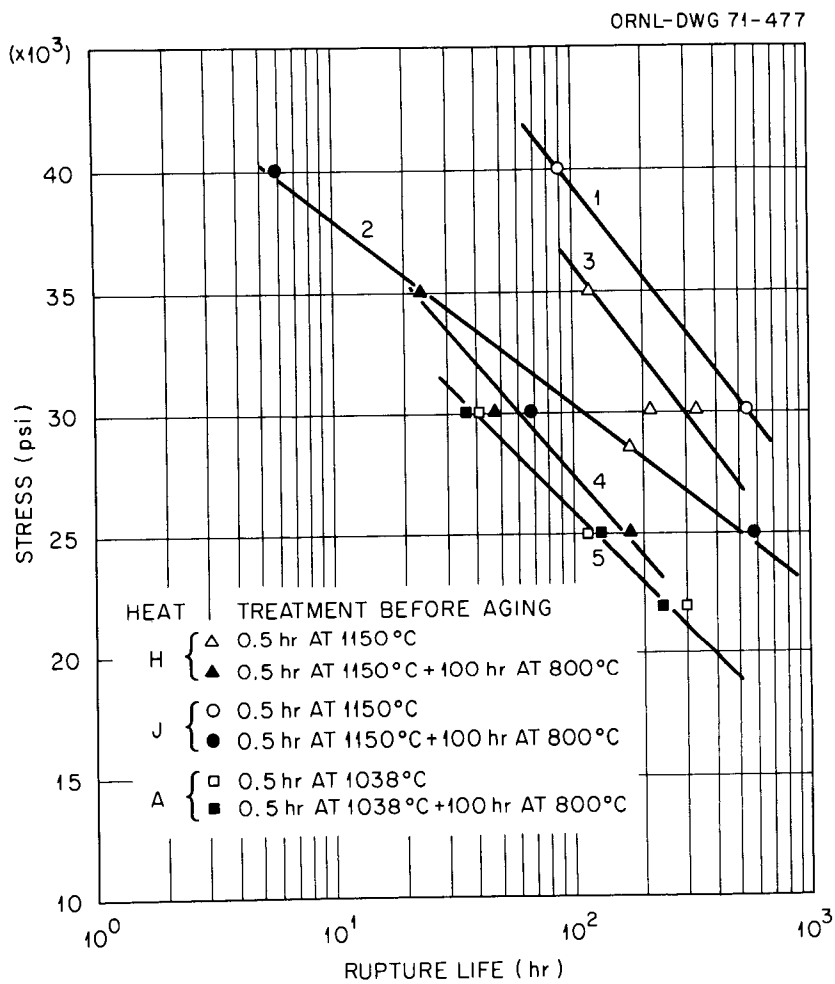

Fig. 3.15. Creep-Rupture Properties of Experimental Heats of Incoloy 800 at 650°C After Aging 1000 hr at 500°C.

shortest lives were for heat A, which had low C content. The heat treatment to agglomerate carbides most strongly influenced heat J, which contained the highest Ti content and presumably the highest density of precipitates. There was no difference in the rupture lives for heat A, which had low C content, as shown by the two sets of data points on the same line.

The fracture elongations ranged from 13 to 68% for the tests reported in Table 3.7. The lowest values (15 to 25%) were for samples for heat J that had high-Ti content and that had not been heat treated to agglomerate the carbides. The highest ductilities were for the heat with low-C content that had not been heat treated to agglomerate the carbides.

Thus, we find significant differences in the aging response of Incoloy 800 depending on the C content and upon whether or not the alloy was heat treated to agglomerate the carbide precipitates before aging. In view of these trends for unirradiated material, it is not too surprising that similar but more detrimental results were found for irradiated material.

Irradiation Damage to Refractory Metals

Formation of Voids in Niobium and Nb–1% Zr (F. W. Wiffen)

Specimens of Nb and Nb–1% Zr irradiated under identical conditions were examined by transmission electron microscopy to evaluate the effect of the alloying on the population of voids. Sheet specimens of Nb annealed 1 hr at 1150°C and of Nb–1% Zr annealed 1 hr at 1200°C were irradiated in subassembly X 034 in row 2 of the EBR-II. Both specimens were in the same capsule at a position 5 5/8 in. below the reactor midplane. The capsule was irradiated in a static Ar atmosphere to a fluence of 2.5×10^{22} neutrons/cm^2 (> 0.1 MeV). The irradiation temperature was determined from design calculations to be 790±25°C. Specimens 1/8 in. square were cut from these 0.020-in.-thick sheets and thinned by standard techniques to examine material near the center of the specimen thickness. We determined foil thicknesses by the stereographic technique for use in evaluating the number density of voids. We

determined void size by classifying void diameters on a Zeiss Particle Size Analyzer.

Examples of the microstructure of these two materials, as revealed by absorption contrast in the electron microscope, are shown in Fig. 3.16. Figure 3.16(a) shows voids in a typical area of the Nb sample, and Fig. 3.16(b) shows a similar area in a sample of Nb–1% Zr. The density

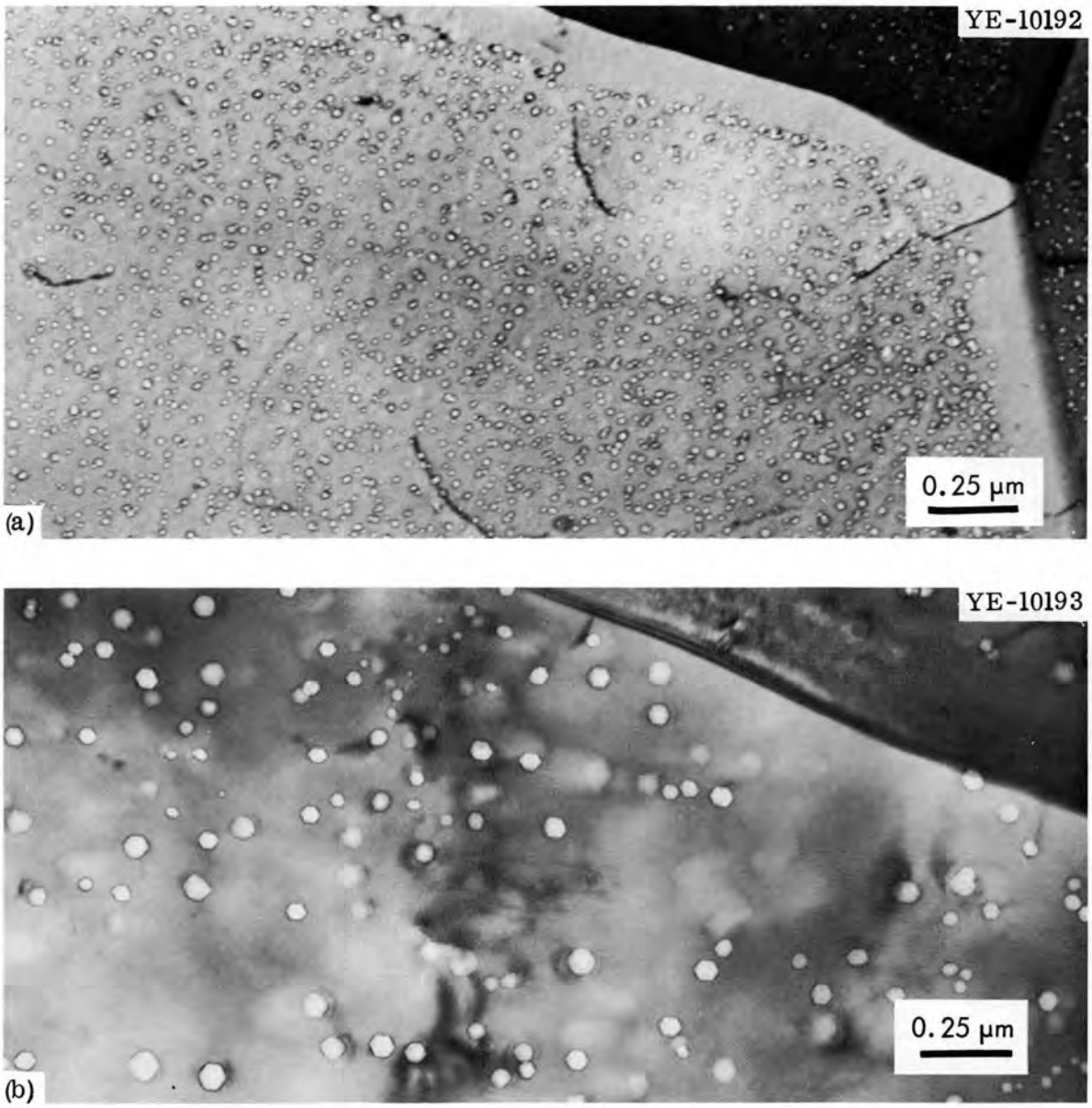

Fig. 3.16. Void Microstructure After Irradiation to 2.5×10^{22} neutrons/cm^2 (> 0.1 MeV) at 790°C. (a) Niobium. (b) Nb–1% Zr.

and size of the voids for both materials are given in Table 3.8. The void density in the unalloyed Nb was approximately constant in measurements on three foils. Void densities were often higher in the narrow area adjacent to the denuded zone at the grain boundaries, and in some cases the voids in this zone were appreciably larger than those found elsewhere. Void densities in the Nb–1% Zr were definitely not constant.

Table 3.8. Void Characteristics for Niobium and Nb–1% Zr Irradiated to 2.5×10^{22} neutrons/cm^2 (> 0.1 MeV) at 790°C

Sample	Void Density in Measured Area	Void Density (voids/cm^3)	Diameter, Å		Calculated Swelling (%)
			Average	Maximum[a]	
Nb	Typical	2.82×10^{15}	185	240	1.03
Nb–1% Zr	High	1.9×10^{14}	507	685	1.46[b]
Nb–1% Zr	Low	2.2×10^{13}	500[c]		0.17[b,c]

[a]95% of void diameters less than this value.

[b]Swelling values for local volumes only. Estimated sample swelling 0.9±0.4%.

[c]Approximate.

The variation in void density shown in Table 3.8, about an order of magnitude, was typical of the variations found from grain to grain and in some cases even within a grain. Void densities measured at three points within a single grain, all at points well removed from grain boundaries, varied by a factor of 12; the values were near the range shown in the table. Figure 3.17 shows a large area of the Nb–1% Zr sample in which void density varied over short distances by probably nearly an order of magnitude. This figure suggests that low concentrations of voids are associated with higher-than-average concentrations of precipitate. The influence of grain boundaries on the distribution of voids was less regular in the alloy than in the pure metal. Many grain boundaries were bordered by denuded zones, as in the pure metal, but in some cases voids formed up to the boundaries. Some detail can be seen at the grain boundaries in Fig. 3.17, but Fig. 3.18 better illustrates

Y-102559

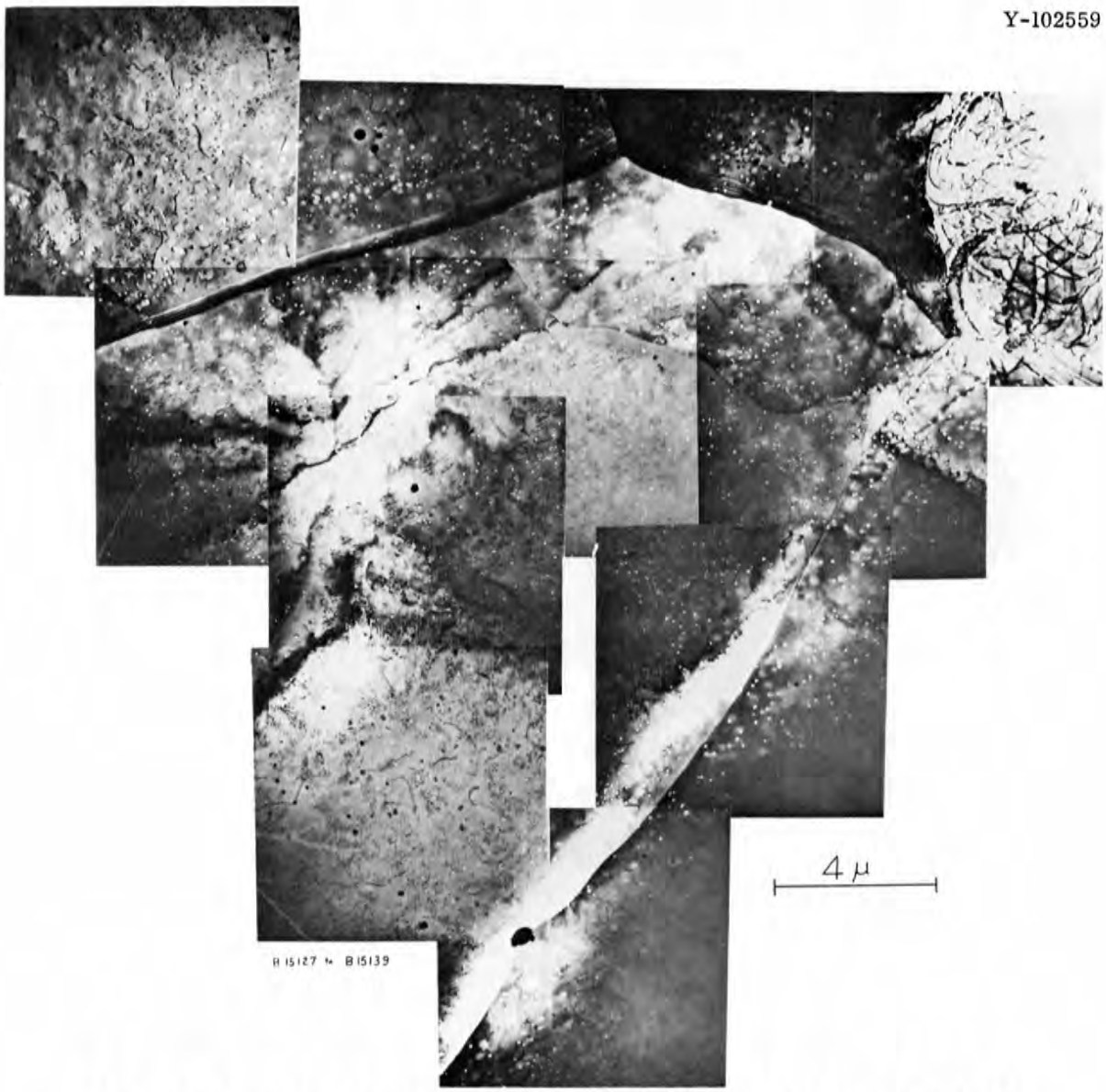

Fig. 3.17. Microstructure of Nb–1% Zr Irradiated to 2.5×10^{22} neutrons/cm^2 (> 0.1 MeV) at 790°C. Note the local variations in void density and the effect of the grain boundaries on the void population.

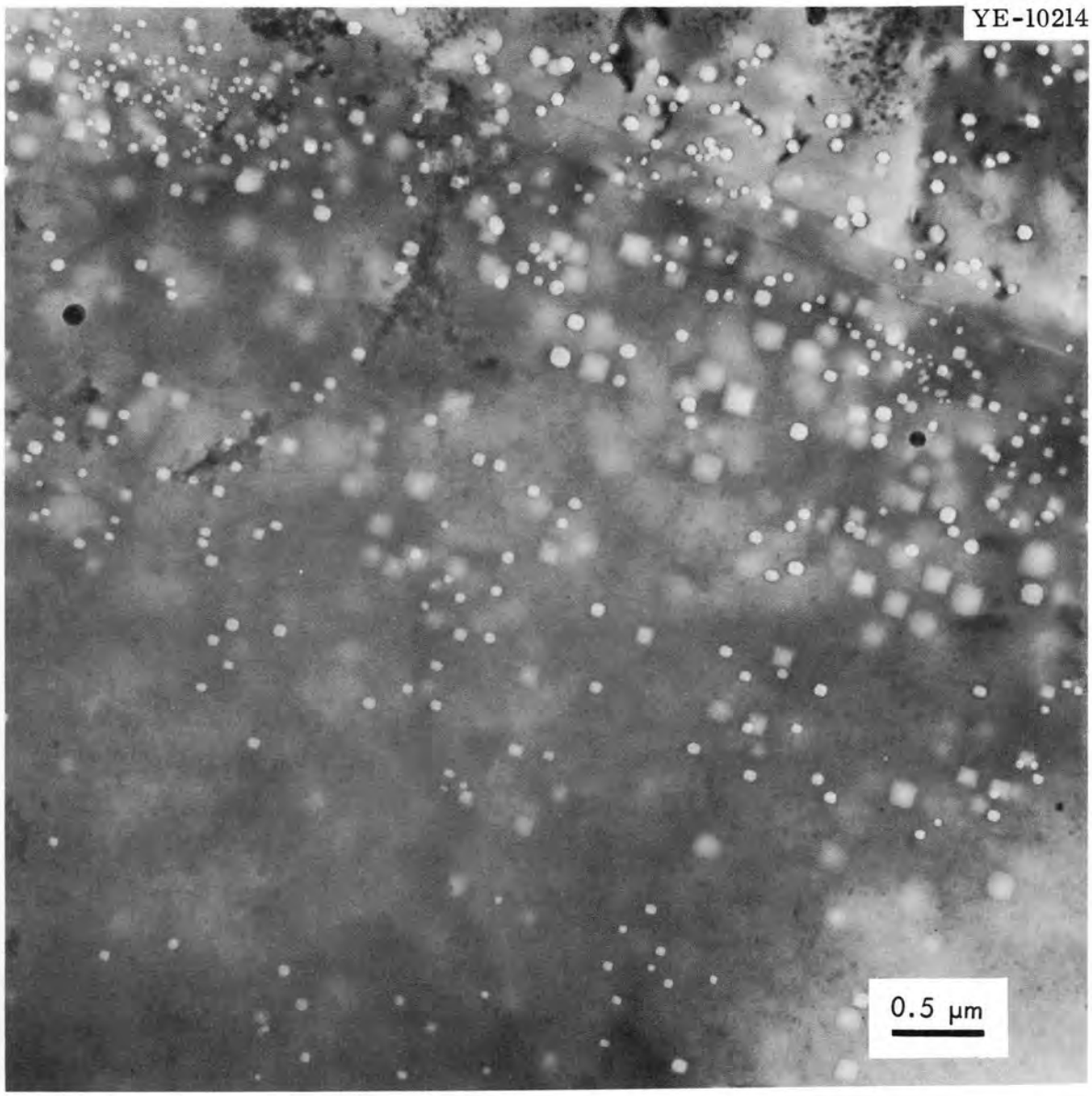

Fig. 3.18. Microstructure of Nb–1% Zr Irradiated to 2.5×10^{22} neutrons/cm^2 (> 0.1 MeV) at 760°C. This shows a clear example of one of the grain-boundary effects seen in this material. (The fuzzy features are surface pits produced by chemical attack at voids that intersect the surfaces.)

these unusual effects and also shows a large variation in void density over a short distance. The lower void density that results from alloying is balanced by an increased void size and, as shown in Table 3.8, the net result is that the total swelling is nearly equal in the Nb and the Nb–1% Zr. The swelling calculated for the alloy is only approximate

because the variation in void density has not yet been completely analyzed.

The difference of an order of magnitude in void density and the approximately equal total void volume in these two samples suggest that the addition of Zr to Nb greatly reduced the rate at which voids were nucleated. The alloying had little effect on the total number of vacancies observed in the final void populations.

The voids in the Nb sample were not located completely randomly but showed a tendency to be ordered on a body-centered cubic (bcc) superlattice of voids that was parallel to the bcc metal lattice. An example of the appearance of this ordering at near-optimum specimen alignment is shown in Fig. 3.19. The void alignments observed in this {111} oriented foil were in the ⟨112⟩ direction and represented the traces of the three

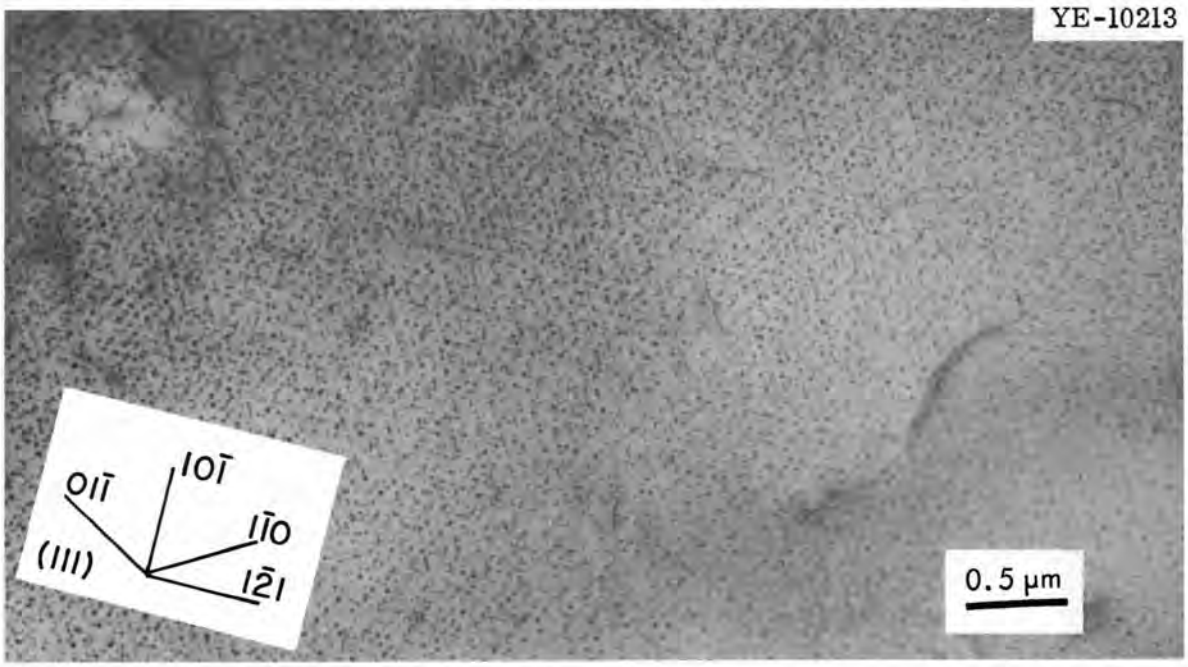

Fig. 3.19. Void Alignment in Niobium Irradiated to 2.5×10^{22} neutrons/cm^2 (> 0.1 MeV) at 760°C. Foil orientation is near {111}, and the void alignment seen is the ⟨112⟩ traces of the three {110} planes that are normal to the foil surface. The voids are ordered on a body-centered cubic superlattice that is colinear with the body-centered cubic metal lattice and has a lattice constant of about 665 Å. The superlattice points are about 45% occupied by voids. (Voids are darker than background because they are imaged here in an overfocused condition.)

{110} planes parallel to the viewing direction. Tilting the foil with respect to the electron beam established that the void alignment was three dimensional and became visible whenever an orientation was reached in which a {110} plane was parallel to the electron beam.

This ordering of voids occurred throughout the sample, but it was a very imperfect ordering. If Fig. 3.19 is viewed at a low angle to the page it can be seen that the perfect order occurs only over short distances. Some void planes can be traced for long distances, but the ordering can best be described as a general, rather than local, tendency. Measurement of the spacing of the {110} void planes for several areas in several grains in which the ordering was clearly seen gave an average separation of 470 Å for these {110} void planes. This gives a lattice constant of 665 Å for the bcc void superlattice and a density of 6.8×10^{15} superlattice points per cubic centimeter. Comparison of this density with the measured density of 2.8×10^{15} voids/cm^3 shows that about 45% of the superlattice sites are occupied. This site occupancy description of the degree of ordering is an oversimplification; for the ordering often breaks down locally, and the number of points on the superlattice is less than calculated above. There was no ordering of the voids in the Nb–1% Zr sample, where the void density was an order of magnitude lower.

Both the Nb and the Nb–1% Zr contained dislocation segments and a very few dislocation loops. The few dislocations that can be seen in weak contrast in Fig. 3.16(a) are approximately representative of both materials. These dislocation segments are assumed to be part of a large-scale dislocation network that resulted from the formation and extensive growth of interstitial dislocation loops.

Notes

1. E. E. Bloom and J. O. Stiegler, Fuels and Materials Development Program Quart. Progr. Rept. Sept. 30, 1970, ORNL-4630, pp. 79–90.

2. E. E. Bloom and J. O. Stiegler, "Effect of Fast Neutron Irradiation on the Creep Rupture Properties of Type 304 Stainless Steel at 600°C," paper presented at Symposium on the Effects of Irradiation on Structural Material, Toronto, Canada, June 22–25, 1970. To be published in the proceedings.

3. E. E. Bloom and J. O. Stiegler, "Effects of Fast Neutron Irradiation on the Tensile Properties of Austenitic Stainless Steels," paper presented at Second International Conference on the Strength of Metals and Alloys, Pacific Grove, California, August 30 to September 4, 1970 (to be published in the proceedings).

4. E. E. Bloom and J. R. Weir, Jr., "Development of Austenitic Stainless Steels with Improved Resistance to Elevated-Temperature Irradiation Embrittlement," pp. 261–289 in Irradiation Effects in Structural Alloys for Thermal and Fast Reactors, Spec. Tech. Publ. 457, American Society for Testing and Materials, Philadelphia, 1969.

5. W. H. Martin and A. M. Price, Determination of Irradiation Dose and Temperature in Graphite Irradiation Experiments Performed in the Dounreay Fast Reactor, TRG Report 1117(C) (1966).

6. J. L. Straalsund et al., Irradiation Effects on Reactor Structural Materials, Quart. Progr. Rept. Nov., Dec., 1969, Jan. 1970, BNWL-1318-1, pp. 11.40–11.58.

7. J. Wettman et al., Trans. Am. Nucl. Soc. 13(2), 557 (1970).

8. E. E. Bloom and J. O. Stiegler, J. Nucl. Mater. 36, 331–334 (1970).

9. E. E. Bloom and J. O. Stiegler, Fuels and Materials Development Program Quart. Progr. Rept. Sept. 30, 1970, ORNL-4630, pp. 73–78.

10. W. C. Leslie et al., "The Annealing of Cold-Worked Iron," pp. 119–216 in Iron and Its Dilute Solid Solutions, Interscience, New York, 1963.

11. W. R. Martin and J. R. Weir, Jr., Solutions to the Problems of High-Temperature Irradiation Embrittlement, ORNL-TM-1544 (June 1966).

12. E. P. Abrahamson, II and B. S. Blakeney, Jr., Trans. Met. Soc. AIME 218, 1101 (December 1960).

13. A. Seeger and G. Schottky, Acta Met. 7, 495 (1959).

14. P. J. Feltham, J. Inst. Metals 89, 354 (1961).

15. A. L. Sutton and W. Hume-Rothery, Phil. Mag. 46, 1295 (1955).

16. D. G. Harman, Nucl. Appl. 9, 561–571 (October 1970).

17. D. G. Harman, Fuels and Materials Development Program Quart. Progr. Rept. June 30, 1969, ORNL-4440, pp. 123–128.

18. D. G. Harman, Fuels and Materials Development Program Quart. Progr. Rept. Dec. 31, 1968, ORNL-4390, pp. 127–134.

19. D. G. Harman, Fuels and Materials Development Program Quart. Progr. Rept. June 30, 1970, ORNL-4600, pp. 118–123.

4. FABRICATION DEVELOPMENT FOR FBR CLADDING

G. M. Adamson, Jr. W. R. Martin

The purpose of this program is to develop and evaluate techniques for fabricating thin-walled tubing of high quality for cladding in FBR's. We are examining the relationships among processing variables, mechanical properties at elevated temperature, and the physical defects of the tubing.

Effect of Fabrication Variables During Mandrel-Plug Drawing on the Quality and Properties of Type 316 Stainless Steel Tubing

Studies of Artificial Defects (K. V. Cook, R. W. McClung)

The primary objective of this study is to establish the effect of flaws of various sizes [simulated by electrodischarge-machined (EDM) notches] on the mechanical properties of 1/4-in.-OD type 316 stainless steel tubing. Notches such as these are normally used to establish test sensitivity for both ultrasonic and eddy-current tests; those that we are using are as narrow as we can now machine them (0.0023 in.).

Three 1/4-in.-OD × 0.015-in.-wall-thickness tubes designated BA1-1, BA1-2, and BA1-3 were ultrasonically inspected for discontinuities equivalent to a 0.001-in.-deep × 0.0023-in.-wide × 0.030-in.-long EDM reference and marked for sectioning into 4-in.-long tube sections. A total of 31 specimens sectioned from the three tubes were returned to us for further testing and documentation before they were fabricated into specimens for tube burst tests. Only a few of the specimens will require EDM notches since the primary purpose for this series is to establish better reference data on mechanical properties for tubing without defects.

Study of Discontinuities Introduced During Fabrication (K. V. Cook, R. W. McClung)

The primary objective of this study was to establish the size of discontinuity that might be introduced into cladding during insertion or removal of the fuel pellets. Results of tests of mechanical properties

of tubing that contains EDM notches, both as machined and altered, should establish the importance of discontinuities introduced during loading of the fuel.

A tube (MAT 48-9) of 0.230-in.-OD × 0.015-in.-wall-thickness type 316 stainless steel fabricated by Carpenter Technology in accordance with FFTF specifications, which required ultrasonic inspection for defects equivalent to an 0.001-in.-deep × 0.030-in.-long EDM reference notch, was purchased for this study. We ultrasonically tested the tube against such a reference notch to confirm its integrity before loading it with fuel. We selected a 30-in.-long section of the tube as a convenient length for handling and inserted 14 depleted UO_2 fuel pellets. The pellets, which were 0.0025 in. smaller in diameter than the tube, did not bind but rather slid back and forth in the tube as it was inverted. We unloaded the tube and again tested it ultrasonically against the reference notch; the test revealed no change. We reloaded the tube with the same pellets, which were then forced to bind, and used a welding rod as a plunger to push the pellets back and forth inside the tube. We definitely heard the sound of scratching, apparently caused by a binding pellet. We unloaded the pellets and again tested the tube ultrasonically; we detected no indications equivalent to the 0.001-in.-deep × 0.030-in.-long reference notch. This would be expected if the scratches were less than 0.001 in. deep, since we made no attempt to set the ultrasonic system to detect smaller discontinuities. Since we knew scratching had occurred, we replicated the inner surface and measured scratch depths on the replica by means of a differential focusing technique with a microscope. The deepest scratch detected was about 0.0002 to 0.0003 in. deep. A metallographic cross section of this scratch is shown in Fig. 4.1.

Effects of Artificially Induced Defects on the Mechanical Properties of Unirradiated Annealed Type 316 Stainless Steel Tubing (R. T. King, G. A. Reimann, K. V. Cook)

An experimental program to determine the effects of flaws on 0.25-in.-OD × 0.016-in.-wall-thickness type 316 stainless steel tubing is in progress. The variables under study include the shape and size of the defect, the metallurgical condition of the tubing, and the stress and temperature

Fig. 4.1. Photomicrograph of Surface Defect from Fuel Loading.

at which the tubing is tested. We previously reported the effects of 0.030-in.-long × 0.0025-in.-wide EDM notches on the burst properties of cold-worked type 316 stainless steel.[1] Here we report tests of tubing fabricated according to schedule BA1-1 (ref. 2) from Allegheny-Ludlum Steel Corporation heat 65808 type 316 stainless steel. These tubes have longitudinal EDM notches 0.25 in. long by 0.0025 in. wide on either the inner or outer surface. We studied three notch depths, approximately 10, 33, and 66% of the wall thickness of the tubing. All tubing received a final anneal of 1 hr at 925°C in H_2 before testing, but the experimental procedures were otherwise the same as those described earlier.[1]

The results of these tube burst tests are given in Table 4.1. For most of these tests, the strain near the bottom of the tube was greater than that near the top. Because of an inadvertent change in loading arrangement, the specimens were positioned incorrectly in the furnace, so that the top of each tube operated at a temperature slightly lower than that at the bottom. However, since all of the notch-bearing tubes fractured at the notch, which was in every case in a 650°C zone of the furnace, these results are valid for the stated test temperature.

Table 4.1. Stress-Rupture Behavior of Annealed Type 316 Stainless Steel Tubing with Electrodischarge-Machined Notches

Specimen Number	Notch Surface Location	Notch Depth (in.)	Hoop Stress (psi)	Modified Hoop Stress (psi)	Rupture Time (hr)	Circumferential Strain Calculated for Ellipse, %		
						Near Failure Point	Near Tube	
							Bottom	Top
			$\times 10^3$					
11-13		0	40		10.9	19.5	19.5	11.8
11-14		0	35		10.8	7.4	10.8	10.8
11-15		0	30		50.3	18.4	18.4	9.2
12-26	Outer	0	30		55.5	6.0	7.0	7.0
8-39		0	40		5.0	20.0	20.0	11.0
8-40		0	35		14.5	24.6	20.2	11.0
10-1		0	30		40	17.5	17.3	14.2
15-51		0	30		54.4	16.4	10.0	16.4
11-16	Outer	0.0014	40	43.8	4.4	10.0	17.7	9.8
11-17	Outer	0.0014	30	32.9	50.6	8.4	12.8	8.3
12-19	Outer	0.0049	40	57.7	0.5	4.7	4.5	4.6
12-20	Outer	0.0048	30	42.8	35.4	4.3	5.28	4.4
12-22	Outer	0.0081	40	81.0	< 0.1	1.6	1.8	1.9
12-23	Outer	0.0080	30	60.0	0.7	0.9	1.1	1.0
8-29	Inner	0.0014	40	43.8	3.9	20.6	20.6	12.0
8-30	Inner	0.0014	30	32.9	49	12.8	22.4	8.6
8-32	Inner	0.0044	40	55.2	0.2	4.2	4.2	4.1
8-33	Inner	0.0043	30	41.0	14.1	4.0	3.8	2.9
8-35	Inner	0.0081	40	81.0	< 0.1	2.2	2.2	2.1
8-36	Inner	0.0083	30	62.3	< 0.1	2.5	2.1	2.2

The effects on rupture life of notches on the outer and inner surfaces are shown in Figs. 4.2 and 4.3, respectively. In both cases, notches with depths of 10% of the wall thickness appear to reduce the rupture life (the statistical significance of this statement must be evaluated later). Rupture life progressively decreases with increasing

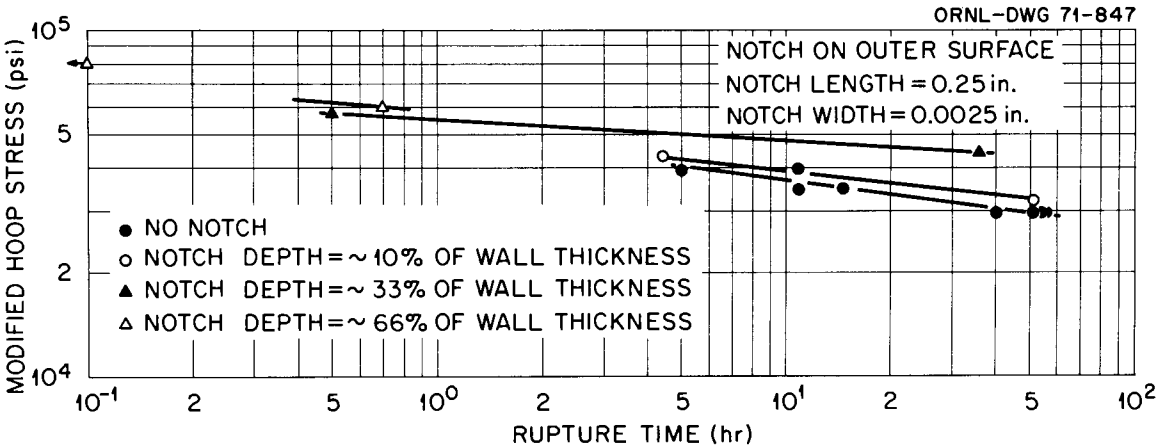

Fig. 4.2. Effect of Notches Electrodischarge Machined on the Outside Surface of Annealed Type 316 Stainless Steel Tubing on the Rupture Time at 650°C.

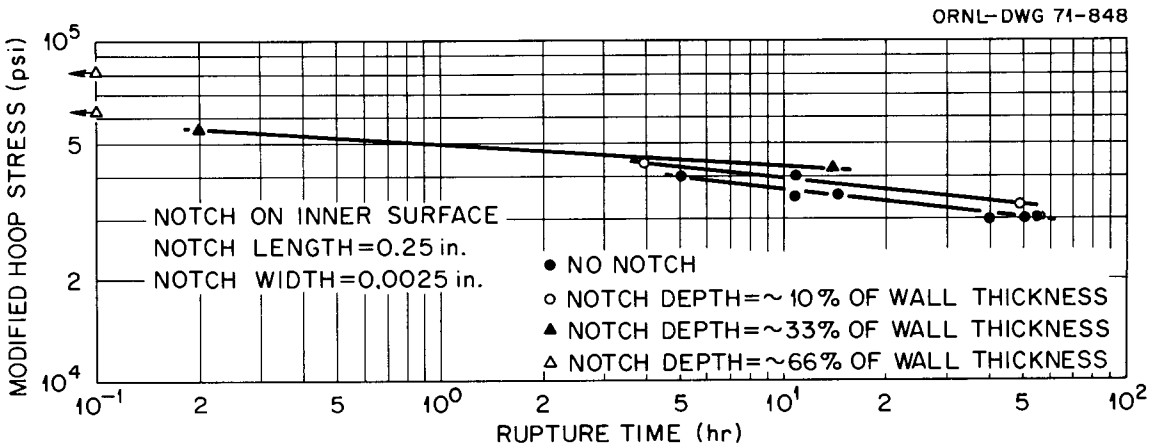

Fig. 4.3. Effect of Notches Electrodischarge Machined on the Inside Surface of Annealed Type 316 Stainless Steel Tubing on the Rupture Time at 650°C.

notch depth. The limited data available suggest that the effect of notches becomes smaller with decreasing stress. If this should prove to be true, then stress relaxation caused by plastic deformation probably plays an important role in the deformation process. The rupture time is plotted versus the modified hoop stress in Figs. 4.4 and 4.5. Modified hoop stress is the hoop stress calculated for the reduced wall thickness beneath the flaw,

$$\sigma' = \frac{P_d}{2(t - n)} ,$$

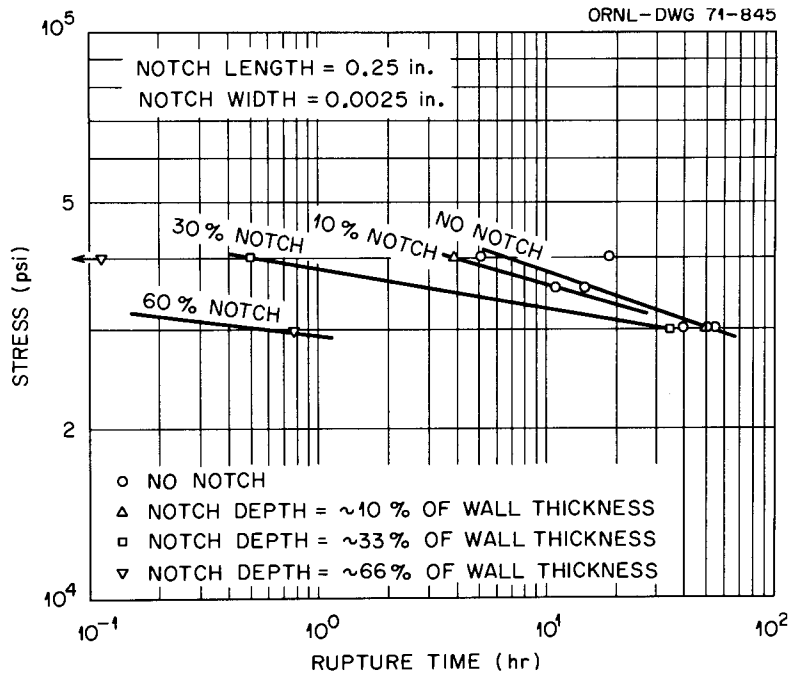

Fig. 4.4. Rupture Life Versus Modified Hoop Stress Near Notch in Outer Surface of Type 316 Stainless Steel Tubing at 650°C.

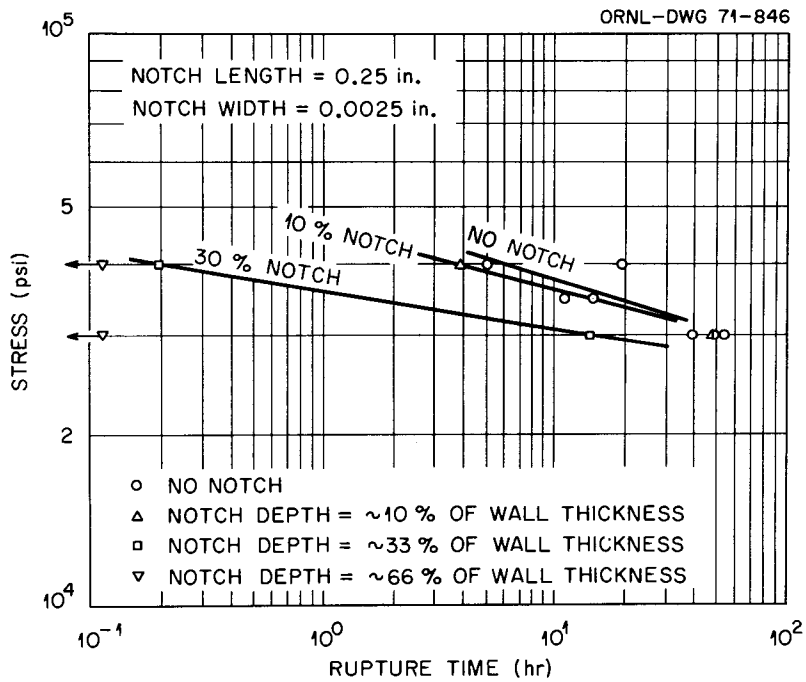

Fig. 4.5. Rupture Life Versus Modified Hoop Stress Near Notch in Inner Surface of Type 316 Stainless Steel Tubing at 650°C.

where P is internal pressure, d is the tube diameter, t is the wall thickness, and n is notch depth. The notched tubes are stronger than the control specimens in that they exhibit longer rupture times for any applied modified hoop stress than do the control specimens.

The circumferential strain near the rupture point is plotted versus applied stress in Figs. 4.6 and 4.7. Although the control specimens usually exhibited over 16% strain, two control specimens (12-26 and 11-14) strained less than 10%. The low ductility of specimen 12-26 can be discounted, since the specimen failed by the opening of a pinhole leak in the weldment of the bottom end cap. However, we cannot explain the low ductility of specimen 11-14 without involving some natural defect that ultrasonic testing failed to detect. This result should serve as a warning to any who feel that present inspection techniques for fast-reactor cladding are sufficient to detect all natural flaws that play a role in the fracture of thin-walled stainless steel cladding.

Figures 4.6 and 4.7 show that, within the limits of experimental uncertainty, notches with depths only 10% of the wall thickness can reduce the ductility of annealed type 316 stainless steel tubing. The statistical significance of this statement will be evaluated quantitatively when more data are available. Ductility progressively decreases with increasing notch depth.

Development of Type 316 Stainless Steel with Ultrafine Grain Size
(G. A. Reimann)

We continued our study of methods for producing a very fine grain size in type 316 stainless steel. Previously, we demonstrated our capability of producing type 316 stainless steel tubing with a grain size of ASTM 14 (about 2 μm) for the purpose of improving the postirradiation properties of fuel cladding. However, to obtain very substantial reduction in irradiation embrittlement and swelling, it was considered necessary to decrease the average grain diameter to 0.1 μm, which corresponds to a grain size of ASTM 20 and is more than an order of magnitude smaller than the finest grain size previously obtained.

We devised a series of experiments to evaluate the potential of using as a starting material stainless steel powders with a very fine

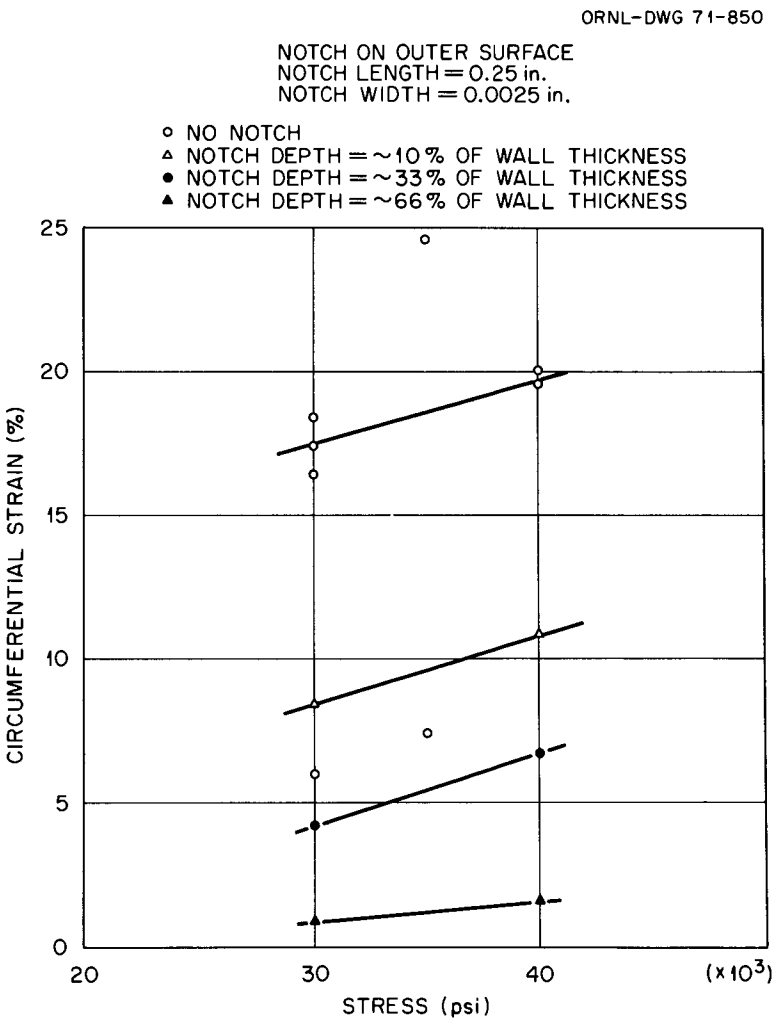

Fig. 4.6. Effect of Notches Electrodischarge Machined on the Outer Surface of Annealed Type 316 Stainless Steel Tubing at 650°C on the Circumferential Strain Near the Point of Rupture.

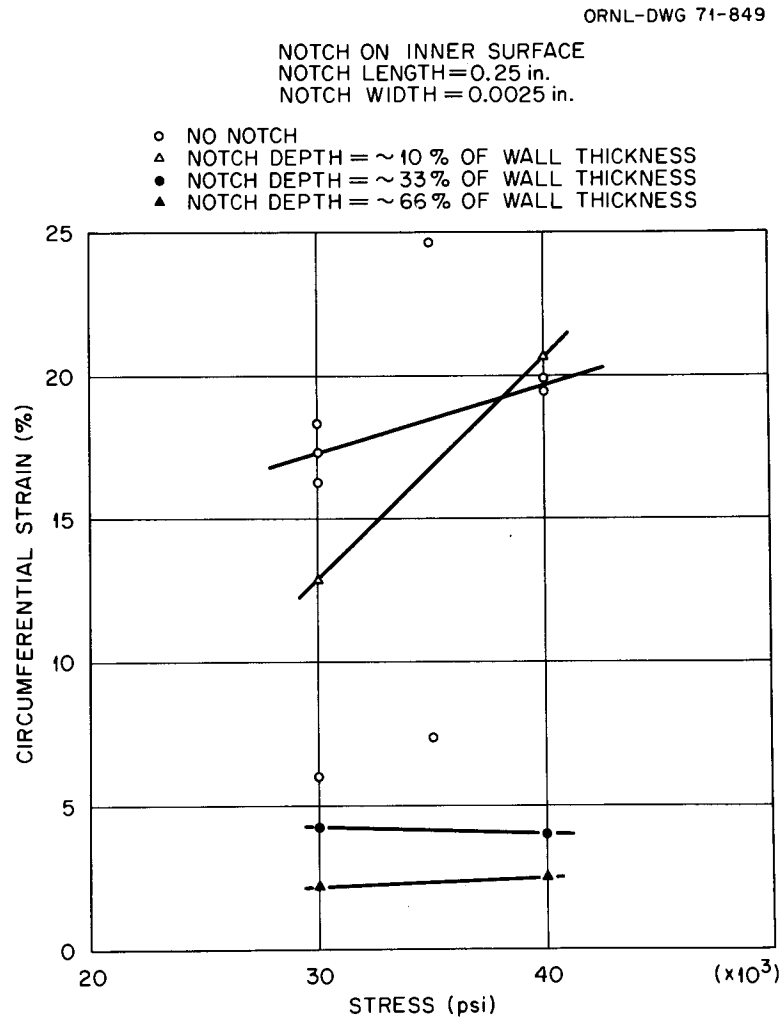

Fig. 4.7. Effect of Notches Electrodischarge Machined on the Inner Surface of Annealed Type 316 Stainless Steel Tubing at 650°C on the Circumferential Strain Near the Point of Rupture.

grain size that would be carefully fabricated into tubing by means of our processing technique for producing fine grain size. To eliminate the encumberance of fabricating tubing and to permit use of sample-sized quantities of material, we use as a starting material powder-product pellets that are then fabricated by various routes into rod for examination.

Several powders are available for this study. The first trials were made using a batch of −325 mesh type 316 stainless steel powder of the following composition (supplier's analysis): Fe–0.017% C–0.89% Si–0.17% Mn–0.019% S–16.92% Cr–13.20% Ni–2.10% Mo.

The powder was sieved to −400 mesh, and a portion of it was annealed 1 hr in H_2 at 900°C to reduce the O content. We pressed the powder at 40 tsi into 1-in.-diam × 1 1/4-in.-long pellets. Pellets intended for hot swaging were sintered at 1250°C for 1 hr in a vacuum and coined. Pellets for extrusion were degassed only before they were inserted into an extrusion billet. Hot swaging was done at 1000°C; extrusion was done at 900°C. Both techniques produced a 3/8-in.-diam fully recrystallized rod. Both types of rod were cold swaged or cold drawn to 1/8-in.-diam wire. Samples were removed after each 50% reduction. The material was annealed at low temperature (700 to 760°C) before each sampling.

Thus, the 3/8-in.-diam hot-worked rod originated from both as-received and H_2 annealed powder and was fabricated by hot swaging or extrusion. The four types of rod were subsequently swaged or drawn to the final 1/8-in.-diam wire.

The structures obtained were very fine grained and difficult to examine optically or by transmission electron microscopy. By means of transmission electron microscopy, we estimated the grain size to average 1 to 1.5 μm; this was somewhat smaller than that obtained previously with tubing but far short of the objective of 0.1 μm.

The supplier reported the powder to contain 0.016 to 0.017% C; an analysis at ORNL reported 0.021 to 0.022% C. Since this amount of C would remain in solution during annealing at 700 to 760°C, a fine C precipitate could not develop to restrict grain growth. But the thin coating of oxide on each particle was expected to produce a similar dispersion during fabrication and assist in restricting grain growth. A portion of the powder was annealed in H_2 at 900°C to reduce the oxide

level and provide a basis for studying the effect of oxide particles on grain size. The O level was essentially unaffected by this treatment. The 900°C temperature was chosen because higher temperatures cause agglomeration of powders so that satisfactory pellets cannot be obtained.

When structures were examined by transmission electron microscopy, the electrochemical thinning technique used for sample preparation selectively attacked the oxide inclusions so there would not be enough sufficiently thinned areas available to produce satisfactory micrographs. Enough area could be examined, however, to allow us to determine how much recrystallization, if any, resulted from a specific heat treatment.

We found that we could not reliably obtain complete recrystallization below 740°C in fine-grained material containing 50% cold work. Neither could we discern differences in structure that could be attributed solely to the mode of fabrication.

Future efforts will be directed at higher levels of cold work, additional variations in heat treatment, and examination of other lots of powder in order to determine the processing technique capable of producing the finest obtainable grain size.

Effect of Planetary Swaging on the Structure and Creep Properties of Type 316 Stainless Steel

Production of Type 316 Stainless Steel by Planetary Swaging (G. A. Reimann)

We continued the study of the planetary swaging process to determine its applicability to the production of high-quality cladding for reactor fuel. From previous work,[3] we concluded that it was impractical to use planetary swaging for heavy initial breakdown of tubing; therefore, recent activity was confined to studying the application of the process to the final, finishing steps.

To produce some tubing for burst tests at elevated temperature, the starting stock was mandrel drawn in a conventional manner from Allegheny-Ludlum Steel Corporation heat 65808 into 0.267-in.-OD × 0.230-in.-ID tubing. The tubing was annealed for 1/4 hr at 900°C and planetary swaged to 0.250-in.-OD × 0.218-in.-ID final size.

Final size was achieved in four passes with no difficulty with the swager rotating at 1000 rpm and the bench speed at 12 in./min. Similar results were achieved with either three or two passes. Final size could not be obtained in a single pass of 20% reduction, mainly because of tube springback and mandrel elasticity. The planetary swager itself is sufficiently rigid and powerful to accomplish such a reduction with ease on this size tubing. The drawbench will be equipped so that a WC drawing plug can be substituted for the hardened steel mandrel rod to determine if it is possible to obtain final size with a single 20% reduction.

The tube samples are being processed for testing at elevated temperature, and metallographic samples are being prepared for examinations of structure and measurements of hardness.

Notes

1. R. T. King, G. A. Reimann, and K. V. Cook, Fuels and Materials Development Program Quart. Progr. Rept. Sept. 30, 1970, ORNL-4630, pp. 99–106.

2. G. A. Reimann, Fuels and Materials Development Program Quart. Progr. Rept. June 30, 1970, ORNL-4600, pp. 130–132.

3. G. A. Reimann, Metals and Ceramics Div. Ann. Progr. Rept. June 30, 1970, ORNL-4570, p. 86.

5. WELDING DEVELOPMENT FOR FBR STAINLESS STEEL COMPONENTS

J. R. Weir, Jr. G. M. Slaughter G. M. Goodwin

We are evaluating the behavior of weldments in austenitic stainless steel at 370 to 650°C as a function of both welding process and the variables within a process for application to liquid-metal-cooled fast breeder reactor (LMFBR) vessels and components. The solidification substructure of the weld metal markedly influences the mechanical properties of a weldment at elevated temperature; since the size and type of substructure are significantly influenced by factors that the welder can control, our approach is to determine this link between welding variables, the solidification substructure that these variables produce, and the resultant mechanical properties. Also included in the studies are corrosion behavior, irradiation stability, and the effect of heat treatment on structure and properties.

Study of Submerged-Arc Process

Investigations of Mechanical Properties (R. G. Berggren, G. M. Goodwin)

We continued our studies of the mechanical properties of 1-in.-thick submerged-arc weldments. Although our emphasis was on heat treatment of shielded metal-arc weldments, we completed three creep-rupture tests and began a fourth.

We previously reported[1] the results of creep-rupture tests at 650°C (1200°F) for a weld (SA-2) prepared with medium energy input and Arcos S-4 flux. The first four entries in Table 5.1 are the results of tests at 650°C and 25,000 psi of welds also made with Arcos S-4 flux at low, medium, and high energy input (SA-3, SA-4, and SA-5, respectively). Additional creep-rupture tests will be conducted on these welds at 650°C but at lower stresses to obtain longer rupture lives and determine what differences exist between these welds.

Table 5.1. Creep-Rupture Properties of Transverse Specimens of All Weld Metal From Submerged-Arc Welds in Stainless Steel[a]

Weld Number	Energy Input (kJ/in.)	Test Temperature (°C)	Stress (psi)	Rupture Time (hr)	Total Elongation (%)	Reduction of Area (%)
SA-2[b]	68 (Medium)	650	25,000	4.8	19	16
SA-3	40.8 (Low)	650	25,000	11.8	18	54
SA-4	68 (Medium)	650	25,000	11.4	23	47
SA-5	272 (High)	650	25,000	13.4	23	36
SA-4	68 (Medium)	595	20,000	1225.0	10	41
SA-4[b]	68 (Medium)	595	25,000	283.3	24	16
SA-4[b]	68 (Medium)	595	28,000	129.8	23	26

[a]All welds made with Arcos S-4 flux.

[b]Reported previously. Repeated for comparison.

We reported[1] the creep-rupture properties of the welds made with low, medium, and high energy input (SA-2, SA-3, and SA-4) with Arcos S-4 flux and tested at 595°C (1100°F) and 28,000 and 25,000 psi. The results of a test of the weld (SA-4) made with medium heat input at a lower temperature and, therefore, longer rupture life are presented in the lower portion of Table 5.1. The ductility, as measured by total elongation, for the long-term test, dropped significantly from the values obtained at shorter rupture lives. In Fig. 5.1 are plotted the rupture lives and total elongations of transverse specimens of all weld metal from our submerged-arc weldments. With the exception of the weldment made with Hobart HS-300 flux, the rupture

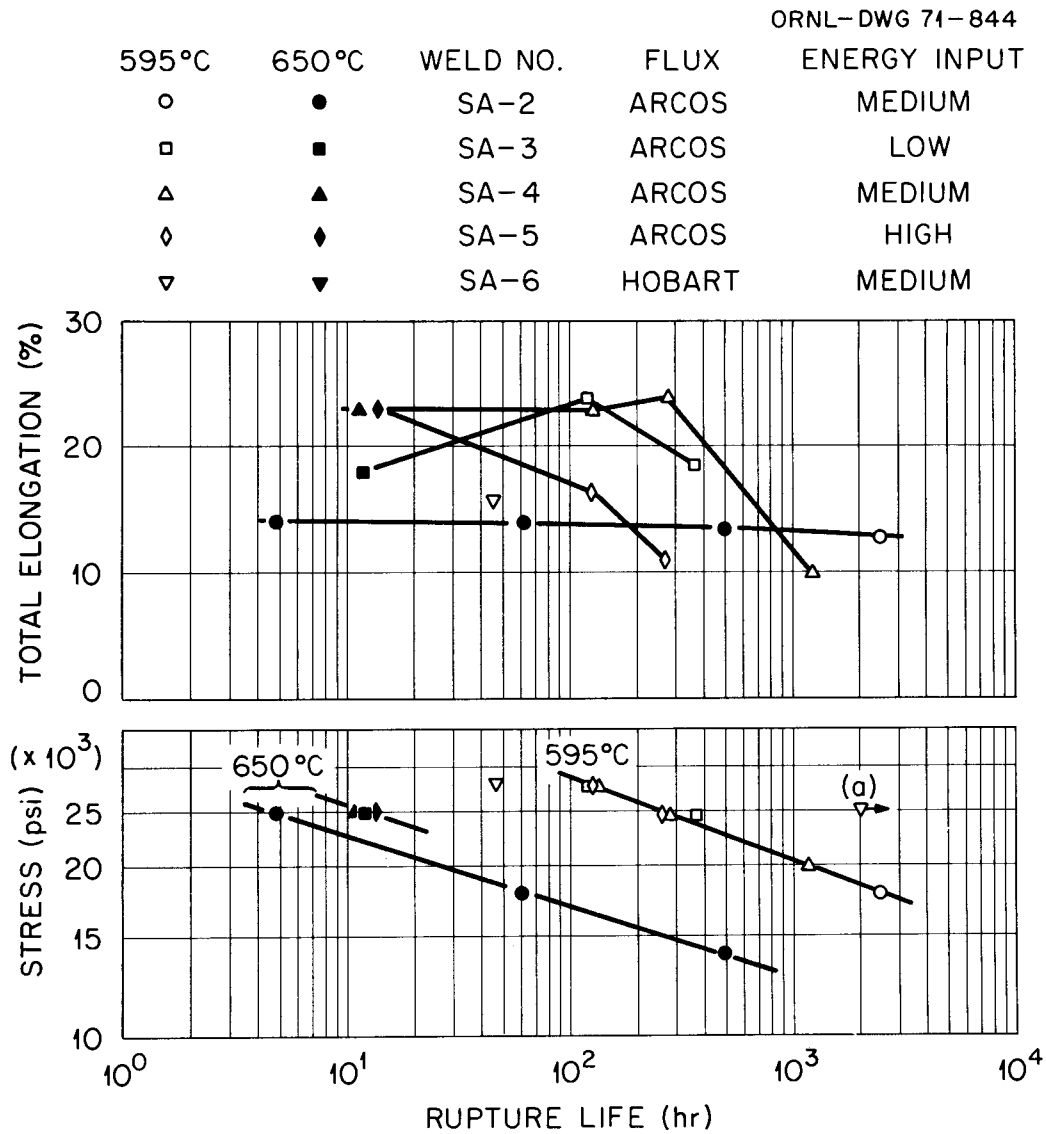

Fig. 5.1. Creep-Rupture Properties of Stainless Steel Submerged-Arc Welds (a) Test Still in Progress.

lives at 595°C (1100°F) lie on a common curve for stress versus rupture time. At 650°C (1200°F), there appears to be some difference between the rupture lives of weld SA-2 and the others, but this may not be significant. The values for total elongation, however, are markedly different for the several welds. We previously reported no reduction in total elongation as a function of rupture time. The results presented

in Fig. 5.1 indicate that ductilities, measured by total elongation, decreased at long rupture times and that the decrease occurred at a rupture life that was dependent on energy input and/or composition.

The rupture lives for the weld (SA-6) prepared with the Hobart HS-300 flux do not seem to fit the pattern observed for the other submerged-arc welds. The specimen creep tested at 595°C (1100°F) and 28,000 psi ruptured sooner than the others, but a specimen creep tested at 595°C and 25,000 psi is still in test at 2000 hr, which is significantly longer than the rupture times of the other submerged-arc welds.

Tensile Tests (N. C. Binkley)

The longitudinal, buttonhead specimens of all weld metal described previously[2] are being heat treated. Three groups of 25 specimens were prepared a follows: (1) as welded; (2) solution annealed 2 hr at 1065°C (1950°F); and (3) solution annealed 2 hr at 1065°C and then heat treated 10 hr at 800°C (1470°F) to agglomerate the carbides.

Each group of 25 specimens was then subdivided into five equal subgroups, each of which received one of the following treatments: (1) no aging, (2) aging at testing temperature for 1000 hr, (3) aging at 540°C (1000°F) for 100 hr, (4) aging at 595°C (1100°F) for 100 hr, or (5) aging at 650°C (1200°F) for 100 hr. All of the treatments were completed except the 1000-hr treatments, which are now in progress.

The five specimens in each subgroup will be tested at one tensile strain rate but at different temperatures: 315, 425, 540, 595, and 650°C (600, 800, 1000, 1100, and 1200°F). Tensile testing will begin soon.

Study of Gas Metal-Arc Process

Preparation of Weldment Specimens (D. R. Frizzell,[3] G. M. Goodwin)

Using conditions identical to those previously described,[4] with the exception of shielding gas, we prepared a gas metal-arc weldment in a 98% Ar–2% O_2 gas mixture. This weldment, along with the one

previously prepared in a 90% Ar–7.5% He–2.5% CO_2 gas mixture, was radiographed and found to be sound and will now be sectioned into specimens for tests of mechanical properties.

Study of Shielded Metal-Arc Process

Preparation of Weldment Specimens (N. C. Binkley, G. M. Goodwin)

We procured about 16 in. of weld in 2-in. plate prepared at Combustion Engineering, Inc., Chattanooga, Tennessee, under the conditions shown below:

Electrode identification	E308-15
Electrode diameter, in.	1/4
Plate identification	P-11829
Plate material, type stainless steel	304
Plate thickness, in.	2
Backing bar identification	P-11885
Current, amp	310
Welding technique	side bead

The compositions of base and weld metals are shown in Table 5.2. Note that this weld was prepared with 1/4-in.-diam electrodes with controlled amounts of minor elements and is thus the most "prototypic" weldment yet available to us for testing. The weld was sectioned into wafers for the Strauss test and specimen blanks for tests of mechanical properties.

Table 5.2. Composition of Base and Weld Metals for Shielded Metal-Arc Weld F21

	Composition, %											
	Si	S	P	Mn	C	Cr	Ni	Mo	Ti	B	N_2	Fe
Base metal	0.68	0.019	0.023	1.66	0.052	18.83	9.80	0.44	0.01	0.002	0.038	Bal
Weld deposit	0.48	0.010	0.054	1.81	0.066	19.83	10.21	0.15	0.05	0.009	0.047	Bal

Investigations of Mechanical Properties (R. G. Berggren, N. C. Binkley, G. M. Goodwin)

We are investigating the effects of commercially feasible heat treatments on the shielded metal-arc welds containing B that were made by Combustion Engineering, Inc. These weld-metal compositions appeared the most promising of the 18 compositions investigated thus far in the program. The heat treatments selected for study are feasible for the fabrication of FBR stainless steel components such as pressure vessels. They were annealed at either 1065°C (1950°F) to remove ferrite or at 955°C (1750°F) to retain some ferrite in the weld metal. The specimens were cooled at a controlled rate of 85°C/hr (150°F/hr) to 800°C (1470°F), held at that temperature for 10 hr to agglomerate the carbides, and then cooled at a controlled rate of 220°C/hr (400°F/hr). Some of the specimens were then reheated to 650°C (1200°F), held at that temperature for 100 hr to produce σ phase if possible, and then cooled slowly 55°C/hr (100°F/hr). Other specimens were heat treated similarly except that they were cooled slowly at 55°C/hr (100°F/hr) after the treatment at 800°C to agglomerate carbides.

The results of creep-rupture tests on specimens given some of these heat treatments are presented in Table 5.3. In addition, results of creep-rupture tests on as-welded specimens are presented for rupture times longer than 1000 hr. The heat treatments studied reduced the rupture lives of these welds but did not reduce the ductilities and, in a few cases (heat treatment 4), even appeared to improve the ductility markedly.

The ductilities of these welds (F-12, -13, -17, and -18) as welded were significantly better than those of the other shielded metal-arc welds studied for rupture lives longer than 1000 hr.

It is interesting to note that one specimen of weld F-18, as welded, fractured at the fusion line. Occasional fractures at unexpectedly low ductility have been observed in the past, but we have never known the exact location of the fusion line. Recently, we began eddy-current

Table 5.3. Creep Properties at 650°C of Shielded Metal-Arc Welds in Stainless Steel That Contains Boron

Weld Number	Coating	Specimen Type[a]	Heat Treatment[b]	Stress (psi)	Rupture Life (hr)	Total Elongation (%)	Reduction of Area (%)
F-12	0.016% P, 0.004% B	LW	1	20,000	1167	7.5	25
F-13	0.017% P, 0.006% B	LW	1	20,000	1160	7.8	28
F-17	0.037% P, 0.005% B	LW	1	20,000	2632	11.7	58
F-18	0.033% P, 0.002% B	LW	1	20,000	1940	8.9	34
F-17	0.037% P, 0.005% B	TW	1	21,000	650+	c	c
F-17	0.037% P, 0.005% B	TW	3	21,000	148	33	66
F-17	0.037% P, 0.005% B	TW	7	21,000	85	29	73
F-17	0.037% P, 0.005% B	TW	8	21,000	132	34	69
F-17	0.037% P, 0.005% B	TW	4	18,500	454	37	73
F-18	0.033% P, 0.002% B	TW	1	21,000	436[d]	3.4	1.6
F-18	0.033% P, 0.002% B	TW	3	21,000	155	34	67
F-18	0.033% P, 0.002% B	TW	7	21,000	106	29	42
F-18	0.033% P, 0.002% B	TW	8	21,000	70	21	51
F-18	0.033% P, 0.002% B	TW	4	18,500	448	57	50

[a]LW is longitudinal specimen of all weld metal. TW is transverse specimen of all weld metal (fusion line may be at or near the ends of gage length).

[b]Heat treatments

1: as welded.
3: 2 hr at 1065°C (1950°F), cooled at 85°C/hr (150°F/hr) to 800°C (1470°F), held 10 hr at 800°C, cooled at 220°C/hr (400°F/hr) to 455°C (850°F), and water quenched.
4: same as treatment 3 plus 100 hr at 650°C (1200°F), cooled at 55°C/hr (100°F/hr) to 455°C (850°F), and water quenched.
7: 2 hr at 955°C (1750°F), cooled at 85°C/hr (150°F/hr) to 800°C (1470°F), held 10 hr at 800°C, cooled at 220°C/hr (400°F/hr) to 455°C (850°F), and water quenched.
8: same as treatment 7 plus 100 hr at 650°C (1200°F), cooled at 55°C/hr (100°F/hr) to 455°C (850°F), and water quenched.

[c]Test still in progress.

[d]Fractured near shoulder at fusion line.

examination of all specimens before testing to locate the fusion lines. By this means, we were able to determine that this low-ductility fracture occurred at the fusion line. Whether this was due to inclusions or a metallurgical problem is not yet known.

Irradiation Studies (G. M. Goodwin, R. G. Berggren)

The weldments in the irradiation experiment in the EBR-II (ref. 5) accumulated a peak fluence of 2×10^{21} neutrons/cm^2 before the recent outage of that facility and are now awaiting startup for completion of the exposure.

A lot of 232 weldment specimens prepared and heat treated as reported previously[5] were delivered to WADCO for irradiation testing.

Heat-Treatment Studies (Nancy C. Cole, G. M. Goodwin, T. M. Kegley)

We are heat treating welds in austenitic stainless steel to determine the effects of various temperatures and times upon their microstructures and properties. Heat treatments in addition to those reported previously[6] are being studied. They include solution anneals of

1. 10 hr at 1065°C (1950°F) and water quench,
2. 2 hr at 1095°C (2000°F) and water quench, and
3. 2 hr at 1190°C (2175°F) and water quench,

and aging treatments of

1. 1000 hr at 595°C (1100°F) and water quench,
2. 1000 hr at 650°C (1200°F) and water quench,
3. 100 hr at 705°C (1300°F) and water quench,
4. 100 hr at 760°C (1400°F) and water quench, and
5. 10 hr at 870°C (1600°F) and water quench.

As reported, much of the ferrite in the welds was taken into solution after 2 hr at 1065°C (1950°F); more was dissolved in the shielded metal-arc welds than the submerged-arc welds. To determine if more ferrite would go into solution if the welds were held longer

at 1065°C (1950°F), we extended the time to 10 hr. As shown in representative welds in Fig. 5.2, little if any change occurred in the amount of ferrite. After 2 and 10 hr, only a very small amount of ferrite remained in the shielded metal-arc welds, and that which remained had become agglomerated. Much of the ferrite remained in the submerged-arc welds, and partial agglomeration occurred. Tests at longer times will be conducted to see if the ferrite will dissolve at 1065°C (1950°F).

Increasing the temperature to 1095°C (2000°F) for 2 hr did not appear to change the amount of ferrite substantially. In fact, 2 hr at 1190°C (2175°F) only appeared to decrease the size of ferrite slightly in the shielded metal-arc welds [Fig. 5.3(a)]. Much of the ferrite dissolved in the submerged-arc welds made with low and medium heat input [Fig. 5.3(b)]. The submerged-arc weld made with high heat input still retained a large amount of ferrite, as shown in Fig. 5.3(c). It was very difficult to detect a difference in the amount of ferrite in the submerged-arc welds made with high heat input and treated at 1065 or 1090°C (1950 or 2175°F).

We found more evidence to substantiate our belief that the size of ferrite substructure has a great effect on the rate at which the ferrite dissolves. We heat treated an electroslag weld in which the ferrite distribution was considerably coarser than that found in the submerged-arc welds made with high heat input. After solution annealing, practically all of the ferrite was retained. This again substantiated our belief that the larger particles of ferrite require higher temperatures and/or longer times to dissolve.

The aged specimens are being examined metallographically. The base metals are slightly sensitized after 1000 hr at 595°C (1100°F). They become more sensitized with increasing time and temperature until after 10 hr at 870°C (1600°F) the C dissolves in the low C (0.026% C) base metal. However, the base metal with the regular C level (0.062% C) is still sensitized after this treatment.

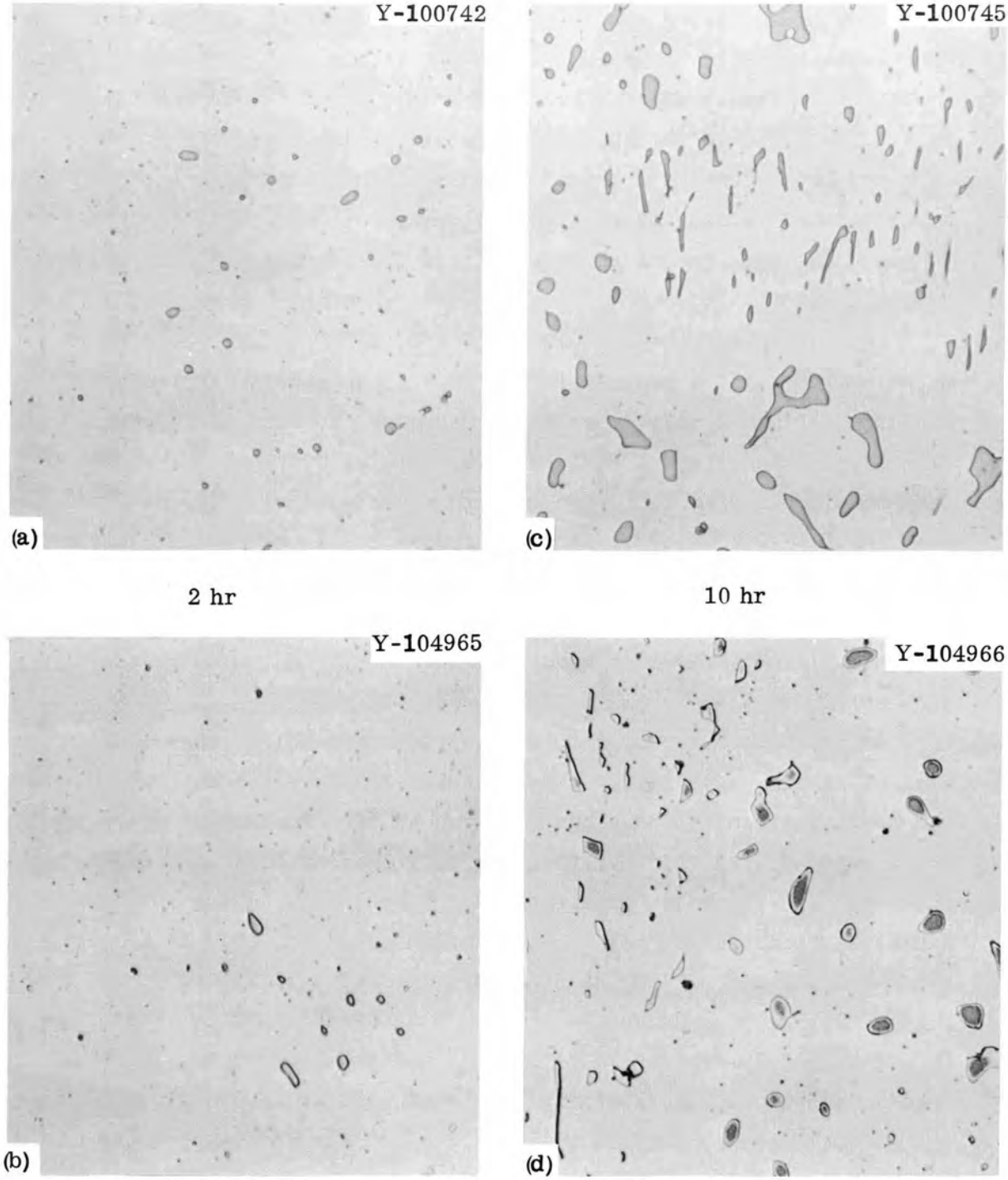

Fig. 5.2. Austenitic Stainless Steel Welds Heat Treated 2 and 10 hr at 1065°C (1950°F). (a) and (b) Shielded metal-arc welds. (c) and (d) submerged-arc welds made with high energy input. Murakami etchant. 500×.

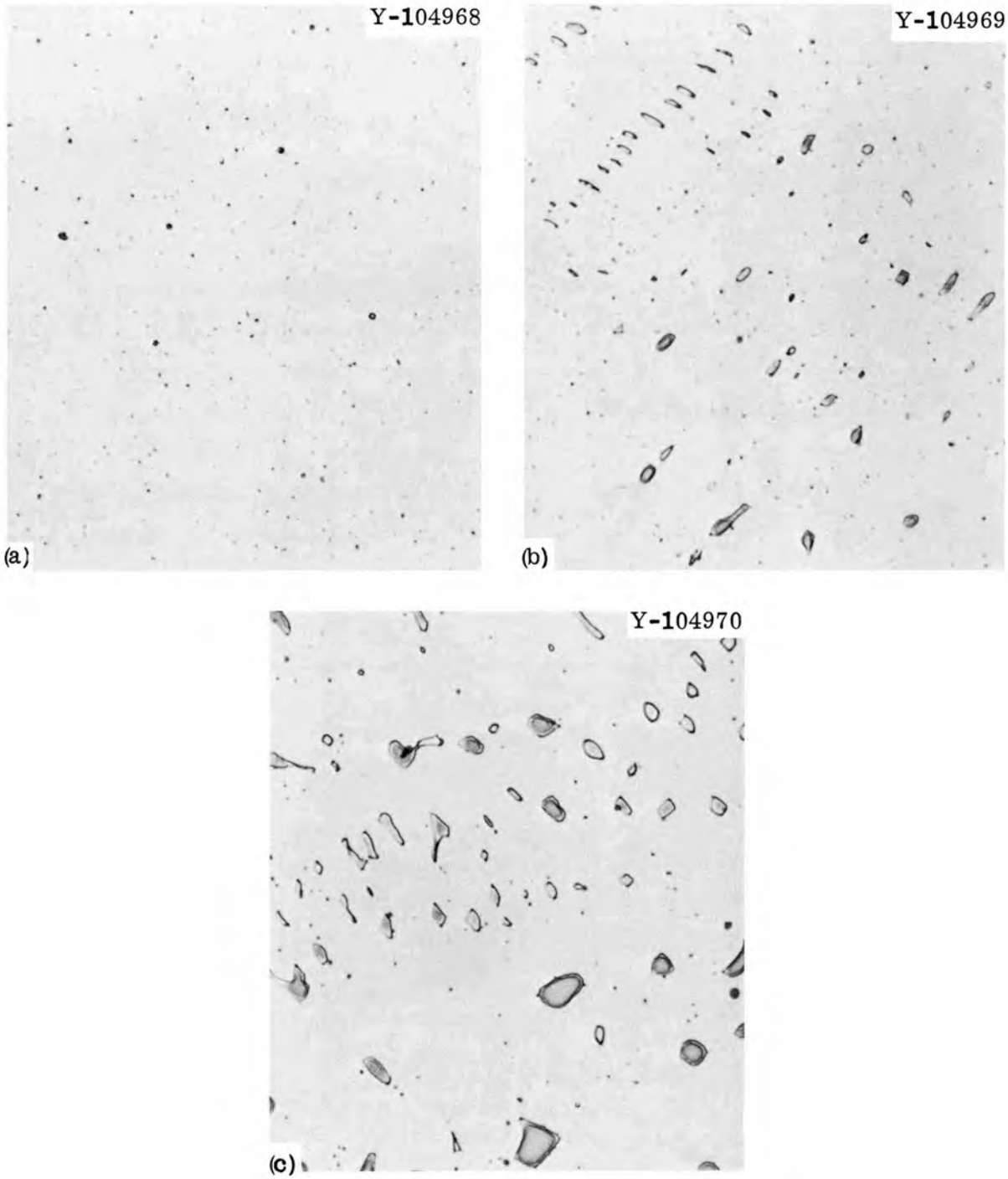

Fig. 5.3. Austenitic Stainless Steel Welds Heat Treated 2 hr at 1090°C (2175°F). (a) Shielded metal-arc weld. (b) Submerged-arc weld made with medium heat input. (c) Submerged-arc weld made with high heat input. Murakami etchant. 500×.

We are now studying the amount of σ phase that formed in these aged specimens. It appears that σ phase formed from ferrite in very large amounts.

Corrosion Studies (G. M. Goodwin, Nancy C. Cole)

We began destructive metallographic examination of the specimens for the Strauss test described[7] previously. Based upon these test results, the second series of specimens, 15 through 56, were machined, heat treated as shown in Table 5.4, and made ready for shipment to Combustion Engineering, Inc.

Table 5.4. Summary of Heat Treatment of Specimens for Strauss Test

Strauss Test Number	Weld Number	Heat Treatment
15	F17	
16	F18	(1) As welded
17	F01	
18	F21	
19	SA8	
20	F17	(2) 100 hr at 650°C (1200°F), cooled at 55°C/hr (100°F/hr) to 455°C (850°F), water quenched
21	F18	
22	F21	
23	F17	(3) 2 hr at 1065°C (1950°F), cooled at 85°C/hr (150°F/hr) to 800°C (1470°F), held 10 hr, cooled at 220°C/hr (400°F/hr) to 455°C (850°F), water quenched
24	F18	
25	F21	
26	SA8	
27	F17	(4) 2 hr at 1065°C (1950°F), cooled at 85°C/hr (150°F/hr) to 800°C (1470°F), held 10 hr, cooled at 220°C/hr (400°F/hr) to 455°C (850°F), water quenched, 100 hr at 650°C (1200°F), cooled at 55°C/hr (100°F/hr) to 455°C (850°F), water quenched
28	F18	
29	F01	
30	F21	
31	SA8	
32	F17	(5) 2 hr at 1065°C (1950°F), cooled at 85°C/hr (150°F/hr) to 800°C (1470°F), held 10 hr, cooled at 55°C/hr (100°F/hr) to 455°C (850°F), water quenched
33	F18	
34	SA8	

Table 5.4. (Continued)

Strauss Test Number	Weld Number	Heat Treatment
35	F17	(6) 2 hr at 1065°C (1950°F), cooled at 85°C/hr (150°F/hr) to 800°C (1470°F), held 10 hr, cooled at 85°C/hr (150°F/hr) to 455°C (850°F), water quenched, 100 hr at 650°C (1200°F), cooled at 55°C/hr (100°F/hr) to 455°C (850°F), water quenched
36	F18	
37	F01	
38	SA8	
39	F17	(7) 2 hr at 955°C (1750°F), cooled at 85°C/hr (150°F/hr) to 800°C (1470°F), held 10 hr, cooled at 220°C/hr (400°F/hr) to 455°C (850°F), water quenched
40	F18	
41	F01	
42	F21	
43	SA8	
44	F17	(8) 2 hr at 955°C (1750°F), cooled at 85°C/hr (150°F/hr) to 800°C (1470°F), held 10 hr, cooled at 220°C/hr (400°F/hr) to 455°C (850°F), water quenched, 100 hr at 650°C (1200°F), cooled at 55°C/hr (100°F/hr) to 455°C (850°F), water quenched
45	F18	
46	F01	
47	F21	
48	SA8	
49	F17	(9) 2 hr at 955°C (1750°F), cooled at 85°C/hr (100°F/hr) to 800°C (1470°F), held 10 hr, cooled at 55°C/hr (100°F/hr) to 455°C (850°F), water quenched
50	F18	
51	F01	
52	SA8	
53	F17	(10) 2 hr at 955°C (1750°F), cooled at 85°C/hr (150°F/hr) to 800°C (1470°F), held 10 hr, cooled at 55°C/hr (100°F/hr) to 455°C (850°F), water quenched, 100 hr at 650°C (1200°F), cooled at 55°C/hr (100°F/hr) to 455°C (850°F), water quenched
54	F18	
55	F01	
56	SA8	

Notes

1. R. G. Berggren and G. M. Goodwin, Fuels and Materials Development Program Quart. Progr. Rept. Sept. 30, 1970, ORNL-4630, pp. 111–115.

2. N. C. Binkley, Fuels and Materials Development Program Quart. Progr. Rept. Sept. 30, 1970, ORNL-4630, pp. 115–116.

3. Plant and Equipment Division.

4. D. R. Frizzell and G. M. Goodwin, Fuels and Materials Development Program Quart. Progr. Rept. Sept. 30, 1970, ORNL-4630, p. 116.

5. G. M. Goodwin and R. G. Berggren, Fuels and Materials Development Program Quart. Progr. Rept. Sept. 30, 1970, ORNL-4630, pp. 121–122.

6. Nancy C. Cole, G. M. Goodwin, and T. M. Kegley, Fuels and Materials Development Program Quart. Progr. Rept. Sept. 30, 1970, ORNL-4630, pp. 123–135.

7. G. M. Goodwin and Nancy C. Cole, Fuels and Materials Development Program Quart. Progr. Rept. Sept. 30, 1970, ORNL-4630, pp. 135–137.

6. PROPERTIES OF FERRITIC STEEL WELDS

J. R. Weir, Jr. G. M. Slaughter

The use of ferritic steels for tubing, piping, and headers in high-integrity steam generators requires that their overall weldability and the mechanical properties of weld metal and heat-affected zone at elevated temperatures (290 to 595°C) be assessed. The susceptibility of both the weld metal and the heat-affected zones to cracking is of particular interest.

This program deals with four classes of ferritic steel that are candidates for use in either liquid-metal-cooled or water-cooled reactors. The purpose of the program is to compare the weldabilities of these various steels and to determine the advantages and limitations of each. We emphasize determining susceptibility to cracking associated with the weld and the effects of welding on mechanical properties at the expected service temperatures.

Plain Carbon Steels

Preparation of Specimens (D. A. Canonico, N. C. Binkley)

We are conducting tests on C steel material that was received too late in the last fiscal year to permit adequate testing at that time.

The Lehigh restraint specimens, described previously,[1] were welded. These specimens contained variations in their degree of restraint from essentially zero to a fully restrained condition. Although we anticipate no sensitivity to underbead cracking, we are evaluating this tendency. We shall also determine the effect of restraint on the impact properties of weldments in this class of steel. This property will be assessed at both conventional testing temperatures and at their suggested service temperatures.

Conventional 2.25% Cr–1% Mo Low-Alloy Steel

Preparation of Specimens (D. A. Canonico, N. C. Binkley)

The Lehigh restraint specimens prepared from this grade of steel were welded at two different levels of preheat. The degree of restraint during welding varied from zero to fully restrained. These welds are being evaluated to determine their tendencies to cracking.

Low-Carbon Low-Alloy Steels

Literature Search and Information Gathering (D. A. Canonico, N. C. Binkley)

The literature search for information pertaining to this grade of steel is well under way and should be completed soon.

Procurement of Material and Preparation of Specimens (D. A. Canonico, N. C. Binkley)

We have on hand limited quantities of low-C plate and tubing. Three 1-in.-thick forged slabs of C 2 1/4% Cr–1% Mo steel with different C contents were rolled to 1/2-in.-thick plate. The amount of material available for study is as follows:

0.0031% C – 1/2 × 10 × 6 in.
0.035% C – 1/2 × 18 × 9 in.
0.11% C – 1/2 × 24 × 12 in.

Some material from the 1/2-in.-thick plates was removed and swaged to 0.125-in.-diam rod for use as filler metal in welding these plates under fully restrained conditions.

The tubing is being machined to provide specimens for our welding study.

Stabilized Low-Alloy Steels

Literature Search (D. A. Canonico, N. C. Binkley)

The literature search for the stabilized low-alloy steels was completed and is being reviewed internally. It will be published in the near future.

Procurement of Material (D. A. Canonico, N. C. Binkley)

Only a limited amount of material has been available for use in this program, but this problem should be alleviated shortly. Two commercial sources were located, and material was ordered. Delivery is imminent from Sandvik Steel, Inc., of two heats (total weight about 265 lb) of stabilized low-alloy steel with ratios of C:Nb of 0.08:1.08 and 0.08:0.91.

Tubing, plate, and forgings were ordered from the second commercial source, and we anticipate early delivery.

Preparation and Testing of Specimens (D. A. Canonico, N. C. Binkley)

We welded 6-in. lengths of Sandvik HT 8×6 (Nb-stabilized 2.25% Cr–1% Mo–0.5% Ni) steel tubing by the gas tungsten-arc process. The joint design consisted of a 90° included angle, a root face of 0.040 in. (about 1/2 of the 0.079-in.-thick wall) and root-face opening of 1/8 in. The weld was made with a single pass at a current of 60 A. The composition of the filler metal (Böhler SCM 2-IG) was similar to that of the tubing. Our analysis of the tubing and the nominal vendor's analysis of the filler metal are given in Table 6.1. Figure 6.1 is a photograph of a section of a sample as welded. No cracks or porosity are evident. Figure 6.2 contains photomicrographs of the heat-affected zone of representative welds. These photomicrographs show the presence of a eutectic in the heat-affected zone. Additional tubular welds are being prepared for tensile and burst tests at room temperature and 595°C.

We began an extensive metallographic and electron-beam microprobe study of the TIGAMAJIG specimens previously reported.[2] Our previous report noted that the TIGAMAJIG specimens, as welded, were free from visually detectable weld-associated cracks. These specimens were 1/4-in. thick, and the base metal was prepared by rolling to the desired thickness

Table 6.1. Identification and Vendor's Analysis of Material Employed in Welding Studies[a]

Material Identification	Diameter, in.		Chemical Composition, wt %					
	Outside	Inside	C	Mn	Cr	Ni	Mo	Nb
Sandvik HT 8×6								
Seamless Tubing	0.785	0.079	0.08	0.46	2.18	0.54	0.94	1.08
Bar	1.0		0.09	0.50	2.18	0.56	0.97	0.91
Gebr. Böhler SCM-2-IG	3/32		< 0.06	0.6	2.3		1.0	Present

[a]Additional analyses being conducted at ORNL.

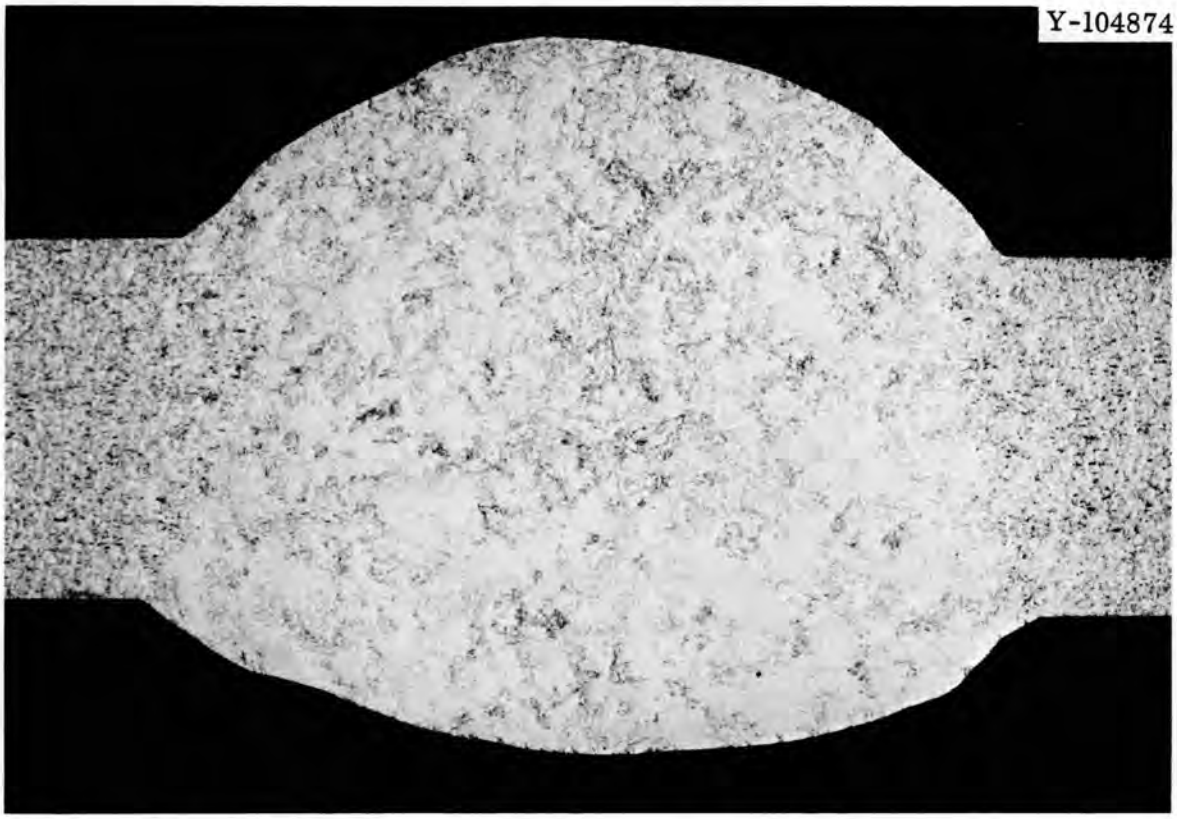

Fig. 6.1. Weld in Sandvik HT 8×6 Steel Tubing. No cracking or porosity is evident.

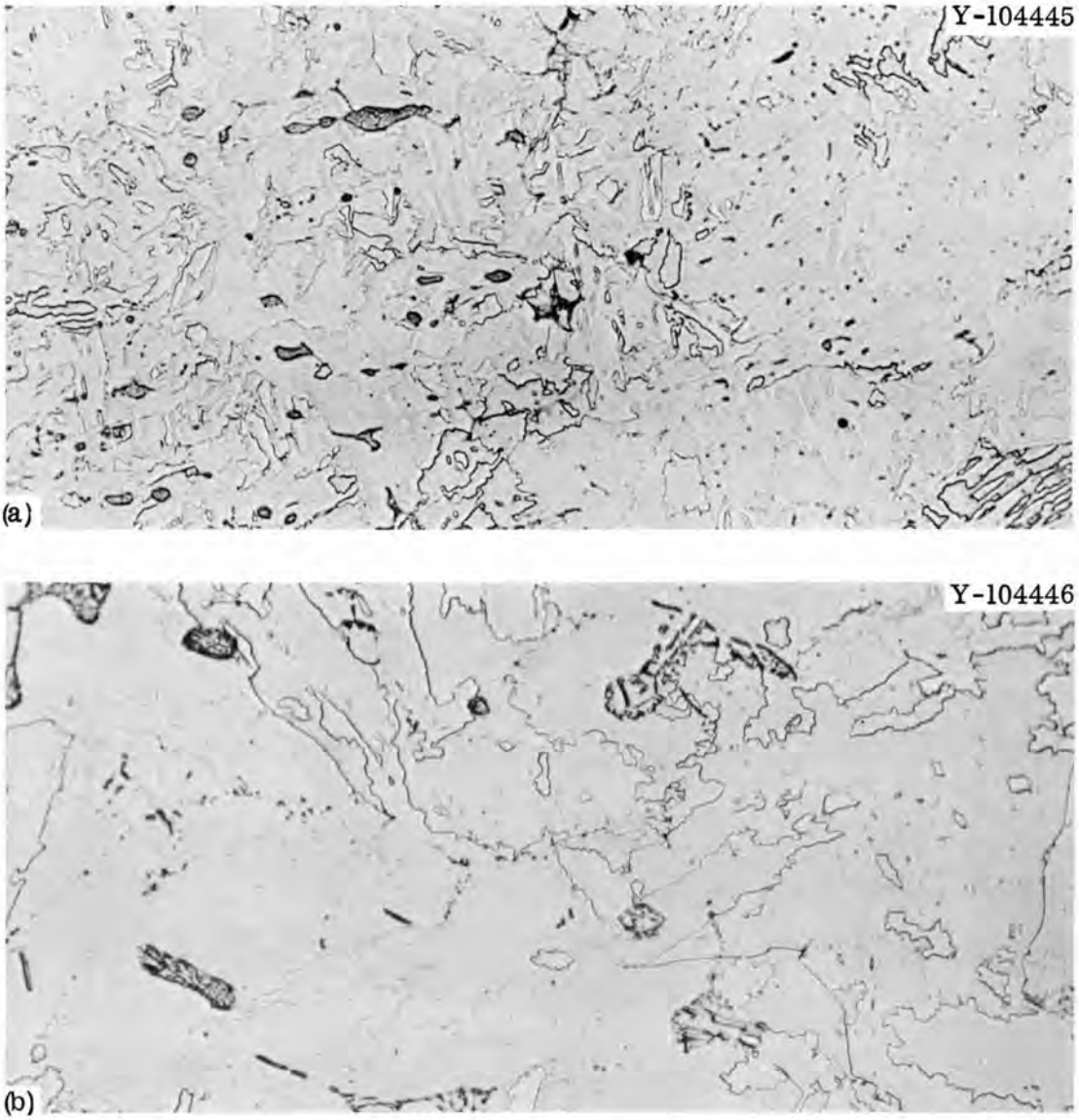

Fig. 6.2. Photomicrographs of the Heat-Affected Zone of Tubular Weldments. The eutectic patches are associated with the carbides. (a) 250×, (b) 1000×.

from the 1-in.-diam Sandvik HT 8×6 bar stock. The analysis of the bar stock is given in Table 6.1. The TIGAMAJIG investigation included welds made with both high and low heat input. We sectioned and polished the specimens and found that they both contained cracks. The degree of sensitivity to cracking apparently was dependent on the heat input; the weld samples made at the higher heat input contained the largest cracks. Figure 6.3 contains photomicrographs of the polished surfaces of the

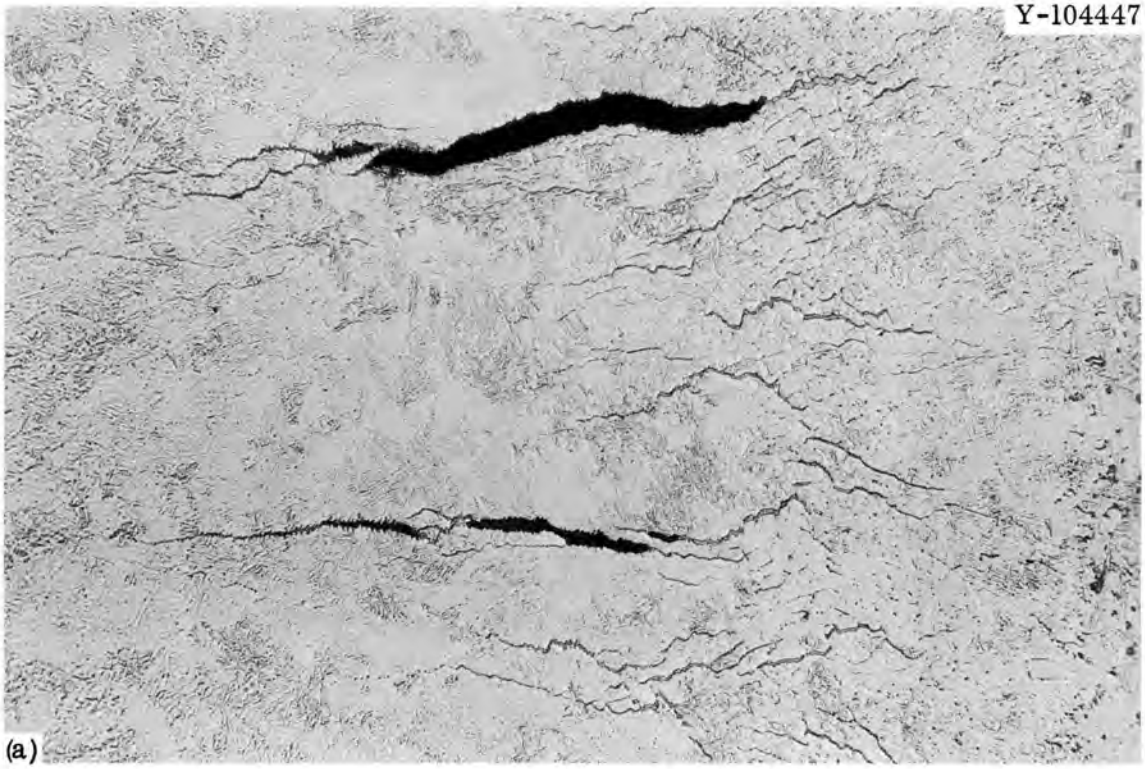

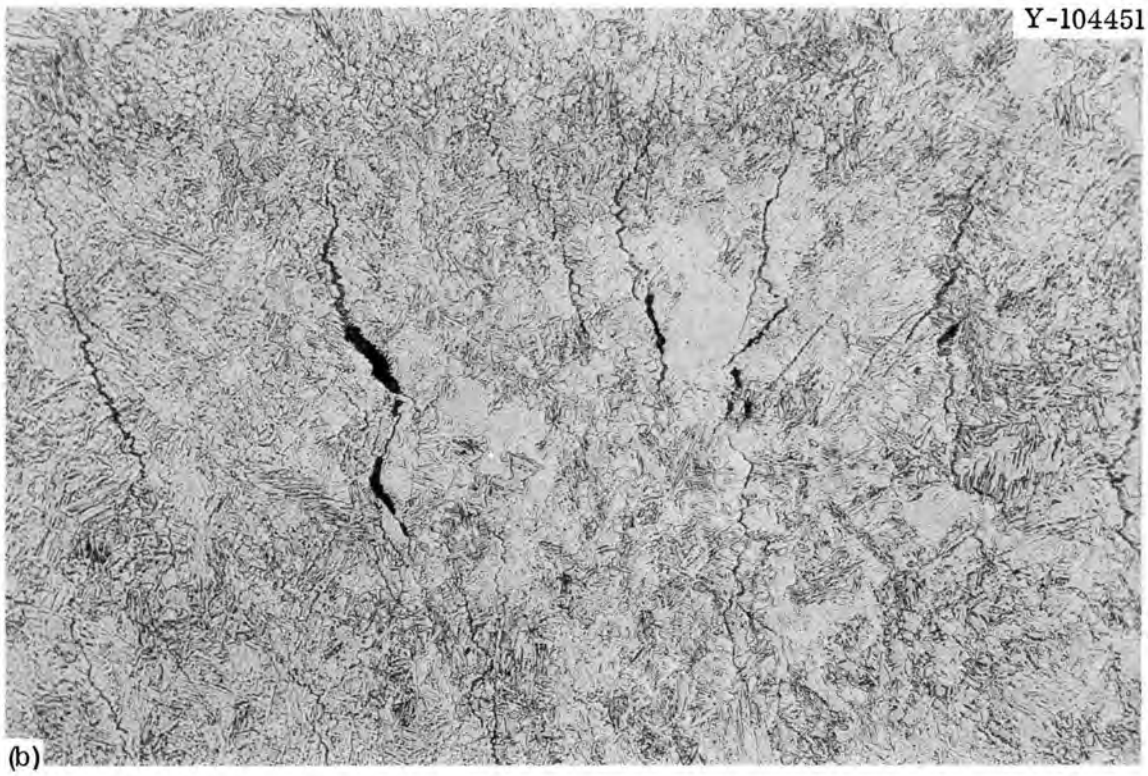

Fig. 6.3. Polished Surfaces of TIGAMAJIG Specimens. (a) Weld made at high heat input. (b) Weld made at low heat input. 100×.

TIGAMAJIG specimens. The cracks are located in the region of the heat-affected zone that experienced high strain. Both specimens contained evidence that the cracks were backfilled. This backfilling phenomenon probably explains our previous observation that there were no cracks.[2] The backfilled cracks shown in Fig. 6.3(a) are shown at higher magnification in Fig. 6.4. Figure 6.5 shows a network outlining the austenite grains in the heat-affected zone of the weld made with low heat input [Fig. 6.3(b)]. This provides evidence that a liquid phase occurred at temperatures somewhat below the melting point of the steel matrix.

The microstructures of weldments in the stabilized low-alloy steel were analyzed by electron-beam microprobe. We previously reported[2] the results of our analysis of the precipitates in the microstructure of the base metal, which we found to be rich in Nb. Figure 6.6 contains the results of the microprobe study. The only metallic element detected in the precipitate was Nb.

The microstructures shown in Figs. 6.2, 6.4, and 6.5 were also analyzed by electron beam microprobe. Figure 6.7 contains the results of this study. Figure 6.7(a) contains the scanning images of the Nb-rich eutectic structure shown in Fig. 6.2. Figure 6.7(b) and (c) shows further evidence of the presence of the Nb-rich phase. The backfilling of the cracks [Fig. 6.7(b)] proves that the phase was liquid at temperatures below the melting point of the surrounding steel matrix. The network shown in Fig. 6.5 was also rich in Nb and probably was also liquid at the welding temperature.

A semiquantitative analysis of the network shown in Figs. 6.5 and 6.7(c) is shown below:

	Content, wt %	
	Fe	Nb
Matrix	95.9	0.7
Grain boundary	86.6	8.2

These evidences of the presence of a Nb-rich liquid phase at elevated temperatures are supported by the Fe-Nb equilibrium diagram.[3] A eutectic occurs between Fe_2Nb and δ-phase Fe at 1370°C. This temperature

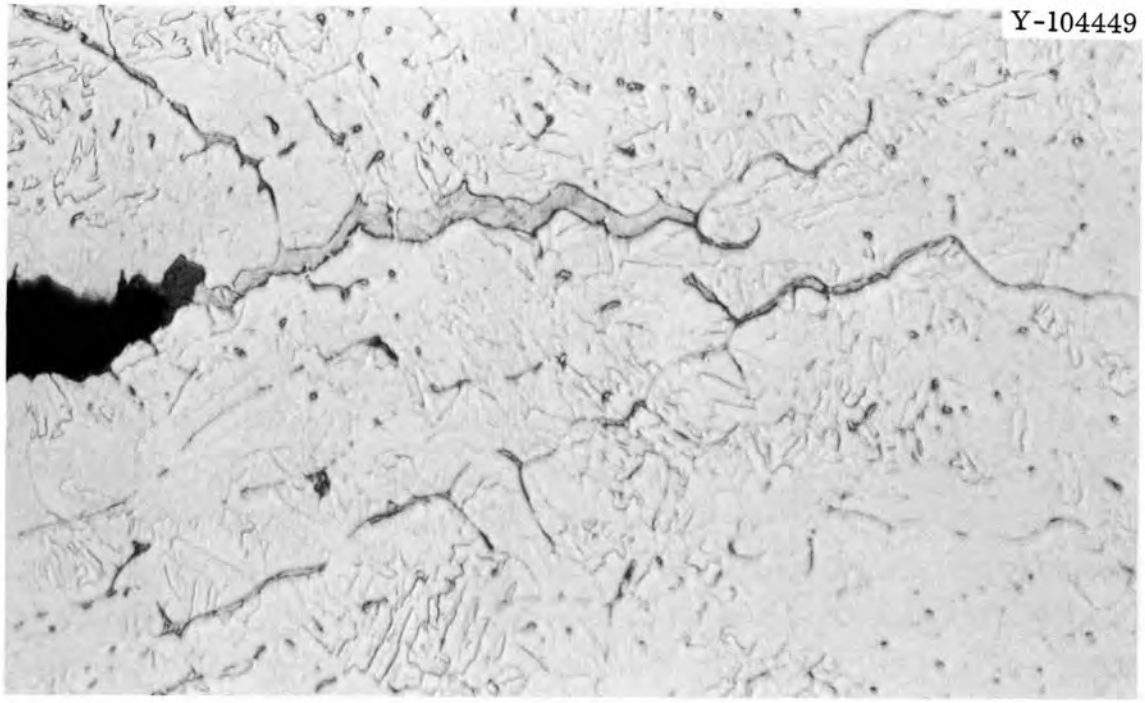

Fig. 6.4. Backfilled Crack Tip. 500×.

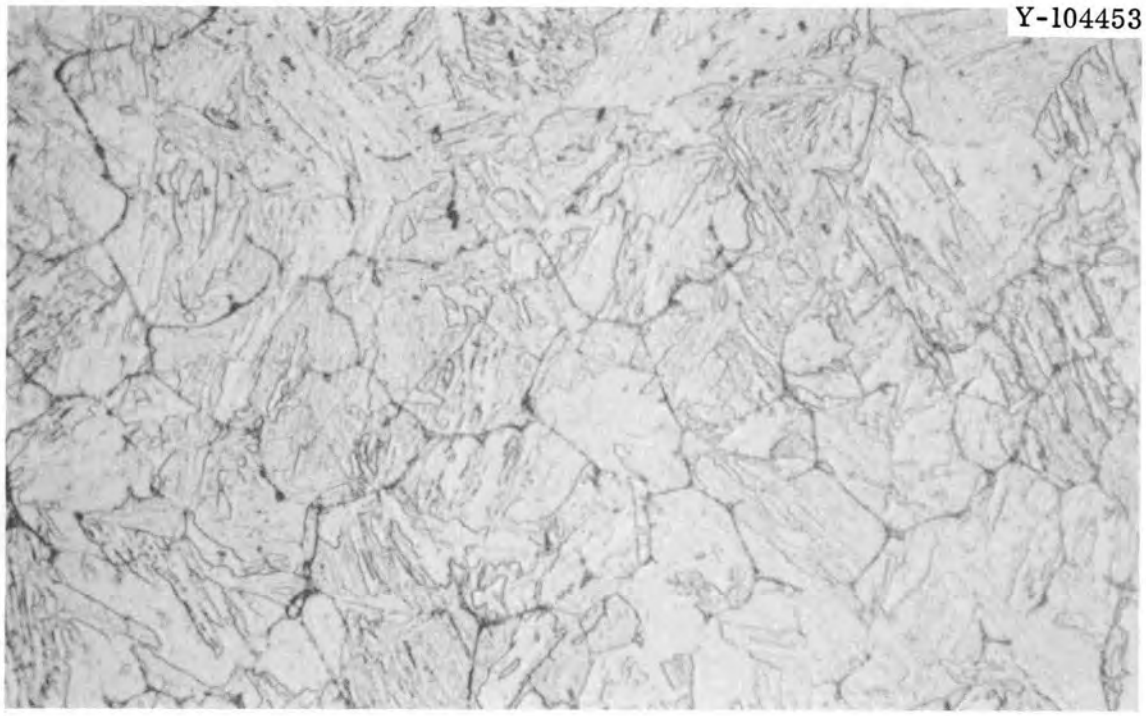

Fig. 6.5. Heat-Affected Zone in TIGAMAJIG Weld made at Low Heat Input. Note the network outlining the austenite grains. This phase resembles that observed in the backfilled cracks. 1000×.

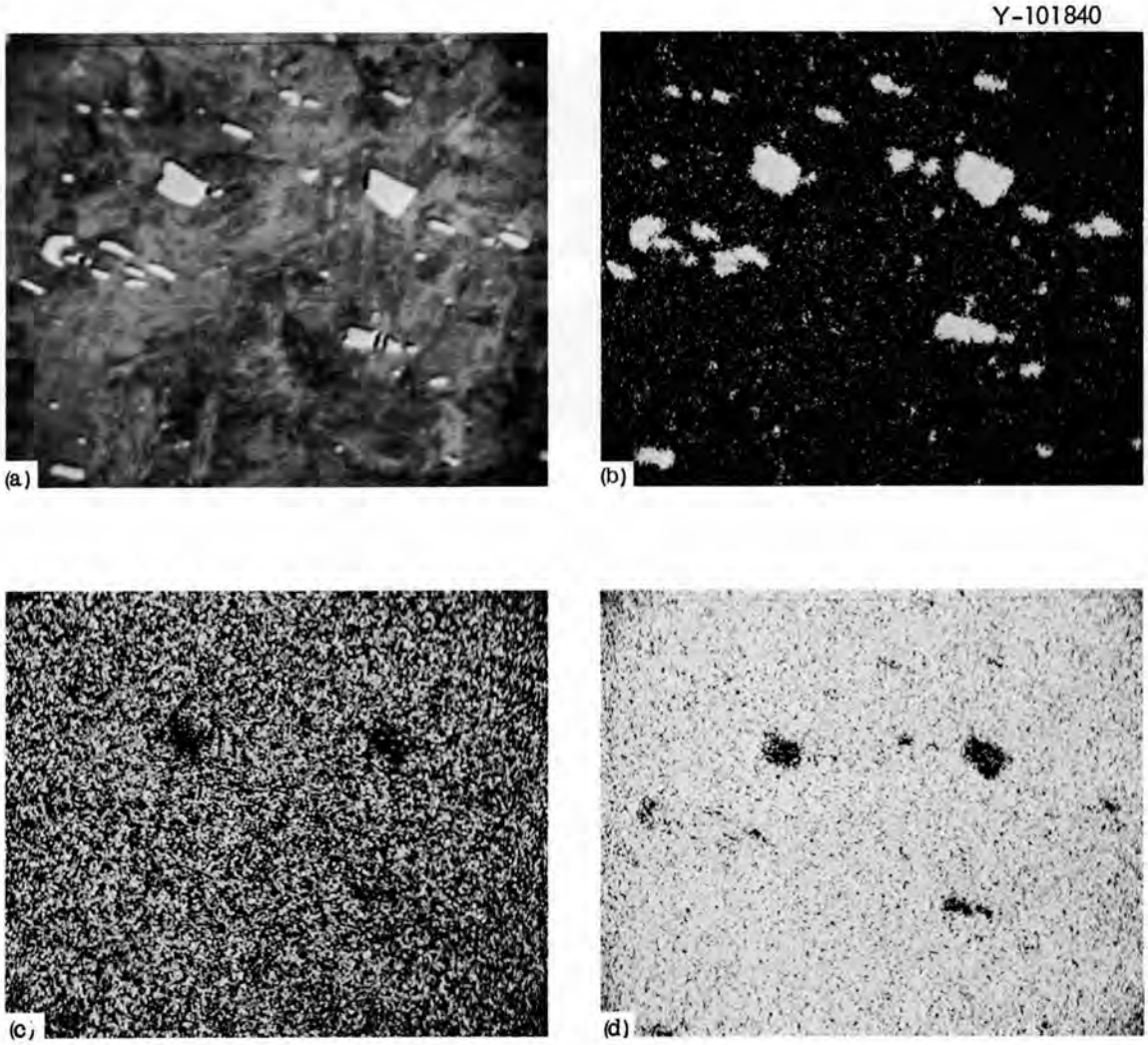

Fig. 6.6. Electron-Beam Scanning Images of Stabilized Low-Alloy Steel Base Metal. The precipitates were shown to have a near stoichiometrical fit with NbC. (a) Backscatter, (b) NbLα, (c) CrKα, and (d) FeKα.

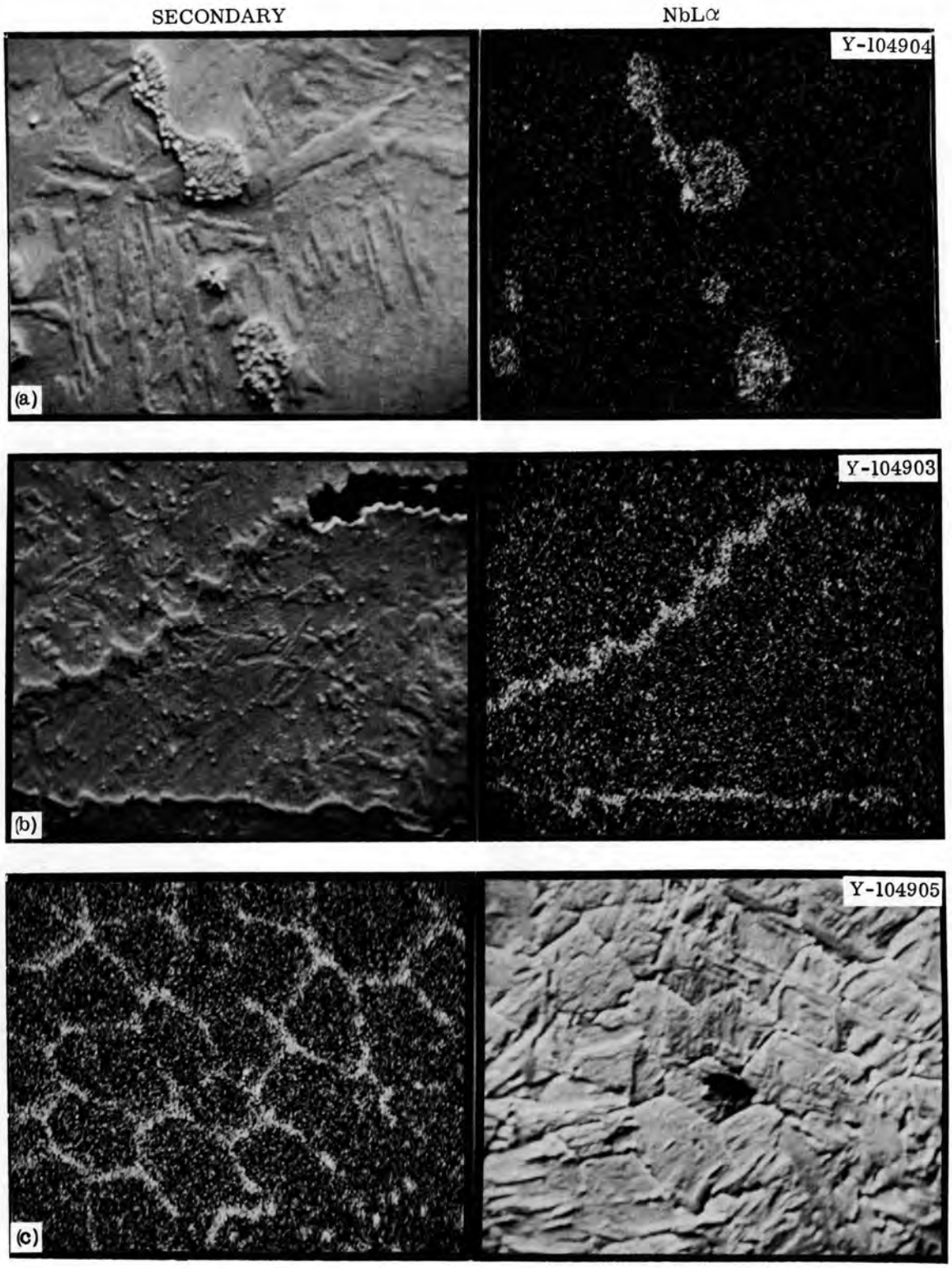

Fig. 6.7. Results of the Electron-Beam Microprobe Analysis of the Microstructures Observed in Weldments in Stabilized Low-Alloy Steel. (a) Area shown in Fig. 6.2, (b) area shown in Fig. 6.4, and (c) area shown in Fig. 6.5.

corresponds to that at which we observed complete melting of specimens in the previously reported tests made with the Duffer's Gleeble.[2]

Our present hypothesis is that the NbC precipitate decomposes at elevated temperatures. The diffusivity of the C is sufficiently high at these temperatures to permit it to diffuse into the austenite to the extent that it is distributed to levels below its solubility limit. This is confirmed by a calculation suggested by Shewmon[4] that provides a root-mean-square distance for penetration of the C into the steel matrix. The value determined for the penetration from conservative values for time and diffusion coefficients is between 0.001 and 0.005 in. The eutectic patches shown in Fig. 6.2 are less than 0.001-in. wide. The diffusion of the C results in an area enriched in Nb, which can then combine with the Fe to provide the Fe_2Nb.

This is the first real evidence that we have seen that can explain the poor weldability occasionally attributed to the stabilized low-alloy steels. It is possible that, if the Nb and C are not correctly balanced, the presence of excessive quantities of a phase that melts at low temperature could lead to cracking in the heat-affected zones under conditions of low to moderate restraint. This could occur in the base metal, but the heterogeneous mode of solidification of weld metal would, indeed, tend to exaggerate this phenomenon, particularly in multipass welds in which the previous passes become the subsequent heat-affected zone.

Notes

1. N. C. Binkley and D. A. Canonico, Fuels and Materials Development Program Quart. Progr. Rept. June 30, 1970, ORNL-4600, p. 147.

2. N. C. Binkley and D. A. Canonico, Fuels and Materials Development Program Quart. Progr. Rept. Sept. 30, 1970, ORNL-4630, pp. 141–143.

3. R. P. Elliot, Constitution of Binary Alloys, First Supplement, McGraw-Hill Book Co., New York, 1965.

4. P. G. Shewmon, Diffusion in Solids, p. 43, McGraw-Hill Book Co., New York, 1963.

7. NONDESTRUCTIVE TESTING TECHNIQUES FOR LMFBR

W. O. Harms R. W. McClung

We are developing new methods, techniques, and equipment for nondestructively evaluating materials or components related to LMFBR's. Among the methods being studied are electromagnetic induction, ultrasonics, and penetrating radiation. Special emphasis is being given to developing techniques for measuring the degree of cold work in stainless steel tubing with a small diameter.

Development of Advanced Techniques

Development of Eddy-Current Instrument (C. V. Dodd)

We are continuing the development of an eddy-current instrument to measure both the size of defects and their depth beneath the surface. We assembled the standard inductor, the standard capacitor, and the standard resistor into a phase-shifting network. The instrument drifted more than the allowable 0.02°, possibly because of amplifier noise. We are constructing a tuned 1-KHz amplifier to reduce this drift.

We started work on a module that consists of a dual-frequency oscillator and power amplifier for use in the instrument. This module will enable us to measure simultaneously two parameters (e.g., conductivity and thickness).

Ultrasonic Schlieren Techniques for Evaluation of Welds (H. L. Whaley, K. V. Cook)

Optical techniques for visualizing ultrasound have proved useful in allowing us to gain an understanding of interactions that are difficult to analyze by conventional ultrasonic methods. We are using a folded-mirror schlieren system with provisions for either continuous or pulsed operation, a 6-in.-diam working area, and a television display. We recently added a video tape recorder to eliminate the obvious problem of efficient preservation of data with such a system.

We are using the schlieren technique in conjunction with two techniques for inspecting welds by ultrasonics to study the response of ultrasound to various types of defects in welds in samples of 1-in.-thick butt-welded plates of Al and stainless steel. The welded samples contain intentional defects such as porosity, inclusions, incomplete fusion, and incomplete penetration. We are now inspecting the stainless steel welds by the Delta technique.[1] Figure 7.1 is a plan-view recording that shows the results of a Delta inspection of one of the welds in Al. This sample was intentionally welded with incomplete fusion at various points in the weld metal. Many such areas are clearly shown along with two reference holes drilled about half way through the plate from the back surface. It is characteristic of the Delta technique that the shape of the discontinuity may be quite different from the indication obtained in the recording. In many cases, multiple indications will be obtained for a given flaw. The advantage of the technique lies in its relative insensitivity to the orientation of the flaw within the material.

We also continued to determine operating characteristics of the prototype of the multiple-sensor transducer. One problem that has been encountered is the presence of interfering signals caused by spreading

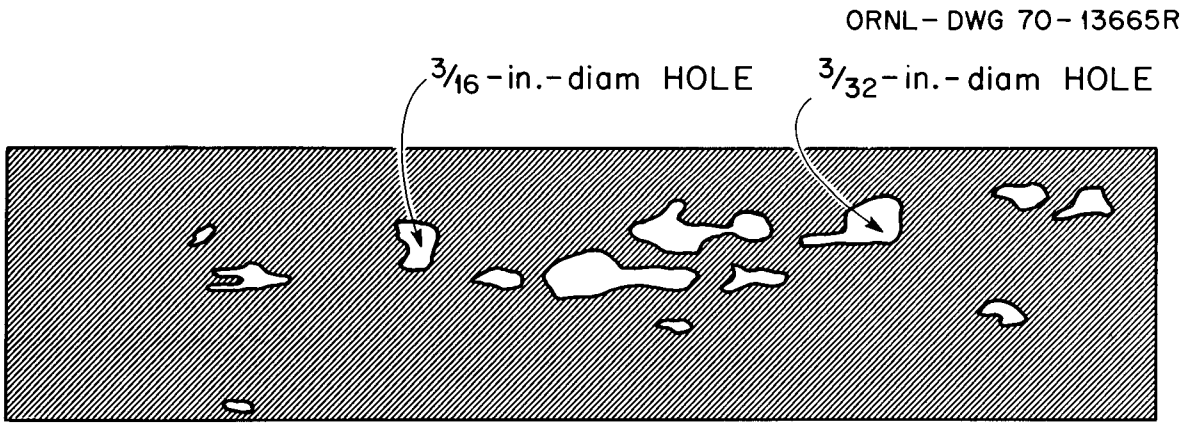

Fig. 7.1. Delta Scan of Weld Area in Sample with Incomplete Fusion.

of the beam from the source. We are also investigating the possibilities of using a Bragg diffraction system for actually imaging flaws in welds. Since the optics for Bragg diffraction are quite similar to those of schlieren, minor modifications may allow us to use our visualization system in a dual capacity to increase its usefulness.

Measurement of Cold Work in Stainless Steel Tubing

Instrument Development (C. V. Dodd, W. A. Simpson)

We are investigating methods for nondestructively measuring the degree of cold work in stainless steel tubing that has a small diameter. We emphasize the use of electromagnetic induction for detecting the changes in magnetic permeability produced by cold work.

We improved the stability of the amplifier and constructed the amplifier, the bridge, and the rectifiers and filters as separate plug-in modules for our low-frequency eddy-current instrument. We are using the instrument to measure the permeability variation in 0.300-in.-OD rods of FFTF material produced at Argonne National Laboratory. Since the outside diameter of the rods was much larger than that of the tubes we had previously checked,[2] we had to design and wind new coils. Although we have not carefully measured all the rods, preliminary measurements indicate that the change in permeability for a given amount of cold reduction is less for the rods than for the tubes.

The series resistance in the coils contributes much of the error to the measurement of the permeability. If this error were considerably reduced, it would then become worthwhile to reduce the smaller errors due to conductivity and wall thickness. We are programming a new configuration of coil that uses two separate driver and detector coils that will eliminate these problems. If our computer studies show that the new configuration will improve the accuracy of the measurements, we shall construct and test the appropriate coils.

Notes

1. H. L. Whaley and K. V. Cook, Fuels and Materials Development Program Quart. Progr. Rept. June 30, 1970, ORNL-4600, pp. 153–155.

2. C. V. Dodd and W. A. Simpson, Fuels and Materials Development Program Quart. Progr. Rept. Sept. 30, 1970, ORNL-4630, pp. 146–149.

8. SODIUM CORROSION STUDIES

W. O. Harms J. H. DeVan

The purpose of this program is to investigate the chemical and metallurgical effects produced in refractory metals during exposure to molten Na. Of principal interest are the corrosion properties of V-base alloys, which have been under development as cladding materials for high-temperature fuels for LMFBR systems.

Comparative Corrosion Tests on Refractory Alloys

J. H. DeVan

Since refractory alloys strongly resist dissolution by Na, they have promise as advanced materials for cladding and control rods for Na-cooled reactor systems. However, the interactions of refractory alloys with impurities in Na must be understood before the feasibility of using these alloys for cladding can be decided. Accordingly, our studies of the compatibility of refractory metals with Na are aimed at effects associated with O supplied by the Na and with C and N supplied by stainless steel.

Effect of Oxygen on the Compatibility of Vanadium and Vanadium Alloys with Sodium (R. L. Klueh)

We previously reported[1–3] the distribution of O in V alloy specimens exposed for 100, 200, 300, and 600 hr at 600°C to static Na that contained 2000 ppm O. The alloys tested were V–5% Cr, V–10% Cr, V–15% Cr–5% Ti, V–1.3% Zr, V–5% Zr, V–20% Mo, Vanstar 7, Vanstar 8, and Vanstar 9.

We recently compared the microhardness profiles of these specimens, and the results corroborate the conclusions on the distribution of O that we previously drew from data for weight change, O analyses,[1,2] and metallography.[3] Table 8.1 shows the microhardness profiles for representative alloys before test (annealed 1 hr at 900°C) and after 100 and 600 hr exposures to Na that contained 2000 ppm O. Hardness changes provide a qualitative measure of O uptake when O is in solid

Table 8.1. Hardness Profiles for the Vanadium and Vanadium Alloys Exposed to Sodium that Contained 2000 ppm O at 600°C

Distance From Edge (μm)	Knoop Hardness Number (at 50-g load)		
	Before Test	After 100 hr	After 600 hr
		Vanadium	
20	60	425	250
80	60	350	275
200	50	250	250
300	50	120	240
400		100	240
		V–5% Cr	
20	100	375	210
80	100	205	230
200	110	190	230
300	110	145	240
400		125	240
		V–15% Cr	
20	215	355	310
80	190	340	320
200	215	327	285
300	215	270	285
400		225	285
		V–20% Ti	
20		720	1195
50	285	242	620
100	285	242	235
200	287	242	235
300	290	242	235
500			
		V–5% Zr	
20			
50	130	326	392
100	130	137	341
200	130	120	107
300	130	117	107
500		117	107

solution (V-Cr alloys and V–20% Mo) and also for alloys in which O is precipitated (V-Zr and V-Ti alloys). In the case of the V-Cr alloys and V-20% Mo, a hardness gradient is evident after exposure to Na for 100 hr but not after 600 hr; the disappearance of the hardness gradient shows that the specimens had essentially equilibrated with O after 600 hr.

For alloys that contained Zr or Ti, oxidation occurred at a slowly moving precipitation front (internal oxidation), and there was an abrupt change in hardness between the zone of internal oxidation and the unaffected alloy matrix. This change in hardness was apparent even after 600 hr.

We previously discussed[3] a technique for determining the effect of Cr and Mo on the solubility and diffusion coefficient of O in V. We have now doped specimens of V, V–5% Cr, V–10% Cr, V–15% Cr, and V–20% Mo and exposed specimens of each alloy with a V specimen in a type 304L stainless steel capsule as follows: V alloy–0.5% O with V undoped; V alloy undoped with V–0.5% O; and V alloy–0.5% O with V–0.5% O. Each pair of specimens was exposed for 250 and 1000 hr at 600°C; the specimens are being analyzed for changes in O concentration.

Oxidation of Vanadium and Vanadium Alloys (R. L. Klueh)

Corrosion studies of V and V alloys in Na indicate that oxidation effects closely parallel those produced by exposure of these alloys to gaseous O_2 at relatively low chemical activity.[4] We are, therefore, supplementing our corrosion tests in Na with tests of V alloys in O_2 at relatively low pressures. These tests will be used to determine the effects of various alloying components on oxidation kinetics and to evaluate oxidation products formed in and on the various alloys.

The test system consists of a semi-micro recording balance positioned over a furnace tube that contains a sheet specimen of V alloy. The system is maintained under vacuum, and the partial pressure of O_2 in the system is controlled by a variable leak valve. The system has been assembled, tested, and used to oxidize the V and V alloy specimens for the tests described above.

Early studies of the corrosion of V–20% Ti in Na revealed what investigators described as a "hardened zone" immediately below the surface. We showed[4] that the kinetics of penetration of the "hardened zone" followed those predicted for movement of O into the alloy when TiO_2 is precipitated in place. Because of the low diffusivity of Ti at the oxidation temperature (about 650°C), the precipitates were very finely

divided and, thus, could not easily be resolved by metallographic examination.

To verify this, we oxidized V–20% Ti specimens for various times at 1000°C at a pressure of 5×10^{-5} torr O_2, after which we sectioned the specimens and examined them metallographically. Figure 8.1 shows a specimen oxidized for 2 hr. Below the exposed surface was a precipitation front or "hardened zone" similar to that reported at 650°C, except that the precipitates appeared much coarser at 1000°C. After longer anneals, the depth of precipitation increased; also, as shown in Figs. 8.2 and 8.3 for specimens oxidized 4 and 7 hr, respectively, a second zone of different etching characteristics formed at the surface of the specimen and moved inward behind the internal oxidation front.

Figure 8.4 shows a specimen oxidized for 400 hr at 600°C; two zones are again evident. This microstructure is identical to that observed by Levin and Greenberg[5] in V–10% Ti exposed to Zr-gettered Na at 650°C. Measurements of Knoop microhardness (at a 50-g load), superimposed on

Fig. 8.1. Microstructure of V–20% Ti Oxidized 2 hr at 1000°C and 5×10^{-4} torr O_2. 500×.

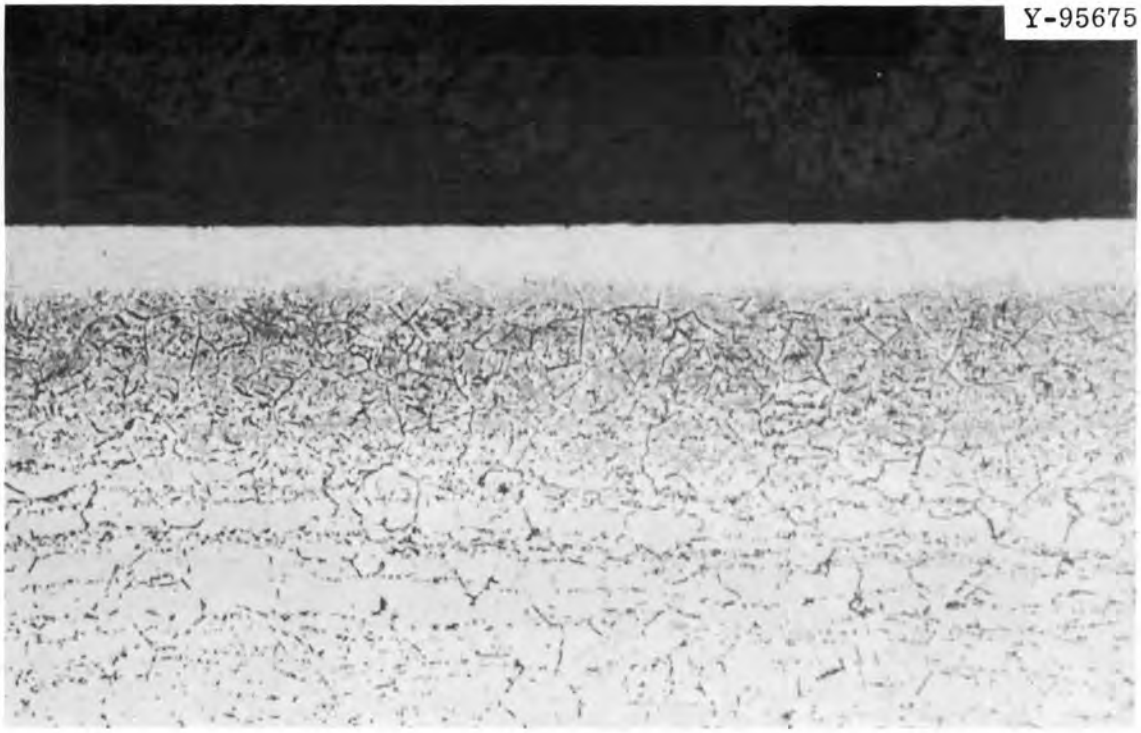

Fig. 8.2. Microstructure of V–20% Ti Oxidized 4 hr at 1000°C and 5×10^{-4} torr O_2. 500×.

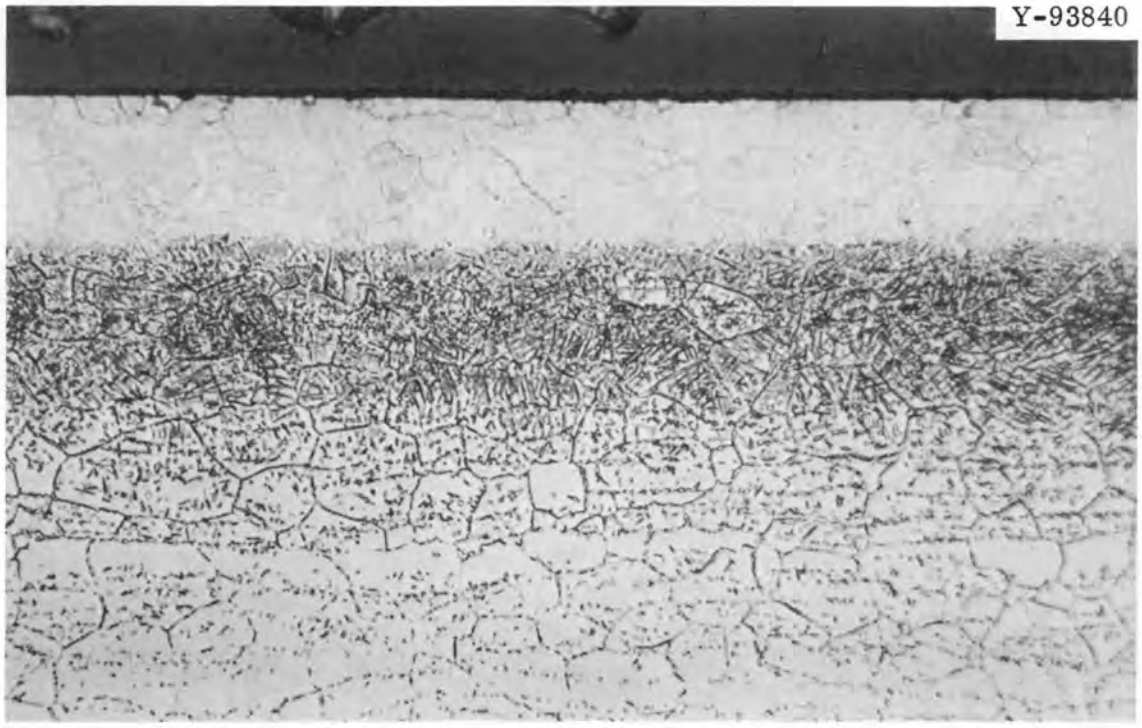

Fig. 8.3. Microstructure of V–20% Ti Oxidized 7 hr at 1000°C and 5×10^{-4} torr O_2. 500×.

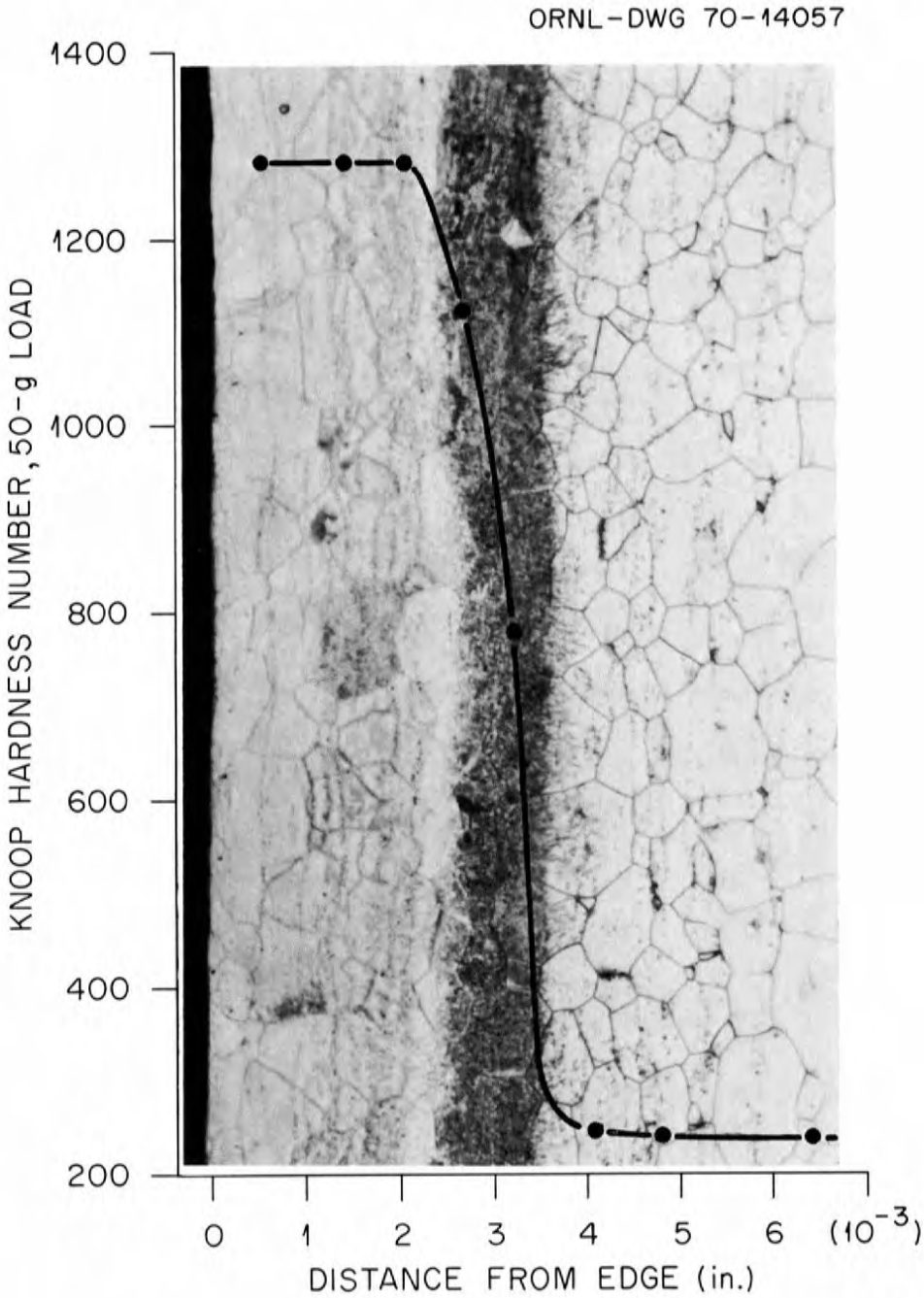

Fig. 8.4. Microstructure of V–20% Ti Oxidized 400 hr at 600°C and 5×10^{-4} torr O_2. A superimposed hardness profile shows the difference in hardness between material affected and that unaffected by oxygen.

Fig. 8.4, reveal a constant hardness of 1290 through the light region, a rapid decrease in hardness through the dark zone (apparently a zone of fine precipitate particles), and then a constant hardness of about 250 in the unaffected alloy matrix.

As a tentative explanation of the two zones, we propose that O diffuses into the alloy and reacts with the Ti to precipitate Ti oxide and thus produce the first zone observed. As the Ti in solid solution in this region is depleted, O dissolves in the V matrix comprising this zone and causes a concentration gradient to develop between the specimen surface, where the O concentration is determined by the partial pressure of O_2, and the precipitation front, where the concentration of dissolved O is essentially zero. The concentration of O in the region depleted of Ti eventually approaches the surface concentration, which under our test conditions is evidently large enough to produce the $\alpha \rightarrow \beta$ phase transformation[6]

$$\alpha V(\text{bcc}, \underline{\text{ss}}) \rightarrow \beta V(\text{bct}, \underline{\text{ss}}) \ .$$

The rate of movement of the transformation front is controlled both by the rate of Ti depletion ahead of the front and the rate of O diffusion across the region of β phase. Hardness measurements made at Ames Laboratory[7] on α and β solid solutions are consistent with the hardness measured for the inner and outer oxidation zones of the V–20% Ti specimen. Since the $\alpha \rightarrow \beta$ phase transformation has not been observed for unalloyed V similarly oxidized in a Na or gaseous environment, it appears that the O concentration for the transformation is lower in the V-Ti system, possibly because of the internal stresses generated by the oxide precipitates.

Notes

1. R. L. Klueh, Fuels and Materials Development Program Quart. Progr. Rept. March 31, 1970, ORNL-4560, pp. 129–132.

2. R. L. Klueh, Fuels and Materials Development Program Quart. Progr. Rept. June 30, 1970, ORNL-4600, pp. 157–159.

3. R. L. Klueh, Fuels and Materials Development Program Quart. Progr. Rept. Sept. 30, 1970, ORNL-4630, pp. 150–154.

4. R. L. Klueh and J. H. DeVan, The Oxidation of Vanadium and Vanadium Alloys in Sodium, ORNL-TM-2827 (March 1970).

5. H. A. Levin and S. Greenberg, An Exploratory Study of the Behavior of Niobium- and Vanadium-Base Alloys in Oxygen-Contaminated Sodium, ANL-6982 (January 1968).

6. J. L. Henry et al., J. Less-Common Metals 21, 115–135 (1970).

7. O. N. Carlson and D. G. Alexander, Reactor Materials Development Quart. Rept. Jan.–March 1967, IS-RD-17, pp. 15–18.

9. SODIUM REMOVAL AND CAUSTIC EFFECTS

W. O. Harms J. H. DeVan

The purpose of this program is to evaluate the corrosion of structural components caused by the products of Na oxidation or hydrolysis. The program deals with the effects of leakage or spillage of Na on metal surfaces that are in contact with mixtures of N_2 and air. It is also concerned with corrosion effects that result from the cleaning and storage of materials after exposure to Na. Both tasks are in direct support of the FFTF.

Examination of ALCO/BLH Steam Generator

J. H. DeVan G. M. Slaughter

We began an examination of the ALCO/BLH steam generator,[1,2] which failed while under test at the Liquid Metal Engineering Center (LMEC). After installation at the Sodium Components Test Installation of the LMEC in 1965, the steam generator operated intermittently with Na for 7600 hr and with steam for 4100 hr. A water leak on the feedwater chest was found in May 1970, and subsequent cursory inspection revealed an area of extensive cracking in the lower tube sheet. In view of the vital role of steam generators in the LMFBR demonstration program and the well-documented fabrication and operational history of this unit, the unit is being examined to determine the mechanism of failure and to evaluate other metallurgical features of interest.

We hope to determine (1) the mechanism of tube sheet cracking, (2) the reasons for tube failures early in the operation of the unit, (3) the extent of any corrosion at the interface between cover gas and Na, (4) the effect of crevices, (5) the integrity of the duplex tubing, (6) the integrity of the tube sheet overlay, (7) reliability of the weld between tube and tube sheet, and (8) additional items of interest such as the distortion of components and baffle wear. We shall remove and examine the head, shell, shroud, and tube sheet from the lower end of

the unit. We shall also attach strain gages to critical areas for a limited stress analysis. All components will be examined nondestructively, and all stages of the investigation will be photographed. About 200 metallographic specimens will have to be prepared and evaluated.

The steam generator arrived at ORNL on December 7, 1970, and was placed in the Experimental Gas Cooled Reactor Turbine Building for examination. Figure 9.1 shows the unit on the truck when it arrived. Figure 9.2 shows it being lowered onto the positioning fixtures by an overhead crane. Figure 9.3 shows the extent of cracking in the massive lower tube sheet as revealed by dye-penetrant techniques.

An extensive series of tests, including dye-penetrant inspection, checkout of thermocouples, and leak testing, is now under way before disassembly.

Fig. 9.1. The ALCO/BLH Steam Generator as It Arrived at ORNL.

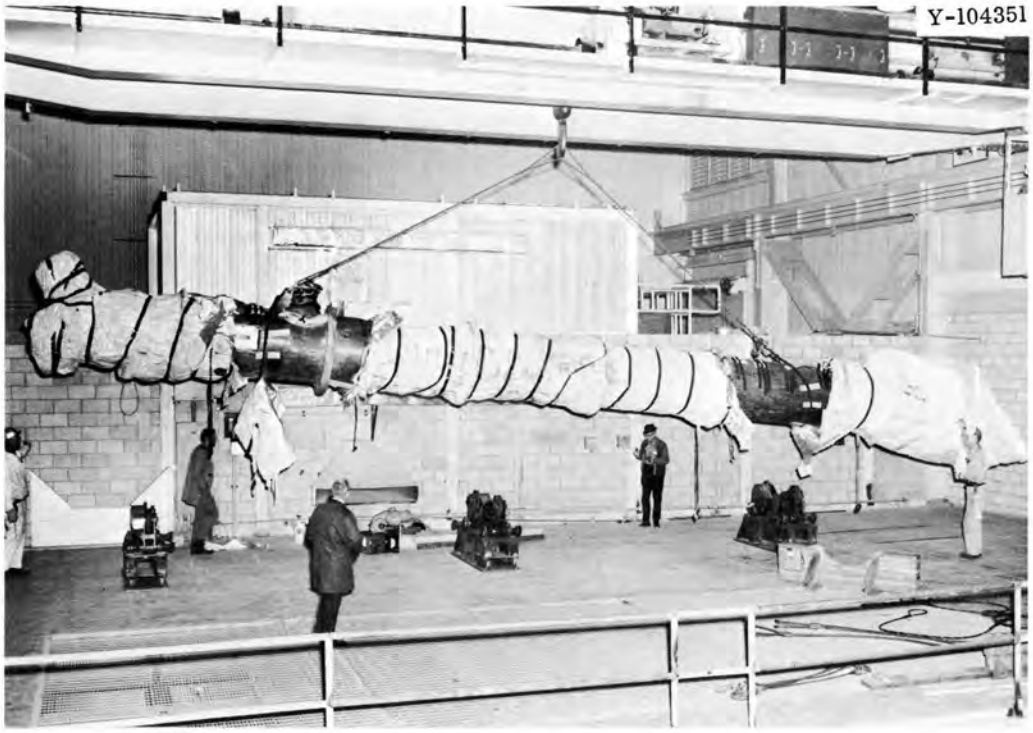

Fig. 9.2. Steam Generator Being Lowered Onto Positioning Fixtures by Overhead Crane.

Fig. 9.3. Crack Network in Lower Tube Sheet as Revealed by Dye-Penetrant Inspection.

Corrosion Effects of Sodium Leaks or Spills in Gases Containing Oxygen

J. H. DeVan

Liquid and crystalline Na oxidize rapidly when exposed to atmospheres that contain O_2, CO_2, or water vapor. The resultant oxidation products are potentially damaging to structural components used in LMFBR systems. At 500°C or higher, damage accrues from the fluxing effects of Na oxides on otherwise protective base-metal oxides. At lower temperatures, damage can result from dissolution and stress-corrosion effects of hydrated caustic residues.

Accordingly, we began a test program to evaluate the debilitating effects of Na (or Na compounds) on stainless steel in mixtures of N_2 and air. This program will build upon the experimental results of a recently completed study[3] to evaluate the combined effects of Na and insulation on the oxidation of stainless steel. The current work is aimed specifically at the problem of a leak or spill in the annulus between the containment vessel of the FFTF Reactor and the outer guard vessel. The atmosphere within this annulus will consist of N_2 that contains 0.5 to 2 vol % O_2 and up to 100 ppm (by volume) H_2O.

Design of Oxidation Experiments (J. E. Strain,[4] D. H. Jansen)

We completed the design of a test apparatus that will permit the controlled leakage of Na through a stainless steel test specimen into a blanket gas of known composition. The apparatus, pictured schematically in Fig. 9.4, consists of a glass bell jar that will contain the desired blanket gas and house the inductively heated test specimen. The test specimen, shown in Fig. 9.5, is composed of two adjoining stainless steel plates that are welded on three sides and open on the fourth. Sodium is forced into the interface between the two plates, and leakage occurs at the open face. The specimen is connected to a Na tank outside the glass bell jar by a 1/8-in.-diam tube inserted through a compression fitting in the top of the bell jar. The rate of Na leakage is continuously measured by means of a resistance bridge in the Na tank. At the

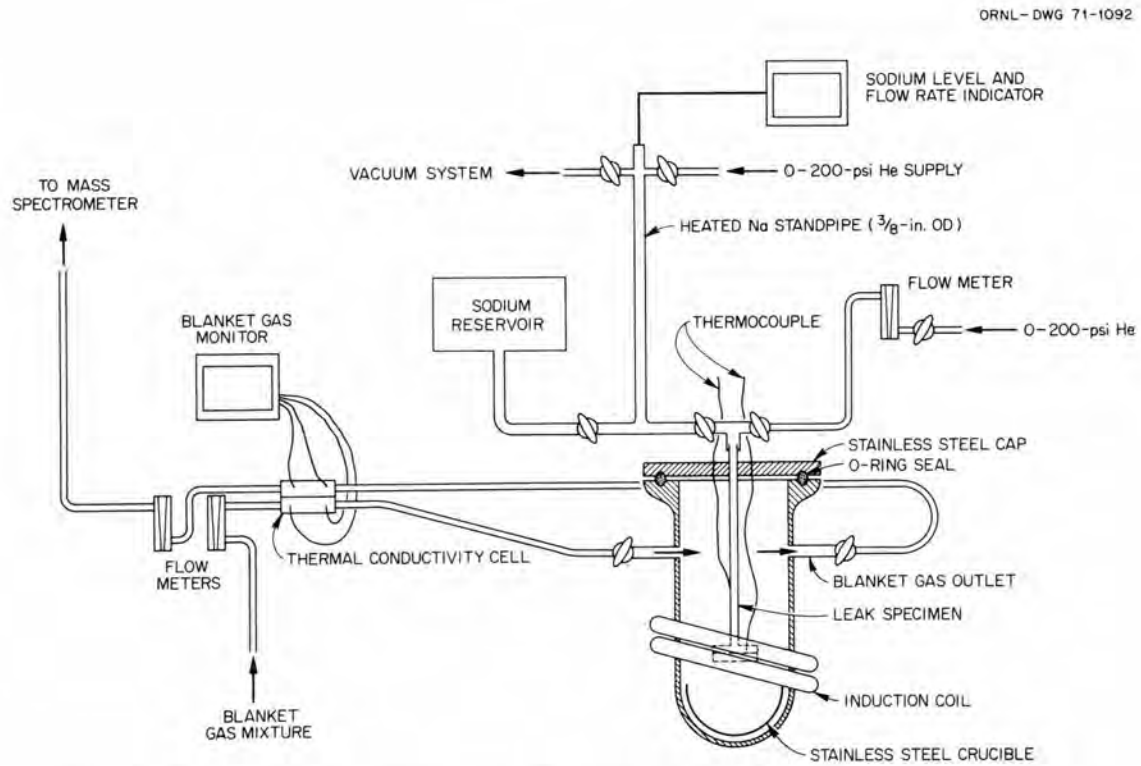

Fig. 9.4. Schematic Drawing of Test Apparatus Designed to Study the Corrosion Effects of Sodium Leaks on Stainless Steel in an Oxidizing Atmosphere.

Fig. 9.5. Design of Test Specimen for Studying Effects of Sodium Leakage.

conclusion of the run, the bell jar is valved off from the remainder of the system and transferred to an inert atmosphere for disassembly and examination of the test specimen.

The blanket gases will be mixed and compressed into cylinders before the test to avoid uncertainties in the composition of the blanket gas during testing. The comparative analysis of the blanket gas as it passes through the guard vessel plus the ability to fix the time of initiation of the leak will make it possible to determine the sensitivity of gas analysis as a means of leak detection. The glass bell jar will also permit the observation of any other phenomena that would make rapid leak detection practical (e.g., smoke generation or light flashes).

Notes

1. ALCO Products, Inc., 30 Mw Heat Exchanger and Steam Generator for Sodium-Cooled Reactor System, APAE-112, vol I, Thermal and Mechanical Final Design (Jan. 31, 1962); vol II, Chemical and Stress Analysis, (Feb. 28, 1962); vol III, Material and Welding Specifications, (June 29, 1962); vol IV, Operation and Maintenance Procedures, (May 15, 1962), ALCO Products, Inc., New York.

2. G. S. Budney, Liquid-Metal-Heated Steam Generator Operating Experience, NAA-SR-12534 (Nov. 1, 1967).

3. J. H. DeVan, Fuels and Materials Development Program Quart. Progr. Rept. June 30, 1970, ORNL-4600, pp. 165–166.

4. Analytical Chemistry Division.

10. DEVELOPMENT OF FBR NEUTRON-ABSORBER MATERIALS

G. M. Adamson, Jr. W. R. Martin

The prime candidate material for the safety and shim rods in the FTR and LMFBR is boron carbide pellets in a stainless steel cladding. In spite of the widespread use of boron carbide as a neutron absorber in thermal reactors, basic data have never been obtained. The material has never been fully characterized for structure, homogeneity range, effect of fabrication variables, and the effects of varying composition. The objective of our work is to characterize the material sufficiently to provide measurable control parameters to properly evaluate fabrication techniques and the effects of irradiation. The irradiation studies will emphasize basic effects of materials variables in both thermal- and fast-reactor environments. A secondary effort of this program will be the preliminary characterization of alternate materials that possess possible advantages over boron carbide for use in fast reactors.

Characterization of Boron Carbide

Indexing of Powder X-Ray Diffraction Patterns (H. L. Yakel)

The indexing of an x-ray diffraction powder pattern of boron carbide through Bragg diffraction angles (2θ) of 166° was reported previously.[1] Although this indexing was substantially correct there were still six unidentified weak lines and some inconsistencies in calculated and observed intensities, which take into account several families of planes that have identical interplanar spacings (d values) but different intensities. The weak lines not belonging to boron carbide were identified as an impurity, β-phase SiC. Using improved intensity calculations and the $CuK\alpha_1$ and $CuK\alpha_2$ radiation wavelengths, we assigned unambiguous indices to each line in a well-exposed film of Norbide 325F boron carbide in a standard 114.6-mm-diam Debye-Sherrer camera with graphite monochromatic $CuK\alpha$ x-radiation. Using the 29 highest angle reflections in this pattern, a least-squares calculation of the lattice constant yielded, for the hexagonal cell, $\underline{a}$ = 5.6009±0.0002 Å and $\underline{c}$ = 12.0728±0.0004 Å. These

values are in substantial agreement with those calculated earlier, but the precision of the lattice constant calculated by least-squares techniques is much improved. Computed 2θ values for the least-squares fit differed from the corresponding observed values by no more than twice the error in the measurement of 2θ.

The extreme care required in analyzing the high-angle regions of CuKα powder patterns prompted investigation of x rays with longer wavelength for diffraction since they would produce fewer reflections and, therefore, fewer overlapping reflections, in the region of interest for precise calculations of the lattice constant. We exposed a sample of Norbide 325F boron carbide (a different sample from the same lot of material as that mentioned above) in a 114.6-mm-diam camera to appropriately filtered CrKα, FeKα, CoKα, NiKα, and monochromatic CuKα x radiation. The observed high-angle 2θ and d values for these films are given in Table 10.1. Rhombohedral and hexagonal reflection indices, Bragg angles, and interplanar spacings computed from a set of specified lattice constants, and a measure of relative reflection intensities are included. The assumed wavelengths of the x rays are given in Table 10.2.

Least-squares fits of the data from each x-ray exposure gave the hexagonal lattice constants listed in Table 10.3. A Nelson-Riley extrapolation function was assumed for each computation. Unbiased estimates of the mean lattice constants and the standard deviations of the unbiased means are $\underline{a}$ = 5.6010±0.0001 Å and $\underline{c}$ = 12.0731±0.0003 Å. Weighted estimates of the mean lattice constants and the standard deviations of the weighted means are $\underline{a}$ = 5.6010±0.00006 Å and $\underline{c}$ = 12.0731±0.00018 Å. Rhombohedral lattice constants corresponding to this rhombohedrally centered hexagonal unit cell are $\underline{a}$ = 5.1626±0.0001 Å and α = 65·703±0.004°. The axial ratio and cell volume for the hexagonal cell are $\underline{c}$:$\underline{a}$ = 2.1555±0.0001 Å and V = 328.01±0.003 Å^3.

The net result of this phase of our study is that we recommend that powder photographs of boron carbides be made with x rays with as long a wavelength as practicable (CrKα, if possible) in a camera of large radius. Problems of reflection indexing are thereby minimized with little or no sacrifice in precision. The selection of x rays with the optimum wavelength for examining irradiated boron carbide powders will vary with the

Table 10.1. Observed Diffraction Angles (2θ) and Interplanar Spacings (d) for Norbide 325F Boron Carbide Powder with Different Radiation Sources

Rhombohedral Indices	Hexagonal Indices	Values Observed with Different Radiation Sources[a,b]										Calculated[c] d Spacing (Å)	Relative Intensity[d] (mF^2)
		CrKα		FeKα		CoKα		NiKα		CuKα			
hkl	hk·l	2θ (deg)	d (Å)	2θ (deg)	d (Å)	2θ (deg)	d (Å)	2θ (deg)	d (Å)	2θ (deg)	d (Å)		
$1\bar{2}2$	$3\bar{4}\cdot1^{\alpha_1}_{\alpha_2}$	117.70(3) 118.06(3)	1.3377(2) 1.3374(2)									1.3370	981.6
$31\bar{1}$	$22\cdot3^{\alpha_1}_{\alpha_2}$	119.89(2) 120.17(3)	1.3227(1) 1.3230(2)									1.3225	917.6
$30\bar{1}$	$31\cdot2^{\alpha_1}_{\alpha_2}$	121.32(3) 121.62(3)	1.3133(2) 1.3136(2)									1.3131	1104.0
422	$20\cdot8^{\alpha_1}_{\alpha_2}$	126.58(3) 126.91(3)	1.2816(2) 1.2819(2)									1.2813	312.6
411 330	$30\cdot6\alpha_1$ $03\cdot6\alpha_2$	130.52(2) 130.96(2)	1.2605(1) 1.2604(1)									1.2604	217.2 345.6
421	$21\cdot7^{\alpha_1}_{\alpha_2}$	131.36(2) 131.79(2)	1.2563(1) 1.2563(1)									1.2562	990.0
$2\bar{1}3$	$34\cdot\bar{4}^{\alpha_1}_{\alpha_2}$	NR NR										1.2289	321.6
432	$11\cdot9^{\alpha_1}_{\alpha_2}$	142.23(2) 142.86(4)	1.20995(8) 1.2098(1)									1.2098	255.6
$3\bar{1}\bar{1}$	$40\cdot1^{\alpha_1}_{\alpha_2}$	143.10(3) 143.73(3)	1.2069(1) 1.2067(1)									1.2066	252.0
$2\bar{2}2$	$4\bar{4}\cdot2^{\alpha_1}_{\alpha_2}$	148.72(2) 149.40(2)	1.18882(6) 1.18889(6)	108.93(3) 109.30(3)	1.1895(2) 1.1892(2)							1.1889	558.0
410	$31\cdot5^{\alpha_1}_{\alpha_2}$	153.86(2) 154.72(3)	1.17526(5) 1.17524(7)	110.82(2) NR	1.1759(2)							1.1752	195.6
433	$10\cdot10^{\alpha_1}_{\alpha_2}$	155.47(3) 156.40(5)	1.17156(7) 1.1715(1)	111.22(3) NR	1.1730(2)							1.1716	146.4
314	$2\bar{3}\cdot8^{\alpha_1}_{\alpha_2}$	158.60(2) 159.63(2)	1.16506(4) 1.16511(4)	112.32(2) 112.63(2)	1.1654(1) 1.1657(1)							1.1652	516.0
420	$22\cdot6^{\alpha_1}_{\alpha_2}$	169.87(3) 172.2(1)	1.14929(3) 1.14940(7)	114.68(2) 115.04(2)	1.1498(1) 1.1498(1)							1.1494	321.6
400	$40\cdot4^{\alpha_1}_{\alpha_2}$			118.61(3) 118.96(3)	1.1257(2) 1.1260(2)							1.1252	105.0
$30\bar{2}$	$32\cdot1^{\alpha_1}_{\alpha_2}$			NR NR								1.1081	3.7
$1\bar{2}3$	$3\bar{5}\cdot2^{\alpha_1}_{\alpha_2}$			124.31(3) 124.75(3)	1.0947(2) 1.0947(2)							1.0944	124.8
$3\bar{1}3$	$4\bar{4}\cdot5^{\alpha_1}_{\alpha_2}$			126.46(4) NR	1.0842(2)							1.0837	19.8
424	$2\bar{2}\cdot10^{\alpha_1}_{\alpha_2}$			127.12(3) 127.55(3)	1.0811(1) 1.0813(1)	111.63(3) 112.02(4)	1.0813(2) 1.0811(3)					1.0808	273.6
434	$1\bar{1}\cdot11^{\alpha_1}_{\alpha_2}$			NR NR		NR NR						1.0705	0.1
304	$3\bar{4}\cdot7^{\alpha_1}_{\alpha_2}$			NR NR		NR NR						1.0608	0.1
$3\bar{1}\bar{2}$	$41\cdot0^{\alpha_1}_{\alpha_2}$			NR NR		115.27(4) NR	1.0590(2)					1.0585	26.4
$41\bar{1}$	$32\cdot4^{\alpha_1}_{\alpha_2}$			135.95(2) 136.54(2)	1.04420(8) 1.04416(8)	117.84(2) 118.29(3)	1.0444(1) 1.0442(2)					1.0441	243.6
522 441	$30\cdot9\alpha_1$ $03\cdot9\alpha_2$			139.27(2) 139.92(2)	1.03252(7) 1.03246(7)	120.08(3) 120.52(3)	1.0324(2) 1.0324(2)					1.0324	315.6 442.8
$40\bar{1}$	$41\cdot3^{\alpha_1}_{\alpha_2}$			141.96(3) 142.61(3)	1.0239(1) 1.02399(9)	121.72(4) 122.20(4)	1.0241(2) 1.0239(2)					1.0237	10.1
$32\bar{2}$	$14\cdot3$											1.0237	90.8
$2\bar{1}4$	$35\cdot\bar{5}^{\alpha_1}_{\alpha}$			NR NR		NR NR						1.0106	10.3
532	$21\cdot10^{\alpha_1}_{\alpha_2}$			NR NR		NR NR						1.0083	16.8
444	$00\cdot12^{\alpha_1}_{\alpha_2}$			148.34(2) 149.08(3)	1.00614(5) 1.00636(8)	125.44(2) 125.92(3)	1.0064(1) 1.0064(1)					1.0061	134.8
521	$31\cdot8^{\alpha_1}_{\alpha_2}$			NR 149.90(2)	1.00442(2)	NR NR						1.0042	48.0
533	$20\cdot11^{\alpha_1}_{\alpha_2}$			150.92(3) 151.79(3)	1.00002(7) 1.00011(7)	126.86(3) 127.34(4)	1.0001(1) 1.0000(2)					0.9999	41.4
511	$40\cdot7^{\alpha_1}_{\alpha_2}$			154.67(3) 155.70(4)	0.99212(6) 0.99218(8)	128.70(3) NR	0.9923(1)					0.9920	41.4
531	$22\cdot9^{\alpha_1}_{\alpha_2}$			NR		134.83(3) NR	0.9688(1)					0.9687	204.0
$2\bar{3}2$	$5\bar{5}\cdot1^{\alpha_1}_{\alpha_2}$					NR NR						0.9670	58.2
$4\bar{1}\bar{1}$	$50\cdot2^{\alpha_1}_{\alpha_2}$					NR NR						0.9578	10.2
543	$11\cdot12^{\alpha_1}_{\alpha_2}$					NR NR						0.9468	0.2
404	$4\bar{4}\cdot8^{\alpha_1}_{\alpha_2}$					142.20(2) 142.69(3)	0.94543(6) 0.94554(9)					0.9453	55.8
425	$2\bar{3}\cdot11^{\alpha_1}_{\alpha_2}$					143.49(3) NR	0.94186(8)					0.9417	69.6
510	$41\cdot6^{\alpha_1}_{\alpha_2}$					145.34(3) NR	0.93700(8)	124.42(3) NR	0.9370(1)			0.9368	32.4
$43\bar{1}$	$14\cdot6$											0.9368	0.2
520	$32\cdot7^{\alpha_1}_{\alpha_2}$					146.08(3) NR	0.93513(8)	124.81(3) NR	0.9353(1)			0.9351	159.6
$30\bar{3}$	$33\cdot0^{\alpha_1}_{\alpha_2}$					146.69(3) 147.52(2)	0.93363(8) 0.93365(5)	NR 125.72(2)	0.93363(9)			0.9335	385.2
$3\bar{2}3$	$5\bar{5}\cdot4^{\alpha_1}_{\alpha_2}$					151.09(3) 152.03(4)	0.92371(6) 0.92376(8)	127.66(4) NR	0.9236(2)			0.9236	8.4
$1\bar{3}3$	$4\bar{6}\cdot1^{\alpha_1}_{\alpha_2}$					156.21(3) NR	0.91409(5)	130.14(3) NR	0.9141(1)			0.9141	54.0
544	$10\cdot13^{\alpha_1}_{\alpha_2}$					157.39(3) 158.67(3)	0.91216(5) 0.91215(5)	130.67(3) NR	0.9121(1)			0.9121	135.0
$41\bar{2}$	$33\cdot3^{\alpha_1}_{\alpha_2}$					159.21(3) 160.62(2)	0.90939(5) 0.90937(3)	131.44(3) 132.06(3)	0.9094(1) 0.9093(1)			0.9094	314.4
$40\bar{2}$	$42\cdot2^{\alpha_1}_{\alpha_2}$					161.42(2) 163.01(3)	0.90635(3) 0.90633(4)	132.27(3) 132.87(3)	0.9064(1) 0.9064(1)			0.9063	130.8
500	$50\cdot5^{\alpha_1}_{\alpha_2}$					167.08(2) NR	0.90018(2)	134.10(2) NR	0.90018(7)			0.9002	195.6
415	$3\bar{4}\cdot10^{\alpha_1}_{\alpha_2}$					NR NR		134.63(3) NR	0.8984(1)			0.8985	134.4
305	$3\bar{5}\cdot8^{\alpha_1}_{\alpha_2}$					NR		135.51(3) 136.14(2)	0.8956(1) 0.89566(7)			0.8956	799.2
	B			157.35(4)	0.89570(5)								
$2\bar{2}4$	$46\cdot4^{\alpha_1}_{\alpha_2}$							141.88(2) 142.58(2)	0.87699(6) 0.87719(5)	122.84(2) 123.33(2)	0.87715(9) 0.87729(9)	0.8771	148.8
$4\bar{1}\bar{2}$	$51\cdot1^{\alpha_1}_{\alpha_2}$							145.10(2) NR	0.86890(5)	124.86(2) NR	0.86894(8)	0.8689	265.2
535	$2\bar{2}\cdot13^{\alpha_1}_{\alpha_2}$							145.83(3) 146.61(2)	0.86718(7) 0.86740(5)	125.30(2) 125.78(2)	0.86721(8) 0.86749(8)	0.8673	345.0
$2\bar{3}3$	$5\bar{6}\cdot2^{\alpha_1}_{\alpha_2}$							148.08(2) 148.99(2)	0.86215(5) 0.86222(5)	126.61(2) 127.12(2)	0.86217(8) 0.86239(8)	0.8623	386.4
$51\bar{1}$	$42\cdot5^{\alpha_1}_{\alpha_2}$							150.59(2) 151.57(3)	0.85699(4) 0.85709(6)	127.97(2) NR	0.85708(8)	0.8570	802.8
622	$40\cdot10^{\alpha_1}_{\alpha_2}$							151.36(3) 152.32(4)	0.85550(6) 0.85569(8)	NR NR		0.8556	477.6
633 552	$30\cdot12\alpha_1$ $03\cdot12\alpha_2$							152.13(4) 153.17(2)	0.85406(8) 0.85415(4)	NR 129.34(2)	0.85429(7)	0.8542	240.6 21.6
632	$31\cdot11^{\alpha_1}_{\alpha_2}$							154.19(2) 155.38(2)	0.85040(4) 0.85040(4)	129.83(2) 130.44(2)	0.85046(7) 0.85046(7)	0.8504	195.6
545	$1\bar{1}\cdot14^{\alpha_1}_{\alpha_2}$							NR NR		NR NR		0.8491	53.4
$52\bar{1}$	$33\cdot6^{\alpha_1}_{\alpha_2}$							156.41(2) 157.67(3)	0.84681(3) 0.84688(5)	130.85(2) NR	0.84697(7)	0.8468	134.4
$4\bar{1}4$	$5\bar{5}\cdot7^{\alpha_1}_{\alpha_2}$							157.25(3) 158.37(2)	0.84553(5) 0.84559(3)	131.25(2) 131.91(2)	0.84562(7) 0.84553(7)	0.8455	151.8
$50\bar{1}$	$51\cdot4^{\alpha_1}_{\alpha_2}$							NR NR		NR NR		0.8370	20.4
621	$41\cdot9^{\alpha_1}_{\alpha_2}$							NR NR		135.95(2) 136.62(2)	0.83089(6) 0.83100(6)	0.8310	141.6
540	$14\cdot9$											0.8310	156.8
643	$21\cdot13^{\alpha_1}_{\alpha_2}$									NR NR		0.8285	34.8
$3\bar{2}4$	$5\bar{6}\cdot5^{\alpha_1}_{\alpha_2}$									140.04(2) NR	0.81959(5)	0.8195	69.6
631	$32\cdot10^{\alpha_1}_{\alpha_2}$									NR NR		0.8183	100.8
642	$22\cdot12^{\alpha_1}_{\alpha_2}$									NR NR		0.8171	79.2
611	$50\cdot8^{\alpha_1}_{\alpha_2}$									NR NR		0.8161	91.8
515	$4\bar{4}\cdot11^{\alpha_1}_{\alpha_2}$									142.37(2) 143.18(2)	0.81375(5) 0.81382(5)	0.8138	412.8
644	$20\cdot14^{\alpha_1}_{\alpha_2}$									NR NR		0.8125	48.0
$3\bar{1}5$	$4\bar{6}\cdot7^{\alpha_1}_{\alpha_2}$									NR NR		0.8095	55.2
$4\bar{2}\bar{2}$	$60\cdot0^{\alpha_1}_{\alpha_2}$									144.64(2) 145.55(2)	0.80845(5) 0.80844(5)	0.8084	220.2
555	$00\cdot15^{\alpha_1}_{\alpha_2}$									146.24(2) 147.16(3)	0.80495(5) 0.80499(6)	0.8049	104.6
$40\bar{3}$	$43\cdot1^{\alpha_1}_{\alpha_2}$									150.94(2) 152.06(3)	0.79570(4) 0.79570(4)	0.7957	22.8
$5\bar{1}\bar{1}$ $33\bar{3}$	$60\cdot3\alpha_1$ $06\cdot3\alpha_2$									152.75(2) 153.95(2)	0.79256(4) 0.79256(3)	0.7926	37.2 636.6
$1\bar{3}4$	$4\bar{7}\cdot2^{\alpha_1}_{\alpha_2}$									NR 155.17(3)	0.79065(5)	0.7906	111.6
620	$42\cdot8^{\alpha_1}_{\alpha_2}$									NR NR		0.7835	1.7
416	$3\bar{5}\cdot11^{\alpha_1}_{\alpha_2}$									NR NR		0.7814	0.6
536	$2\bar{3}\cdot14^{\alpha_1}_{\alpha_2}$									161.56(2) 163.33(2)	0.78034(2) 0.78041(2)	0.7804	93.6
610	$51\cdot7^{\alpha_1}_{\alpha_2}$									NR NR		0.7776	3.1
$4\bar{1}\bar{3}$	$52\cdot0^{\alpha_1}_{\alpha_2}$									165.15(3) NR	0.77676(3)	0.7767	43.2
654	$11\cdot15^{\alpha_1}_{\alpha_2}$									NR NR		0.7736	5.3
$51\bar{2}$	$43\cdot4^{\alpha_1}_{\alpha_2}$									NR		0.7710	285.6

(a) Numbers in parentheses represent estimates of error in the last decimal place.

(b) NR ≡ not recorded either because of low intensity or because of overlap with neighboring reflections.

(c) Calculated d values assume the lattice constants $\left\{\begin{array}{l}\underline{a} = 5.6010\ \text{Å}\\ \underline{c} = 12.0731\ \text{Å}\end{array}\right\}$; that is, the weighted means of the five measurements.

(d) m ≡ multiplicity; F^2 computed with atom coordinates of Clark and Hoard, J. Am. Chem. Soc. 65, 2115–2119 (1943).

Table 10.2. Assumed Wavelengths of Radiation Used

Radiation Source	Wavelength, Å			
	α_1	α_2	Weighted Mean of α_1 and α_2	β
CrK	2.28962	2.29351	2.29092	2.08480
FeK	1.93597	1.93991	1.93728	1.75653
CoK	1.78892	1.79278	1.79021	1.62075
NiK	1.65784	1.66169	1.65912	1.50010
CuK	1.54051	1.54433	1.54178	1.39217

Table 10.3. Hexagonal Lattice Constants Determined by Least-Squares Technique with Different Radiation Sources

Radiation Source	Lattice Constant a, Å		Lattice Constant c, Å	
	Value	Estimated Standard Deviation	Value	Estimated Standard Deviation
CrKα	5.6007	0.0002	12.0721	0.0004
FeKα	5.6015	0.0003	12.0739	0.0005
CoKα	5.6011	0.0001	12.0731	0.0004
NiKα	5.6009	0.0002	12.0725	0.0005
CuKα	5.6010	0.0001	12.0737	0.0003

irradiation conditions. Usually, CrKα will be the best choice of radiation, but CoKα could be selected if the changes in lattice constant are expected to be small. [In this case, the fact that a increases but c decreases on irradiation would split the 50·5 (CoKα_2) and the 34·10 (CoKα_1) reflections that are overlapped in CoKα patterns of unirradiated Norbide 325F.] It must be remembered that, whatever x-radiation is used, the precision of the estimate of the c lattice constant of irradiated boron carbides will become progressively less than that of the estimate of the a lattice constant as the radiation fluence increases.[2]

Irradiation Behavior of Boron Carbide

Thermal Reactor Tests (G. L. Copeland)

Nine capsules (0-4 through 0-12) were evaluated after irradiation for 6 weeks in the isotopes stringer of the ORR. Data for these capsules are summarized in Table 10.4; data for capsules 0-1 through 0-3 are repeated for comparison. Capsules 0-1, 0-2, and 0-3 were irradiated 3 weeks in the same position. These capsules were fabricated the same as 0-1 through 0-3 (ref. 3). It was difficult to remove the powders from capsules 0-3 through 0-12, whereas the first three capsules were unloaded easily. The disassembly resulted in Cu shavings being mixed with the boron carbide powder. The subsequent removal of the Cu powder may have affected the x-ray results, as discussed below. In addition, part of the boron carbide powders were lost either during disassembly or during removal of the Cu. The capsule is being redesigned to avoid this problem for the next series of experiments.

The difficult disassembly of the capsules also resulted in some breakage of the SiC temperature monitors. Two of the monitors were broken too badly to use. The ends of the others had to be ground to make them smooth and perpendicular for reliable measurements. Monitors from capsules 0-5, 0-10, 0-11, and 0-12 gave very good annealing curves and showed a clear break when annealing began to remove the irradiation damage. The SiC monitors from capsules 0-6, 0-7, and 0-8 did not show a clear-cut change during annealing; therefore, the irradiation temperatures of these capsules were not as accurately known as those of the other capsules.

The procedure for unloading the irradiated capsules was as follows:

1. The inner Cu capsule was removed.
2. The Cu capsule was punctured with the laser puncturing device.
3. The gas was collected and measured.
4. The ends of the Cu cylinder were removed.
5. Since the boron carbide powder and the SiC could not be removed by tapping or pushing with a small rod, the powder was worked out by hand-twisting a small drill bit; however, some small Cu shavings were included with the powder.

Table 10.4. Results of Irradiations of Boron Carbide Powder in the ORR

	Capsule Number											
	0-1	0-2	0-3	0-4	0-5	0-6	0-7	0-8	0-9	0-10	0-11	0-12
	Norbide 325F, B:C = 3.6						Norbide 325F with Added B, B:C = 4.5					
	Annealing Temperature[a] (°C)		As Received	Annealing Temperature[a] (°C)		As Received	Annealing Temperature,[a] °C					
	1500	2000		1500	2000		1000	1500	2000	1000	1500	2000
Irradiation temperature, °C												
Design	350	350	350	500	500	500	350	350	350	500	500	500
Actual	340	b	360	b	625	410	425	200	b	510	540	575
Burnup,												
depletions/cm^3 ($\times 10^{20}$)	18.3	19.5	13.7	13.9	10.6	12.1	16.4	13.4	7.85	17.7	15.5	13.0
% ^{10}B	8.8	9.4	6.6	6.7	5.1	5.8	7.5	6.1	3.6	8.1	7.1	5.9
Gas release,												
cm^3	0.248	0.235	0.161	0.1024[c]	0.0929	0.0808	1.0968	0.359	0.1230	0.0932[c]	0.423	0.0964[c]
% He generated	5.8	5.2	5.0	3.1	4.2	2.5	29.9	11.6	7.6	2.2	12.6	3.3

[a]All samples annealed 1 hr at indicated temperature.

[b]Measurement not available; SiC temperature monitor broken.

[c]Possible leak during irradiation.

6. Since the Cu interfered with x-ray powder patterns, it was removed by leaching with HNO_3, which was then analyzed for Li so that the Li lost during leaching could be added to the Li content determined in the final analysis for burnup.

The burnups as calculated from the Li contents were about the same or lower for capsules 0-4 through 0-12 than for capsules 0-1 through 0-3 even though they were irradiated 6 weeks as compared to 3 weeks.

Although there are several inconsistencies in the data, possibly due to either the small size of the sample or the unusual procedures required to disassemble the capsules, several comments may be made. Gas release was lower for samples 0-4 through 0-6 than for their corresponding samples (0-1 through 0-3) irradiated at a lower temperature.

Samples 0-7 through 0-12 were made by blending Norbide 325F boron carbide powder with B powder to increase the ratio of B:C to 4.5 and then annealing at 1000, 1500, or 2000°C to homogenize the powders. Previous experiments showed that almost no intraparticle voids were produced during annealing when B powder was added.[4] X-ray diffraction powder patterns showed that the powders used in samples 0-7, 0-8, and 0-11 contained a small amount of free B and that the powder for samples 0-9 and 0-12 contained no free B. The gas releases corresponded well with these results. The gas release was much greater from the samples that contained free B. Again, temperature, in this range, does not seem to play a dominant role in gas release.

Seven additional capsules were irradiated for 3 weeks. Capsules 0-13 through 0-16 contained boron carbide with a B:C ratio of 4.5 and particle sizes of −80+325 mesh and −325 mesh at temperatures of about 350 and 500°C. These four capsules are now being evaluated. Capsule 0-17 contained small platelets of a dense pellet of boron carbide. One of these was successfully thinned for transmission electron microscopy. Capsules 0-18 and 0-19 contained several small single crystals of boron carbide and were irradiated at about 350 and 500°C. These crystals are now being evaluated.

Fast Reactor Tests (G. L. Copeland, R. G. Donnelly, G. W. Keilholtz[5])

The test of boron carbide in the EBR-II was assigned the number X 099. The experiment was placed in the reactor in position 7F5 after run 47A and just before the coolant temperature was lowered for maintenance. Present plans are to irradiate the assembly for about 1 year.

X-Ray Diffraction Study of Irradiated Boron Carbide (V. J. Tennery)

Boron carbide samples with ratios of B:C of 3.6 and 4.5 and with 1-hr anneals at the various annealing temperatures shown in Table 10.4 were irradiated at about 350 and 500°C to about 7% burnup of ^{10}B. The x-ray diffraction patterns of these samples were examined for evidence of formation of a new phase. The data were compared with those obtained for previous samples irradiated at about 350°C to about 9% burnup of ^{10}B (ref. 6).

The samples and experimental conditions are listed in Table 10.5. The x-ray powder patterns of all of the unirradiated samples were reasonably sharp, and B_4C was the major phase. The boron carbide contained

Table 10.5. Boron Carbide Samples

Sample Number for Unirradiated Specimen	Annealing Temperature (°C)	Comparable Sample Number for Annealed and Irradiated Specimen	Approximate Irradiation Temperature (°C)
	Ratio B:C = 3.6		
B_4C-A (control)	350		
0-1-A	1500	0-4	500
0-2-A	2000	0-5	500
0-3-A	None	0-6	500
	Ratio B:C = 4.5		
0-7-A	1000	0-7	350
0-8-A	1500	0-8	350
0-9-A	2000	0-9	350
0-7-A	1000	0-10	500
0-8-A	1500	0-11	500
0-9-A	2000	0-12	500

free graphite as received. The x-ray patterns were made with a CuKα radiation source and a Debye-Scherrer camera 114.95 mm in diameter. The tables that follow contain the listings of all of the interplanar d spacings observed in the various samples between $2\theta = 0°$ and $2\theta \cong 83°$ and are arranged so that the interplanar spacings of a particular sample can be easily compared to the published values[7] for B_4C (ASTM data card 6-055) and graphite (ASTM data cards 13-148 and 12-212).

Irradiated samples 0-5, 0-6, and 0-9 were not suitable for the x-ray study even after leaching in acid because of contamination problems from the Cu specimen holder used during irradiation. As noted previously,[6] irradiation of as-received boron carbide at 350°C led to the disappearance of free graphite from the sample. After we heat treated this same boron carbide for 3 weeks at 350°C, the free graphite was still present, as shown in Table 10.6. The d spacings of samples 0-1-A and 0-2-A are also given in Table 10.6. Note that annealing to 2000°C for 1 hr did not lead to the disappearance of the graphite when the ratio of B:C was 3.6. Sample 0-2-A exhibited a large number of lines that could not be identified readily.[6] Since sample 0-6 was lost and sample 0-5 was too badly contaminated to be used, we can now only compare samples 0-1-A and 0-4. These data are shown in Table 10.6. Note that under irradiation the predominant 3.35 Å line for graphite present in 0-1-A disappeared in 0-4. There is some evidence that some graphite remained in 0-4 (i.e., the 2.03, 1.675, 1.546, and 1.240 Å lines correspond to some of the weaker lines of graphite). This ambiguity still remains unexplained. Also, a phase or phases with d spacings of 6.02, 4.70, 3.20, 2.53, 2.45, 2.11, 1.96, 1.91, and 1.37 Å appeared during irradiation or chemical treatment of the sample after irradiation. Since all of the irradiated samples were badly contaminated with Cu and organic matter during removal from the irradiation capsules, HNO_3 was used to leach the Cu from the samples.

Specimens 0-7-A, 0-8-A, and 0-9-A were annealed at 1000, 1500, and 2000°C, respectively. The observed d spacings are given in Table 10.7. When the ratio of B:C was 4.5, annealing at 1000°C resulted in the presence of graphite and free B along with B_4C, but annealing at 1500 and 2000°C caused the disappearance of the lines attributable to graphite

Table 10.6. Interplanar Spacings (d) and Relative Intensities[a] (RI) for Annealed and Irradiated Samples of Boron Carbide with Ratio of Boron to Carbon of 3.6 Compared with Published Values

Hexagonal Miller Indices	Annealed Samples[b]						Irradiated Sample[c]		Published Values[d]			
	Control B_4C-A		0-1-A		0-2-A		0-4		B_4C		Graphite	
hkl	d (Å)	RI	d (Å)	RI	d (Å)	RI	d (Å)	RI	d (Å)	RI	d (Å)	RI
							6.02	vw				
					5.40	m						
							4.70	w				
(101)	4.52	m	4.51	m	4.49	m	4.50	m	4.49	m		
	4.21	vw			4.21	vvw						
(003)	4.04	m	4.04	m	4.03	m	4.03	m	4.02	m		
(002)	3.795	s	3.79	s	3.77	s	3.78	s	3.79	s		
	3.396	w	3.39	vw	3.39	vw					3.35	s
							3.20	m				
					2.90	vw						
(110)	2.808	m	2.81	w	2.79	w	2.78	m	2.81	m		
					2.69	vw						
	2.643	vw	2.64	vvw	2.62	vw						
(104)	2.572	s	2.57	s	2.56	s	2.57	s	2.57	s		
					2.50	vw	2.53	s				
					2.43	vw	2.45	w				
(201)	2.385	s	2.38	s	2.37	s	2.38	vs	2.38	s		
(113)	2.310	w	2.31	w	2.29	w			2.30	w		
					2.21	w						
					2.16	vw	2.18	vw				
	2.13	vw	2.13	m	2.12	vw					2.13	m
(006)	2.04	vw					2.03	vvw			2.04	m
							1.96	m				
(204)	1.90	vw			1.89	vw	1.91	vvw				
			1.85	vw	1.84	vw	1.86	vw				
(211)	1.82	w	1.82	w	1.82	w	1.81	w	1.82	w	1.80	m
(205)	1.717	m	1.715	m	1.710	m	1.708	w	1.714	m		
							1.675	vvw			1.675	m
(107)	1.631	w	1.631	vw	1.625	vw			1.637 1.628	w w		
(214)	1.571	vw	1.571	vw	1.600	vw	1.598	vvw				
							1.546	m			1.541	m
					1.530	m						
(303)	1.5044	m	1.504	m	1.500	m	1.500	w	1.505	m		
(215)	1.4629	m	1.4630	m	1.459	m	1.4580	w	1.463	m		
(108)	1.4441	m	1.4447	m	1.4403	m	1.4395	w	1.446	m		
(220)	1.4043	m	1.4037	m	1.4000	m	1.4008	m	1.407 1.403	m m		
							1.3703	w				
(311)	1.3400	m	1.3402	w	1.3347	m	1.3364	w	1.345 1.342	w w		
(223)	1.3256	m	1.3273	w	1.3217	m			1.326	w		
(312)	1.3144	m	1.3155	w	1.3110	m	1.3177	m				
(208)	1.2844	w	1.2844	vw	1.2798	w			1.286	vw		
(306) (036)	1.2590	m	1.2606	w	1.2573	w	1.2602	w	1.261	w		
	1.236	vw	1.23	vw			1.2408	vw			1.230	s
(401)	1.2107	w	1.2096	vw	1.2060	vw						
(4$\bar{4}$2)	1.1911	w	1.1921	vw	1.1888	vw	1.1882	vw	1.191	w		

[a]Relative intensities designated w = weak, m = medium, s = strong, v = very.

[b]Control sample B_4C-A annealed 3 weeks at 350°C in Ar; sample 0-1-A annealed 1 hr at 1500°C in vacuum; sample 0-2-A annealed 1 hr at 2000°C in vacuum.

[c]Sample 0-4 irradiated at 500°C.

[d]ASTM Data Cards 6-055 (B_4C) and 13-148 and 12-212 (Graphite) Inorganic Index to the Powder Diffraction File, 1969, ASTM Publ. PDIS-19i, American Society for Testing and Materials, Philadelphia.

Table 10.7. Interplanar Spacings (d) and Relative Intensities[a] (RI) for Annealed Samples of Boron Carbide with Ratio of Boron to Carbon of 4.5 Compared with Published Values

Hexagonal Miller Indices	Annealed Samples[b]						Published Values[c]			
	0-7-A		0-8-A		0-9-A		B_4C		Graphite	
hkl	d (Å)	RI	d (Å)	RI	d (Å)	RI	d (Å)	RI	d (Å)	RI
	5.52	vvw								
	5.02	w								
(101)	4.50	m	4.53	m	4.51	m	4.49	m		
	4.18	vw	4.23	vvw	4.18	vvw				
(003)	4.03	m	4.05	m	4.04	m	4.02	m		
(102)	3.78	s	3.80	s	3.78	s	3.79	s		
	3.53	vvw								
	3.36	vvw							3.35	s
(110)	2.80	m	2.81	m	2.81	m	2.81	m		
	2.63	vw	2.64	vw	2.64	vvw				
(104)	2.56	s	2.57	s	2.57	s	2.57	s		
	2.45	vvw								
(201)	2.38	s	2.38	s	2.38	s	2.38	s		
(113)	2.30	m	2.31	w	2.30	w	2.30	w		
	2.18	vvw							2.13	m
	2.05	vvw							2.04	m
(006)	2.00	vvw								
(204)	1.90	vw								
(211)	1.81	w	1.82	w	1.82	w	1.82	w		
	1.765	vvw								
(205)	1.713	m	1.718	m	1.713	m	1.714	vw		
(107)	1.626	w	1.632	vw	1.628	w	1.637 1.628	w w		
(214)	1.567	vw	1.572	vvw	1.570	vvw				
	1.542	vw							1.541	m
(303)	1.5005	m	1.5040	m	1.501	m	1.505	m		
(215)	1.4594	m	1.463	m	1.462	m	1.463	m		
(108)	1.4407	m	1.4449	m	1.4440	m	1.446	m		
(220)	1.4008	m	1.4030	m	1.4020	m	1.407 1.403	m m		
(311)	1.3367	m	1.3407	m	1.338	m	1.345 1.342	w w		
(223)	1.3231	m	1.3264	m	1.3250	m	1.326	w		
(312)	1.3109	m	1.3142	m	1.3140	m				
(208)	1.2812	w	1.2838	w	1.2840	w	1.286	vw		
(306) (036)	1.2579	m	1.2590	m	1.2595	m	1.261	w		
	1.2339	vvw							1.23	s
(401)	1.2077	w	1.2099	w	1.2098	w				
($4\bar{4}2$)	1.1898	w	1.1904	w	1.1908	w				

[a]Relative intensities designated w = weak, m = medium, s = strong, v = very.

[b]Samples 0-7-A, 0-8-A, and 0-9-A annealed 1 hr in vacuum at 1000, 1500, and 2000°C, respectively.

[c]ASTM Data Cards 6-055 (B_4C) and 13-148 and 12-212 (Graphite) Inorganic Index to the Powder Diffraction File, 1969, ASTM Publ. PDIS-19i, American Society for Testing and Materials, Philadelphia.

and B. All three specimens contained unidentified spacings of about 4.2, 2.64, and 1.57 Å. If these lines belong to an extraneous phase it was also present in O-1-A, O-2-A, and the unirradiated boron carbide control sample, B_4C-A, annealed at 350°C for 3 weeks.

The irradiated samples exhibited x-ray diffraction patterns of much poorer quality than the previous O-1, O-2, and O-3 samples in which the ^{10}B burnup was much lower. No readable diffraction lines were observed at d spacings below about 1.0 Å, and the lines that did exist on the patterns were much more diffuse than those observed in the samples irradiated to lower burnup.

The effect of the ratio of B:C on the phases observed after irradiation is indicated in Table 10.8. Previously we showed[6] that annealing at high temperature before irradiation led to the disappearance of graphite from samples with a ratio of B:C of 4.5. Sample O-11 contained a very weak line at 3.44 Å that may be attributable to the strong line of graphite at 3.35 Å. More importantly, however, a new phase or phases with d spacings of about 6.0, 3.2, 2.6, 2.1, 1.59, 1.54, and 1.37 Å appeared during irradiation or chemical treatment.

The phase with the d spacing of about 6 Å was also observed in sample O-4; therefore, its presence is apparently not strongly dependent upon the ratio of B:C but is a result of some other phenomenon. Many attempts were made to identify this phase. The most promising correlation observed was for cubic B_2O_3. Direct comparison of the published spacings for B_2O_3 (ASTM cards 6-0297 and 13-570) and those in these samples can be made from Table 10.8.

The results observed for sample O-8 and the d spacings for the unirradiated sample O-8-A are shown in Table 10.8. Again, essentially the same results were obtained for irradiation at 350 and 500°C (Table 10.8); that is, the phase with strong x-ray reflections at about 6.0 and 3.2 Å was present in the irradiated sample. The results obtained for irradiated samples O-7, O-10, and O-12 are given in Table 10.8. The x-ray pattern of sample O-10 was of such poor quality that only seven diffraction lines were observed in the range of values selected for presentation in the tables. The pattern of sample O-12 definitely did not contain the diffraction line at 6 Å, but this line was quite prominent

Table 10.8. Interplanar Spacings (d) and Relative Intensities[a] (RI) for an Annealed Sample and Irradiated Sample of Boron Carbide with Two Ratios of Boron to Carbon Compared with Published Values

Hexagonal Miller Indices	Annealed Sample[b] (B:C = 4.5) 0-8-A		Irradiated Sample[c] (B:C = 3.6) 0-4		Irradiated Samples[d] (B:C = 4.5) 0-7		0-8		0-10		0-11		0-12		Published Values[e] B_4C		Graphite		B_2O_3	
hkl	d (Å)	RI	d (Å)	RI	d (Å)	RI	d (Å)	RI	d (Å)	RI	d (Å)	RI	d (Å)	RI	d (Å)	RI	d (Å)	RI	d (Å)	RI
			6.02	vw	6.02	m	6.02	s			6.04	w							6.08	m
			4.70	w																
(101)	4.53	m	4.50	m	4.50	s	4.50	m			4.50	s	4.50	s	4.49	m				
	4.23	vvw																		
(003)	4.05	m	4.03	m	4.01	vvw	4.00	vw	3.39	vw	4.00	m	4.01	m	4.02	m				
(102)	3.80	s	3.78	s	3.80	m	3.80	m	3.78	vw	3.78	s	3.78	s	3.79	s			3.80	m
											3.45	vvw					3.35	s		
			3.20	m	3.20	s	3.19	s			3.15	w							3.21	s
					2.95	vvw	2.95	vw	3.00	vvw										
(110)	2.81	m	2.78	m	2.83	vvw	2.83	vw			2.81	w	2.80	vw	2.81	m			2.92	w
	2.64	vw			2.65	vvw	2.66	vw	2.66	vw	2.65	vvw	2.64	vvw					2.60	w
(104)	2.57	s	2.57	s	2.55	s	2.56	w	2.55	vw	2.57	s	2.56	s	2.57	s				
			2.53	s							2.53	s	2.52	w						
			2.45	w									2.45	vvw					2.49	w
(201)	2.38	s	2.38	vs	2.40	s	2.39	vs	2.38	vw	2.38	s	2.38	s	2.38	s				
(113)	2.31	w					2.31	vvw			2.31	vvw	2.30	w	2.30	w			2.26	w
							2.24	vvw												
			2.18	vw							2.17	vw					2.13	m		
			2.11	vvw	2.09	w	2.09	w			2.09	vw							2.09	w
(006)			2.03	vvw	2.04	vvw							2.03	w			2.04	m		
			1.96	m															1.98	w
			1.91	vvw																
			1.86	vw									1.86	vvw					1.88	w
(211)	1.817	w	1.81	w	1.81	vvw					1.819	vw	1.81	vw	1.82	w	1.80	m		
(205)	1.718	m	1.708	w	1.75	vw	1.741	vw			1.710	m			1.714	m				
			1.675	vvw													1.675	m	1.68	vw
(107)	1.632	vw			1.61	vw					1.620	vvw	1.62	vvw	1.637 1.628	w w			1.60	vw
	1.572	vvw	1.598	vvw			1.600	vw			1.593	vvw								
			1.546	m	1.556	w	1.546	vvw			1.544	w	1.542				1.541	m		
(303)	1.504	m	1.500	w	1.506	vw	1.506	vw			1.504	w	1.506	w	1.505	m				
(215)	1.463	m	1.4580	w	1.464	vw	1.458	vw			1.4602	m	1.461	w	1.463	m				
(108)	1.4449	m	1.4395	w							1.4379	w	1.4435	vw	1.4446	m				
(220)	1.4030	m	1.4008	m	1.4080	w	1.4054	w	1.405	vvw	1.4024	m	1.4009	m	1.407 1.403	m			1.41	vw
(311)	1.3407	m	1.3703 1.3364	w w	1.3825 1.3462	vvw vvw	1.3687 1.342	vvw vw			1.3706 1.3398	vvw w	1.3657 1.3365	vvw w	1.345 1.342	w				
(223)	1.3264	m			1.3236	w									1.326	w				
(312)	1.3142	m	1.3177	m			1.3174	w			1.3188	m	1.3174	w						
	1.2838	w									1.2809	vvw	1.2799	vvw	1.286	vw				
(306) (036)	1.2590	m	1.2602	w vw	1.2629	vvw	1.2489	vvw			1.2586	w	1.2599	vw	1.261	w				
			1.2408	vw							1.2377	vvw					1.230	s		
(401)	1.2099	w									1.2071	vvw								
(4$\bar{4}$2)	1.1904	w	1.1882	vw			1.1954	vvw			1.1888	vw			1.191	w				

[a]Relative intensities designated w = weak, m = medium, s = strong, v = very.

[b]Sample 0-8-A annealed 1 hr in vacuum at 1500°C.

[c]Sample 0-4 irradiated at 500°C.

[d]Samples 0-7 and 0-8 irradiated at about 350°C; samples 0-10, 0-11, and 0-12 irradiated at about 500°C.

[e]ASTM Data Cards 6-055 (B_4C), 3-148 and 13-212 (Graphite) and 6-0297 (B_2O_3) Inorganic Index to the Powder Diffraction File, 1969, ASTM Publ. PDIS-19i, American Society for Testing and Materials, Philadelphia.

on the pattern of sample 0-7. Even though the x-ray patterns of sample 0-9 were not suitable for quantitative evaluation, we determined that the phase with the d spacing of about 6 Å was present in the irradiated sample. Sample 0-12 appeared to be unique in not containing this phase. The significance of the ratio of B:C in the appearance of this phase during irradiation could not be evaluated due to the loss of sample 0-5 from the experiment.

The results obtained to date may be summarized as follows. The Norbide boron carbide powders contain two prominent phases, boron carbide and graphite. This material has a ratio of B:C of about 3.6. Annealing at temperatures as high as 2000°C does not lead to the solution of all of the graphitic C into the boron carbide structure. Irradiation of this material at about 350°C to about 9% burnup of ^{10}B leads essentially to the disappearance of the graphite[1] and persistence of a diffraction line at 2.64 Å, which may actually belong to the boron carbide phase.

Blending B powder into the boron carbide powder (to provide a ratio of B:C of 4.5) and then annealing the powder at high temperature results in a three-phase mixture of boron carbide, graphite, and B (the case for a 1-hr anneal at 1000°C, sample 0-7-A). Increasing the annealing temperature to 1500°C (sample 0-8-A) resulted in the disappearance of the diffraction lines belonging to the graphite and B. The boron carbide phase was all that was observed in the patterns of samples 0-8-A and 0-9-A, except for unidentified lines at about 4.2 and 1.57 Å.

Irradiation of the material with a ratio of B:C of 3.6 or 4.5 at 500°C to 7% burnup of ^{10}B led to changes in the phase composition that were not observed at 9% burnup of ^{10}B. A phase with a d spacing of about 6 and 3.2 Å appeared in every case except for sample 0-12. The phase was tentatively identified as cubic B_2O_3. It is doubtful that a source of O was available in the capsules during irradiation, and the B_2O_3 or B_2O_3-like phase may have been formed in the samples as a result of the acid leaching required to remove Cu contamination.

Transmission Electron Microscopy of Irradiated Boron Carbide (C.K.H. DuBose, D. N. Braski,[8] G. L. Copeland)

We obtained transmission electron micrographs of irradiated boron carbide by means of two techniques. For the first method, we irradiated platelets of boron carbide that had been partially prepared for thinning. Three irregularly shaped 1/8 in.-diam platelets from a high-density pellet of Norbide 325F (B:C ratio of 3.6) were metallographically polished on one side after thinning to 0.003, 0.005, and 0.009 in. thick. These platelets were irradiated in capsule 0-17 at about 400°C to a fluence of about 1.8×10^{20} neutrons/cm^2. The samples appeared to be in good condition after irradiation. Some curvature was noticed, and a piece had broken off of one of the samples. The two thicker samples were mounted in plastic and mechanically ground to the desired thinness for ion milling. However, the samples disintegrated when the plastic mount was dissolved. The 0.003-in.-thick sample was loaded directly into the ion-bombardment milling machine for further thinning. The sample was extremely brittle and broke into three pieces after thinning sufficiently for electron transmission. Each piece was large enough for use in the microscope, however. Figures 10.1 through 10.5 are typical of the structure observed in this sample. The damage was typical of that observed in metals at very high fluences. In metals, the black spots are believed to be lattice strains caused by displacements; in the boron carbide, we probably observed lattice strains caused primarily by the Li and He reaction products as well as some caused by displacements. The damage appeared to be very uniform. Figure 10.1 shows a twin [different sample tilt angles were used for Fig. 10.1(a) and (b) to change the contrast]. There appeared to be no change in the damage at the twin boundary. Likewise, as shown in Fig. 10.2, there was no observable change in the damage at grain boundaries. The two grains in Fig. 10.2 are in different contrast and reveal the same amount of damage as the sample is tilted. However, in Fig. 10.3, at higher magnification, the damage is still not distinctly resolved. Figure 10.4 shows some of the numerous microcracks observed in the sample. Although many of these cracks were probably formed during handling after irradiation, some of them appear to have formed during irradiation.

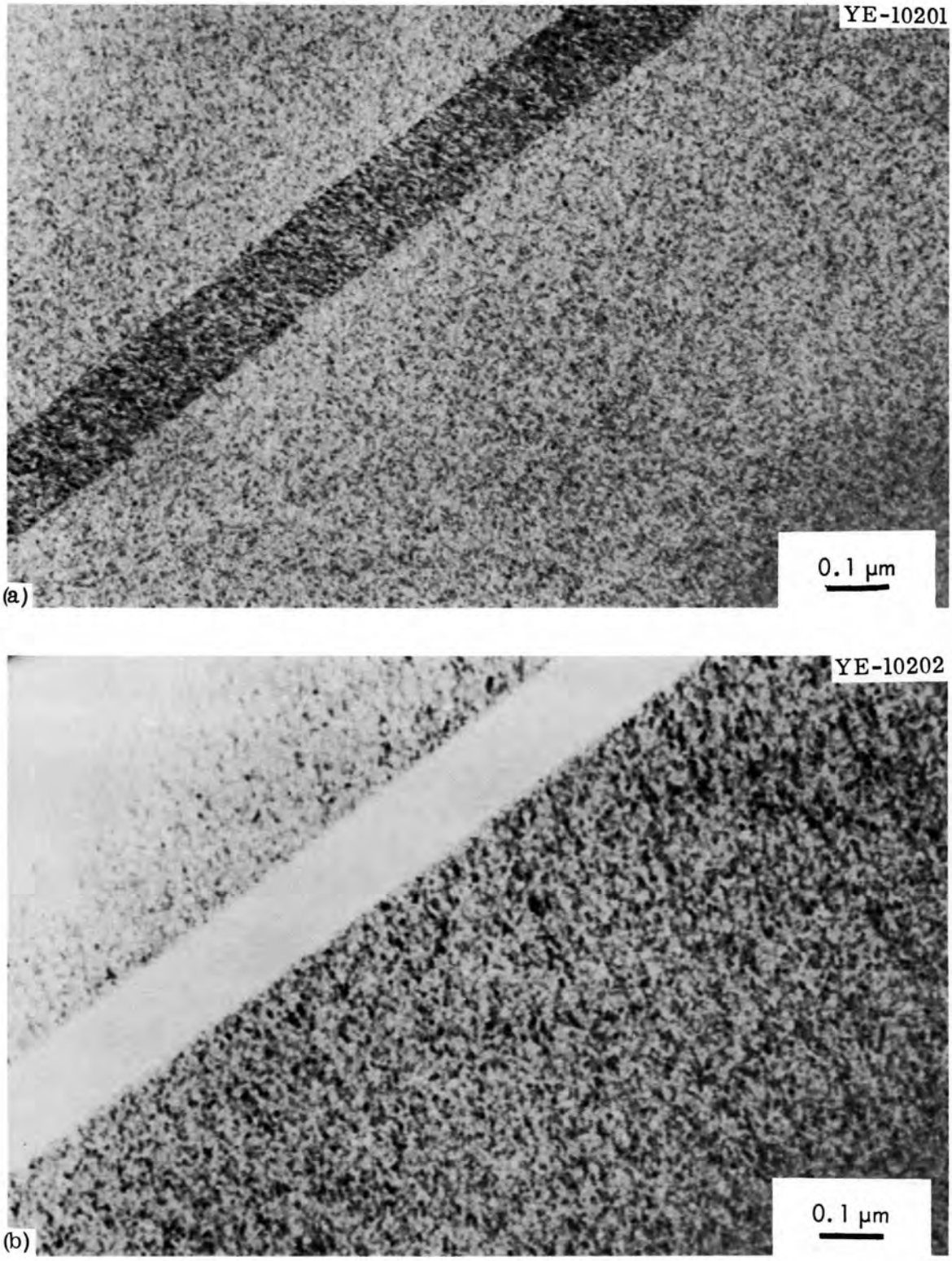

Fig. 10.1. Transmission Electron Micrographs of Irradiated Boron Carbide Foil Showing a Twinned Region. Specimen tilt in (a) is changed in (b) to change contrast. 105,000×.

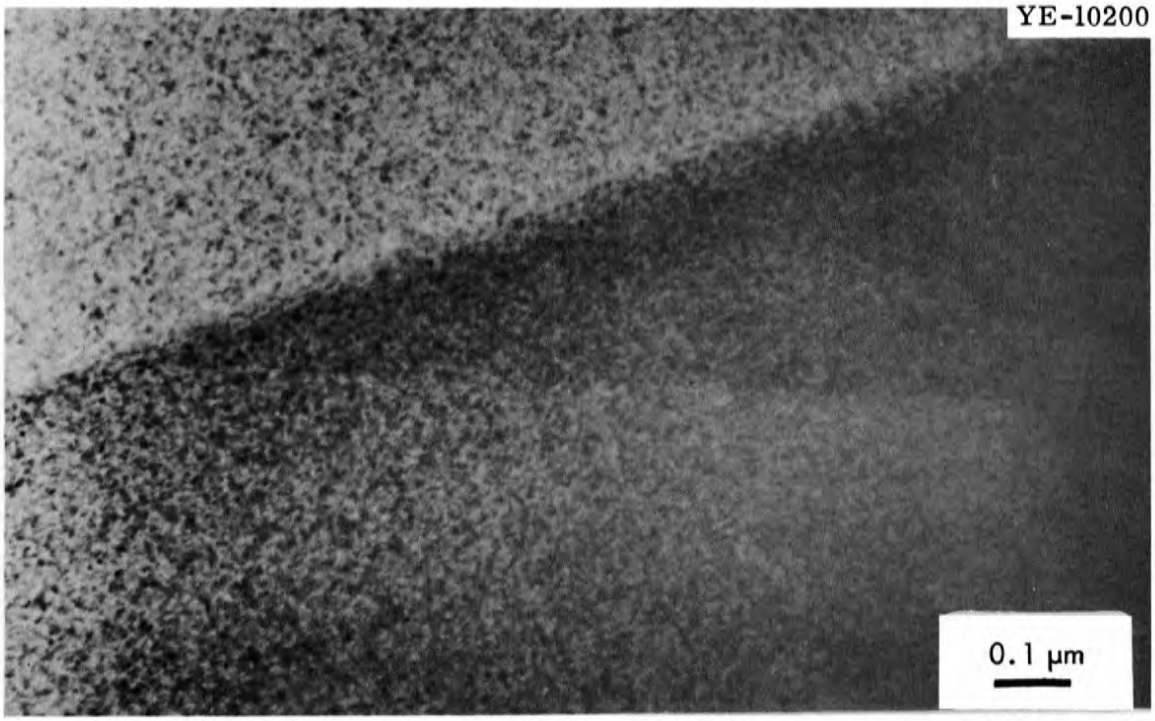

Fig. 10.2. Transmission Electron Micrograph of Grain Boundary in Irradiated Boron Carbide Foil. 105,000×.

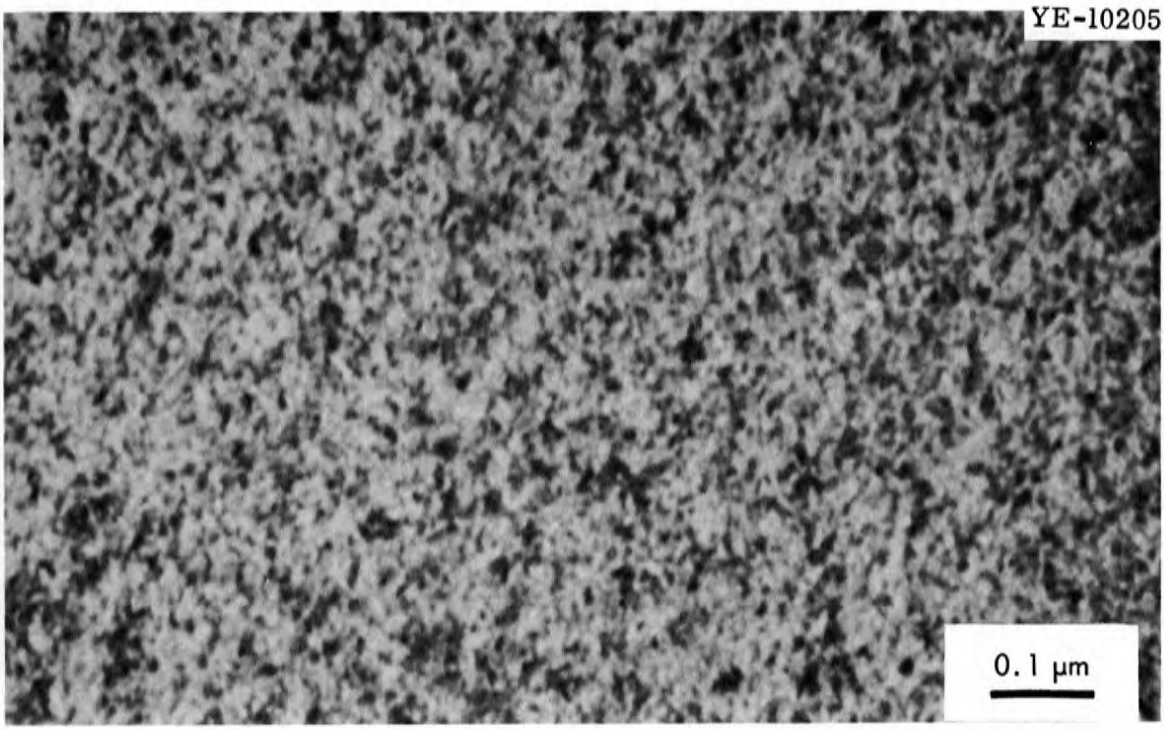

Fig. 10.3. Transmission Electron Micrograph of Typical Region in Irradiated Boron Carbide Foil. 140,000×.

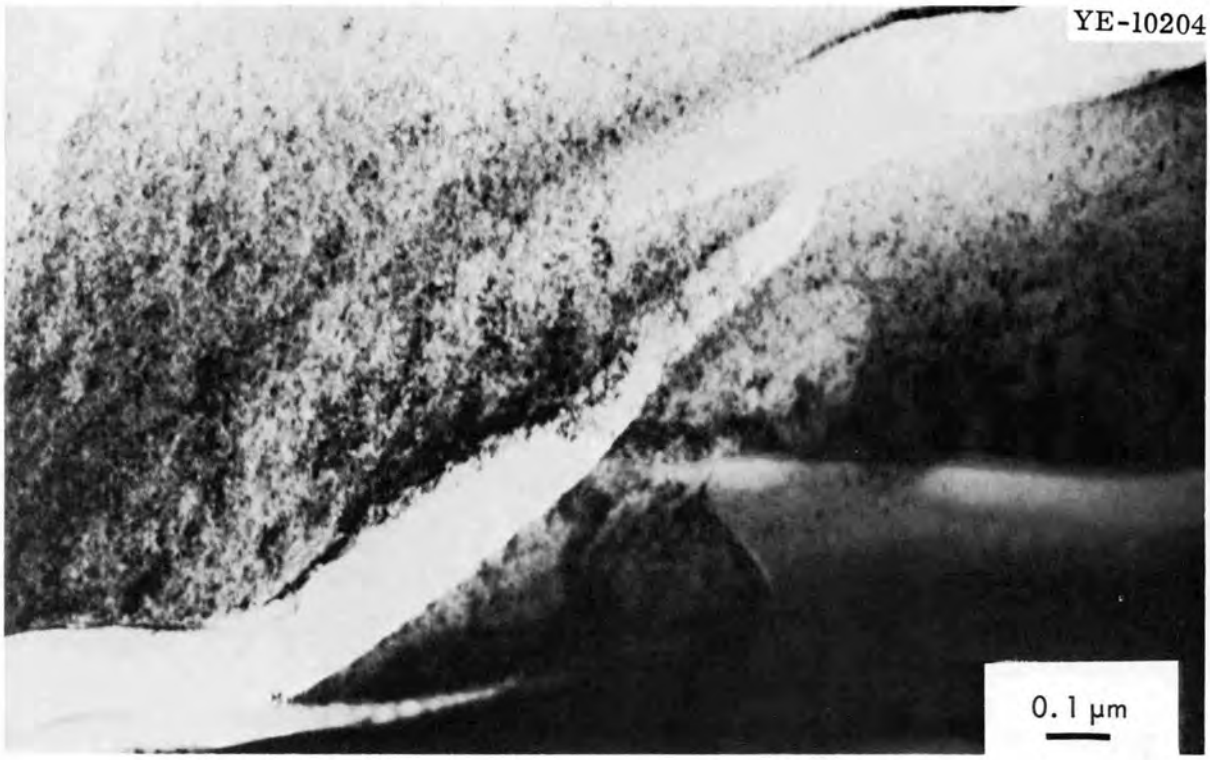

Fig. 10.4. Transmission Electron Micrograph of Microcrack Typical of Many Observed in Irradiated Boron Carbide Foil. 82,500×.

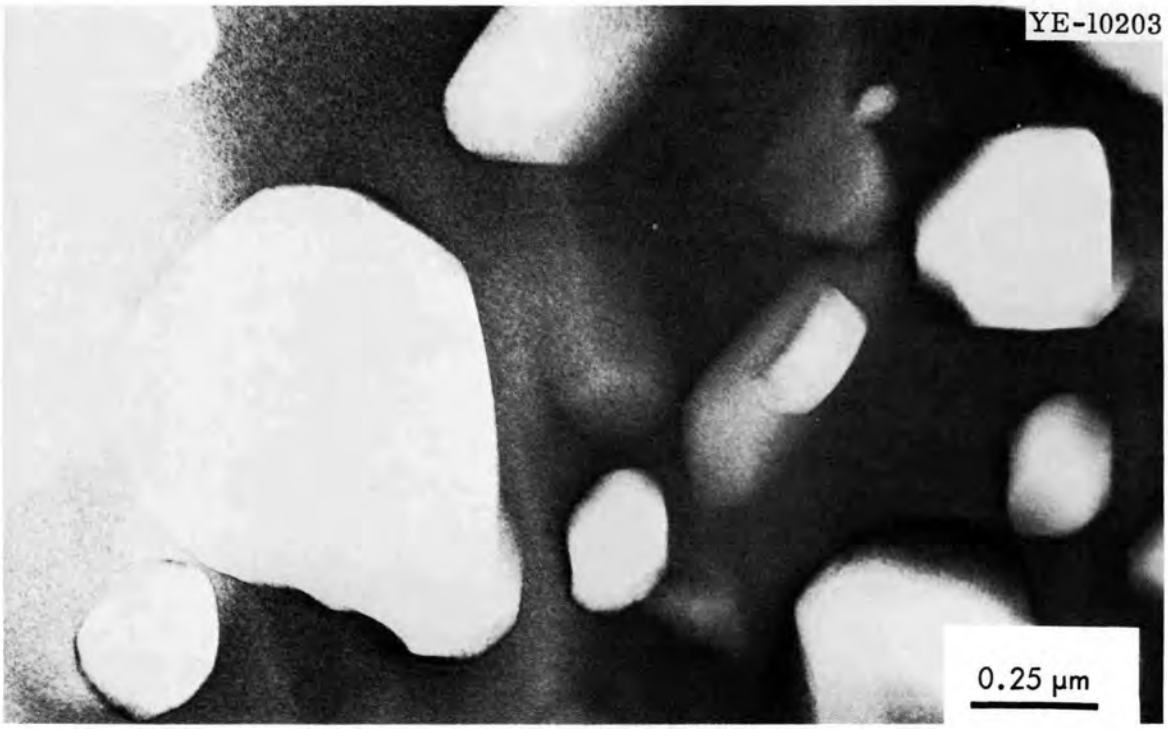

Fig. 10.5. Transmission Electron Micrograph of Irradiated Boron Carbide Showing a Region Containing Intraparticle Voids Produced During Fabrication. 70,000×.

Figure 10.5 shows some of the intraparticle voids observed in the pellet. The voids appear the same as they did before irradiation. No difference was observed in the density of the damage near the edge of the voids.

For the second method, we dispersed powders from capsule 0-7 (see Table 10.4) in Al and thinned specimens by the technique discussed previously.[9] The Al exceeded its melting point during the hot-pressing, and there appeared to have been a slight reaction at the interfaces between the Al and boron carbide particles. The boron carbide appeared to have about the same level of damage as the platelet examined previously. As shown in Fig. 10.6, the damage appeared to be uniform right up to the edge of the particles. Figure 10.7 shows no evidence of change in the density of damage at a grain boundary in one of the particles. One anomaly was observed: one particle, shown in Fig. 10.8, had a mottled

Fig. 10.6. Transmission Electron Micrograph of Irradiated Boron Carbide Particle Dispersed in Aluminum After Irradiation. There is no noticeable difference in damage at the particle edge. 82,500×.

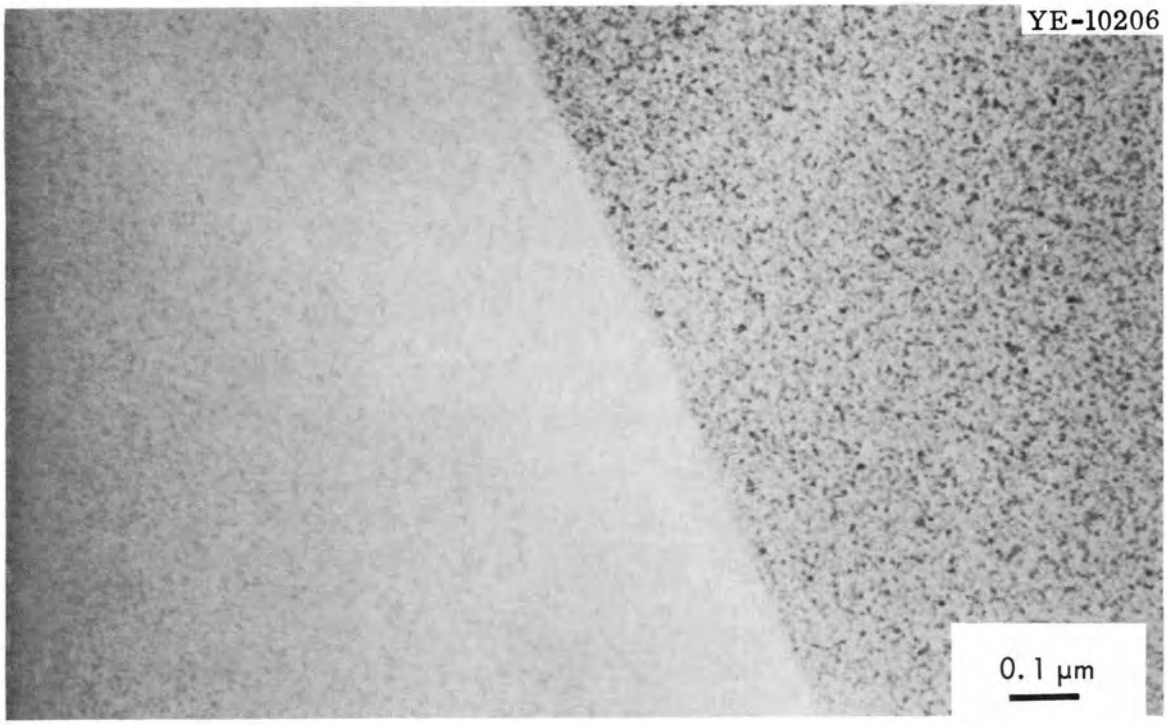

Fig. 10.7. Transmission Electron Micrograph of Irradiated Boron Carbide Particle Showing Uniform Damage at Grain Boundary. 90,000×.

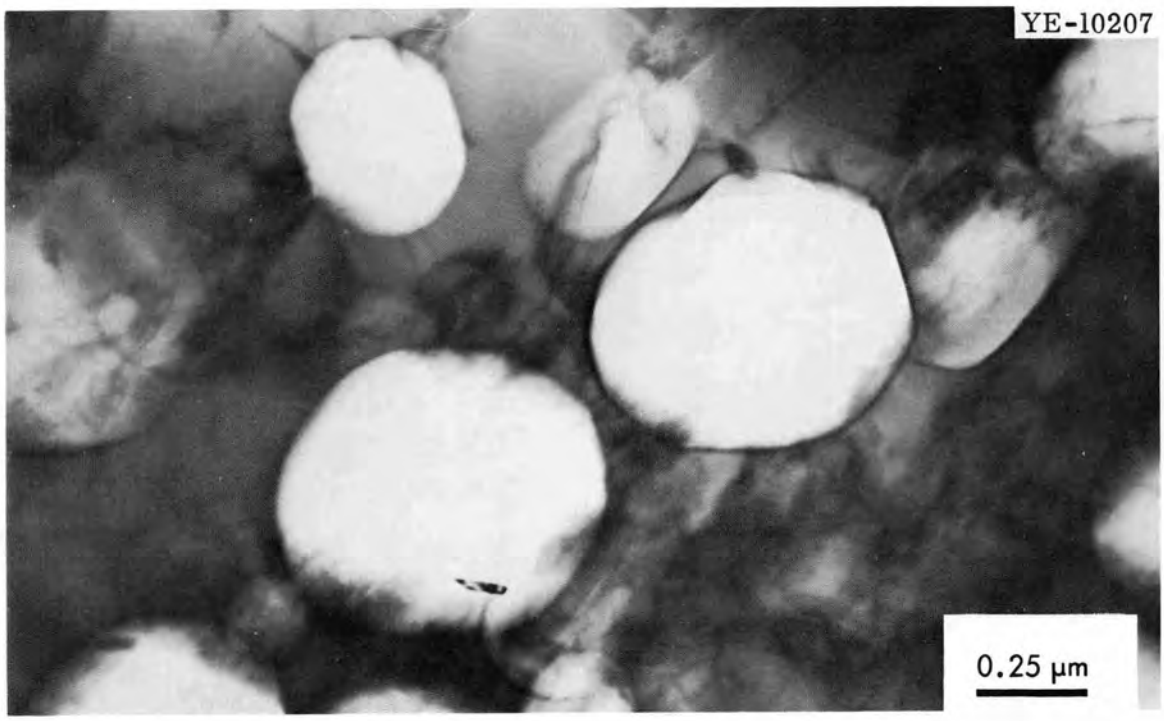

Fig. 10.8. Transmission Electron Micrograph of an Irradiated Boron Carbide Particle Showing Voids Present Before Irradiation and Mottled Dislocation Structure. 60,000×.

dislocation structure and intraparticle voids. This was our first observation of a tangled, relatively high density of dislocations in boron carbide. This particle did not show the heavy, black, irradiation damage. We do not yet have an explanation for this, but one possibility is that the dislocation movements relieved the strains and another is that burnup would have been much lower if this particle was from the center of the capsule.

In general, the irradiation damage observed in the boron carbide was similar to that observed in metals after very high fluences. There was no evidence (with the possible exception of Fig. 10.8) of movement or agglomeration of the reaction products. No bubbles or agglomerates were observed in any part of the samples.

Notes

1. R. S. Mateer and G. L. Copeland, Fuels and Materials Development Program Quart. Progr. Rept. Sept. 30, 1970, ORNL-4630, pp. 163–167.

2. C. W. Tucker, Jr., and P. Senio, Acta. Cryst. 8, 371 (1955).

3. G. L. Copeland, Fuels and Materials Development Program Quart. Progr. Rept. Dec. 31, 1969, ORNL-4520, pp. 189–190.

4. G. L. Copeland, Fuels and Materials Development Program Quart. Progr. Rept. March 31, 1970, ORNL-4560, pp. 143–146.

5. Reactor Chemistry Division.

6. V. J. Tennery and G. L. Copeland, Fuels and Materials Development Program Quart. Progr. Rept. March 31, 1970, ORNL-4560, pp. 146–153.

7. Inorganic Index to the Powder Diffraction File, 1969, ASTM Publ. PDIS-19i, American Society for Testing and Materials, Philadelphia.

8. Isotopes Division.

9. C.K.H. DuBose, D. N. Braski, and G. L. Copeland, Fuels and Materials Development Program Quart. Progr. Rept. Sept. 30, 1970, ORNL-4630, pp. 168–171.

PART II

SPACE POWER TECHNOLOGY

FUELS

11. DEVELOPMENT OF URANIUM MONONITRIDE FUELS

P. Patriarca J. L. Scott

Uranium mononitride (UN) is potentially attractive as fuel for space nuclear reactors because of its excellent stability at high temperatures, high thermal conductivity, and good irradiation stability up to 1000°C. The purpose of this program is to determine the basic mechanisms of fuel swelling and gas release at temperatures above 1000°C. Results will be used to develop a model for predicting the performance of UN as a function of temperature, burnup, and cladding restraint.

Irradiation Testing

T. N. Washburn

The basic objective of the ORNL program[1] for irradiation testing of UN is to investigate the capability of this fuel material for performance at high temperatures and low heat ratings. We are interested in fuel temperatures of 1000 to 1500°C, temperatures at the outside surface of the cladding of 900 to 1400°C, and linear heat ratings from 5 to 10 kW/ft. Fuel properties of most interest are swelling rate, release of fission gas, and compatibility with the cladding materials. The irradiation tests are conducted in the poolside facilities of the ORR. These facilities allow adjustment of the position of the test capsule relative to the reactor face and thereby make it possible to maintain a constant temperature at a selected reference point on the test specimen as the reactor flux profile changes or as the fissile content of the test fuel is diminished.

Postirradiation Examination of Capsule UN-3 (T. N. Washburn, E. L. Long, Jr., D. R. Cuneo[2])

We previously reported the nondestructive portion of the examination of the three fuel pins of capsule UN-3 (ref. 3) and the metallographic

examination of the middle fuel pin (T-111 cladding) that had failed during the irradiation test,[4] the bottom fuel pin (T-111 cladding)[5] and the top fuel pin (W–25 wt % Re cladding).[6]

The fuel pins and operating conditions of capsule UN-3 are described in Fig. 11.1. The scheduled 10,000 hr irradiation experiment was terminated after 5800 hr when detection of fission gases in the capsule indicated that one of the fuel pins had failed. We do not know what led to failure of the T-111 cladding of the middle fuel pin and incipient failure of the T-111 cladding of the bottom fuel pin. Our summary conclusion is that this batch of T-111 was not a satisfactory cladding material under the conditions of this experiment (1400°C at outside surface of cladding and 1500 to 1550°C at fuel center). The W–25 wt % Re cladding showed no evidence of unsatisfactory performance at 1300°C at the outside surface of the cladding and 1400°C at the fuel center.

All three of the fuel pins in this test had acceptable diametral swelling of less than 0.5% $\Delta D/D$ (where D is diameter). The middle and

ORNL-DWG 70-7916

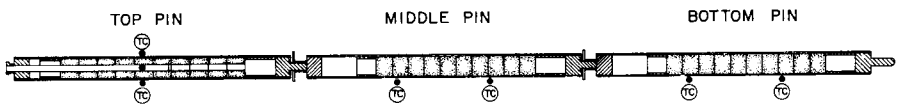

	TOP PIN	MIDDLE PIN	BOTTOM PIN
Cladding			
Material	W–25 wt % Re	T-111	T-111
Outside diameter (in.)	0.365	0.365	0.365
Wall thickness (in.)	0.030	0.027	0.027
Linear material		CVD tungsten	CVD tungsten
UN Fuel			
Type pellets	Annular	Solid	Solid
Density (% of theoretical)	95	95	95
^{235}U enrichment (%)	20	12.9	12.9
Operation			
Cladding temperature (°C)	1300	1400	1400
Fuel central temperature (°C)	1380–1330		
Linear heat rate (kW/ft)	6–8	8.8	8.8
Fuel burnup (atom %)	1.45	1.75	1.75

Fig. 11.1. Fuel Pins of Capsule UN-3.

bottom pins, which were clad with T-111, had maximum swelling of 0.5 and 0.4%, respectively; the top pin, which was clad with W-25 wt % Re, had decreased 0.7% in diameter. The T-111 pins also had local regions of diametral decrease caused by the creep collapse of the claddings at 350 psi overpressure applied to prevent the NaK heat-transfer medium from boiling. The creep was uniform; the claddings were not wrinkled or significantly oval.

Although the diametral changes of the fuel pins were low, the fuel volume increased 3.3, 6.0, and 4.5% for the top, middle, and bottom pins, respectively. These volume increases were accommodated by the initial gap between the fuel and cladding and by an increase in the fuel length of 2.3% in each pin.

The release of fission gases generated from the fuel bodies was low (0.1% for the top pin and 7.1% for the bottom pin), but the method by which the fission gas was retained led to swelling. The typical appearance of irradiated UN fuel from the bottom pin is shown in Fig. 11.2.

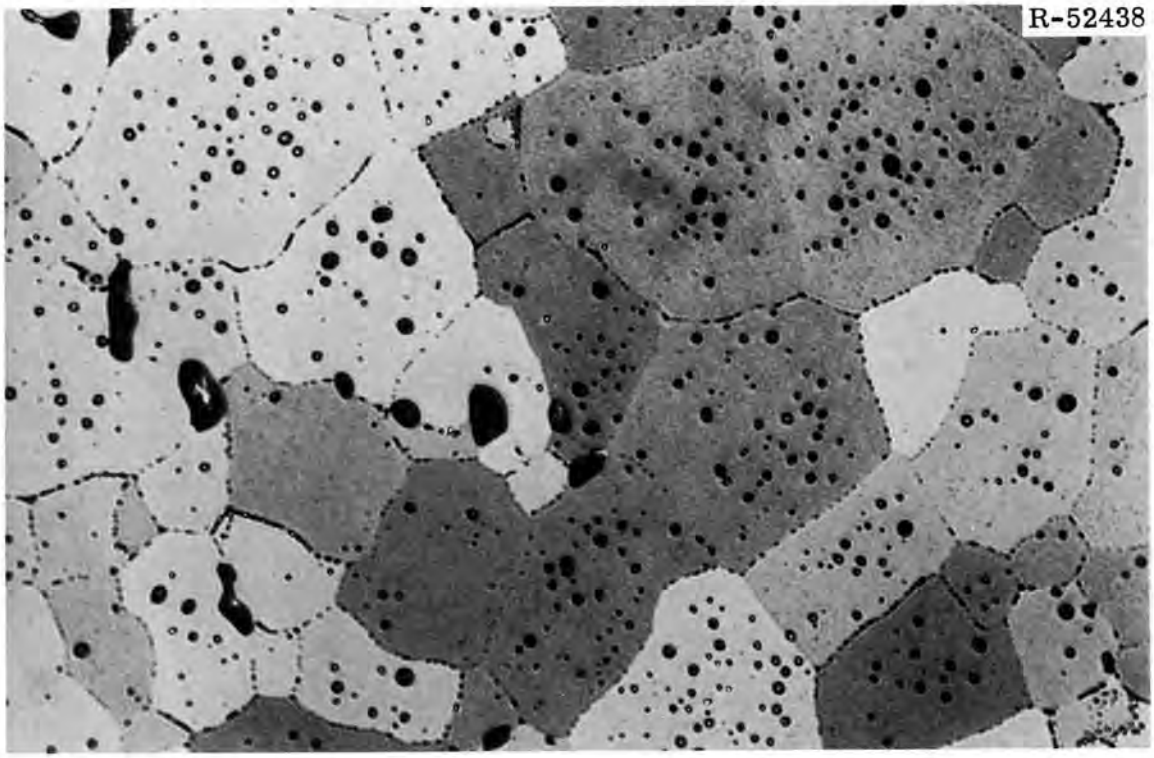

Fig. 11.2. Metallographic Appearance of Irradiated UN Fuel from Bottom Pin of Capsule UN-3. 500×.

The large pores within the grains were principally fabricated porosity, but the porosity at the grain boundaries was caused by accumulation of fission gases. The porosity at the grain boundaries is shown more clearly in Fig. 11.3 by transmission electron microscopy of replicas of fractured UN surfaces. The intergranular fracture shows massive coalescence of bubbles of fission gas at grain boundaries. The transgranular

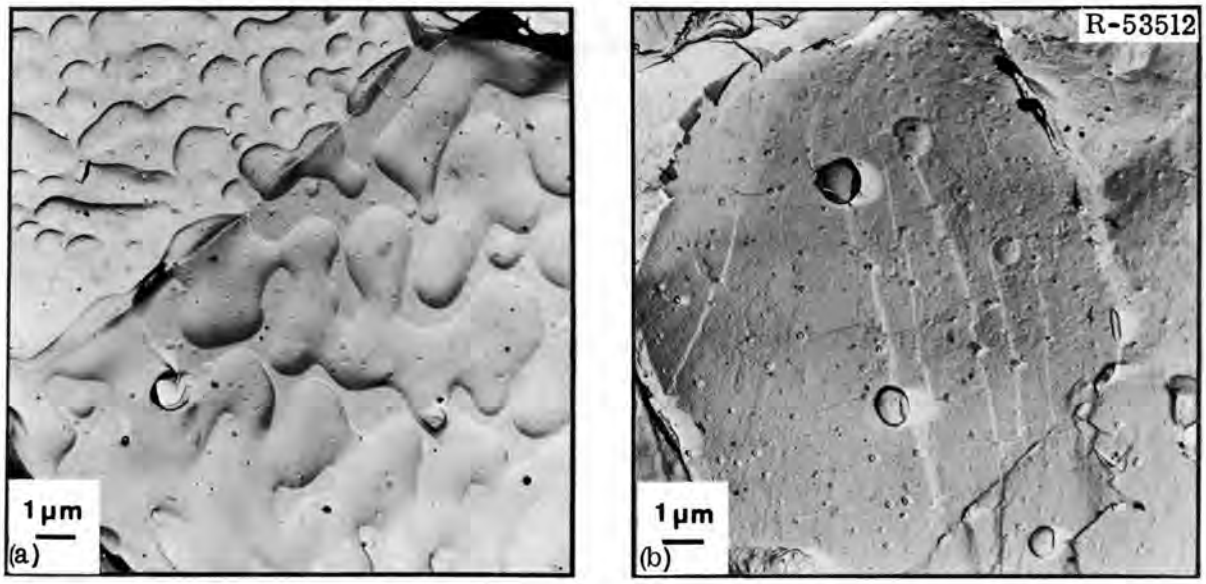

Fig. 11.3. Fractographic Surfaces from the Central Region of a UN Fuel Pellet from Bottom Fuel Pin, Capsule UN-3. (a) Intergranular and (b) transgranular. Carbon replica shadowed with chromium.

fracture shows small bubbles of fission gas in the grain as well as larger pores that we believe to be fabricated porosity. A similar comparison of the appearance of the transgranular and intergranular fractures by scanning electron microscopy of replicas is shown in Fig. 11.4. The coalescence of the fission gases at the grain boundaries forces the grains apart and produces substantial swelling of the fuel, although the fission gases are not released in large quantity from the fuel body. It was established that elimination of grain boundaries by use of single-crystal UN effectively reduces volume increases during irradiation.[7] Other investigators showed similar results by use of large-grained or porous UN fuel.[8]

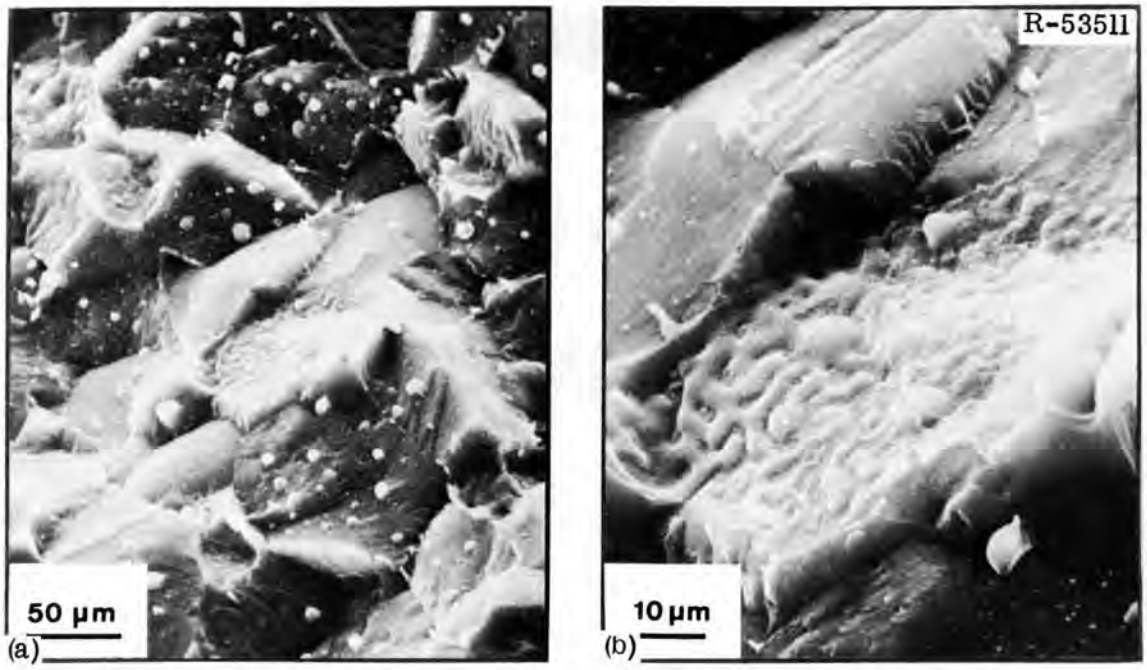

Fig. 11.4. Scanning Electron Fractographs of Central Region of a UN Fuel Pellet from Bottom Pin of Capsule UN-3. (a) Transgranular and intergranular and (b) intragranular. Plastic replica shadowed with gold.

Intergranular Fractures in T-111 in Capsule UN-3 (A. Jostsons,[9] E. L. Long, Jr., D. R. Cuneo[2])

Metallographic sections through the cracked regions of the cladding of the middle fuel pin in capsule UN-3 showed that it failed intergranularly. More detailed metallurgical investigations of failed and unfailed T-111 cladding revealed general cavitation at grain boundaries, which may limit the usefulness of T-111 as a cladding material at high temperatures.

A representative metallographic cross section of the chemically vapor deposited (CVD) W liner and T-111 cladding removed from failure regions is shown in Fig. 11.5. In addition to the band of porosity at the interface between W and T-111, porosity and cracks were present at grain boundaries in both the W liner and the inner parts of the T-111 cladding. Porosity at grain boundaries in T-111 apparently precedes the formation of intergranular cracks. The UN fuel extruded into some of the cracks shown in the W liner in Fig. 11.5, thereby demonstrating that these cracks existed at temperature and that the fuel pin experienced considerable stress. The cracked W liner is apparently ineffective as

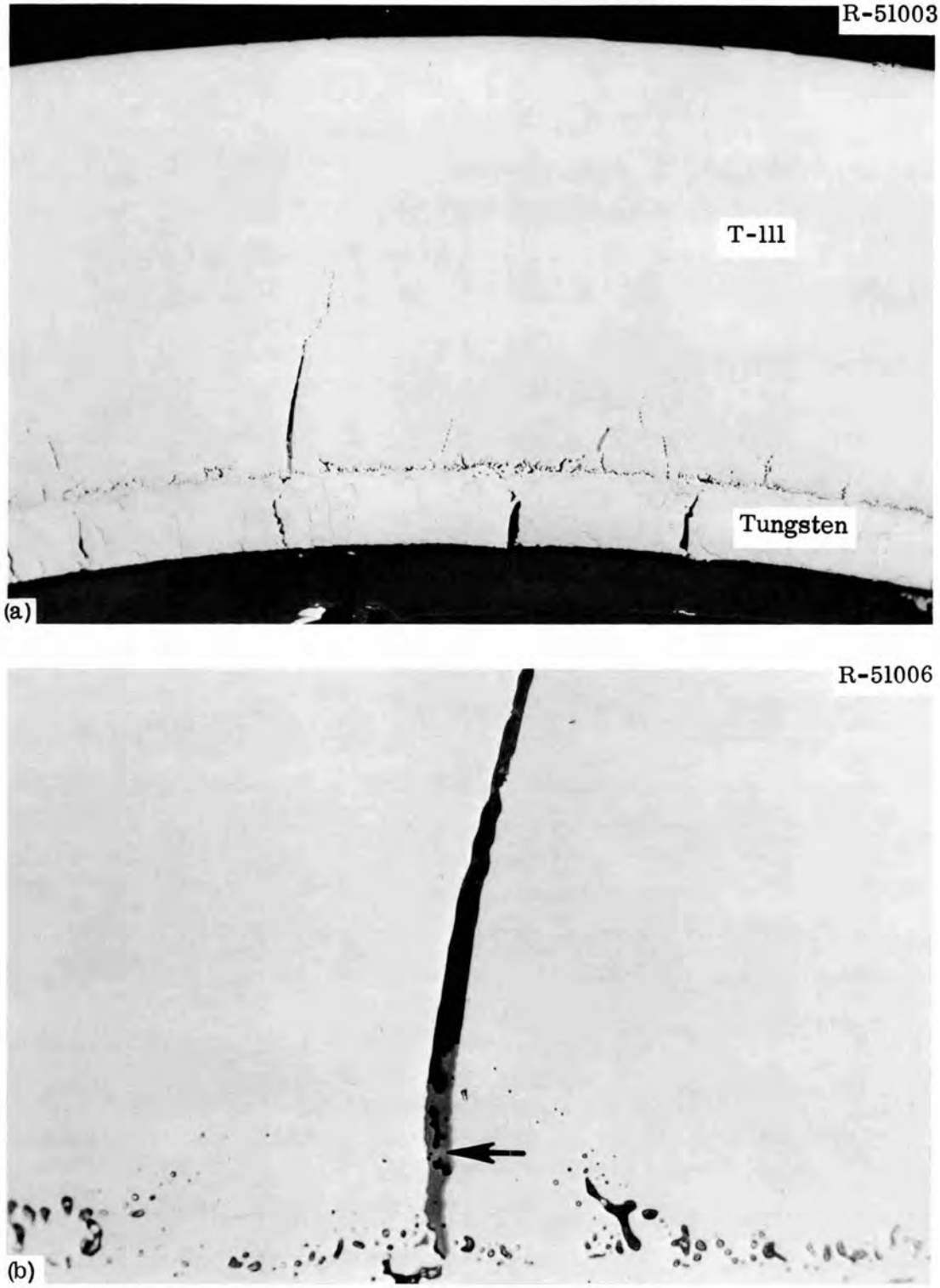

Fig. 11.5. Appearance of a Transverse Section Through Chemically Vapor Deposited Tungsten Liner and T-111 Cladding. (a) 100×, and (b) higher magnification (500×) view of gray phase (arrow) occasionally found in the intergranular cracks in the T-111 and tungsten. As polished.

a barrier to protect the T-111 from gaseous N_2 if the temperature is high enough for a significant N_2 overpressure.

Since the irradiated cladding from both pins was brittle at room temperature, we readily obtained replicas from fresh fractures. Scanning electron micrographs of a replica taken from cladding fractured longitudinally near the failed region are shown in Fig. 11.6. The large variation in grain size between regions about 1 cm apart provides additional support for our earlier hypothesis that localized hot spots developed in the cladding during irradiation. Large cavities at grain boundaries in the T-111 cladding near the interface with the W lines are apparent in Fig. 11.6(a). Higher magnification of the finer grained region, shown in Fig. 11.6(b) also revealed cavities at grain boundaries throughout the thickness of the cladding; the size of the cavities decreased from the inside to the outside surfaces of the cladding. Numerous cavities were present at the grain boundaries in the W liner, which also fractured intergranularly (Fig. 11.7).

Farrell et al.[10] and Stiegler et al.[11] extensively studied the nature of cavities at grain boundaries in CVD W. They concluded

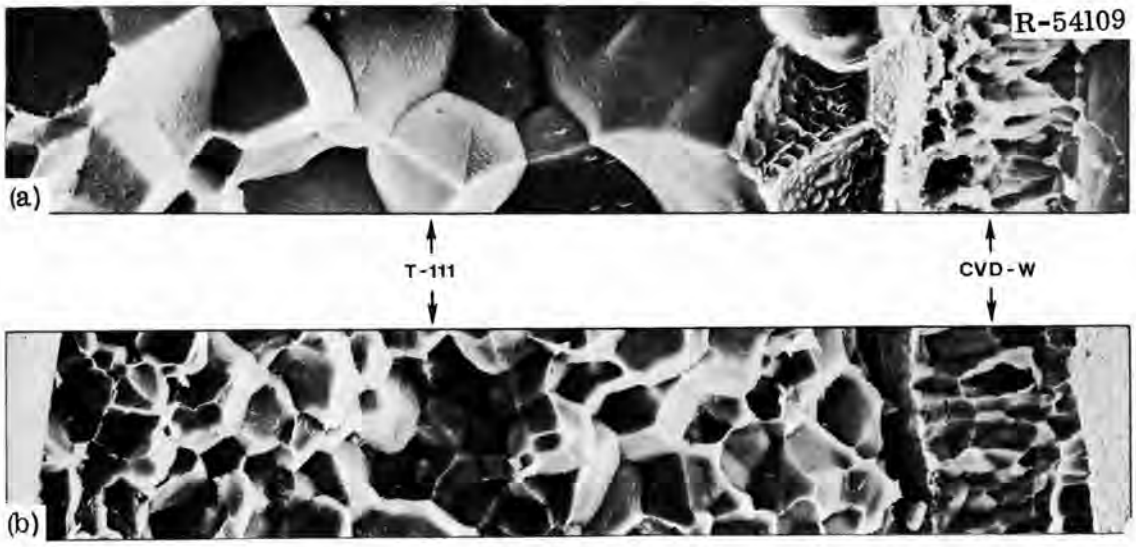

Fig. 11.6. Scanning Electron Micrographs of Two Fracture Surfaces about 1 cm Apart. (a) Region of large grains near failed region of cladding, and (b) region of smaller grains. Plastic replica shadowed with gold. About 200×.

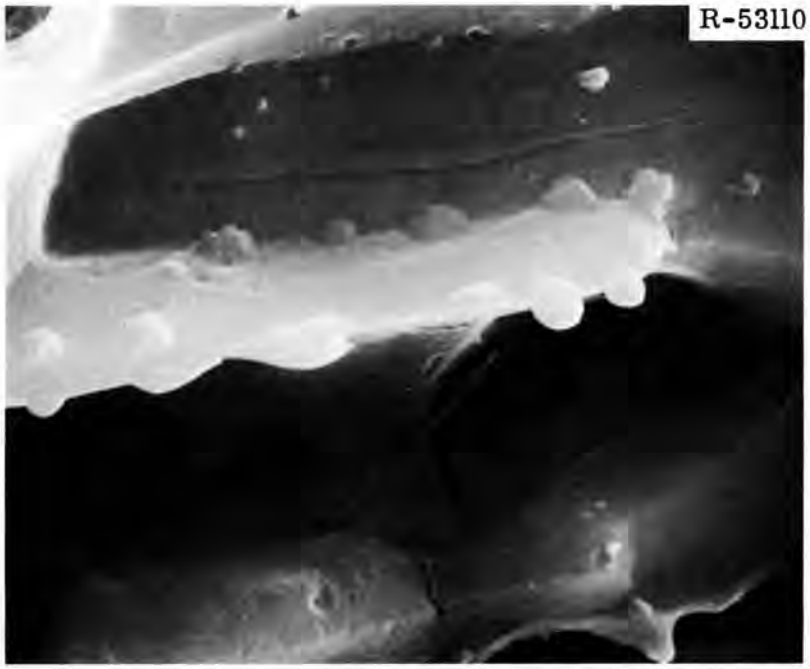

Fig. 11.7. Cavities at Grain Boundaries in Chemically Vapor Deposited Tungsten Liner as Revealed by Scanning Electron Microscopy. Plastic replica of a fracture surface shadowed with gold. 3000×.

that the cavities were small bubbles of a presently unidentified gas. The size of these bubbles was dependent on both temperature and stress. Bubbles were observed at grain boundaries by transmission electron microscopy after annealing at 1400°C or higher. Thus, our present observation of cavities at grain boundaries in the CVD W liner is not surprising, particularly in the presence of stress and supersaturation of vacancies induced by irradiation.

The explanation of cavities at grain boundaries is not as simple for T-111 as it is for CVD W. Creep-rupture specimens of unirradiated T-111 fractured at 1400°C were ductile (fracture strain > 25%) and did not fracture intergranularly even below room temperature.[12] We do not yet know what mechanism is responsible for promoting the formation of cavities at grain boundaries in T-111. We are continuing our investigation of the possible effect of the Hf concentrations at the cavities and are trying to determine the chemical form of the Hf.

Fabrication of Irradiation Capsules (E. J. Manthos)

We are fabricating three capsules for irradiation tests in the ORR. Two of these capsules (UN-4 and UN-5) will each contain three fuel pins of UN pellets in T-111 (Ta–8% W–2% Hf) cladding with a W liner to separate the fuel and cladding to minimize incompatibility of these two materials. The six fuel pins were fabricated, the capsules are being assembled, and the experiments are scheduled to be inserted into the reactor in February 1971. The third capsule (UN-6) will contain three fuel pins with UO_2 pellets. Two of the fuel pins will have Nb–1% Zr cladding, and the third will have T-111 cladding. Incompatibility of fuel and cladding will be minimized with a W liner. The fuel pin loadings are shown in Table 11.1

Table 11.1. Fuel Pin Loadings for Capsule UN-6

Fuel Pin	Cladding	^{235}U Enrichment (at. %)
Top	Nb–1% Zr	10
Middle	T-111	10
Bottom	Nb–1% Zr	8

The fuel burnup in 8000 hr will be 2%, the cladding temperature will be at least 1000°C, and the temperature at the fuel center will not exceed 1600°C.

Fabrication of the pellets was begun and should be completed in January 1971. We procured and are inspecting Nb–1% Zr bar stock for end fittings. Tubing for the fuel cladding is being fabricated from Nb–1% Zr rod.

We have T-111 cladding and end fittings and W liners on hand. Components for a Nb–1% Zr container for NaK were fabricated; the NaK vessel was rejected, however, and a new one will be fabricated. The bulkhead and cap were found to be satisfactory. Capsule UN-6 is scheduled to be inserted into the reactor on April 25, 1971.

Proposed Irradiation Tests of UN in the EBR-II (B. Fleischer, T. N. Washburn, M. K. Preston[13])

We reviewed previous irradiation tests in thermal-flux environments of UN fuel pins clad with refractory metal. Since these tests were generally successful, further testing is warranted to establish the suitability of proposed designs for compact fast-flux reactors. Accordingly, we are developing a program of irradiation tests to evaluate promising combinations of fuel and cladding for a fast flux.

We propose to perform our irradiations in row 6 or 7 in the EBR-II. To select the most desirable site, we calculated relative power levels for typical positions in the reactor. The values for these locations of interest are shown in Table 11.2. The relative power levels shown for a 6N-1 location allow us to achieve heat ratings from 4 to 11.5 kW/ft with only two levels of fuel enrichment. By staggering the withdrawal times, we shall also be able to investigate the effect of burnup at the various power levels. The cladding temperature of 1000°C during the initial tests will allow the use of Nb–1% Zr as well as T-111 and W–25% Re as cladding materials. To provide space for accumulation of gas while keeping the pin short, we shall use 95% dense annular fuel pellets in the initial experiments.

A conceptual design of the proposed test unit was made for an uninstrumented B-7B subassembly that will hold seven test capsules. Each capsule will contain three pins, thus providing 21 test positions. An isometric view of the test unit is presented in Fig. 11.8 together with a list of the materials and dimensions of interest. The fuel pin is thermally coupled to the Nb–1% Zr primary container with either Na or Li. By matching the width of the intermediate He gap to the heat ratings, we shall be able to obtain the desired cladding temperature. The outer Na gap will thermally couple the secondary containment to the outer containment vessel, thus providing a total of 4 containment vessels between the UN fuel and the EBR-II coolant. As applicable, a W barrier material will be used around the UN fuel to prevent physical contact and possible reaction of the UN with either Nb–1% Zr or T-111. Further definition of the test program and improved conceptual design of the capsule are continuing.

Table 11.2. Power Levels of Selected Subassembly Locations in the EBR-II

Subassembly 6N-1		Subassembly 7N-4		Subassemblies 7N-3 and 7N-5	
Pin Location[a]	Relative Power Level	Pin Location[a]	Relative Power Level	Pin Location[a]	Relative Power Level
1B	1.26	1B	1.30	1B	1.27
2B	1.26	2B	1.20	2B	1.20
1C	1.13	3B	1.20	3B	1.14
2C	1.13	1C	1.17	1C	1.13
3B	1.12	4B	1.10	2C	1.08
4B	1.12	1A	1.08	4B	1.08
5B	1.12	2C	1.08	1A	1.05
1A	1.05	3C	1.08	3C	1.01
2A	1.05	5B	1.01	5B	1.01
3C	1.00	6B	1.01	2A	1.00
4C	1.00	2A	1.00	4C	0.96
5C	1.00	3A	1.00	6B	0.95
6B	0.96	4C	1.00	3A	0.95
7B	0.96	4A	0.92	5C	0.91
3A	0.93	7B	0.92	4A	0.90
4A	0.93	5C	0.90	7B	0.89
5A	0.93	6C	0.90	6C	0.85
6C	0.86	5A	0.84	5A	0.85
7C	0.86	6A	0.84	7C	0.80
6A	0.79	7C	0.82	6A	0.79
7A	0.79	7A	0.76	7A	0.74

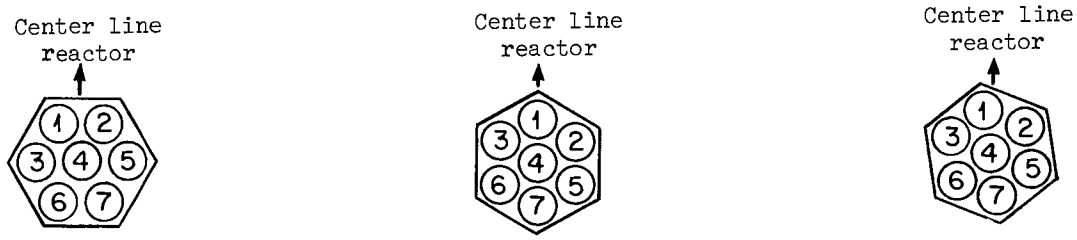

[a]Pin locations are in accordance with drawings at bottom of table. A = top pin; B = middle pins; C = bottom pin. Center of the middle pin located at midplane of reactor core.

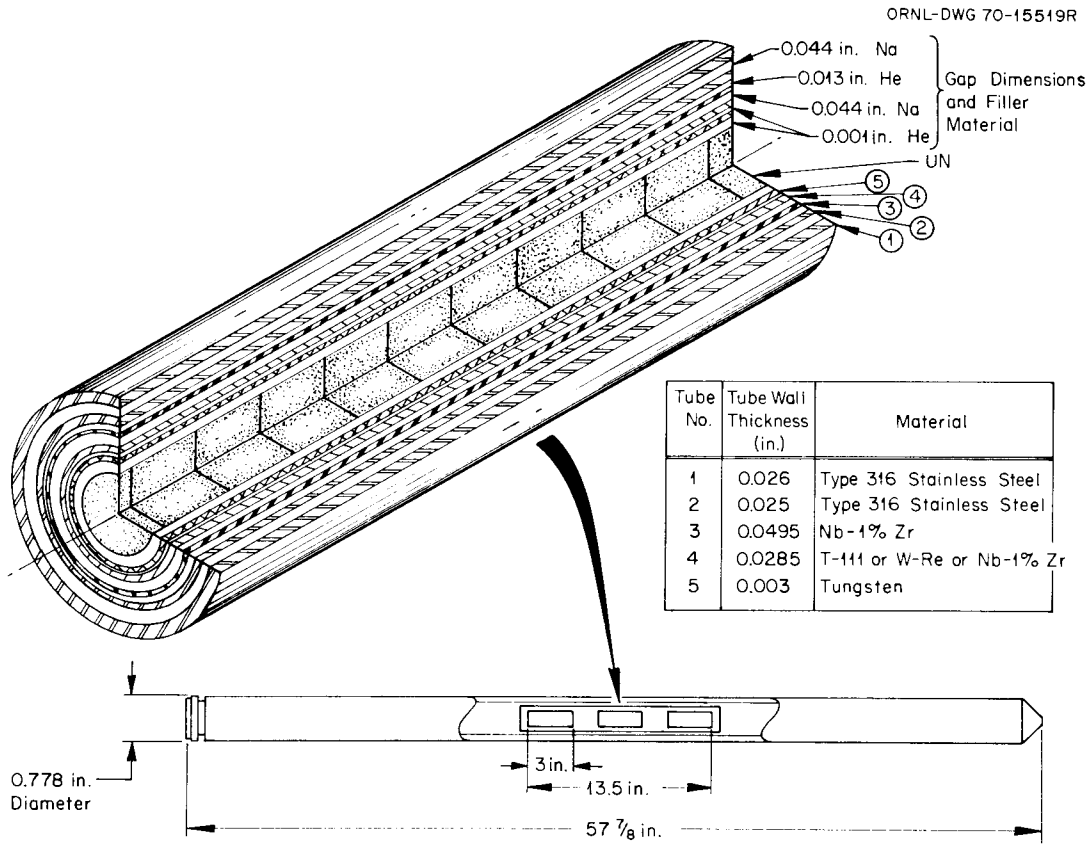

Tube No.	Tube Wall Thickness (in.)	Material
1	0.026	Type 316 Stainless Steel
2	0.025	Type 316 Stainless Steel
3	0.0495	Nb-1% Zr
4	0.0285	T-111 or W-Re or Nb-1% Zr
5	0.003	Tungsten

Fig. 11.8. Capsule for Irradiation of UN and Refractory Metal in EBR-II.

Notes

1. The current program includes work sponsored by the AEC and work sponsored by NASA under Interagency Agreement 40-184-69, NASA Order C-54536-B. Specifically, capsules UN-1, UN-2, UN-3, and UN-5 are funded by the AEC, and capsules UN-4 and UN-6 are funded by NASA.

2. On loan from Reactor Chemistry Division.

3. D. R. Cuneo, Fuels and Materials Development Program Quart. Progr. Rept. Dec. 31, 1969, ORNL-4520, pp. 195–201.

4. D. R. Cuneo and E. L. Long, Jr., Fuels and Materials Development Program Quart. Progr. Rept. March 31, 1970, ORNL-4560, pp. 165–172.

5. D. R. Cuneo and E. L. Long, Jr., Fuels and Materials Development Program Quart. Progr. Rept. June 30, 1970, ORNL-4600, pp. 177–180.

6. E. L. Long, Jr. and D. R. Cuneo, Fuels and Materials Development Program Quart. Progr. Rept. Sept. 30, 1970, ORNL-4630, pp. 180–185.

7. S. C. Weaver, K. R. Thoms, and V. A. DeCarlo, Trans. Am. Nucl. Soc. 12(2), 547 (1969).

8. R. F. Hilbert et al., Trans. Am. Nucl. Soc. 13, 102 (1970).

9. On loan from Australian Atomic Energy Commission.

10. K. Farrell, J. T. Houston, and A. C. Schaffhauser, "The Growth of Grain Boundary Gas Bubbles in Chemically Vapor Deposited Tungsten," pp. 363–390 in Proceedings of the Conference on Chemical Vapor Deposition of Refractory Metals, Alloys, and Compounds, Gatlinburg Tennessee, September 12–14, 1967, ed. by A. C. Schaffhauser, American Nuclear Society, Hinsdale, Illinois.

11. J. O. Stiegler et al., ASM (Am. Soc. Metals) Trans. Quart. 60(3), 494–503 (September 1967).

12. R. L. Stephenson and H. E. McCoy, J. Less-Common Metals 15, 415 (1968).

13. On loan from General Engineering Division.

CLADDING AND OTHER STRUCTURAL MATERIALS

12. CLADDING MATERIALS FOR SPACE ISOTOPIC HEAT SOURCES

P. Patriarca R. G. Donnelly

The purpose of this program is to develop new cladding materials for containment of radioisotopes in power systems for use in space. We are attempting to develop a single alloy with an optimum combination of strength at high temperature, fabricability, environmental stability, and resistance to oxidation in air to take the place of the layered combination of strength member, diffusion barrier, and oxidation-resistant cladding used in present devices. A more immediate goal is to develop a cladding alloy that resists oxidation and has a melting point above 2000°C to replace the Pt-Rh alloys now being used.

Development of Improved Alloys

H. Inouye

Platinum-Base Alloys (C. T. Liu)

We determined the tensile properties of Pt–5% Mo–1% Hf alloy at room temperature and at elevated temperatures (Table 12.1). The tests at elevated temperatures were conducted in a vacuum of 1×10^{-5} torr. For comparison the tensile data for Pt–5% Mo (ref. 1) and Pt–30% Rh (ref. 2) binary alloys are also included. The ternary alloy that contains 1% Hf is much stronger than the binary alloys, especially at high temperature. The ductility of Pt–5% Mo–1% Hf alloy is good in the whole temperature range tested. In fact, this ternary alloy shows 49% elongation and 100% reduction of area at about 1300°C. Thus, we conclude that a small amount of Hf effectively increases the strength of Pt-base alloys without impairing their ductility. The melting point of this alloy is estimated to be about 1860°C.

Some preliminary studies[1] show that the Pt-Rh-W and Pt-Rh-Re alloys and modifications of them that contain a certain amount of Hf, Zr, or Ti

Table 12.1. Tensile Properties of Platinum-Base Alloys at Room Temperature and Elevated Temperatures

Alloy Composition (wt %)	Ultimate Tensile Strength (psi)	Elongation (%)	Reduction of Area (%)
	Room Temperature		
Pt–5 Mo–1 Hf	129,000	19	30
Pt–5 Mo	94,000	22	70
Pt–30 Rh			
	1093°C (2000°F)		
Pt–5 Mo–1 Hf	31,100	14	28
Pt–5 Mo	18,400	20.6	37
Pt–30 Rh	22,000		
	1316°C (2400°F)		
Pt–5 Mo–1 Hf	14,000[a]	49	100
Pt–5 Mo			
Pt–30 Rh	8,000		

[a]Extrapolated from a test at 1290°C.

have great potential for use as fuel cladding for the G. E. Multi-Hundred Watt thermoelectric generators and the NASA Isotope Brayton System. In order to further qualify these alloys, we are conducting the following screening tests.

Fabricability. – The Pt alloys with 26 to 31% Rh and 8 to 10% W are more fabricable in the button form than they are when drop cast. The reason for this behavior is not understood, but it appears to be related to the rate at which the small ingots freeze as they are cast. The Pt-Rh-W alloy buttons show minor edge cracks in the early stage of fabrication. The alloys can be fabricated satisfactorily at room temperature when the poor structure produced by casting is broken. In fact, the Pt–31% Rh–9% W alloy has been cold rolled to 0.020 or 0.030-in.-thick sheets. Some preliminary studies show that the Pt–26% Rh–8% W–1% Hf–0.2% Ti alloy prepared in the 40-g button form can be hot fabricated satisfactorily at 1000 or 1200°C in air.

Melting Point. — Needle specimens of alloys Pt–31% Rh–9.9% Re and Pt–31% Rh–9.7% W were heated at 1960 to 2070°C. Neither alloy melted at 2050°C, but both melted at 2070°C. Thus, the melting point of these alloys is about 2060°C.

Air Oxidation. — The rate at which Pt–31% Rh–9 to 10% W alloys oxidize in air was measured at 649, 1000, and 1200°C. No visible oxide layer was observed on the alloy surface. Metallographic examination of the specimen of Pt–31% Rh–9.7% W exposed to air at 1000°C for 270 hr showed neither oxides nor porosity on the grain boundaries. The alloy lost weight at an average rate of 5.6×10^{-4} mg cm^{-2} hr^{-1} at 1000°C. Some preliminary data indicate that the rate of oxidation is negligible at 649°C and is about 10×10^{-3} mg cm^{-2} hr^{-1} at 1200°C. Alloy Pt–31% Rh–9.9% Re lost weight at a rate of 16×10^{-4} mg cm^{-2} hr^{-1} at 1000°C. From these results, we conclude that the resistance of these alloys to oxidation is excellent.

Compatibility with T-111. — To determine the compatibility of Pt–31% Rh–9% W with T-111, we sandwiched a metallographically polished 0.02 × 0.24 × 0.37-in. sheet specimen between two 0.5-in.-diam disks of T-111. This composite specimen is being annealed at 900°C at about 1×10^{-8} torr. The 1000-hr compatibility test will be completed on January 25, 1971.

Mechanical Properties. — Tensile specimens will be stamped to size from 0.020-in.-thick sheet stock and tested at elevated temperature.

Weldability. — Samples of sheet stock will be gas tungsten-arc welded and subjected to bend tests at room temperature.

Notes

1. C. T. Liu and H. Inouye, Fuels and Materials Development Program Quart. Progr. Rept. Sept. 30, 1970, ORNL-4630, pp. 186–190.

2. General Electric Company, Multi-Hundred Watt, Radioisotopic Thermoelectric Generator Program, GESP-7034 (March 1970).

13. PHYSICAL AND MECHANICAL METALLURGY OF REFRACTORY ALLOYS

P. Patriarca R. G. Donnelly

The purpose of this program is to provide a broad, base-technology evaluation of high-temperature alloys for use in high-performance nuclear reactors and isotopic heat sources for advanced space, terrestrial, and civilian power applications. Principal emphasis is placed on materials problems that involve Ta-, Nb-, Mo-, and V-based alloys.

Physical Metallurgy

H. Inouye

Effect of Nitrogen on Mechanical Properties of T-111 (H. Inouye)

The objective of this study is to determine the creep properties of T-111 exposed to low-pressure N_2. We shall attempt to determine the applicability of long-time creep da' obtained in ultrahigh vacuum to the design of T-111 cladding for UN.

Single tests of T-111 stressed to 10^4 psi were run at 1200 and 1400°C and 1×10^{-6} torr N_2. Table 13.1 compares the preliminary results with literature values obtained from tests in ultrahigh vacuum. The time required to produce 1% creep strain in N_2 was about one-third of that required to produce the same strain in ultrahigh vacuum. The rupture life in N_2, determined on the basis of the single results at 1400°C, was about one-eighth of that in vacuum. We consider these results only indicative of the effect of N_2 contamination since we have not yet tested controls of the same heat of T-111 in vacuum.

Effect of Oxygen on Mechanical Properties of T-111 (C. T. Liu)

The Ta alloy T-111 is now used as the strength member in cladding for power systems fueled with radioisotopes for use in space. However, the refractory alloys may suffer a loss of their superior properties when contaminated with interstitial impurities. We are studying the effects of O contamination on the mechanical properties of T-111. In

Table 13.1. Comparison of Creep Properties of T-111 Stressed to 10^4 psi in 1×10^{-6} torr N_2 and in Vacuum[a]

Time to 1% Strain, hr		Rupture Life, hr		Creep Rate, hr^{-1}	
10^{-9} torr Vacuum	10^{-6} torr N_2	10^{-9} torr Vacuum	10^{-6} torr N_2	10^{-9} torr Vacuum	10^{-6} torr N_2
		Tested at 1200°C			
1260[b]	468			$\sim 1 \times 10^{-5}$[c]	1.3×10^{-5}
		Tested at 1400°C			
8.9[b]	3.5	300[c]	38.5		

[a]Specimens were annealed 1 hr at 1650°C in vacuum before they were tested in N_2.

[b]K. D. Sheffler, Generation of Long Time Creep Data on Refractory Alloys at Elevated Temperatures, TRW-ER-7442 (January 15, 1970).

[c]R. L. Stephenson and H. E. McCoy, Jr., J. Less-Common Metals 15, 415–424 (1968).

applications in space, low-pressure O may come from the decomposition of oxide fuel or the release of gaseous impurities from a graphite heat shield. Mechanical properties, such as impact strength, may change drastically when the level of contamination is beyond the solubility limit of the alloy. Thus, the determination of the limit of O solubility in T-111 may help greatly in interpreting the results of our total program.

Our experimental procedure will consist of

1. contamination of specimens by exposure to about 1×10^{-5} torr O_2 at 1100°C for various times depending on the amount of contamination desired,
2. short anneals at 1650 to 1925°C to simulate reentry conditions and homogenize the alloys,
3. tensile tests at elevated temperature,
4. metallographical examination,
5. chemical analysis of the O content of the alloys, and
6. x-ray diffraction measurement of the lattice constant and identification of phases.

The dynamic system is set up and ready to contaminate the 0.02-in.-thick sheet specimens with controlled amounts of O at 1100°C.

Because of the strong affinity between O and the elements in Group IVA, T-111, which contains 2 wt % Hf, is expected to have a low limit for O solubility. The limit of interstitial solubility in these alloys can be determined by measuring the lattice constant as a function of interstitial content.[1] A series of data points is required to determine it accurately, but recent work shows that, in principle, the solubility can be calculated out from one measurement of lattice constant.

To illustrate the method, let us consider a T-111 alloy containing X_{Hf} at. % Hf and contaminated with X_O at. % O. The formation of HfO_2 is equivalent to the chemical reaction

$$Hf + 2O \rightarrow HfO_2 \;;$$

therefore,

$$\frac{A_{HfO_2}}{A_{Hf}(A_O)^2} = K_1 \quad , \tag{1}$$

where A denotes activity. The activity of HfO_2 at the solubility limit is unity, and Henry's law reduces Eq. (1) to

$$X_{Hf}(X_O^*)^2 = K_2 \ , \tag{2}$$

where X_O^* is the limit of O solubility in the alloy. When the limit of O solubility is exceeded, HfO_2 is precipitated from the β-phase solid solution according to the reaction given above; then

$$(X_{Hf} - X)(X_O - 2X)^2 = X_{Hf}(X_O^*)^2 = K_2 \ , \tag{3}$$

where X equals the amount of Hf precipitated from the β-phase solution by formation of HfO_2 phase.

The effect of O and Hf additions on the expansion of lattice constants of the β phase (A_β) can be expressed by use of Vegard's law as

$$A_\beta = A_{Ta - 8\,W} + A(X_{Hf} - X) + B(X_O - 2\,X) \ , \tag{4}$$

where A and B are constant and can be obtained from literature data.[2,3]

If A_β and X_O are measured from a T-111 specimen contaminated with known levels of O, the limit of O solubility can be then calculated by solving Eqs. (3) and (4) simultaneously.

Development of Age-Hardening Refractory Alloys (C. T. Liu, R. W. Carpenter)

Our objective is to develop age-hardening refractory alloys for use at elevated temperatures. We determined the effect of aging treatment on the strength of a Ta–65% Hf alloy by compression tests at room temperature; the results are summarized in Table 13.2. For specimens with strengths less than 250,000 psi, the test was extended to 5% strain; for specimens with higher strengths, the test was stopped after yielding to avoid damage to the compression rig. The yield strength of the specimens as quenched (σ_y) was 152,000 psi. The aging response at 1030°C was tremendous: the σ_y reached a value of 308,000 psi after a 1 min aging and thereafter dropped continuously. The variation of σ_y with temperature and time is in good agreement with the microhardness data reported

Table 13.2. Effect of Aging on the Strength of the Ta–65% Hf Alloy at Room Temperature

Specimen	Aging Treatment[a]	Yield Strength (psi)
		$\times 10^3$
T(35)-1-80		152
T(35)-1-80-a	1 min at 1030°C	308
T(35)-1-80-b	7 min at 1030°C	271
T(35)-1-80-c	1 day at 1030°C	180
T(35)-1-80-d	7 min at 1150°C	152

[a]All samples homogenized 40 min at 1815°C and oil quenched before indicated aging treatment.

previously.[4] This age-hardening alloy is much stronger than the existing Ta-base alloys. For example, the σ_y of this alloy in the overaged condition [i.e., aged 7 min at 1150°C (ref. 5)] was 250% higher than that of T-111.

The newly-obtained data for the hardness of the Ta–43.5 wt % Zr alloy isothermally aged at 720 and 1300°C are plotted in Fig. 13.1 together with those reported previously.[6] Three types of aging curves are observed. The curve for aging at 270°C is typical; that is, within a short time (7 min) the hardness reaches its maximum value (about 617 DPH) and thereafter drops with time. The curves at 850 and 1030°C show a continuous decrease in hardness with increased aging time, and the curves at 1150 and 1300°C show an increase in hardness after an initial drop. Photomicrographs (Fig. 13.2) of specimens aged at 1150°C for 3 and 25 min, respectively, show some coarsening of uniformly dispersed precipitates with time but provide no information on the cause of the hardness peak at 9 min of aging. However, x-ray diffraction detected the presence of a hexagonal close-packed α phase in the specimen aged 9 min at 1150°C in addition to the two body-centered cubic β phases, which are the equilibrium phases at that temperature. This may indicate that the β to α transformation cannot be suppressed completely by quenching in oil from 1150°C and above.

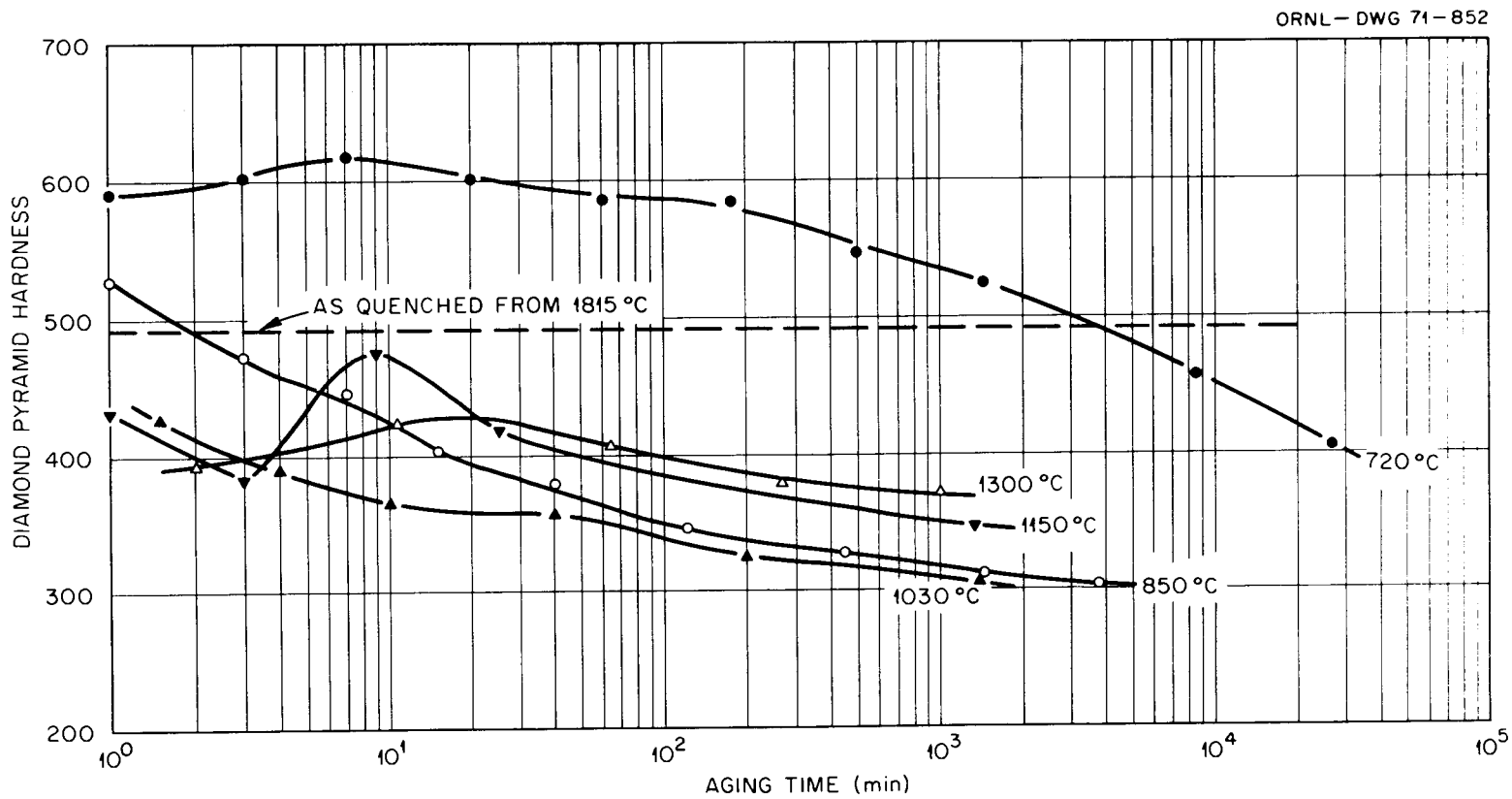

Fig. 13.1. Diamond Pyramid Hardness of Ta–43.5 wt % Zr Alloy Aged Isothermally.

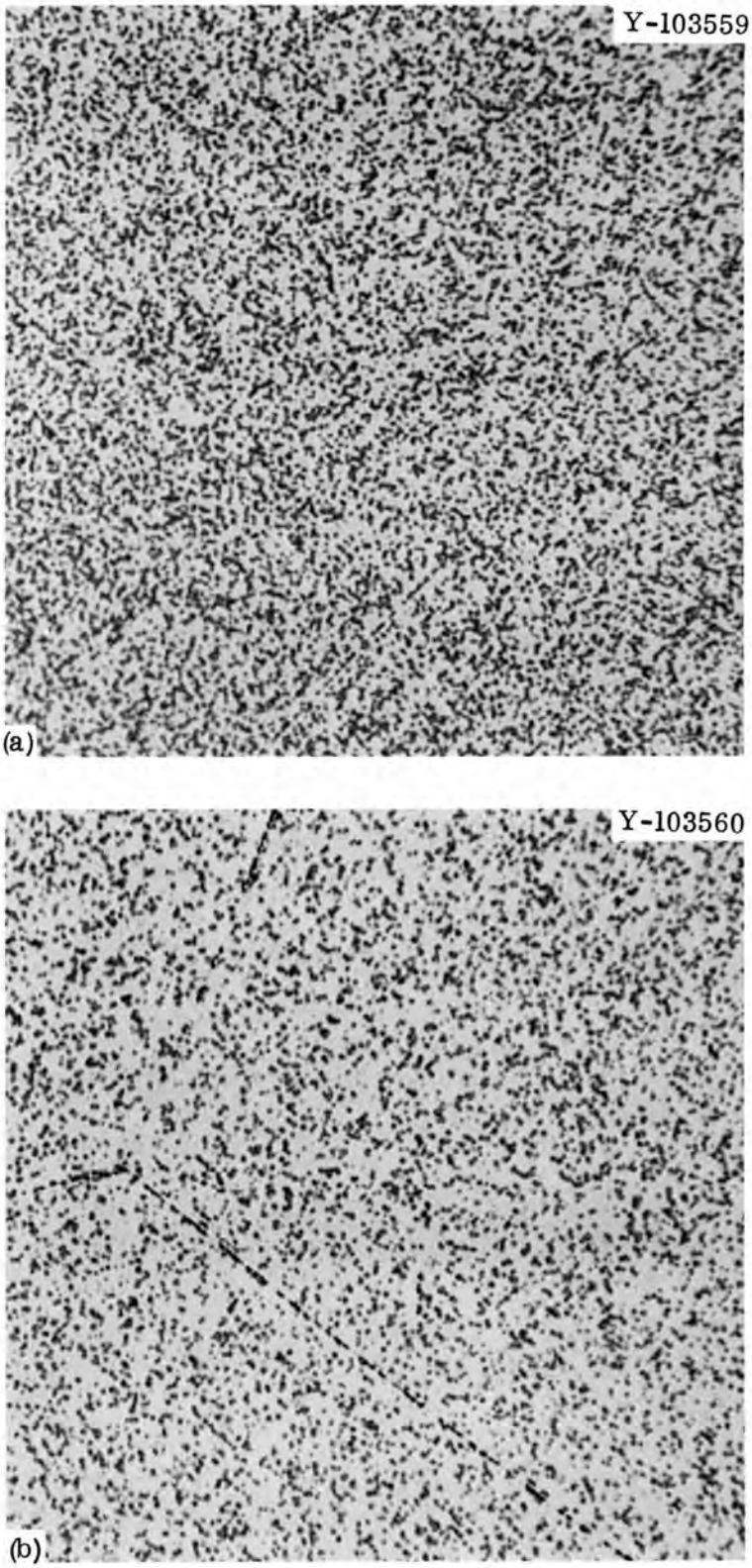

Fig. 13.2. Precipitation in Ta–43.5 wt % Zr Alloy. (a) Aged 3 min at 1150°C and (b) aged 25 min at 1150°C. 500×.

Mechanical Properties

H. E. McCoy, Jr.

Mechanical Properties of Welds (R. L. Stephenson)

Since most practical devices require joining, we consider the creep properties of welds to be of critical importance in evaluating materials for use at high temperatures. Stress-rupture data on transverse welds in Ta–10% W and T-111 were reported previously.[7,8] In both cases, the rupture times of the welds were equal to those of controls at low stresses but were much shorter at high stresses. The stress-rupture properties of transverse welds in T-222 are shown in Fig. 13.3. Again, the rupture times of welds were equal to those of control specimens at low stresses but were shorter at high stresses, at least at the two lower temperatures. At 1650°C, the control point at 9400 psi did not fit this pattern.

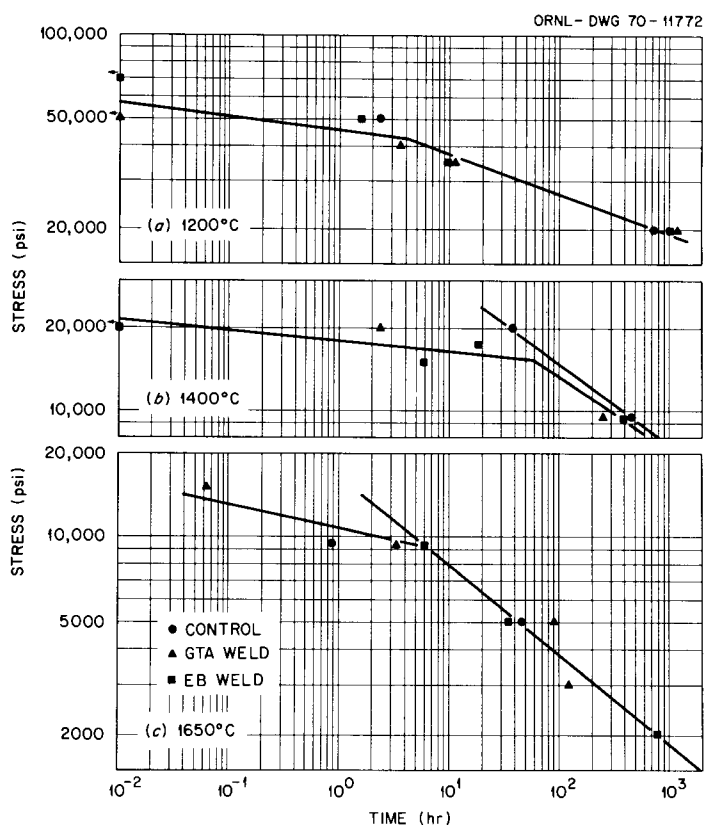

Fig. 13.3. Stress-Rupture Properties of Transverse T-222 Welds.

Long-Time Creep Properties of Refractory Alloys (R. L. Stephenson)

We began testing alloy SU-31 (Nb–17% W–3.5% Hf–0.12% C–0.03% Si). The stress-rupture data obtained to date are shown in Fig. 13.4. This is the strongest Nb-base alloy we have tested.

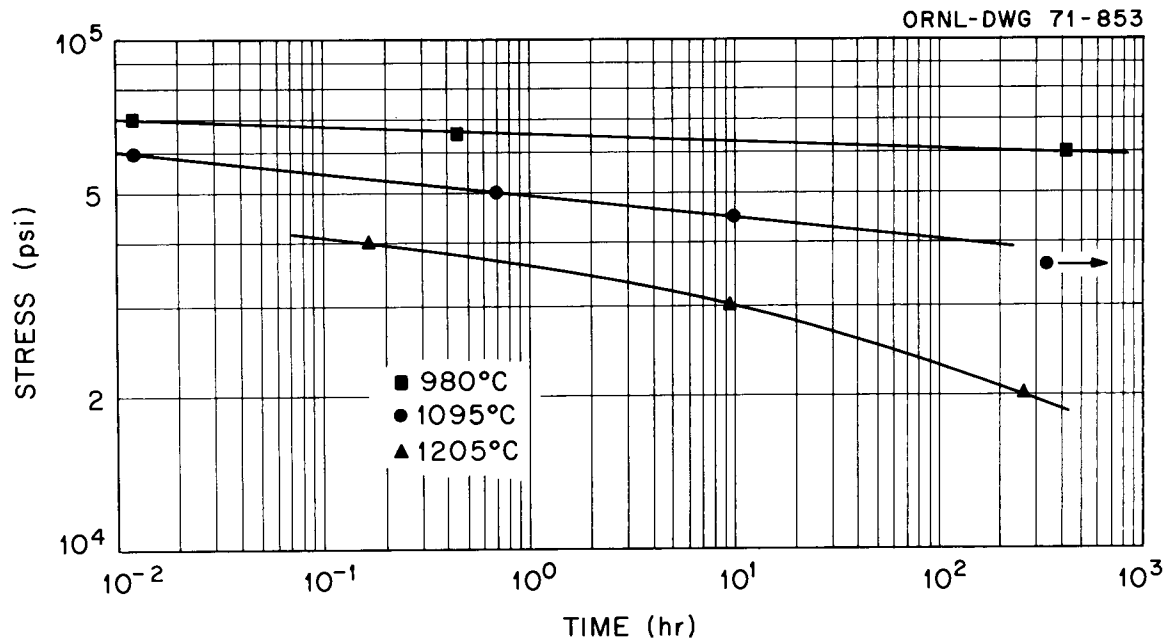

Fig. 13.4. Stress-Rupture Properties of Alloy SU-31.

Joining

G. M. Slaughter

Analysis of Cracking During Welding of TZM and Molybdenum (C. D. Lundin[9])

We continued our study of the morphology of fractures in Mo and TZM. We emphasized identification of the elemental species responsible for hot cracking in TZM and of the fracture characteristics of welds in pure Mo.

We used the Phillips electron microprobe and MAC 400S scanning electron microprobe to determine the composition of the liquid film[10] evident in the hot-cracked areas of TZM welds. Scans for all elements with atomic numbers down to and including N showed no conclusive evidence of the

presence of impurities. X-ray intensity measurements using the Mo:O_2 and Mo:N_2 intensity ratios were made on the hot-cracked and cold-cracked areas. Again, no substantial differences were noted; however, we believe that these measurements are not statistically significant enough to conclusively prove the presence or absence of O_2 and N_2. Additional efforts are being made to identify the elements responsible for hot-cracking.

We fractured Mo welds at room temperature to expose grain boundaries in the fusion zone. The characteristics of the grain boundaries are significant in that all fractures proceed along grain boundaries. Several interesting features were observed on these boundaries, such as rod-like precipitates or rod-like porosity (Fig. 13.5). The occurrence and nature of this feature is a function of the crystallographic orientation of the grain faces exposed by fracturing. Stereographic pairs of micrographs are being prepared to determine whether these features are precipitates or porosity.

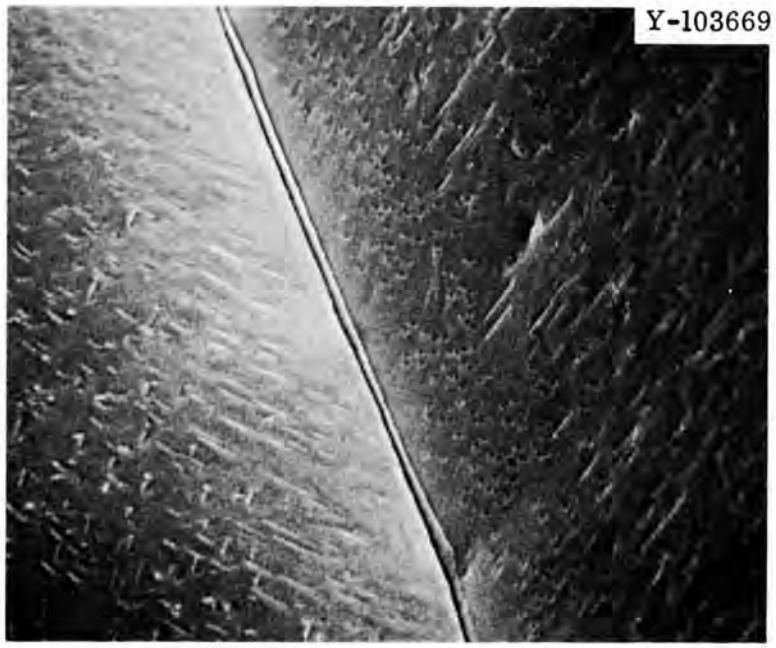

Fig. 13.5. Scanning Electron Micrograph of Fracture at Grain Boundary in Fusion Zone of Weld in Molybdenum. Note precipitate or porosity morphology. 1000×.

Analysis of Cracking in Molybdenum Tubing (C. D. Lundin,[9] A. J. Moorhead)

We have included in our program on the hot cracking of refractory alloys during welding a study of base-metal cracking in Mo tubing. We believe that this study is important, for this type of defect is becoming increasingly important in our fabrication of refractory-metal components. One example is the crack that propagated through the wall of the Mo convection loop during welding.

The initial defect being studied is a longitudinal crack detected by fluorescent penetrant inspection on the inner surface of a 6-in. length of 3/8-in.-OD × 0.025-in.-wall-thickness low-C, Mo tubing drawn from arc-cast stock. Although the crack was about 1/2 in. long and extended to the end of the tube, it apparently did not pass completely through the wall. We say "apparently" because there are some cases in which this type of defect has been undetected by penetrant inspection because metal was smeared over the flaw during fabrication.

We cut the portion of the tube containing the defect longitudinally so that we could examine the surface of the crack with the scanning electron microscope. The micrographs in Fig. 13.6 show that the inner surface of the tube was quite rough, torn, and smeared by the plug or mandrel drawing operation during tube fabrication. We could not discover any reason for propagation of the crack along its particular path.

We split the tube and examined the fracture surfaces of the crack and base metal. Figure 13.7 shows that the original defect apparently was a large elongated grain that failed by cleavage. This type of fracture indicates that the failure occurred below the ductile-to-brittle transition temperature. Apparently, the finer grained structure below the surface prevented further propagation of the crack until the tube was split open for study. Examination of the tube wall revealed that, when the tube was broken open, it failed in a predominately intergranular mode, although an occasional grain failed by cleavage.

Fabrication of Refractory Metal Components (A. J. Moorhead)

The 1 1/2-in.-long crack in the tubing of the Mo convection loop[11] was satisfactorily repaired by welding. We drilled a small hole through

Y-104332

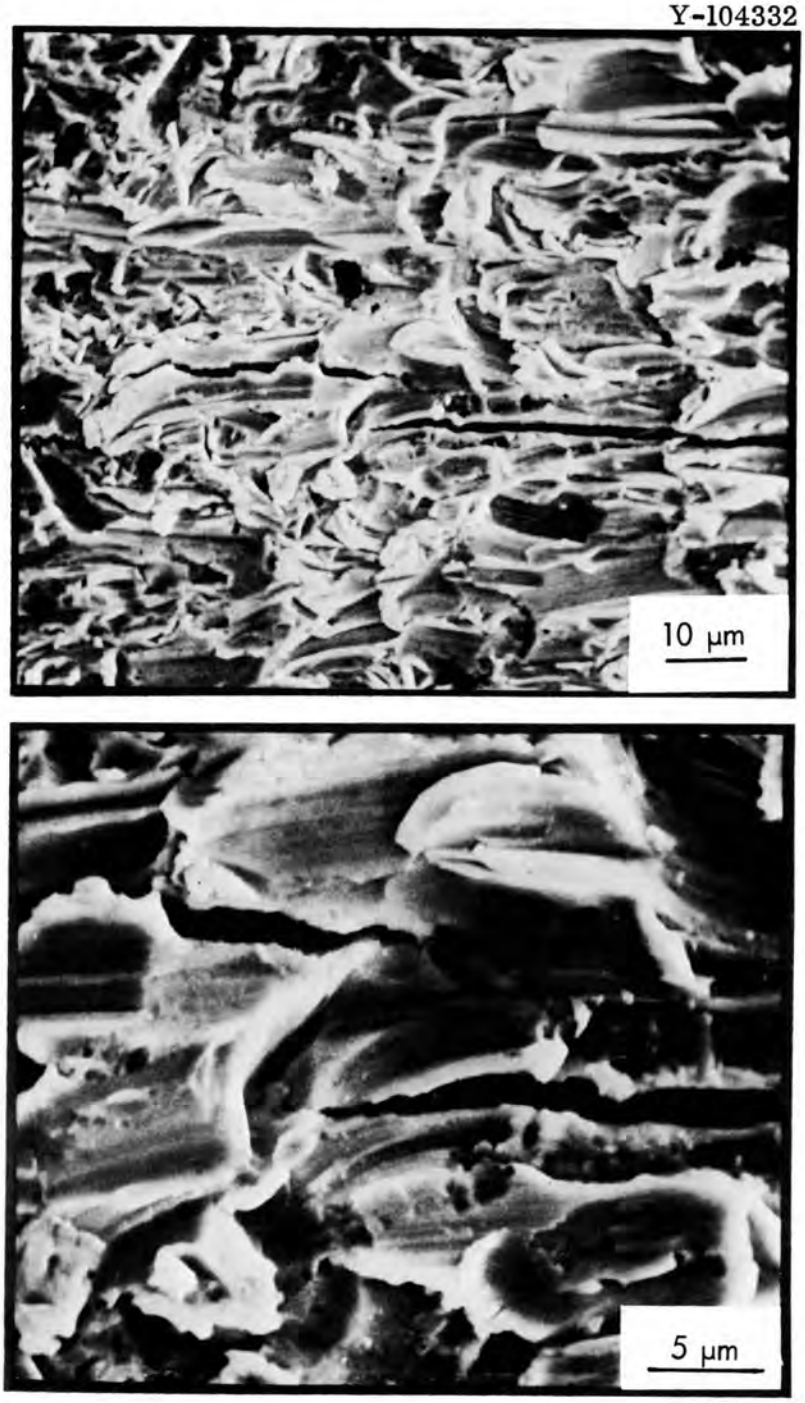

Fig. 13.6. Scanning Electron Micrographs of Inner Surface of Low-Carbon Molybdenum Tube Showing Longitudinal Cracks at Two Different Magnifications.

Y-103221

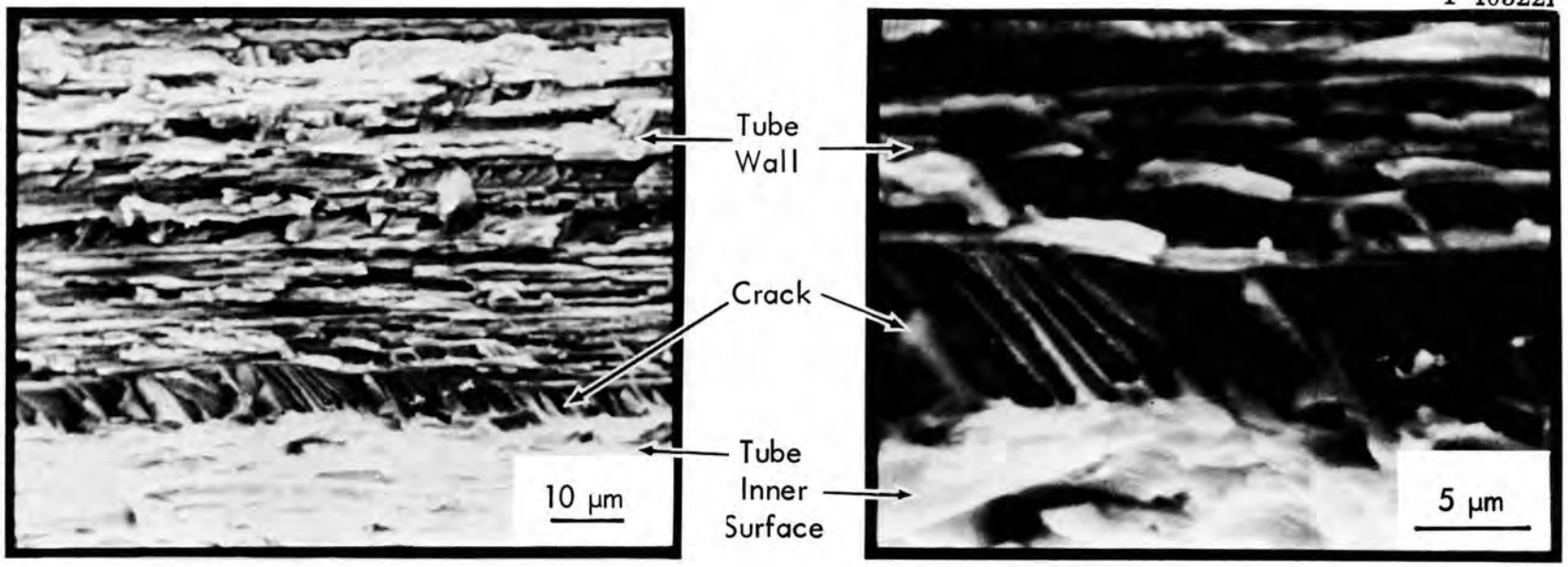

Fig. 13.7. Scanning Electron Micrographs of Low-Carbon Molybdenum Tube Showing Fracture Surface, of Longitudinal Crack and Tube Wall at Two Different Magnifications.

the tube wall at each end of the crack to prevent further propagation. We then machined the crack to produce the beveled weld joint shown in the upper portion of Fig. 13.8. After degreasing the joint with ethanol, we deposited a weld bead by manual gas tungsten-arc welding in an Ar-filled glove box with a low-C Mo filler wire. The loop was completed by inserting tensile specimens in the hot and cold legs and welding on the two end caps and the feed pot. The completed convection loop (Fig. 13.9) had a He leak rate of less than 1×10^{-8} atm cm^3 sec^{-1}.

Y-103572

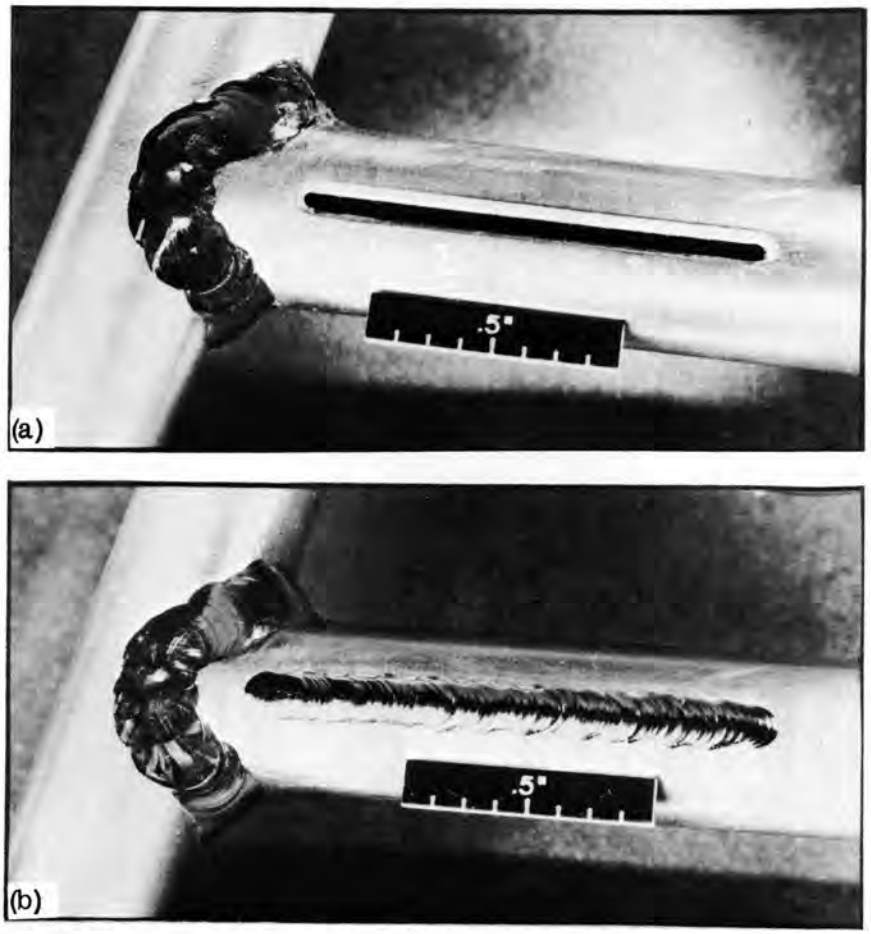

Fig. 13.8. Repair of Crack in Low-Carbon Arc-Cast Molybdenum Thermal Convection Loop by Gas Tungsten-Arc Welding. (a) Crack removed by drilling holes at end and machining to beveled slit. (b) Beveled slit filled by weld deposit.

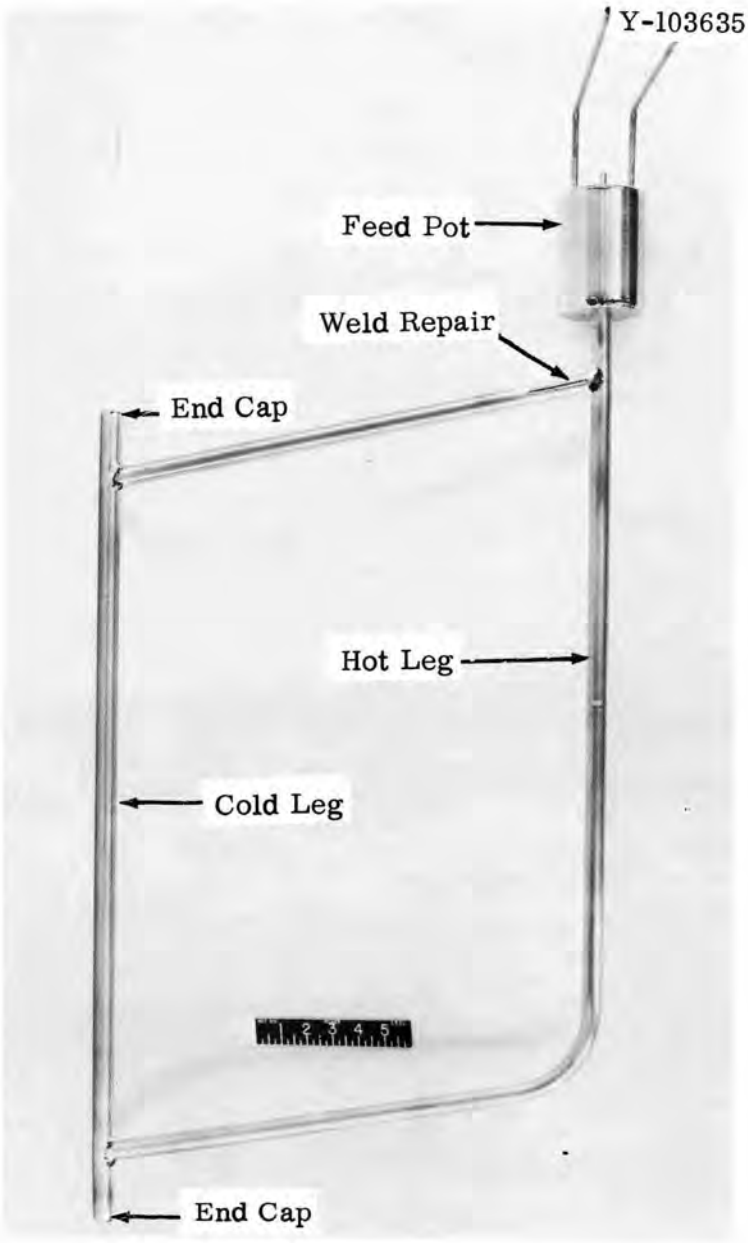

Fig. 13.9. Completed Low-Carbon, Arc-Cast Molybdenum Thermal-Convection Loop.

Investigation of Remelting Temperature in Brazes (D. A. Canonico)

Our study of the reasons for changes in the melting temperature of brazements was concentrated on the Ti–25% Cr–21% V alloy. Previously,[12] we defined remelting temperature and reported the average melting temperature and remelting temperature for brazes made with Ti–48% Zr–4% Be, Ti–46% Zr–8% Ge, and Ti–25% Cr–21% V.

The melting point of the Ti–25% Cr–21% V was determined by a test on a Ta pad to be 1480°C. The pad specimen was single phased, and microprobe analysis showed the braze metal to be chemically homogeneous. The analysis of the initial filler metal and the braze metal are given in Table 13.3. It is evident that the composition of the filler metal was not affected by a thermal excursion through its melting point, 1480°C.

Table 13.3. Analysis of Ti-Cr-V Filler Metal and Braze Metal

Identification	Chemical Composition, wt %			
	Ti	V	Cr	Ta
Bulk filler metal[a]	53.7	21.5	24.3	
Braze metal[b]	56	22.5	19.9	< 0.5
Nominal analysis	54	21	25	

[a]Determined by wet analytical techniques.

[b]Wettability test on Ta pad. Determined by electron-beam microprobe analysis technique.

Remelting temperatures were determined with vacuum-brazed (at about 10^{-5} torr) Miller-Peaslee specimens. The average remelting temperature was about 1900°C, an increase of about 400°C over the melting point of the filler metal. The failed Miller-Peaslee specimens were studied metallographically by both optical microscopy and electron microprobe analytical techniques. The results of the microprobe study reveal an absence of Cr, the temperature-depressing element used in the filler metal, and a high concentration of Ta (75–85%). The Ti concentration was lowered to about 10%, and the V content varied from 1 to 6%. This change in the composition of the filler metal more than adequately explains the higher melting point. The absence of Cr may be due to volatilization (vapor pressure about 10^{-1} torr at the brazing temperature) or diffusion into the base metal. The fracture interface did show indications of voids that might have been caused by the evolution of a gas. This possibility is being studied. A microprobe analysis of the base metal adjacent to the braze did not show any Cr; however, the

quantity may be beyond the analytical capabilities of the microprobe analyzer. An approximate calculation indicates the presence of only 5.5×10^{-3} g of Cr. Hence, the Cr could very easily be diluted in the base metal to undetectable values. For this reason, we cannot yet ascertain whether the Cr volatilized or diffused out of the braze metal.

Physical Properties

D. L. McElroy

Thermal Conductivity of Molybdenum Alloys (R. K. Williams, J. P. Moore)

Previous work[13] showed that thermal conductivity (λ) can be reliably estimated from semitheoretical equations and experimental data for electrical resistivity (ρ). We are extending these studies to dilute Mo-base alloys that contain Nb and Zr in solid solution. Our initial data on Mo indicated that the lattice thermal conductivity (λ_ℓ) of this element was anomalously small while its Lorenz function (L) exceeded the Sommerfeld value (L_o) at high temperatures.[14] Our analysis of data for Cr and W showed that the Lorenz function exceeded the Sommerfeld value for these metals also. In these metals, however, the lattice thermal conductivity was near 80/T, whereas for Mo it was only 10 to 20% of this. Verification of these findings will provide a better basis for estimates of thermal conductivity, but verification will require improvement of our existing longitudinal heat flow apparatus for measurements at low temperatures. Greater accuracy is required because the lattice thermal conductivity is relatively small and must be obtained from calculations involving at least four experimental measurements.[13]

The experimental procedure is being refined by improved control and measurement of temperature and by use of more precise electrical measurements.

Notes

1. D. O. Hobson, Aging Phenomena in Columbium-Base Alloys, ORNL-3245 (March 1962).

2. D. A. Vaughan et al., Trans. Met. Soc. AIME 221, 937 (1961).

3. V. N. Svechnikov et al., Phase Equilibrium Diagram of the Ta-Hf System, NASA-TT-F-10, p. 280 (September 1966).

4. C. T. Liu and R. W. Carpenter, Fuels and Materials Development Program Quart. Progr. Rept. June 30, 1970, ORNL-4600, p. 186.

5. K. D. Sheffler, Generation of Long Time Creep Data on Refractory Alloys at Elevated Temperatures, TRW-ER-7442 (January 15, 1970).

6. C. T. Liu, Fuels and Materials Development Program Quart. Progr. Rept. Sept. 30, 1970, ORNL-4630, pp. 192–193.

7. R. L. Stephenson, Fuels and Materials Development Program Quart. Progr. Rept. Sept. 30, 1970, ORNL-4630, pp. 193–194.

8. R. L. Stephenson, Fuels and Materials Development Program Quart. Progr. Rept. March 31, 1970, ORNL-4560, pp. 181–184.

9. Consultant from the University of Tennessee.

10. C. D. Lundin, Fuels and Materials Development Program Quart. Progr. Rept. Sept. 30, 1970, ORNL-4630, pp. 195–197.

11. A. J. Moorhead, Fuels and Materials Development Program Quart. Progr. Rept. Sept. 30, 1970, ORNL-4630, pp. 197–199.

12. D. A. Canonico, Fuels and Materials Development Program Quart. Progr. Rept. Sept. 30, 1970, ORNL-4630, pp. 199–203.

13. R. K. Williams, J. P. Moore, and D. L. McElroy, Fuels and Materials Development Program Quart. Progr. Rept. Sept. 30, 1970, ORNL-4630, pp. 203–205.

14. R. K. Williams and W. Fulkerson, "Seperation of the Electronic and Lattice Contributions to the Thermal Conductivity of Metals and Alloys," pp. 389–456 in Thermal Conductivity, Proc. 8th Conf., ed. by C. Y. Ho and R. E. Taylor, Plenum Press, New York, 1969.

14. TUNGSTEN METALLURGY

P. Patriarca A. C. Schaffhauser

The objective of this program is to provide the base technology on W alloys for advanced power applications in space and FBR high-temperature thermocouple components. We are developing fabrication processes for W alloys based on modification of conventional extrusion and warm-drawing techniques, direct chemical vapor deposition (CVD), and welding. Since the primary criterion for the use of W alloys for fuel cladding is based on the creep-rupture properties, we are conducting extensive long-time tests at the temperatures of interest and determining the mechanisms that control the creep behavior and the effect of interactions with the vapor species from an isotope or reactor fuel. We are also determining the effect of high-temperature fast-neutron irradiation damage on the physical properties of W alloys.

Primary and Secondary Working of Tungsten Alloys

A. C. Schaffhauser

Extrusion of Tungsten Alloys (R. E. McDonald)

We overhauled and adjusted our 1250-ton extrusion press to permit high-speed extrusion of W and W-base alloys. During the previous three quarters we were unable to extrude W alloys consistently due to sluggish operation of the extrusion press. For the successful extrusion of these materials, particularly for tubular shapes, extrusion speeds of 8 in./sec or greater are required.[1] The overhaul, which consisted of regrinding the critical high-pressure valves and valve operators and plating them with Cr, enables extrusion at ram speeds up to 30 in./sec.

Chemical Vapor Deposition

J. I. Federer

Deposition of Tungsten with a Dispersion of Fine Particles

We are attempting to prepare dispersion-strengthened W by CVD processes. One method we investigated involved producing particles in the deposition chamber by hydrolysis of a metal chloride in a flame (other types of reactions might also be suitable). A potential advantage of flame production of particles is that extremely fine particles can be made.[2] However, our efforts to prepare TiO_2 particles by reacting $TiCl_4$ with H_2O in an H_2-O_2 flame were not successful. The flames were produced from stoichiometric mixtures of H_2 and O_2 with a maximum combined flow rate of 1500 cm^3/min. The maximum flows yielded about 0.8 g/min of H_2O and about 200 W of heat. This amount of heat apparently was not sufficient to convert $TiCl_4$ to TiO_2. Flame nozzles 1/16 and 3/8 in. in diameter produced similar results.

We also tried to introduce particles into deposits by transferring powder into the reaction chamber by gas entrainment. Alumina powder was entrained by passing H_2 upward through a bed of −325 mesh particles. The H_2-Al_2O_3 mixture flowed into a 4-in.-ID × 12-in.-long deposition chamber. In 1-hr calibration runs, transfer rates of 10 to 20 g/hr of Al_2O_3 coated the chamber walls and the substrate with powder; however, the coating of powder on the substrate was noticeably less when the substrate was heated to 600°C, the usual deposition temperature for W. We prepared several W deposits by adding Al_2O_3 powder to the chamber at a rate of about 10 g/hr. Metallographic examination did not reveal any particles in the columnar-grained deposits; however, chemical analysis showed the presence of up to 0.06 wt % Al (0.65 vol % Al_2O_3). Although the particle content was lower than the desired 2 to 5 vol %, the process appeared to be feasible. We shall attempt to increase the particle content of the deposits by increasing the rates of powder flow and deposition. We are also considering electrostatic means of attracting particles to the deposit.

Deposition of Tungsten-Rhenium Alloys

The dependence of the morphology and grain structure of W–5% Re deposits on the ratio of $H_2:(WF_6 + ReF_6)$ was previously reported.[3] The smoothest surfaces with the fewest nodules and the finest grain structure occurred in deposits prepared with a nearly stoichiometric gas mixture. We performed a similar study on nominal W–25% Re deposits because previous attempts to deposit this material usually resulted in rough surfaces and nodular and porous grain structures. As in the previous study, the deposits were formed on resistance-heated Mo substrates 4 in. long by 0.5 in. wide contained in a 4-in.-ID × 12-in.-long chamber.

The conditions and some results of this study are shown in Table 14.1. The rate of H_2 flow varied from 100 to 2000 cm^3/min. The rates of WF_6 and ReF_6 flow, which were determined from the changes in the weights of the source cylinders, were intended to be 75 and 25 cm^3/min, respectively. These flow rates were nearly obtained except for a WF_6 flow rate of 81 cm^3/min in experiment 231C. The ratio of the flow rates of $H_2:(WF_6 + ReF_6)$ varied from 1 to 20. Each deposit was prepared at 750°C and 5 torr.

Chemical analysis showed an unexpectedly high 51.0% Re in the deposit prepared at a ratio of $H_2:(WF_6 + ReF_6)$ of 1.0. The other deposits contained less than 25% Re and showed no clear dependence on the ratio of $H_2:(WF_6 + ReF_6)$. The closest approach to 25% Re was obtained in the deposit prepared with a ratio of $H_2:(WF_6 + ReF_6)$ of 3.1, approximately the stoichiometric mixture. The highest deposition rate and efficiency were obtained at or near the stoichiometric mixture, which is consistent with the results previously obtained for nominal W–5% Re deposits.[3] At ratios of $H_2:(WF_6 + ReF_6)$ of less than 3, sufficient H_2 is not present to react with all of the WF_6 and ReF_6, and reaction rates were low. A gradual decrease in deposition rate and efficiency as the ratio of $H_2:(WF_6 + ReF_6)$ increases above 3 suggests that the deposition reaction is controlled by diffusion of WF_6 and ReF_6 through the boundary layer. Increasing rates of H_2 flow dilute the concentration of WF_6 and ReF_6 in the reaction chamber and decrease their residence time.

Table 14.1. Effect of $H_2:(WF_6 + ReF_6)$ Ratio on the Characteristics of Nominal W–25% Re Deposits[a]

Experiment Number	Flow Rate, cm^3/min			Flow Rate Ratio $H_2:(WF_6 + ReF_6)$	Re Content of Deposit (%)	Deposition Rate[b] (in./hr)	Deposition Efficiency[b] (%)
	H_2	WF_6	ReF_6				
231A	100	75	24	1.0	51.0	0.0037	30.1
231B	300	74	23	3.1	23.9	0.0085	48.5
231C	500	81	24	4.8	18.6	0.0094	42.2
231D	1000	74	24	10.2	22.6	0.0060	32.7
231E	2000	75	23	20.4	23.5	0.0052	29.5

[a]Deposited at 750°C, 5 torr.

[b]Determined at the center of the deposit.

The morphology and grain structure were greatly affected by the ratio of $H_2:(WF_6 + ReF_6)$. The smoothest deposits were obtained at ratios of 3 and 5; at ratios of 1, 10, and 20, the deposits had numerous nodules on the surfaces and rough, nodular edges. The microstructures, shown in Fig. 14.1, ranged from the columnar structure obtained at a ratio of 1 to the noncoherent structures obtained with ratios of 10 and 20, in which the grown-in porosity is quite obvious. The deposits prepared at ratios of 1, 3, and 5 also contained porosity, which was usually along grain interfaces. The bands in these deposits were probably caused by adjustments in temperature or flow rates and do not necessarily represent different compositions.

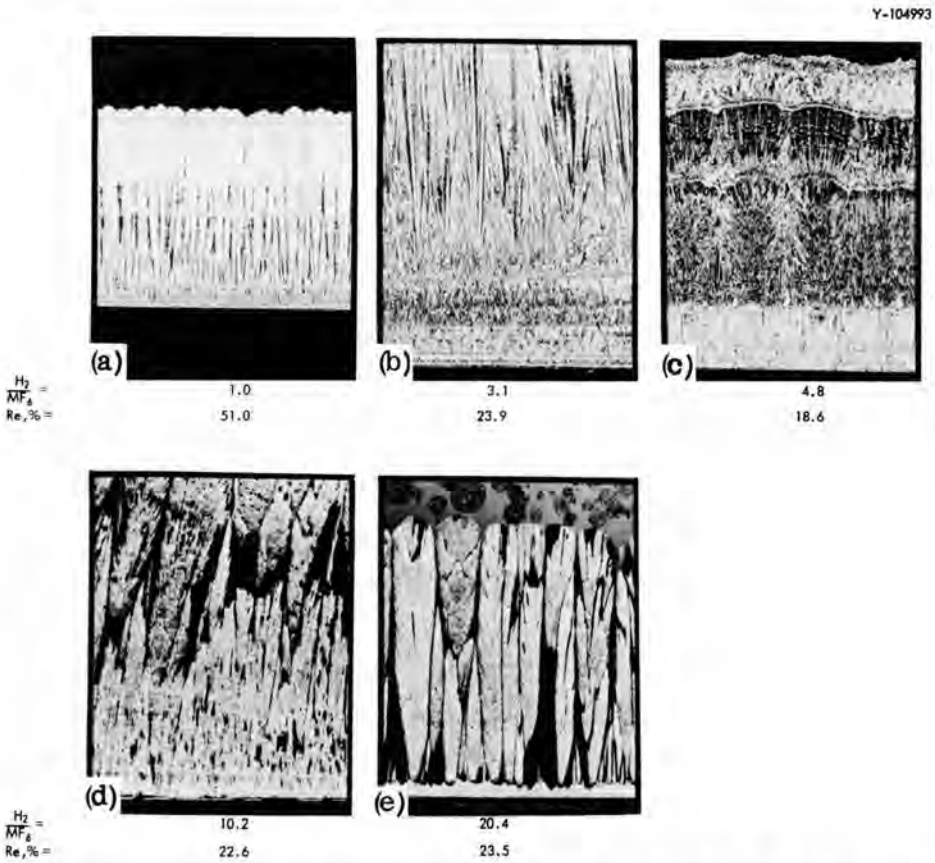

Fig. 14.1. Effect of Ratio of $H_2:(WF_6 + ReF_6)$ on Grain Structure in W-Re Deposits Prepared at 750°C and 5 torr. Ratio of $H_2:(WF_6 + ReF_6)$: (a) 1, (b) 3.1, (c) 4.8, (d) 10.2, and (e) 20.4. Percentage of Re in deposit (a) 51%, (b) 23.9%, (c) 18.6%, (d) 22.6%, and (e) 20.4%.

Although the process for depositing W–25% Re alloys is not yet optimized, these results strongly suggest that deposits of the best quality are obtained with a nearly stoichiometric gas mixture.

Evaluation of Methods for Joining Tungsten Alloys

G. M. Slaughter

Development of Filler Metals (Nancy C. Cole)

We are determining the effect of the addition of dissimilar filler metals on the properties of welds in W alloys. We reported[4] the relative weldability of W and W–25% Re with and without filler metal. We have now determined the ductile-to-brittle transition temperature (DBTT) of some of these welds.

The test specimens were cut from butt-welded W–25% Re sheet. The gas tungsten-arc (GTA) welds were made both with and without W–25 at. % Re–30 at. % Mo or Mo–50% Re filler metals. All specimens were 0.030 in. thick except for the slight increase in thickness caused by the reinforcement of the filler metal. The specimens were bent over a 4T radius at a constant deflection rate of 0.5 in./min. We define the DBTT to be the lowest temperature at which the welds bend 90 to 105°.

The results of the bend tests are shown in Fig. 14.2. The W–25% Re base-metal sheet, which was consolidated by arc melting and tested in the stress-relieved condition, was ductile at room temperature. Welding raised its DBTT considerably above room temperature. The autogeneous welds were tested with either the face or the root of the weld in tension; we found the bends with the root in tension more ductile. A 90° root bend was achieved at 350°C, whereas only a 25° face bend could be reached at 400°C. Probably the slight notch on the face of the weld (due to the weight of the molten metal) contributed to the loss of ductility.

The addition of W–25 at. % Re–30 at. % Mo and Mo–50% Re filler metals apparently impaired ductility. Root specimens bent only 50 to 60° at 350°C. At 400°C, the weld with W–25 at. % Re–30 at. % Mo filler metal bent 89° before it cracked. Because of cracking problems in the

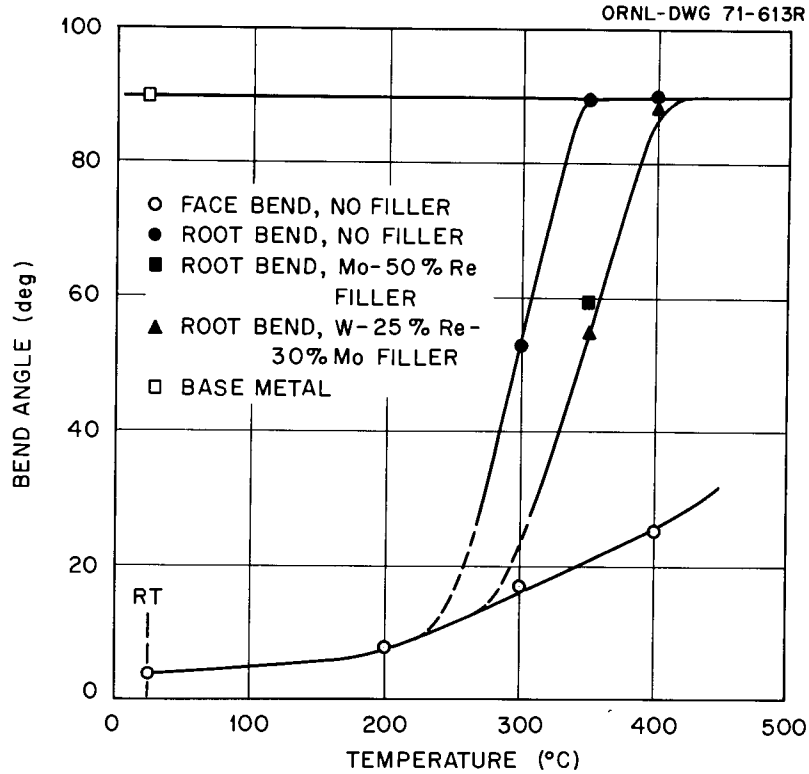

Fig. 14.2. Ductile-to-Brittle Transition Curves of Welded W–25% Re Sheet.

welds made with the Mo–50% Re filler metal (as shown in Fig. 14.3), test specimens of this material were severely limited: we were only able to get one datum point. Many cracks were at the edge of the weld bead; their location may indicate that the restraint was too great at the edge of the reinforced weld. (Figure 14.3 shows part of the weld reinforcement.) However, cracks were also found elsewhere.

Initial results indicate that autogeneous W–25% Re welds are probably the most desirable in both weldability and bend ductility. The W–25 at. % Re–30 at. % Mo filler metal appears to produce more welds without cracks than does the Mo–50% Re filler metal; but, given a weld without cracks, the bend ductility of the two may be nearly the same. We are investigating the possibility that contamination in the filler wire is responsible for the lower ductility we are now finding for these welds.

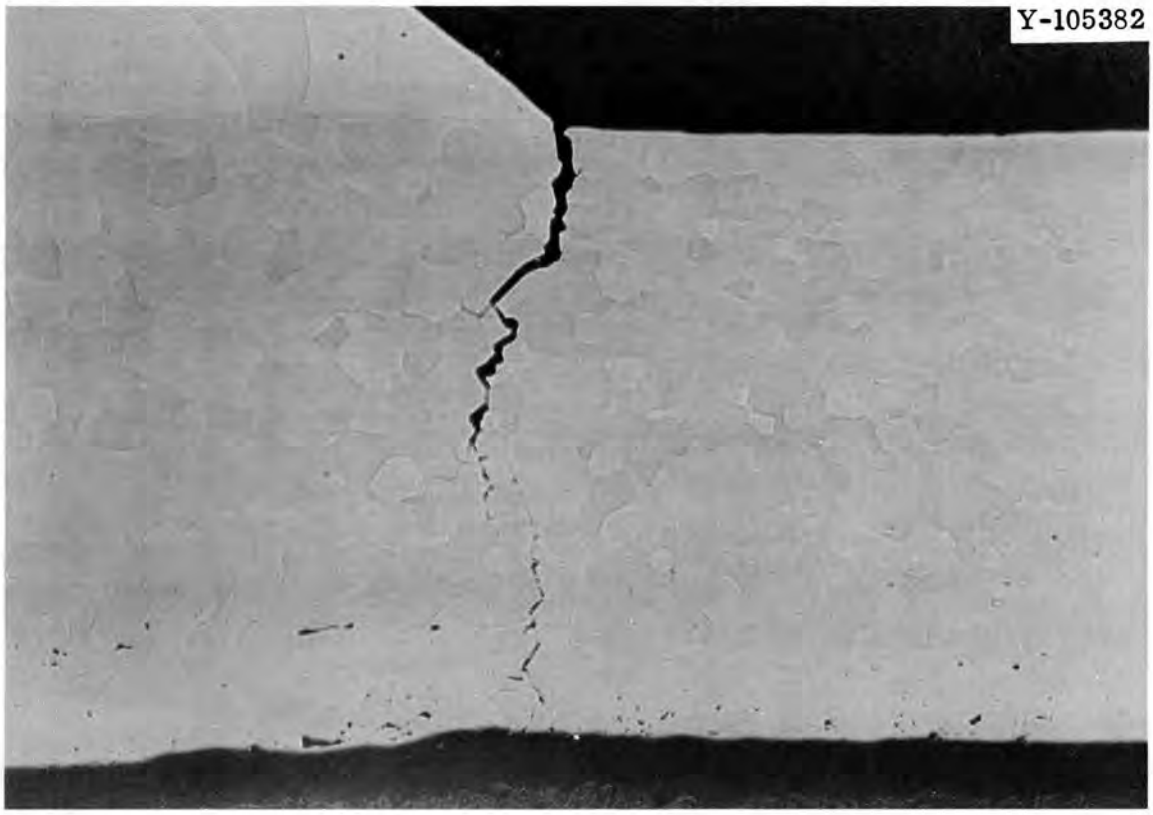

Fig. 14.3. Cracking in W–25% Re Sheet Welded with Mo–50% Re Filler Metal. 100×. As polished.

Creep Behavior of Tungsten and Tungsten Alloys

H. E. McCoy, Jr. H. Inouye

Creep Properties of Chemically Vapor Deposited Tungsten (R. L. Stephenson)

The creep-rupture properties of one lot of CVD W (lot WF-6) compared favorably with those of other W-base materials at 1650°C (ref. 5). We have tested selected specimens from several additional lots of CVD W for comparison. The stress-rupture data were reported previously.[6] Figure 14.4 is a plot of time to 1% creep as a function of stress for four lots of CVD W. In terms of both rupture life and time to 1% creep, the properties of lot WF-6 appear to be representative.

Creep Properties of Advanced Tungsten Alloys (R. L. Stephenson)

Short-time creep tests[7] at 2400 and 3100°C indicate that W–3.8% ThO_2 is much stronger than currently available W-base alloys. We obtained a

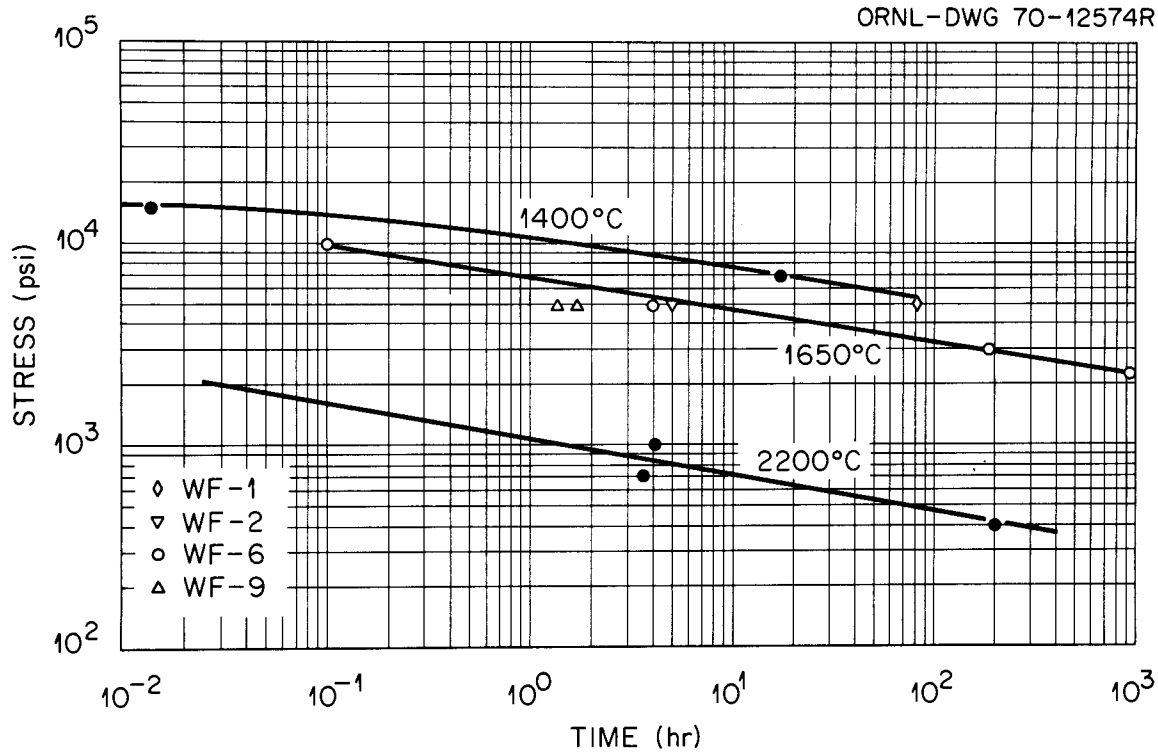

Fig. 14.4. Time to 1% Creep Versus Stress for Chemically Vapor Deposited Tungsten.

quantity of this alloy in the form of 1/4-in.-diam rods that received either 73 or 91% reduction of area during processing from Westinghouse Lamp Division, Bloomfield, N. J., for long-time creep tests and evaluation. The results to date for the material reduced 91% are shown in Fig. 14.5. In the time range studied, the stress-rupture properties of this material at 2200°C were about equivalent to those of unalloyed W at 1650°C. Hence, for equivalent rupture stresses, the use of this material would allow an increase in temperature of 500 to 600°C. In terms of strength at constant temperature, the rupture stress of this alloy at 1650°C was roughly double that of unalloyed W. However, our data indicated that the material we received was weaker than the material tested in the previous study.[7] The strength of the current material at 2000 and 2200°C is about the same as that of the material tested previously at 2400 and 3100°C.

We also received a quantity of W–4% Re–0.3% Hf–0.043% C alloy sheet from NASA-Lewis Research Center, Cleveland, Ohio, for long-time creep

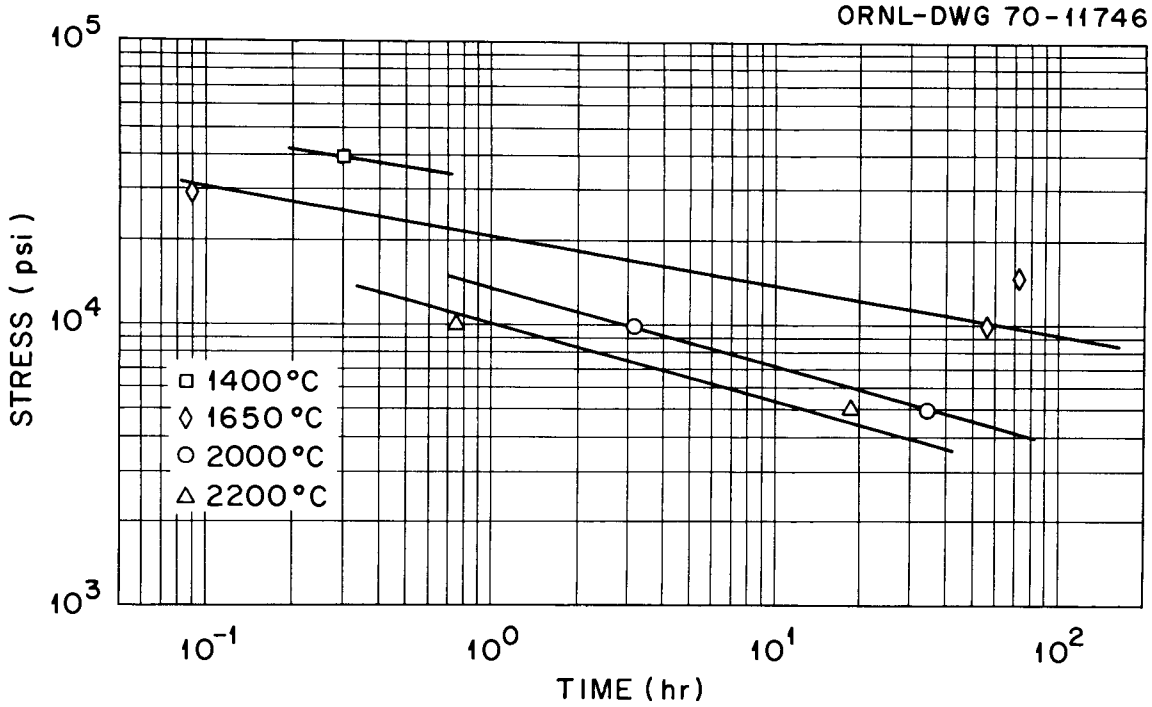

Fig. 14.5. Stress-Rupture Curves for W–38% ThO_2.

testing. The material was machined into specimens, and testing was begun.

New Equipment (R. L. Stephenson)

Six ion-pumped ultrahigh-vacuum high-temperature creep machines were procured and installed. This equipment has provision for optical strain measurement and will be used primarily for 1000- to 10,000-hr tests at low stresses. We expect them to be checked and placed in operation during the next report period.

Effect of Low-Pressure Oxygen on the Creep Properties of W–25% Re (H. Inouye)

The creep properties of 0.035-in.-diam W–25% Re wire are being measured in low-pressure O_2 to simulate its interaction with the O_2 derived from the decomposition of an oxide fuel at thermionic temperatures. We previously reported that the creep properties (except for rupture ductility) were better in low-pressure O_2 than in vacuum.[8,9] The improvement of the creep strength in O_2 was attributed to a surface film of the W-Re

σ phase. We have since then determined some characteristic effects of this reaction product.

Figure 14.6 shows several creep curves for W–25% Re stressed to 2000 psi at 1800°C. The tests in 8×10^{-5} torr O_2 and in vacuum were reported previously[9] and are reproduced for comparison. The creep curves for the two tests in 7.9 and 2.6×10^{-5} torr O_2 coincide for times up to the beginning of tertiary creep and show that the creep rates are independent of the test pressure. This is the expected result if a surface film governs the deformation process. To further illustrate this pressure independence, an unstressed specimen was pretreated in 8×10^{-5} torr O_2 for 25 hr at 1800°C to form a film estimated to be less than 0.001-in. thick[10] and then creep tested in 10^{-8} torr vacuum. The creep data are shown as the bottom curve in Fig. 14.6, which is parallel to the curve for the specimens tested in O_2. The creep rate of this specimen is, therefore, equal to that of the specimens tested in O_2 and, as stated previously, is independent of the O_2 pressure. Thus, a surface film appears to be the only requirement for improved resistance to creep. Because sublimation of the alloy as volatile oxides reduces the cross

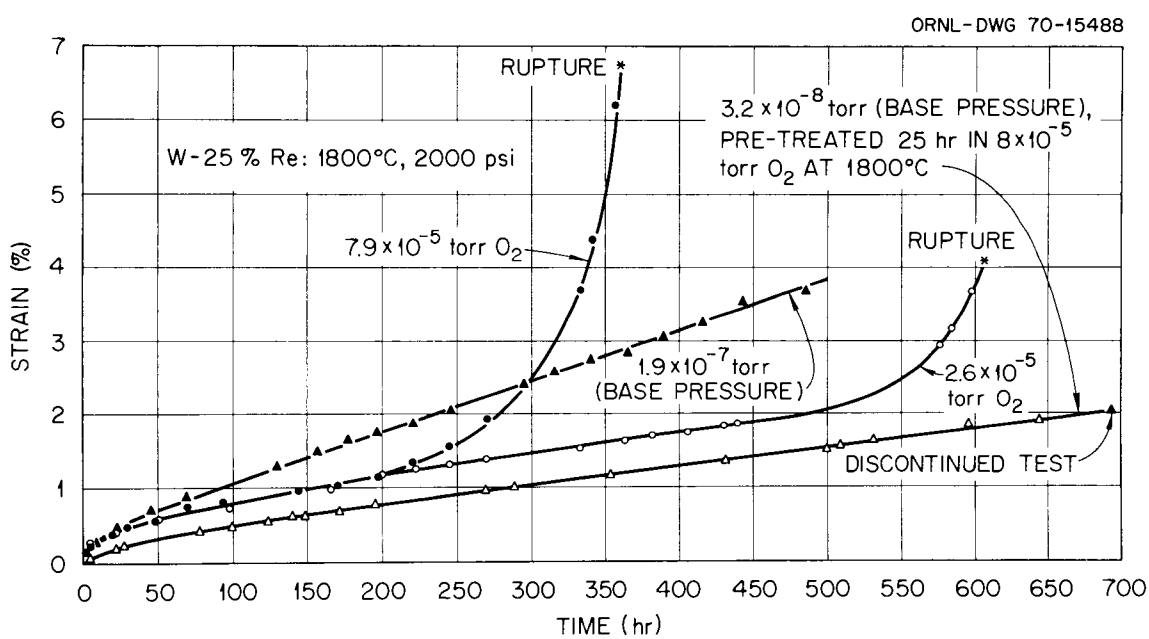

Fig. 14.6. Creep Curves for W–25% Re in Vacuum and in Low-Pressure Oxygen.

section of the specimen the lowest O_2 pressure capable of forming the film should give optimum rupture lives as well as low creep rate.

The creep properties of W–25% Re at 1800°C are summarized in Table 14.2; the creep properties of W are included to illustrate the relative strengths of the two materials in the two environments. These data confirm that W is stronger than W–25% Re in vacuum but that the reverse is true in low-pressure O_2.

Table 14.2. Creep Properties of Tungsten and W–25% Re at 1800°C

Pressure (torr)	Environment	Time for Indicated Strain, hr			Rupture (hr)	Creep Rate (in. in.$^{-1}$ hr^{-1})
		0.5%	1%	2%		
		W, 1000 psi Stress				
1×10^{-7}	Vacuum	81	209	600[a]	b	2.5×10^{-5}
8×10^{-6}	O_2	144	341	725[a]	b	2.6×10^{-5}
8×10^{-5}	O_2	94	141	245	b	c
		W–25% Re, 1000 psi Stress				
5×10^{-8}	Vacuum	12	67			3.0×10^{-5}
8×10^{-6}	O_2					8.8×10^{-6}
8×10^{-5}	O_2	195	290	353	~ 400	9.3×10^{-6}
		W 25% Re, 2000 psi Stress				
2×10^{-7}	Vacuum	23	91	238	b	7.7×10^{-5}
3×10^{-5}	O_2	30	167	477	605	3.1×10^{-5}
8×10^{-5}	O_2	37	160	277	360	3.5×10^{-5}
3×10^{-8}	Vacuum	100	291	675	d	2.4×10^{-5}[e]

[a]Extrapolated from test for 500 hr.

[b]Discontinued test at 500 hr.

[c]Tertiary creep only.

[d]Discontinued test at 693 hr.

[e]Specimen treated 25 hr in 8×10^{-5} torr O_2 at 1800°C before creep test.

Behavior of Tungsten Alloys Under Fast-Neutron Irradiation

H. E. McCoy, Jr. D. L. McElroy A. C. Schaffhauser

Irradiation Damage to Tungsten Alloys (F. W. Wiffen)

Several proposed applications of W or W-base alloys for components in fast reactors have suggested the need for experimental data on the effects of neutron irradiation on the properties of W at high irradiation temperatures. Two specific applications are the W emitters of thermionic diodes in the proposed reactor thermionic systems and the W alloys that will be used as thermocouples for measuring temperatures at the center of the fuel in fast breeder reactor cores. These applications will involve neutron fluences of 1×10^{21} neutrons/cm^2 and higher and temperatures of at least 900 to 1800°C and some thermocouple applications as high as 2400°C. In order to predict the behavior of the closely spaced components in thermionic diodes during irradiation, we must know how much W will swell because of the formation and growth of voids induced by irradiation. Information on the microstructural changes produced by irradiation will be used to evaluate and interpret the mechanical properties of irradiated thermionic diode emitters and W thermocouples. Electrical resistivity and thermoelectric power will be measured for W. These measurements will also provide a more fundamental understanding of the effects of neutron irradiation damage on the properties of materials.

The limited information available in the literature on the effect of neutron irradiation on W and W-base alloys has resulted mainly from work directed toward fundamental rather than applied interests. Most of these studies involved irradiations at low fluence and ambient temperatures in water reactors. The property most frequently measured has been the electrical resistivity at low temperatures, and the data have been used to attempt to explain the migration of point defects and small defect clusters during annealing after irradiation. Some results of electron microscopy characterized the damage[11] and the relationship between damaged microstructure and mechanical properties[12] for W irradiated at 70°C and annealed after irradiation at temperatures up to 1100°C.

Irradiation of powder-metallurgy W at 1000 and 1300°C showed that voids form at both temperatures.[13] Void densities were high and void sizes small. Calculated swelling was 0.04 to 0.05%.

Data from irradiations of other body-centered cubic (bcc) materials suggested that voids form in W at irradiation temperatures between 0.3 and 0.5 Tm, where Tm is the absolute melting temperature (or 832 to 1569°C). Void densities in bcc metals are generally high, 10^{15} to 2×10^{17} voids/cm^3, and the accompanying swelling may be in excess of 1%. There is some evidence that alloying may reduce this swelling and that impurities, such as gases trapped during the process of material preparation, may affect void nucleation processes. No data are yet available to relate these general trends for bcc systems to specific W alloys.

Design of Experiment (F. W. Wiffen, D. A. Dyslin[14])

A single-pin experiment was designed to be irradiated in row 7 of the EBR-II. The experiment is designed to irradiate rod specimens at temperatures between 600 and 1500°C to a neutron fluence near 2.0×10^{21} neutrons/cm^2 (> 0.1 MeV). The experimental design used to achieve the elevated temperatures is basically the same as that used to achieve the elevated temperatures is basically the same as that used for ORNL experiments in EBR-II subassemblies X 034, X 035, X 067, X 099, and X 100. The design balances the heat generated by gamma heating in the cylindrical specimen holder against the width of the Ar-filled conduction gap between the specimen holder and the containment tube. This temperature gradient across the gap gives the desired irradiation temperature. One specimen holder, typical of the six holders that will comprise the experiment, is shown in Fig. 14.7. The specimen loading and the main design elements are shown schematically.

This experiment was planned to evaluate the effect of irradiation temperature and material variables on the damage produced in W and W-Re alloys. Compositions of specimens range from unalloyed W to W–25% Re, and materials will be included that have been prepared by arc casting, powder metallurgy, and CVD processes.

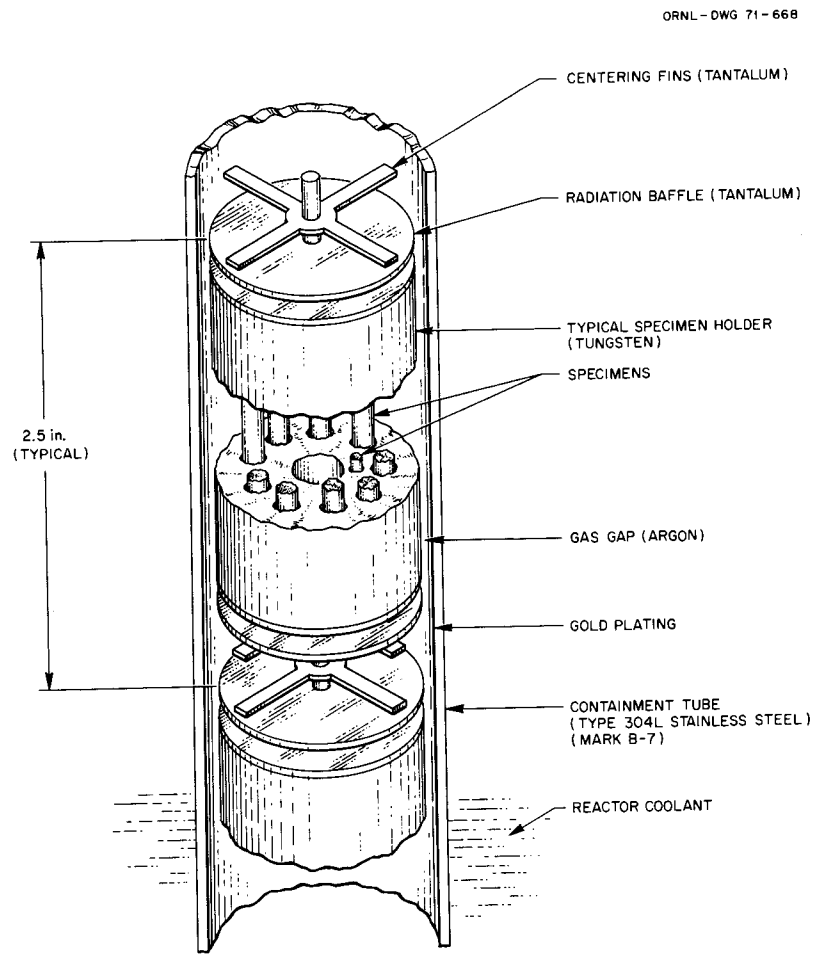

Fig. 14.7. Schematic of Specimen Holder for Tungsten Irradiation Experiment.

The specimens will be examined after irradiation by transmission electron microscopy and measurements of immersion density, thermoelectric power, and electrical resistivity. Electrical resistivity will be measured both below and above the irradiation temperatures to include the temperatures of proposed W application.

This experiment is expected to provide data useful for material selection and design of W reactor components. Critical data will be provided in the following areas:

1. the effect of irradiation temperature on the damage microstructure and formation of voids in W and W alloys,
2. the effect of different methods of metal preparation on the formation of voids in W,

3. the effect of alloying with Re on the formation of voids in W,
4. the effect of impurities on the formation of voids in W,
5. the effect of a high density of voids on the electrical resistivity of W alloys, and
6. the effect of damage microstructures on the thermoelectric power of W alloys used for thermocouples.

Electrical Resistivity of Tungsten (R. K. Williams)

Under some conditions, voids produced by fast-neutron irradiation of W may have a mean separation of 50 to 100 Å. This separation is roughly comparable to the electronic mean free path expected for pure W. The effect of macroscopic voids on the electrical resistivity (ρ) should be given by the Eucken equation:

$$\frac{\rho}{\rho_m} = \left(\frac{1 - \rho}{1 + 0.5\ P}\right),$$

where P is the volume fraction of pores and ρ_m is the electrical resistivity of porous material. However, when the mean void separation becomes comparable to the carrier mean free path, the Eucken equation may seriously underestimate the effect of pores; this appears possible in W. An experimental study of the effect of voids induced by irradiation on the electrical resistivity of W is under way.

Tests showed laser welding an excellent method[15] for attaching Pt vs Pt–10% Rh thermocouples to W. This was further verified by laser welding 0.010-in.-diam Pt and Pt–10% Rh wires to 0.090-in.-diam recrystallized W rods and cycling the assemblies between room temperature and 500, 1000, and 1400°C. Results of these tests indicate that laser welding can be used to attach instrument leads to irradiated W samples.

We are also using our ultrahigh-vacuum furnace[16] to determine the electrical resistivity of a zone-refined W sample. These results will supplement our previous studies[17] and may provide a more accurate reference at temperatures above 1200°C. Preliminary data were obtained at temperatures up to 1700°C. Our calibrated, automatic optical pyrometer and readings from W–3% Re vs W–25% Re thermocouples were also cross checked. The latter data indicate agreement within roughly 2°C between

the two temperature sensors for temperatures below 1400°C and a systematic divergence at higher temperatures.

Notes

1. R. E. McDonald and G. A. Reimann, Floating-Mandrel Extrusion of Tungsten and Tungsten-Alloy Tubing, ORNL-4210 (February 1968).

2. J. I. Federer, W. C. Robinson, Jr., and F. H. Patterson, Nucl. Appl. 6, 298–306 (April 1969).

3. J. I. Federer, Fuels and Materials Development Program Quart. Progr. Rept. Sept. 30, 1970, ORNL-4630, pp. 207–213.

4. Nancy C. Cole, Fuels and Materials Development Program Quart. Progr. Rept. Sept. 30, 1970, ORNL-4630, pp. 213–217.

5. R. L. Stephenson, "Material Selections for Thermionic Capsules," pp. 404–410 in IEEE Conference Record of 1969 Thermionic Conversion Specialist Conference, October 21–23, 1969, Institute of Electrical and Electronics Engineers, Inc., New York (69 C 51-ED).

6. R. L. Stephenson, Fuels and Materials Development Program Quart. Progr. Rept. Sept. 30, 1970, ORNL-4630, pp. 217–218.

7. H. G. Sell, W. R. Morcom and G. W. King, Development of Dispersion Strengthened Tungsten Base Alloys, AFML-TR-65-407, Part II (1966).

8. H. Inouye, Fuels and Materials Development Program Quart. Progr. Rept. June 30, 1970, ORNL-4600, pp. 207–208.

9. H. Inouye, Fuels and Materials Development Program Quart. Progr. Rept. Sept. 30, 1970, ORNL-4630, pp. 221–224.

10. R. L. Wagner, "Sublimation of W–25% Re Between 1550 and 1950°C in Low-Pressure Oxygen," pp. 411–416 in IEEE Conference Record of 1969 Thermionic Conversion Specialist Conference, October 21–23, 1969, Institute of Electrical and Electronics Engineers, Inc., New York (69 C 51-ED).

11. Robert C. Rau, Phil. Mag. 18, 1079–1084 (1968).

12. R. C. Rau et al., J. Nucl. Mater. 24, 164–173 (1967).

13. R. C. Rau et al., J. Nucl. Mater. 33, 324–327 (1969).

14. General Engineering Division.

15. A. J. Moorhead, Laser Welding and Drilling Operations, Y-DA-3123 (Rev. 1) (October 2, 1970).

16. R. K. Williams, Metals and Ceramics Div. Ann. Progr. Rept. June 30, 1969, ORNL-4470, pp. 30–31.

17. J. P. Moore, R. S. Graves, W. Fulkerson, and D. L. McElroy, "The Physical Properties of Tungsten," V-G-1–V-G-35 in The 5th Conference on Thermal Conductivity, Held at Denver, Colorado, October 20, 21, and 22, 1965, Denver University, Department of Metallurgy, College of Engineering, Denver, Colorado, 1967. Volume 1 Sessions I, II, III; Volume 2 Sessions IV, V, VI.

15. FAST-NEUTRON IRRADIATION EFFECTS ON ELECTRICAL INSULATORS

G. M. Watson[1] G. W. Keilholtz[1]

The purpose of this program is to determine the effects of fast neutrons on the mechanical, physical, and electrical properties of materials suitable for use as electrical insulators in thermionic converters and to evaluate the mechanisms of neutron damage in these materials up to 1100°C.

General Survey of Fast-Neutron Effects on Electrical Insulators

R. E. Moore[1] D. A. Dyslin[2] H. E. Robertson[1]

The following advanced materials are being evaluated: (1) synthetic sapphire Al_2O_3, (2) single-crystal MgO, (3) transparent, polycrystalline, zirconia-doped Y_2O_3, and (4) Si_2ON_2.

The results of irradiations at less than 100°C in the mixed spectrum of thermal and fast neutrons of the ETR were encouraging for sapphire Al_2O_3 and Si_2ON_2 (refs. 3, 4). The four advanced materials have since been irradiated for six months, under conditions more like those that will exist in an operating thermionic converter, in the nearly pure fast flux of row 8 of the EBR-II, at nominal temperatures of 400 and 800°C. The assembly contained SiC temperature monitors for determination of actual temperatures. The fast-fluence range is estimated to be from 1.0 to 2.5×10^{21} neutrons/cm^2 (> 1 MeV) from the top and bottom ends of the specimen capsules to the midpoint of the assembly.

The capsule designed to operate at 400°C contained three specimens each of sapphire Al_2O_3, Y_2O_3, Si_2ON_2, and GE Opaque Lucalox. The four capsules designed to operate at 800°C contained a total of four specimens of Si_2ON_2, three specimens of each of the other three advanced materials, and three specimens of GE Opaque Lucalox. Preliminary visual inspections of the irradiated specimens revealed that one specimen of Si_2ON_2 at the top of the capsule designed to operate at 400°C had a large piece broken off its top end. It seems likely that this specimen broke as a result

of expansion of the column of specimens against the end cap at the top of the capsule. None of the other specimens of the assembly appeared to have received any gross damage as a result of irradiation.

All of the Al_2O_3 specimens withstood fast-neutron irradiation at both 400 and 800°C (design temperatures) without fracturing. They did change in appearance, however; they were transparent before irradiation but black after irradiation. Discoloration of materials as a result of irradiation, although an easily observed phenomenon, has little significance as far as basic changes in the physical properties of a material are concerned.

All four of the advanced materials may be regarded as possible alternatives to the use of polycrystalline Al_2O_3 as a thermionic electrical insulator at high temperatures. The results of the irradiation in the EBR-II did not rule out any of these materials. Because polycrystalline Al_2O_3 suffers separation at the grain boundaries after receiving high fast-neutron fluences at high temperatures, its usefulness as an electrical insulator in nuclear-powered thermionic converters is limited to relatively short lifetimes. A comprehensive investigation of the alternate materials, particularly sapphire Al_2O_3 and Si_2ON_2, would seem to be justified as an integral part of a program to develop practical nuclear-powered thermionic converters for long-term applications.

Irradiation of High-Density Commercial Al_2O_3 Products Considered for Thermionic Insulators

R. E. Moore[1] D. A. Dyslin[2] H. E. Robertson[1]

Results from this series of irradiations of commercial polycrystalline Al_2O_3 were reported previously.[5] To obtain additional data on the effect of the nearly pure fast-flux spectrum of the EBR-II, an assembly designated 0-2, which is identical to assembly 0-1 (ref. 5), is being irradiated in row 7 of the EBR-II.

The design temperature was 800°C for the specimens, which are solid cylinders and thin-walled cylindrical shells of three commercial types of Al_2O_3 (Coors AD-995, Wesgo AL-995, and GE Opaque Lucalox). The estimated

fast-fluence range for the specimens is 1.0 to 2.5×10^{21} neutrons/cm^2 (> 1 MeV). This irradiation will be completed about the end of May 1971.

Metal-Clad Al_2O_3 Specimens

R. E. Moore[1] D. A. Dyslin[2] H. E. Robertson[1]

Three assemblies containing bilayers and trilayers supplied by other installations were irradiated in this task.[5] The last assembly of the series was irradiated in row 8 of the EBR-II. The specimens, all furnished by Thermo Electron Corporation, are now being examined.

Notes

1. Reactor Chemistry Division.

2. General Engineering Division.

3. R. E. Moore, D. A. Dyslin, and H. E. Robertson, Fuels and Materials Development Program Quart. Progr. Rept. June 30, 1970, ORNL-4560, pp. 214–215.

4. D. A. Dyslin, R. E. Moore, and H. E. Robertson, Fuels and Materials Development Program Quart. Progr. Rept. Sept. 30, 1969, ORNL-4480, pp. 188–189.

5. D. A. Dyslin, R. E. Moore, and H. E. Robertson, Fuels and Materials Development Program Quart. Progr. Rept. Sept. 30, 1970, ORNL-4630, pp. 226–229.

PART III

GENERAL REACTOR TECHNOLOGY

FUELS

16. DEVELOPMENT OF FUEL ELEMENT FABRICATION

G. M. Adamson, Jr. W. R. Martin

The purpose of this program is to advance the technology for fabricating fuel elements for research reactors by developing fuel elements with lower production cost and improved irradiation performance. Work on this program was recently restricted to irradiation studies and evaluation of the failures of ATR fuel elements.

Irradiation Studies

R. G. Donnelly

Design and Fabrication of HFIR Irradiation Experiments (M. M. Martin)

Our objective is to determine those factors that influence the performance of Al-clad UAl_x and U_3O_8 dispersions in the ATR and HFIR at fission densities to 2.5×10^{21} fissions/cm^3. An experimental facility that would allow this maximum fission density to be achieved in five reactor cycles was built for the reflector region of the HFIR. The experiment, which was described previously,[1,2] is designated PM capsule 1.

Figure 16.1 shows the fabrication and quality-assurance network for the experiment and is a convenient reference to indicate our progress. All machined components, miscellaneous parts, and test fuel plates are completed. We progressed through the ORNL Reactor Experimental Review Committee and completed successfully the relief valve, pressure head, flow tests, assembly of the high-pressure bearing parts, and installation of thermocouples into the instrumented fuel plates. A photo showing the thermocouple insertion into the partially assembled experiment is shown in Fig. 16.2. The experiment is ready for the fit test in the HFIR mock-up facility, and insertion into HFIR is planned for the shutdown January 9, 1971.

ORNL-DWG 71-5668

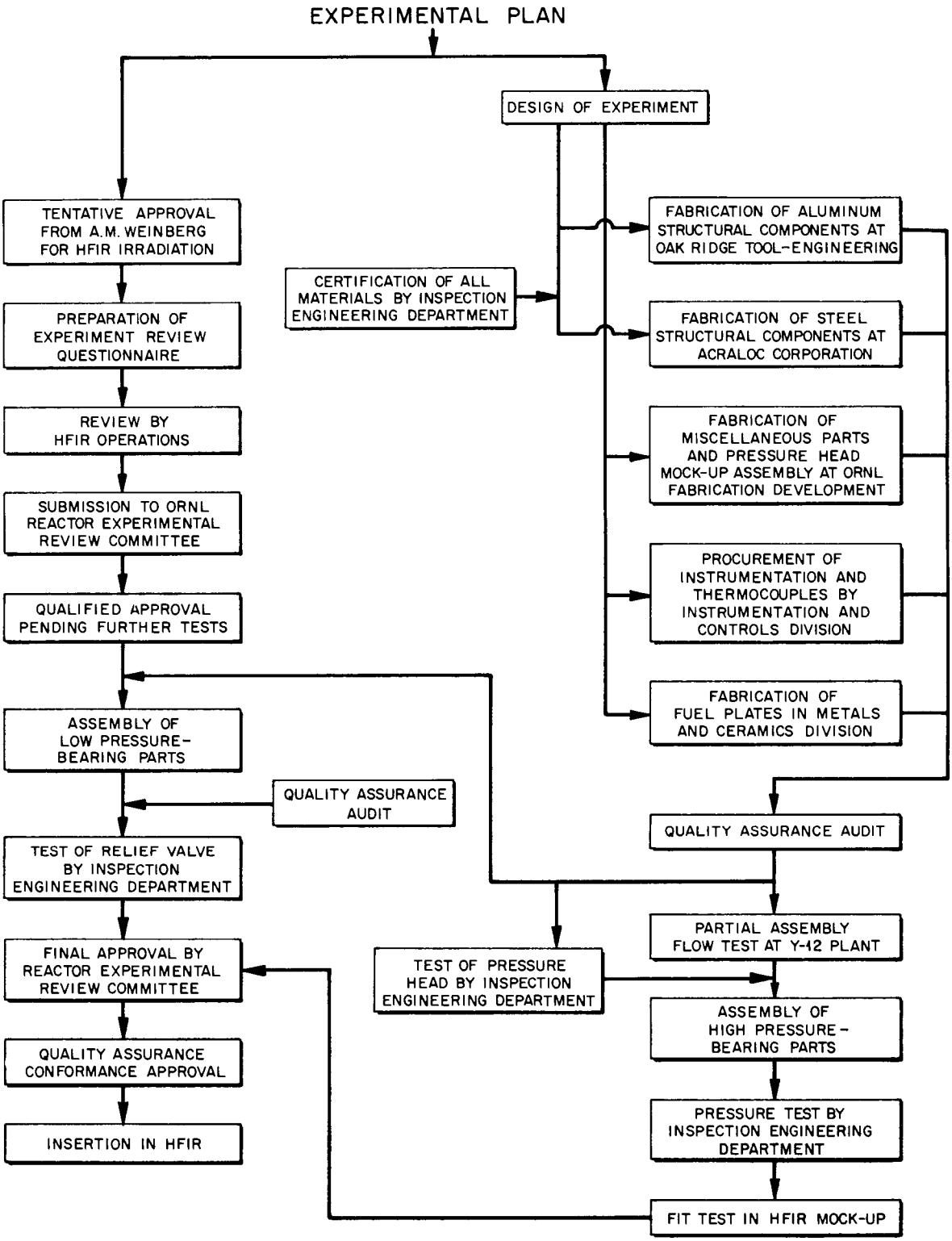

Fig. 16.1. Fabrication and Quality Assurance Network for PM Capsule 1.

Fig. 16.2. Thermocouple Insertion Into Instrumented Fuel Plate Assembly.

Development of HFIR Core with Increased Fuel Loading

W. R. Martin R. W. Knight

Establishment of Standards for Burned U_3O_8 and High-Fired U_3O_8 HFIR Plates (B. E. Foster, S. D. Snyder)

The chemical analysis for U content was completed for the samples cut from one inner- and one outer-annulus plate containing high-fired U_3O_8 in accordance with the standard HFIR loading, for one inner- and one outer-annulus plate loaded to 134.95% of standard, and for four similar plates loaded with burned U_3O_8. These plates were fabricated by Metals and Controls, Inc. This work was requested and funded by the HFIR project. Using these chemical data, we plotted the weight of U in milligrams in each 0.078-in.-diam right circular cylinder through the fuel plate as a function of x-ray attenuation (expressed as readings from the recorder chart) at the normal energy conditions of 50 kVcp and 2.5 mA. As with past data, we observed a bias for the inner-annulus plate containing high-fired U_3O_8 in accordance with the standard HFIR loading when compared with our original calibration data. However, a considerable reduction in point scatter allowed us to see that the bias was very uniform. We attribute the reduction in point scatter to the use of improved control of sample machining and sample identification and to more precise chemical analysis obtained from transistorized coulometers with greatly improved stability.

The uniform bias led us to another search for information about the fabrication of the plates that we used for our original calibration. When these plates were made, the filler section of the inner-annulus cores contained 101 Al, B_4C, and Cd glass. The Cd glass, used as a poison, contained 11.46 wt % Cd. Considering the density and mass-attenuation coefficient this amount of Cd is equivalent from a standpoint of x-ray attenuation to the addition of 0.019 in. of Al to the plate thickness. In subsequent inner-annulus cores, the Cd glass was eliminated, thus introducing the calibration bias that has plagued us recently.

We used a least-squares polynominal fit of the U content versus attenuation data in computer programs to derive in tabular form our calibrations for both the inner- and outer-annulus high-fired U_3O_8 and burned U_3O_8 plates. Also, contrary to past practice, we found that each type plate had its own calibration rather than a continuous calibration covering both the inner and outer annulus for a particular type of oxide. We tested the high-fired U_3O_8 calibrations by determining from data for attenuation scans the content of U in one inner- and one outer-annulus plate fabricated with production techniques and containing a standard loading. These calculated values agreed with the quoted U content of these plates within 0.5%.

Although we developed the tabular calibrations for the burned U_3O_8 and the higher loaded high-fired U_3O_8 at the x-ray energy conditions of 50 kVcp, 2.5 mA, we have not tested these calibrations. Also, since the higher loadings may require a higher x-ray energy for a sensitivity to change in U content comparable to that obtained with the standard loadings, we have to process attenuation data at 60 kVcp and 2.5 mA.

Fabrication Development

R. G. Donnelly

Deformation Behavior of Fuel Cores During Rolling (J. H. Erwin)

In our effort to eliminate nonuniform deformation (dogboning) from fuel cores roll bonded within cladding materials somewhat weaker than the fuel core, we fabricated a limited number of simulated plates from core shapes similar to those developed at the leading and trailing ends during the initial mill passes. These plates represent the completion of this effort to solve the dogboning problem. Before the billets were assembled, each end of the cores was relieved at the center of the thickness by milling a 60 or 90° included angle the full width of the core. For the 60° relief, cores were machined to depths of 0.114, 0.146, and 0.200 in., the equivalent of 3, 5, and 10% of the longitudinal area of the 0.272-in.-thick × 1.800-in.-long cores. For the 90° relief, cores

were machined to depths of 0.087, 0.110, and 0.130 in., the equivalent of 3, 5, and 7.5% of the longitudinal area. The simulated cores were type 2219 Al, and the cladding was type 8001 Al. The billets were standard size for the outer annulus of the HFIR element except for core length. After drilling the frames at all corners to reduce blistering and chemically cleaning all parts, we assembled and rolled the billets at 490°C, one group at reductions according to HFIR schedule on a 12-in.-diam mill and another group at reductions 1.5 times the HFIR schedule on a 20-in.-diam mill. We removed billets from the rolling schedule at thicknesses of about 0.200, 0.100, 0.063, and 0.050 in. to observe the cross section after these reductions.

Visual examination of these simulated cores revealed contrasts with previously reported shaped or short cores:[3]

1. Cores shaped or shortened to produce 10% void cut through the cladding during fabrication at reduction rates of 25% per pass and greater. Cores with a relief equal to 10% void exhibited no indication of cracking of the cladding after reduction at either 25 or 35% per mill pass.

2. The fishtail, common to most cores rolled in cladding of approximately equal strength, was evident in both ends of the cores assembled with 3% void. Cores with 5% or greater void relief develop a fishtail on the lead end and a bullet nose on the opposite or trailing end during the first pass. This bullet end resembled the end of shaped cores but did not continue to develop the dogbone and necking noted with shaped cores.

3. The dogbone appeared to be virtually eliminated but was replaced by extreme fishtailing, particularly as a result of the large void volume and the heavy reduction rate. The core relieved 0.200-in.-deep and rolled at 36% reduction per pass developed approximately 1/2-in. of fishtail.

Notes

1. M. M. Martin and W. K. Crowley, Fuels and Materials Development Program Quart. Progr. Rept. March 31, 1970, ORNL-4560, pp. 222–224.

2. M. M. Martin, Fuels and Materials Development Program Quart. Progr. Rept. June 30, 1970, ORNL-4600, pp. 239–242.

3. J. H. Erwin, Fuels and Materials Development Program Quart. Progr. Rept. Sept. 30, 1970, ORNL-4630, pp. 234–235.

CLADDING AND OTHER STRUCTURAL MATERIALS

17. IRRADIATION DAMAGE TO ALUMINUM AND ALUMINUM ALLOYS

J. R. Weir, Jr. R. T. King

During the past 3 years, evidence from electron microscopy and measurements of the immersion density of irradiated Al alloys has suggested that swelling due to formation of voids is strongly related to chemical composition and microstructure. Irradiation to 1×10^{22} neutrons/cm^2 (> 0.8 MeV) at 60°C caused about 7% swelling in nominally 99.9999% Al and 1% swelling in solid-solution alloys but caused no swelling that could be resolved experimentally in the 6000 series of Al alloys (which are hardened with Mg_2Si precipitate) investigated to date. Because of this unique behavior and because the 6000 series of Al alloys are widely used for reactor components, we examined an existing reactor component of 6061 Al that had been exposed to a neutron fluence of more than 5×10^{22} neutrons/cm^2 (> 0.8 MeV).

The significance of the results extends beyond Al-base alloys, however. Many types of irradiation damage that occur in Al alloys are common in other cladding alloys, particularly in candidate cladding materials for fast breeder reactors. Voids form in stainless steels between about 300 and 600°C, or between about 0.3 and 0.5 of the absolute melting point. This range of homologous temperatures in Al alloys extends from about 0 to 200°C; indeed, in a separate experiment we confirmed that the upper temperature at which voids form in 99.9999% Al in the Oak Ridge Research Reactor (ORR) is about 200°C. The parallel behavior extends to compositional effects, since voids form at lower fluences in both pure Ni and Al than they do in stainless steel or Al alloys. Hence, if we can discover what structural or compositional effects enhance the resistance of the 6000 series of Al alloys to the formation of voids, we may be able to apply the governing principles to cladding for fast breeder reactors.

Material and Irradiation History

The High Flux Isotope Reactor (HFIR) Model "C" target holder sleeve is a perforated cylinder fabricated from 0.063-in.-thick 6061 Al alloy sheet.[1] Blanks of sheet material 14.75 in. wide × 29.5 in. long were shaped to a semicircular cross section with a 5.25-in. radius, annealed at 232°C for an unspecified period, rolled to a 3.75-in. radius, annealed again, and finally rolled to a 2.19-in. radius. These shapes were annealed to the O temper by standard heat treatments[2] and seam welded with the 4043 Al alloy filler metal to form cylinders. The weldments were then planished. The final heat treatment consisted of annealing at 515 to 527°C for 20 min, cooling in circulating air to room temperature, and then aging at $190\,^{+5}_{-25}$°C for 7 hr. The final heat treatment was designed to reduce thermal distortion during fabrication while yielding mechanical properties approaching those of the optimum age-hardened condition, the T6 temper; the final condition is best described as F (as fabricated). Perforations were then drilled into the cylinder.

The microstructure produced during fabrication was examined by transmission electron microscopy and is shown in Fig. 17.1. A mixture of coarse and fine precipitate particles was readily visible at 16,000× (Fig. 17.2). Although this phase has not been analyzed, it was probably the Mg_2Si precipitate that is responsible for age hardening in the 6000 series of Al alloys. The heat-treatment schedule had produced a somewhat overaged condition, for the Mg_2Si precipitates in this alloy aged to optimum hardness are considerably finer than those observed here. Larger second-phase particles that resulted from other impurities were also present.

One model "C" target holder had been in service for a total of 65,713 MWd in the HFIR before it was removed for examination. This corresponded to maximum fast-neutron fluences (at reactor midplane) of 5.36 and 5.47×10^{22} neutrons/cm^2 on the inner and outer walls of the sleeve, respectively, and to thermal-neutron fluences of 1.21 and 1.11×10^{23} neutrons/cm^2 at the same locations.[3] The uncertainty in these calculated fluences is ±15% of the values quoted. The neutron fluences at various other points along the cylinder were estimated from a symmetrical axial

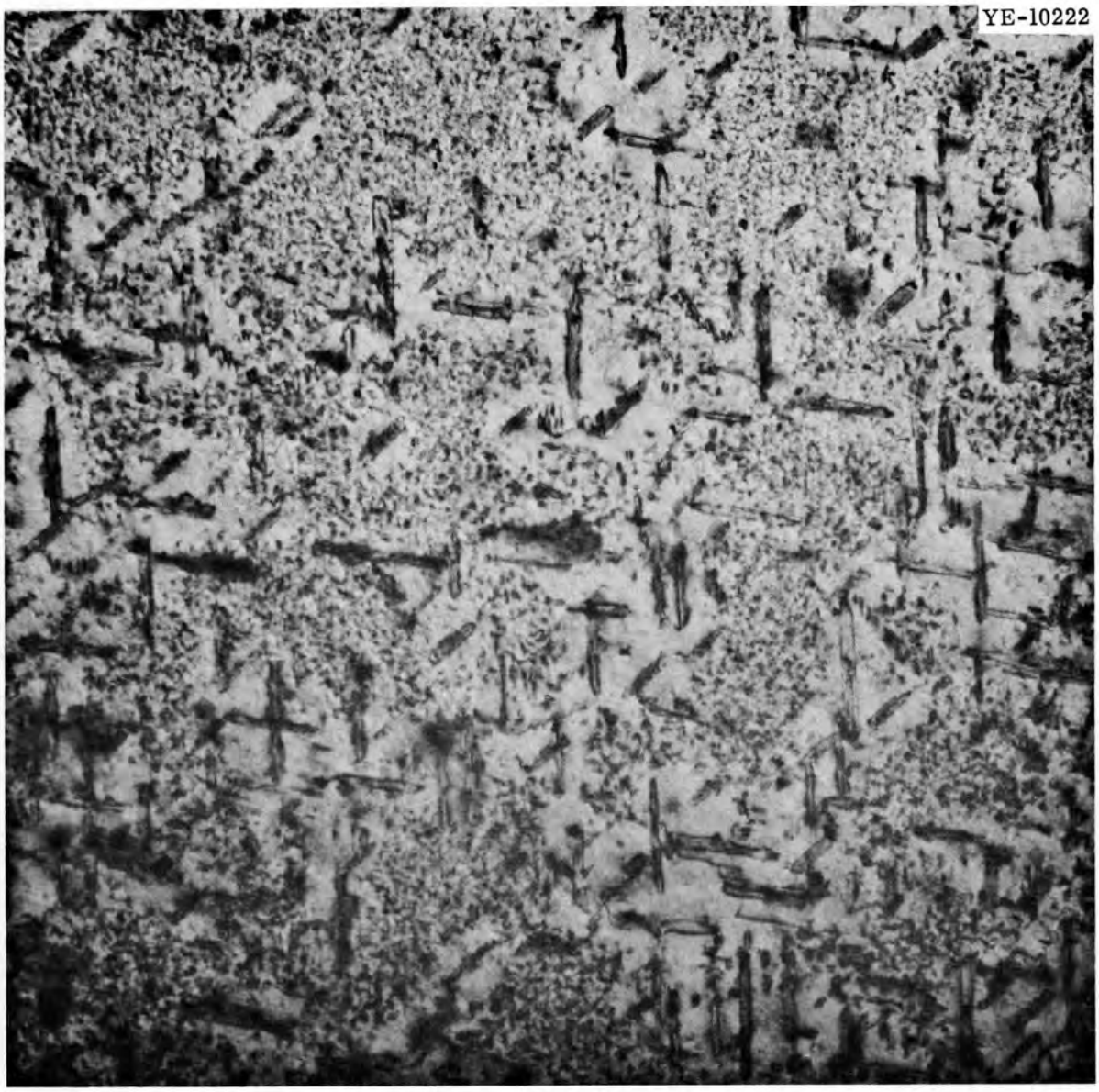

Fig. 17.1. Transmission Electron Micrograph of Mg_2Si Precipitate Particles in Matrix of Unirradiated 6061-F Aluminum. Structure is slightly overaged. 47,000×. Reduced 12.5%.

Fig. 17.2. Large Precipitate Near Grain Boundary of Unirradiated 6061-F Aluminum. 16,000×. Reduced 12.5%.

flux distribution for neutrons of energy greater than 0.183 MeV (ref. 4) that is only strictly applicable along the center line of the reactor for conditions at the start of a fuel cycle. However, it provides adequate accuracy since the other uncertainties in the flux calculations are relatively large.

The operating temperature of the sleeve was slightly higher than that of the coolant water (55°C) with which it was in contact, but uncertainties in the time-dependent thickness and composition of the oxide that formed during irradiation added greatly to the uncertainty of calculations of the operating temperature of each region of the sleeve. However, if we assume that the layers of oxide that formed on both sides of the target holder at reactor midplane were boehmite,[5,6] then the steady-state temperature gradient across the oxide was about 180°C/cm. The thickness of the oxide on the target basket has not yet been measured directly, nor has the type of oxide present in-reactor been established. However, these considerations indicate that the target basket probably operated within a few tens of degrees of the coolant temperature, since the thermal characteristics of most forms of aluminum oxide and hydrated aluminum oxides are probably of similar magnitude.

Measurements of Density and Dimensional Change

We made several attempts to characterize the changes in density and dimensions induced by irradiation in the target holder sleeve. We measured changes in the diameter and length of the irradiated basket,[7] and the immersion densities of a set of irradiated dogbone-shaped tensile specimens were determined in the hot cell. The density of an unirradiated target basket sleeve was determined to be 2.7012 g/cm^3. Finally, we measured the immersion densities of the same set of specimens on a precision balance outside the cell after all oxide had been chemically removed. This provided the most precise measure (±0.02%) of the change in density in the base metal.[8] The results of the density measurements made in the hot cell on specimens with the oxide layer and the measurements outside the hot cell on chemically cleaned specimens are given in Table 17.1. It is clear that the oxide present at the time the immersion

Table 17.1. Relative Change in Density of Dogbone Tensile Specimens Induced by Irradiation and Thickness of Oxide Layer Required to Cause Change

Specimen Number	Neutron Fluence [neutrons/cm^2 (> 0.82 MeV)]	Density Change, %		Total Thickness[c] of Oxide Layer Required to Cause Observed Difference, in.	
		With Oxide[a]	Without Oxide[b]	Gibbsite	Bayerite
	$\times 10^{22}$				
Th-144	0.70	−0.99	−0.02	0.006	0.011
Th-130	1.67	−0.99	−0.14	0.006	0.010
Th-142	2.646	−1.13	−0.18	0.006	0.011
Th-132	3.537	−1.61	−0.60	0.006	0.011
Th-140	4.293	−1.92	−0.76	0.008	0.014
Th-134	4.86	−2.22	−0.92	0.008	0.016
Th-138	5.238	−2.36			
Th-136	5.389	−2.53	−1.06	0.01	0.018

[a]Average of five measurements, precision = ±0.3%.

[b]Result of single measurement, estimated precision = ±0.02%.

[c]Precision = ±0.0015 in.; calculation is based on original metal thickness of 0.0625±0.0015 in.

density was measured was less dense than the base metal and caused the aggregate densities of the metal and oxide measured on the irradiated specimens to be lower than those of the base metal. The oxide formed on another aluminum component from the HFIR was determined by x-ray powder pattern techniques[9] to be β-$Al(OH)_3$ (bayerite) or possibly α-$Al(OH)_3$ (gibbsite), which have theoretical densities of 2.53 and 2.42 g/cm^3, respectively. Simple computations based on these theoretical densities yield the total thickness of either type of oxide required to cause the observed differences in densities; these total thicknesses range from 0.006 to 0.018 in. of oxide on the sleeve (Table 17.1).

The thickness of the oxide layer is important for other reasons than just because it changes the apparent density of the specimen. The oxide spalls during testing at low strains and does not bear any load at the ultimate point, even though its cross-sectional area is included in the stress calculations. Hence, stresses calculated from measured test

loads may be as much as 10% too low. For this reason, we are investigating the thickness of the oxide metallographically.

The most accurate measurements of the density of irradiated specimens without oxide indicate that the total change in density caused by irradiation at 5.4×10^{22} neutrons/cm^2 (> 0.8 MeV) was only −1.06%. However, density changes for reasons other than swelling by void formation. The maximum thermal-neutron fluence causes about 2.1% Si to form by means of the $^{27}Al(n,\gamma)^{28}Al$ reaction followed by β^- decay to ^{28}Si; hence, the control density should be increased by 0.07% to account for the neutrons that were absorbed if the Si remains in substitutional solid solution. However, if the Si produced by transmutation is all transformed to β-Si precipitate particles during irradiation, density could decrease by 0.31%. Other phase transformations that might lead to changes in density are possible during irradiation. Although quantitative analysis of the microstructure by transmission electron microscopy is not complete, we have observed voids ranging up to 500 Å in diameter in specimens irradiated to 5.4×10^{22} neutrons/cm^2 (> 0.82 MeV).

Measurements of Mechanical Properties

The finished components of one target holder are shown in Fig. 17.3. Top and bottom fittings are welded to the perforated sleeve to complete the assembly. Our unirradiated control material all comes from an improperly drilled scrap sleeve that had the same history as the sleeve used in reactor service. Figure 17.4 shows the method of preparation of these specimens and the dogbone shape of the specimen. Sets of specimens were cut from the unirradiated sleeve. Three longitudinal strips of specimens were cut from the irradiated cylinder.

Because the curves for load versus elongation that were recorded are quite similar in shape to those for standard specimens (American Society for Testing and Materials), we calculated both yield and ultimate tensile strengths based on the measured cross-sectional areas of the individual specimens. However, we are more confident in the results for ultimate strength than those for yield strength, even though their behavior is very similar in all respects. For all practical purposes, the

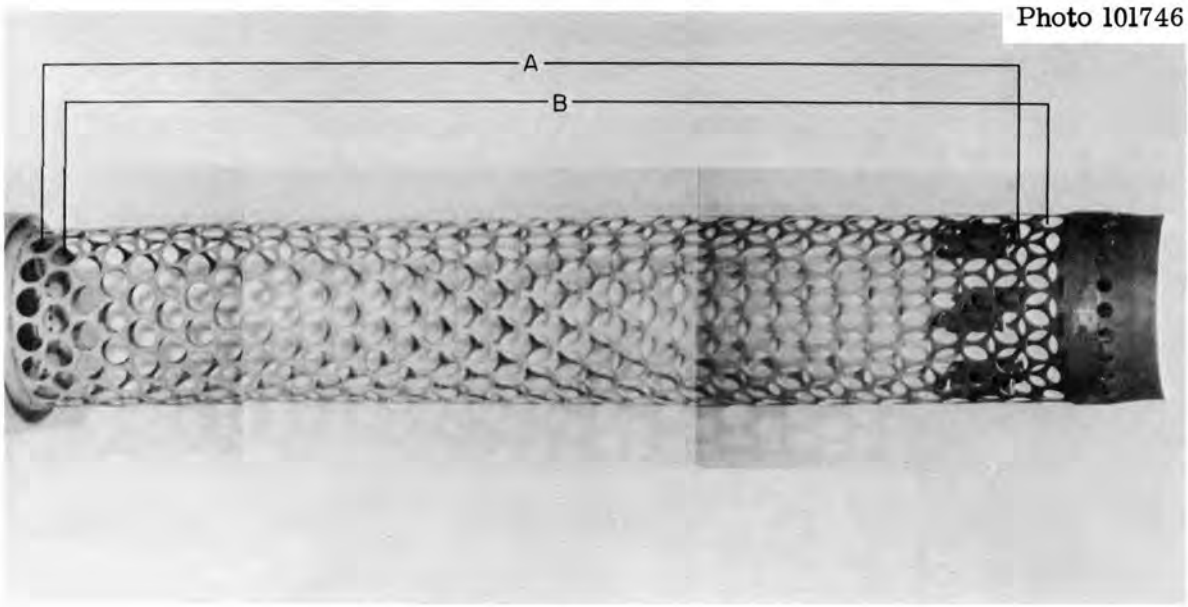

Fig. 17.3. Irradiated Target Holder.

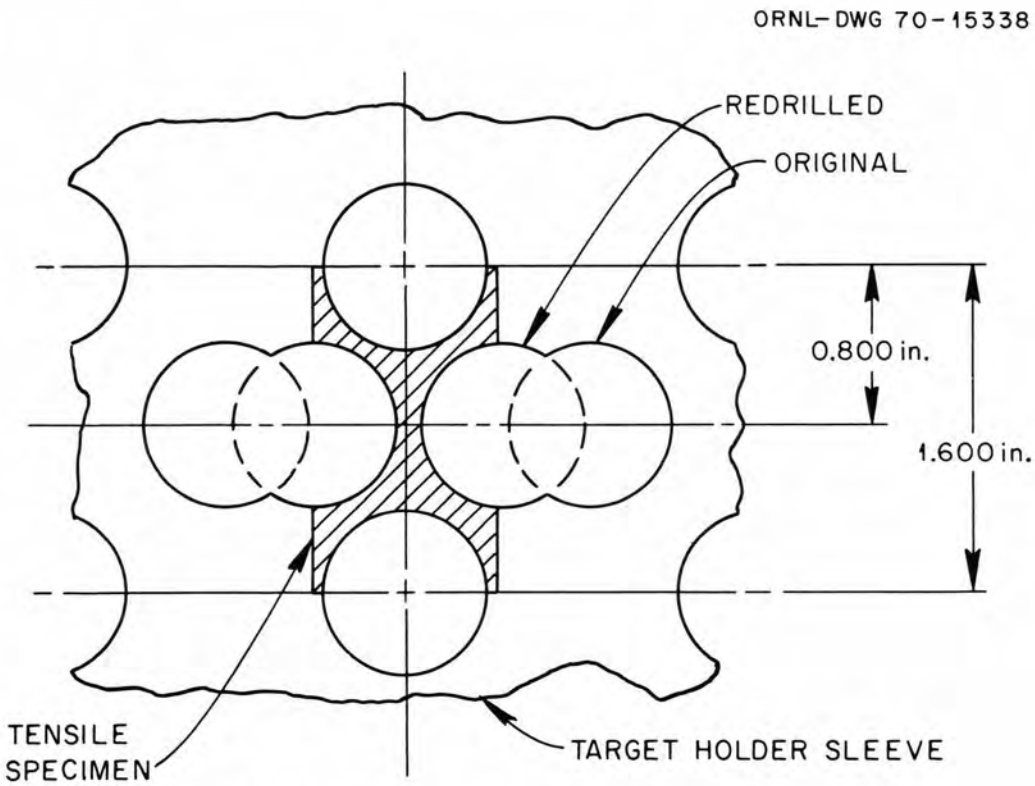

Fig. 17.4. Dogbone Shape of Tensile Specimen.

test may be considered to be a sheet tensile test of specimens with a zero gage length. Hence, neither strain nor strain rate can be defined. The relative crosshead travel after yielding but before fracture and that after yielding but before the ultimate load provide an internally consistent comparison of the total plastic and "uniform" plastic strains for these specimens. Most of the results were obtained between room temperature and 200°C, the anticipated range of operating temperatures for this alloy in the HFIR, although a few tests were performed at temperatures as high as 500°C.

The effect of test temperature on the strength properties of unirradiated control specimens is shown in Fig. 17.5. All of the ultimate

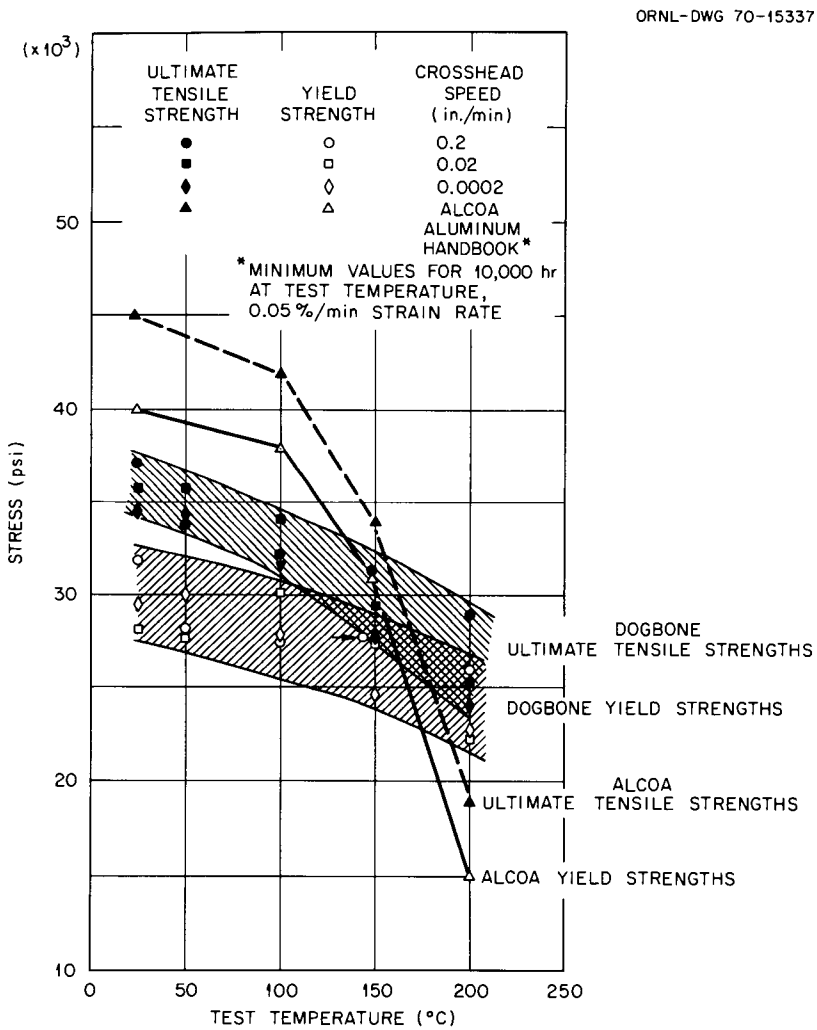

Fig. 17.5. Effect of Test Temperature on Strength Properties of Unirradiated Dogbone-Shaped Tensile Specimens.

tensile strengths and yield strengths of the dogbone specimens fell within scatter bands regardless of the deformation rate. From the widths of the bands, we estimate that the reproducibility of the control data is approximately ±2500 psi. Comparison of these results with other published data is not very meaningful because of the wide range of permissible compositions and consequent strength characteristics; however, published minimum yield and ultimate strengths[10] of 6061 Al alloy in the T6 temper and held 10,000 hr at the test temperature before testing were 40,000 and 45,000 psi, respectively. Because the dogbone specimens were somewhat overaged, the yield and ultimate tensile strengths of the control specimens were somewhat lower, about 30,000 and 36,000 psi. However, specimens[10] tested at 200°C were weaker than our dogbone specimens, because of the overaging that occurs during a 10,000-hr anneal at 200°C.

The effect of increasing test temperatures up to 200°C on the strain properties of the control specimens was to increase the total plastic deformation and decrease the uniform plastic deformation (see Fig. 17.6). Nearly all of the results fell into two scatter bands about 0.005 in. wide regardless of the deformation rate. The exceptions were data for total plastic deformation at 0.2 in./min crosshead speed for tests at 100 to 200°C; these data were about 20% lower than those obtained at faster crosshead speeds.

The yield strengths and ultimate tensile strengths of specimens irradiated to various neutron fluences were significantly increased over those of the unirradiated control specimens for all test temperatures up to 150°C (see Fig. 17.7). At 200°C, strength increased for the test at high strain rate but not for that at low strain rate, evidently because of structural changes during the time of elastic strain, since the specimens that were deformed slowly were annealed under stress for nearly 1 hr longer than those that were strained rapidly. Because of the scatter inherent in the results, it was not always possible to distinguish between two test temperatures. A single smooth curve is used to approximate such data sets.

Figure 17.8 summarizes the strain behavior of specimens tested at 200°C and below at varying neutron fluences. At the crosshead speed of 0.2 in./min, the amount of deformation before fracture decreased from

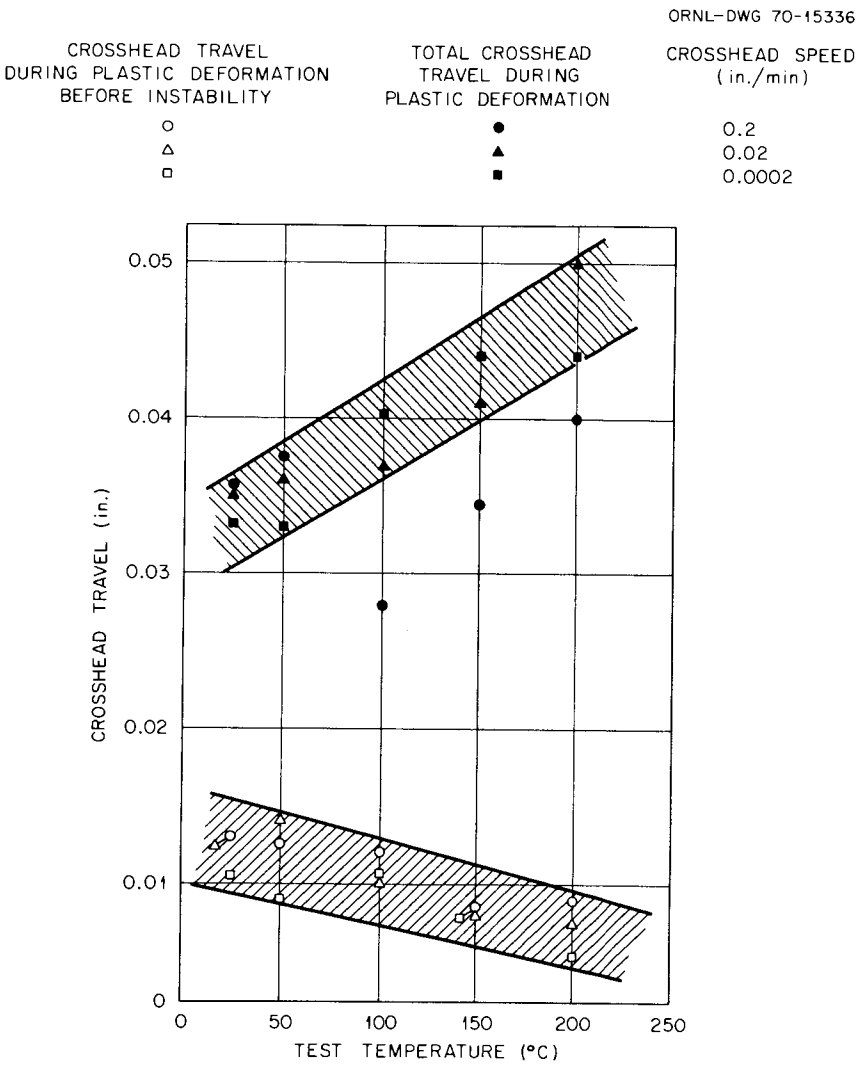

Fig. 17.6. Plastic Deformation of Dogbone-Shaped Tensile Specimens of Unirradiated 6061 Aluminum.

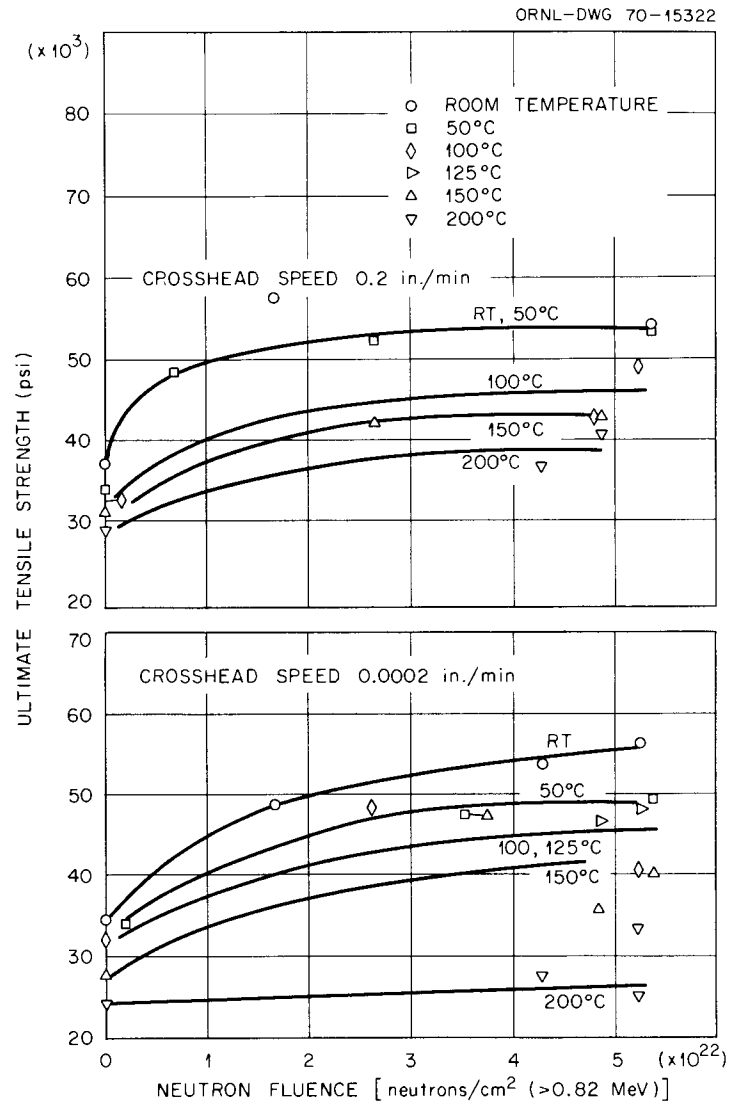

Fig. 17.7. Ultimate Tensile Strength of Dogbone-Shaped Tensile Specimens of 6061 Aluminum from Irradiated High Flux Isotope Reactor Target Basket.

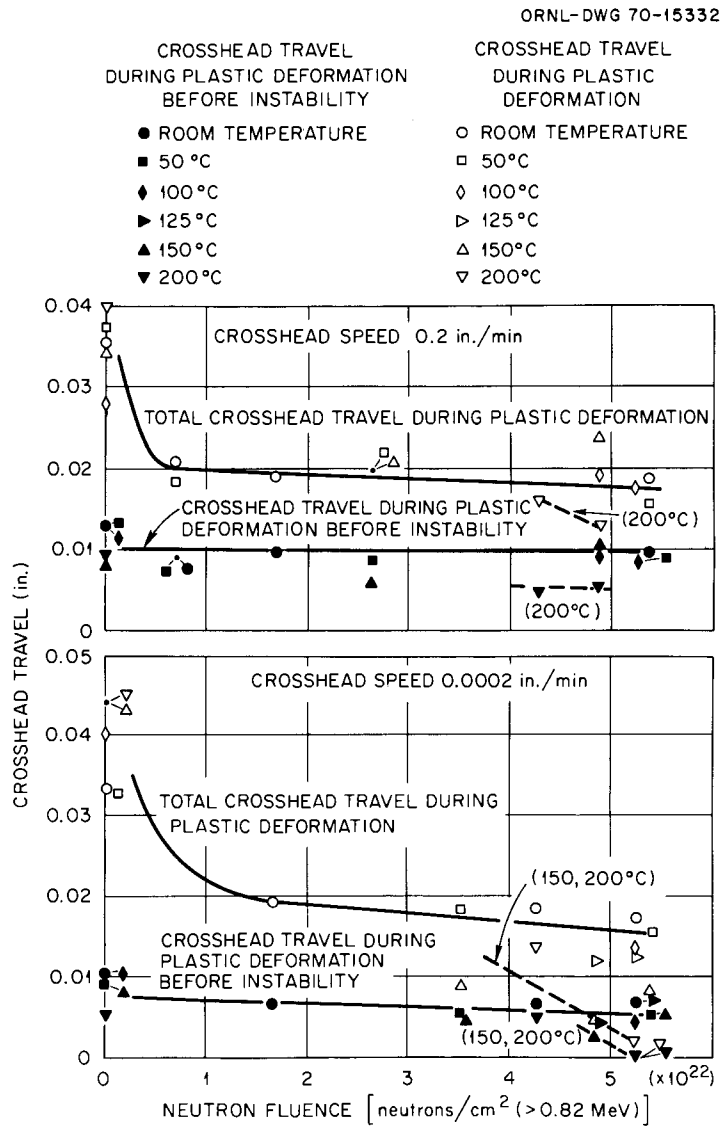

Fig. 17.8. Plastic Deformation of Dogbone-Shaped Tensile Specimens of 6061 Aluminum from Irradiated High Flux Isotope Reactor Target Basket.

0.3 or 0.4 in. to about 0.2 in., regardless of the test temperature. The specimens irradiated to high fluences and tested at 200°C had somewhat lower average ductility than those tested at lower temperatures.

Because the data presented thus far have dealt primarily with the effect of neutron fluence, the specimens involved have come from a variety of locations along the target basket. However, if we examine the data for specimens irradiated to high fluences (e.g., between 4.8 and 5.4×10^{22} neutrons/cm^2), the data under consideration are limited to

those for specimens irradiated close to the reactor midplane at nearly the same temperature and to nearly the same fluence. Elimination of the possible influence of these variables produced a set of conclusions somewhat different from those obtained above.

Figure 17.9 shows the effect of deformation rate, or crosshead speed, on the ultimate tensile strengths at 100, 150, and 200°C for specimens irradiated to greater than 4.8×10^{22} neutrons/cm^2 (> 0.82 MeV). Although the strength properties measured at 2×10^{-1} and 2×10^{-3} in./min crosshead speeds differed little, the crosshead speed of 2×10^{-4} in./min produced consistently lower strengths. The greatest loss of strength occurred at 200°C, which is reasonable if the changes were caused by the annealing out of damage or overaging during the tensile test. Although the data indicate a consistent trend toward lower strengths at slow strain rates, there was as much as 9000 psi difference between duplicate or nearly duplicate tests. Therefore, the data require further statistical interpretation.

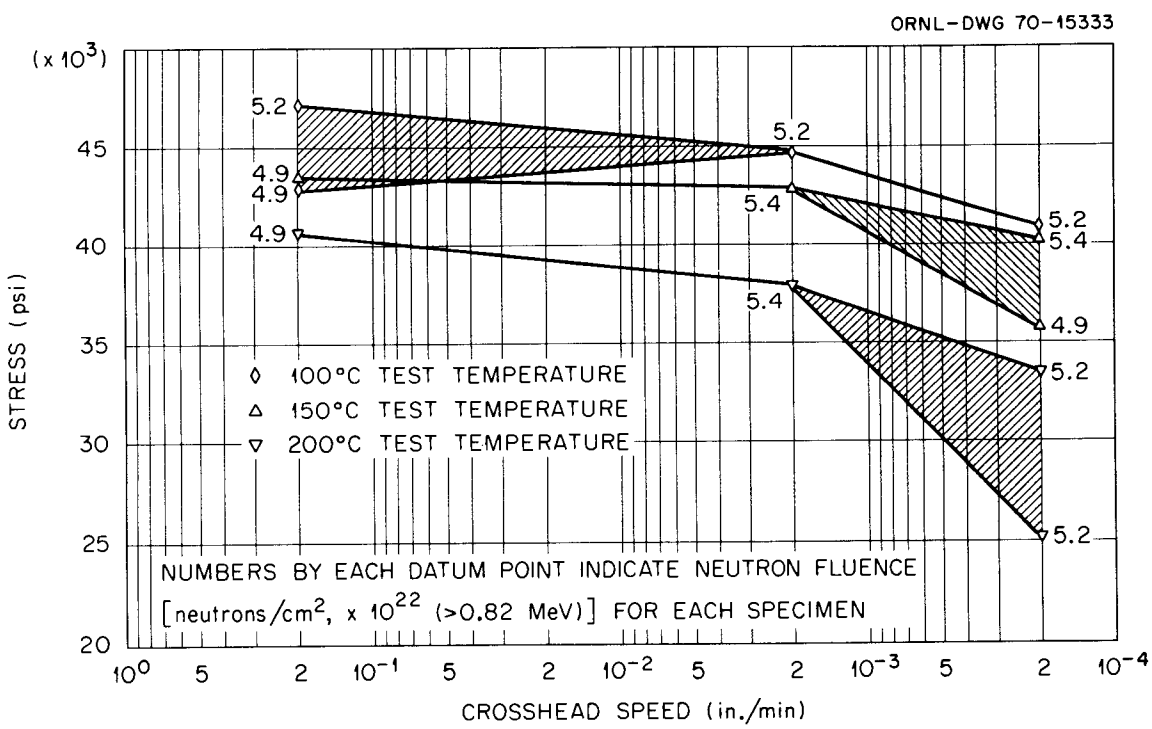

Fig. 17.9. Effect of Crosshead Speed on the Ultimate Tensile Strength of Dogbone-Shaped Tensile Specimens of 6061 Aluminum Irradiated to 4.8 to 5.4×10^{22} neutrons/cm^2 (> 0.82 MeV).

The effect of deformation rate on ductility can be interpreted more easily (see Fig. 17.10). For tests between 100 and 200°C at the faster deformation rates, there was no effect of test temperature on either the uniform plastic deformation or total plastic deformation. However, at the slowest deformation rate, 2×10^{-4} in./min crosshead speed, the effect of test temperature on ductility was quite noticeable; the ductilities of specimens tested at lower temperatures were consistently higher than those of specimens tested at 200°C, and, on the average, ductility decreased with increasing test temperature. Note that a pair of specimens was tested at 125°C to gain further information on the effect of test temperature at low strain rates.

When the ultimate tensile strengths of only those specimens irradiated to a high fluence are plotted versus test temperature from room temperature to 500°C (see Fig. 17.11), there is a tendency for specimens tested at the fast deformation rate of 0.2 in./min to exhibit higher

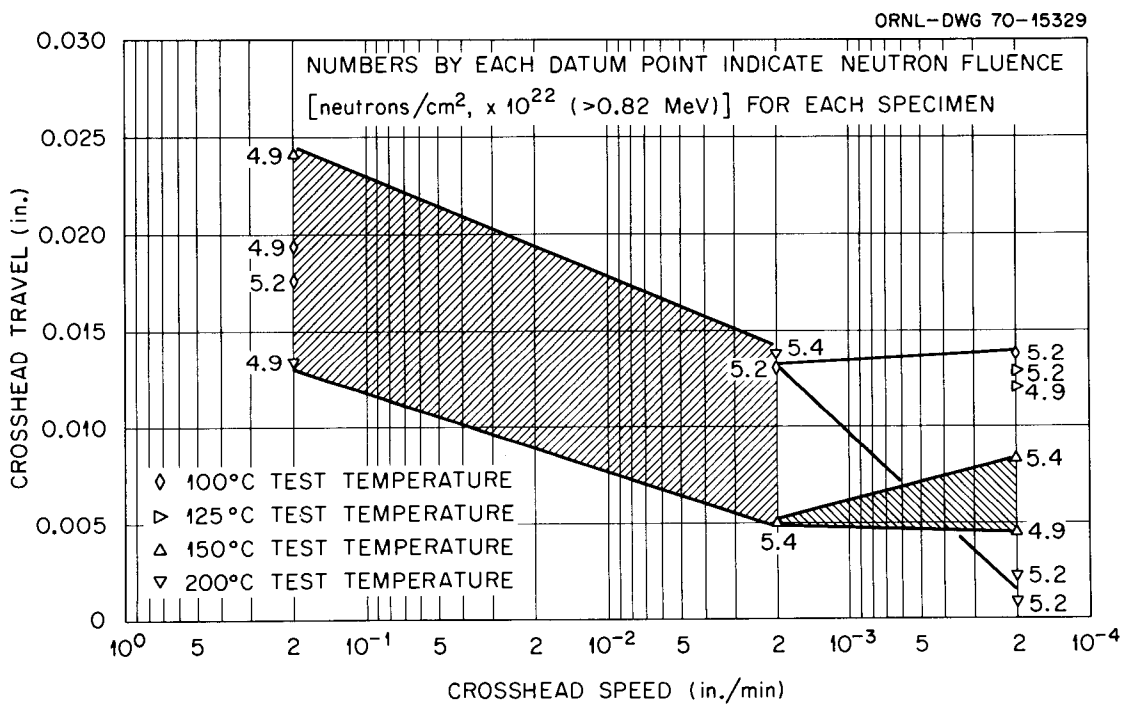

Fig. 17.10. Effect of Crosshead Speed on the Total Crosshead Travel During Plastic Deformation of Dogbone-Shaped Tensile Specimens of 6061 Aluminum Irradiated to 4.8 to 5.4×10^{22} neutrons/cm^2 (> 0.82 MeV).

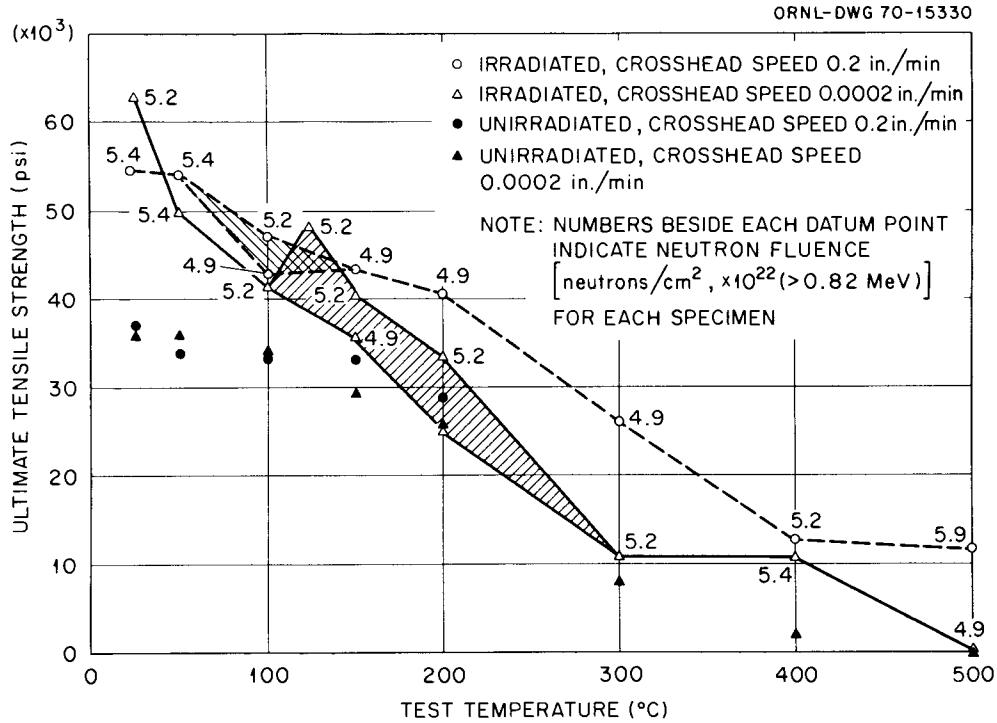

Fig. 17.11. Effect of Test Temperature on the Ultimate Tensile Strength of Dogbone-Shaped Tensile Specimens of 6061 Aluminum Irradiated to 4.8 to 5.4 × 10^{22} neutrons/cm^2 (> 0.82 MeV).

strengths than those tested at 0.0002 in./min. For tests at temperatures above the irradiation temperature, this behavior might be ascribed to annealing effects, since the specimens tested at slow deformation rates have more time to anneal during the early stages of the test. However, this argument cannot be true for temperatures below the irradiation temperature; in fact, at room temperature, the higher ultimate strength was observed for the slower deformation rate.

The effect of test temperature on the ductility of the specimens irradiated to high neutron fluences is shown in Fig. 17.12. The two most important features shown there are the general tendency toward lower plastic deformations at the slower deformation rate and the severe reduction in ductility at about 200°C at the slower strain rate.

Only a limited number of specimens contained the seam weld, and these received a wide range of neutron fluences. The main purposes of testing these specimens were to determine differences in properties between the base and weld metals and to assess whether the welded region

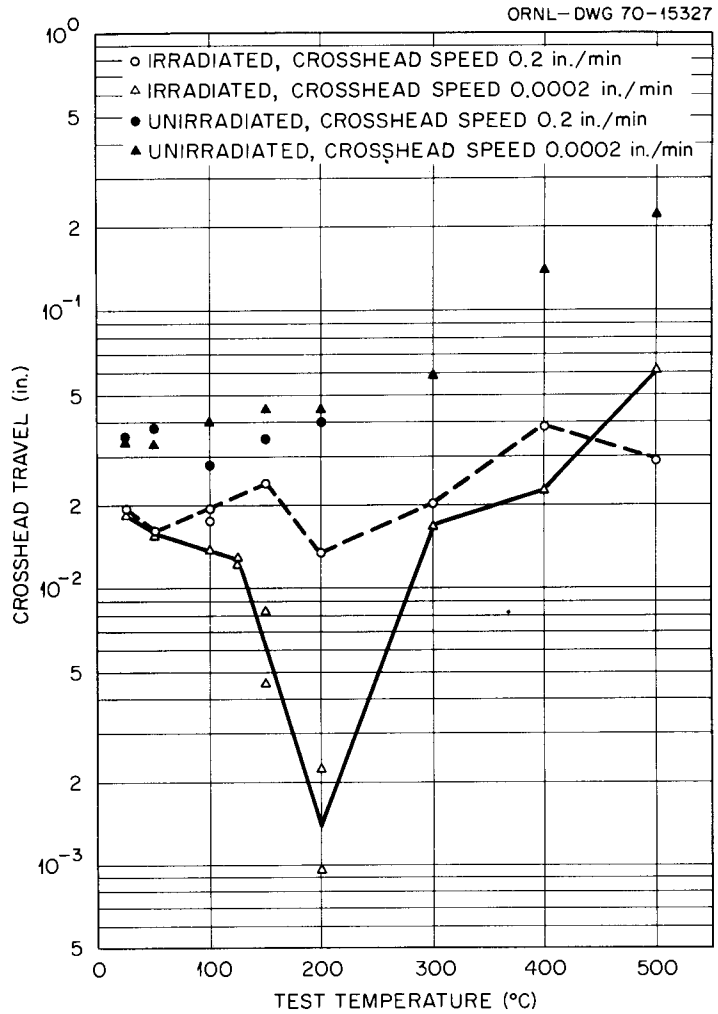

Fig. 17.12. Plastic Strain Between Yield and Failure. Specimens irradiated to 4.8 to 5.4 × 10^{22} neutrons/cm^2 (> 0.82 MeV).

was safe for use in-reactor after exposure to high neutron fluences. Therefore, the specimens that had received the highest fluences were tested under the conditions most likely to occur during normal reactor operation (i.e., at relatively low temperatures). It is unfortunate that good tensile specimens could not be prepared transverse to the weld. The properties measured parallel to the weld were determined over a cross section that contained almost solely fused metal. Since the weldments were 0.2 to 0.3 in. wide while the specimens were 0.15 in. wide, the reduced cross section was composed of a mixture of the fused base metal and the Si-rich 4043 Al filler metal. It must be remembered that

the weldment was heat treated according to the same schedule as the base metal. These tests do provide a meaningful comparison between the base metal and weld metal but do not provide any information on the soundness of the interface between them.

In Fig. 17.13, the ultimate strength of the specimens that contained weldments are plotted versus neutron fluence. For comparison, the smooth curves drawn through the average data for the base metal of Fig. 17.7 are also reproduced, and vertical connecting lines are drawn to show differences between the data for the weld specimen and the

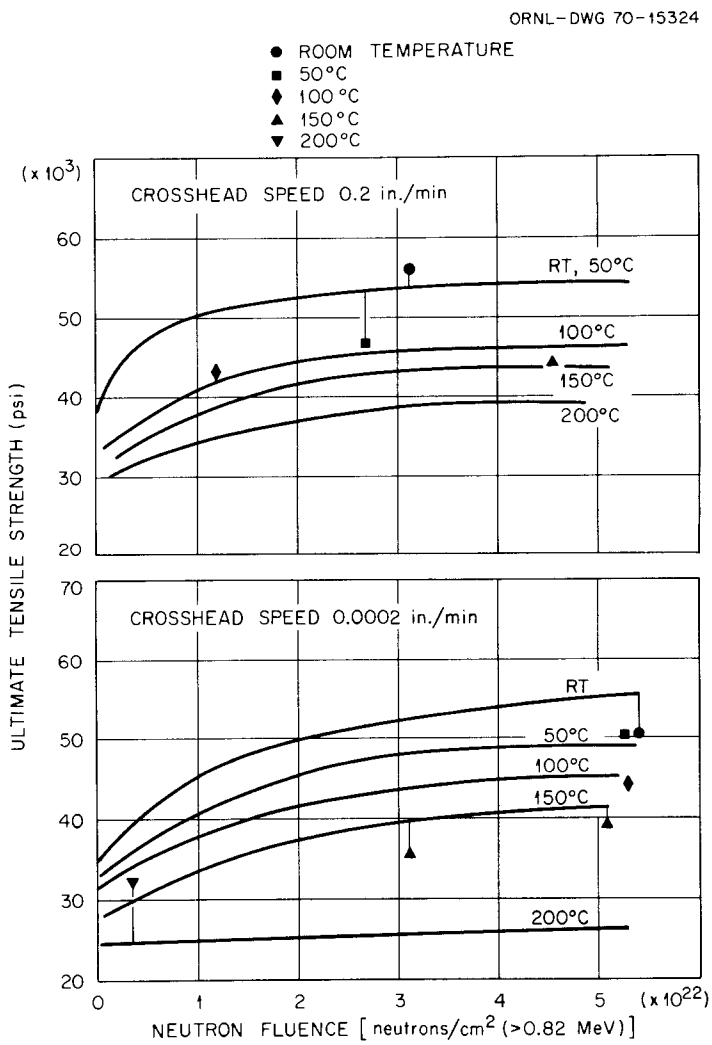

Fig. 17.13. Ultimate Tensile Strengths of Dogbone-Shaped Tensile Specimens of 6061 Aluminum that Contain Weldments from High Flux Isotope Reactor Target Basket.

curves for the base metal. In the overwhelming majority of cases, the weld specimens had lower yield strengths than the specimens of base metal, but the ultimate strengths of the weldments were scattered fairly evenly about the curves for base metal. The data for the ductility of the specimens that contained the weld seam are plotted in Fig. 17.14; it is apparent that the specimens that contained the weld were always less ductile than their base-metal counterparts.

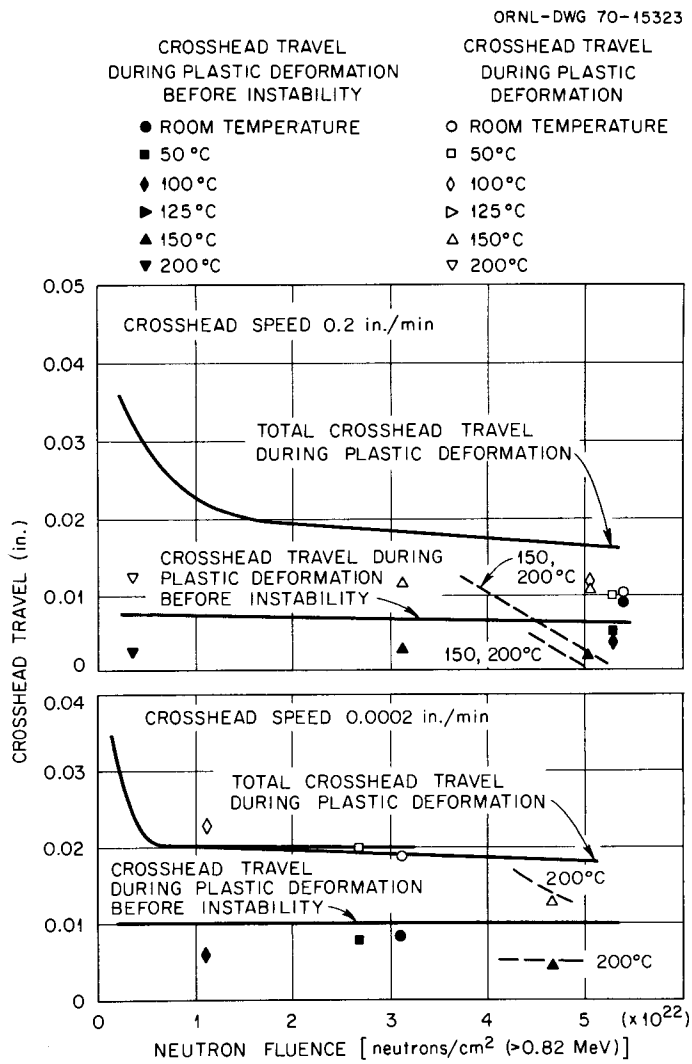

Fig. 17.14. Plastic Deformation of Dogbone-Shaped Tensile Specimens of 6061 Aluminum that Contain Weldments from High Flux Isotope Reactor Target Basket.

Even though the ductility of the weld was lower than that of the base metal, the strength properties of the two were nearly comparable; in fact, the strength of both weld metal and base metal after irradiation exceed those required for unirradiated 6061 Al.

Notes

1. R. M. Hill, Jr., Oak Ridge National Laboratory, private communication.
2. Alcoa Aluminum Handbook, p. 62, Aluminum Company of America, Pittsburgh, Pennsylvania (1967).
3. C. D. Cagle and T. M. Sims, Oak Ridge National Laboratory, private communication.
4. T. M. Sims, Oak Ridge National Laboratory, private communication.
5. J. Griess, The Effect of Heat Flux on the Corrosion of Aluminum by Water, ORNL-3230 (1961).
6. A. F. Zulliger, Oak Ridge National Laboratory, private communication.
7. R. L. Lines, Oak Ridge National Laboratory, private communication.
8. A. Jostsons, Oak Ridge National Laboratory, private communication.
9. V. J. Tennery, Oak Ridge National Laboratory, private communication.
10. Alcoa Aluminum Handbook, p. 38, Aluminum Company of America, Pittsburgh, Pennsylvania (1967).

18. JOINING RESEARCH ON NUCLEAR MATERIALS

J. R. Weir, Jr. G. M. Slaughter

The purpose of this program is to gather the fundamental and applied data needed to understand the weldability of materials that are either being considered or are currently used for nuclear applications. Fundamental studies are concerned with the effects of minor constituents on the behavior of weldments. We are especially interested in the austenitic stainless steels and the alloys that are rich in Ni, such as Incoloy 800 and Inconel 600. In addition, a modest program concerned with the influence of weld defects will provide reference results in this much-talked-about but little-investigated field.

As a result of this broad-based program, we plan to suggest modifications in both alloy composition and procedures needed to improve the quality of weldments used in the various activities of the Commission.

The Effect of Minor Variations in Chemical Composition on Weldability

Our continuing investigation of the effect of minor variations in those elements usually present in structural materials has included Inconel 600, Incoloy 800, and stainless steel.

Weldability of Incoloy 800 (D. A. Canonico)

Fully restrained welds made with our experimental filler metals in 1/2-in.-thick commercial Incoloy 800 plates are being evaluated. Initial results of the program were described previously.[1] Results of bend tests are presented in Table 18.1. The assessment of the bend results includes the designation "marginal"; these specimens did not crack but did have some questionable surface tears that may be associated with the weld and that must be evaluated further. Most of the welds were acceptable (either "pass" or "marginal"). Figure 18.1 is a photograph of the face of a specimen that successfully passed the bend test. Three experimental filler metals cracked during welding, and work was stopped on these

Table 18.1. Bend Test Results for Welds in 1/2-in.-thick Incoloy 800 Plate

Filler Metal Alloy	Bend Test Results[a]	Additions to Nominal Composition, wt %				
		Al	Ti	S	P	C
800-2	M	0.15	0.15			
800-3	P	0.38	0.38			
800-4	M	0.60	0.60			
800-5	M	0.38	0.15			
800-6	P	0.38	0.60			
800-7	P	0.15	0.38			
800-8	P	0.60	0.38			
800-10	P	0.38	0.38	0.015		
800-11	P	0.38	0.38	0.02		
800-15	P	0.38	0.38	0.01	0.01	
800-16	F	0.38	0.38	0.015	0.015	
800-17	M	0.38				
800-18	CDW		0.38			
800-19	CDW			0.015		
800-22	CDW					0.01
800-23	P					0.04
800-24	F					0.08

[a]P = passed; M = marginal; F = failed; CDW = cracked during welding.

Fig. 18.1. Photograph of a Specimen that Successfully Passed the Bend Test. Alloy 800-10 filler metal.

alloys: alloy 800-18 contained Ti, alloy 800-19 contained S, and alloy 800-22 contained low C. Two welds failed during bend testing: alloy 800-16 contained high levels of P and S and alloy 800-24 contained a high level of C. The severity of the cracking is evident in Fig. 18.2.

Tensile specimens were machined from the successful weldments. These were radiographed and are being tested at room temperature and 650°C.

Weldability of Stainless Steels (A. J. Moorhead, D. A. Canonico)

We are studying metallographically the electron-beam (EB) and gas tungsten-arc (GTA) bead-on-plate welds made on annealed and on 50% cold-worked coupons from drop-cast heats 5408 through 5422. The welding conditions used were 100 kV, 7mA, and 25 in./min for the EB welds, and 125 A, 20 in./min, and 1/16-in. arc length, in Ar, for the GTA welds. The coupons were distorted due to rolling so that they were difficult to position with respect to the arc or beam. Consequently, there were variations in depth of penetration and bead contour.

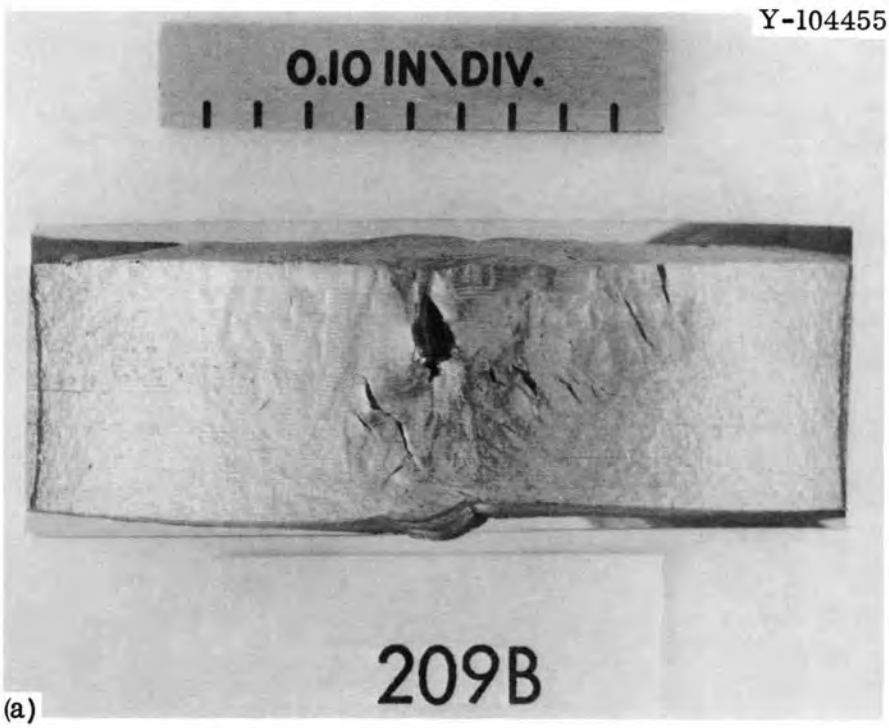

(a)

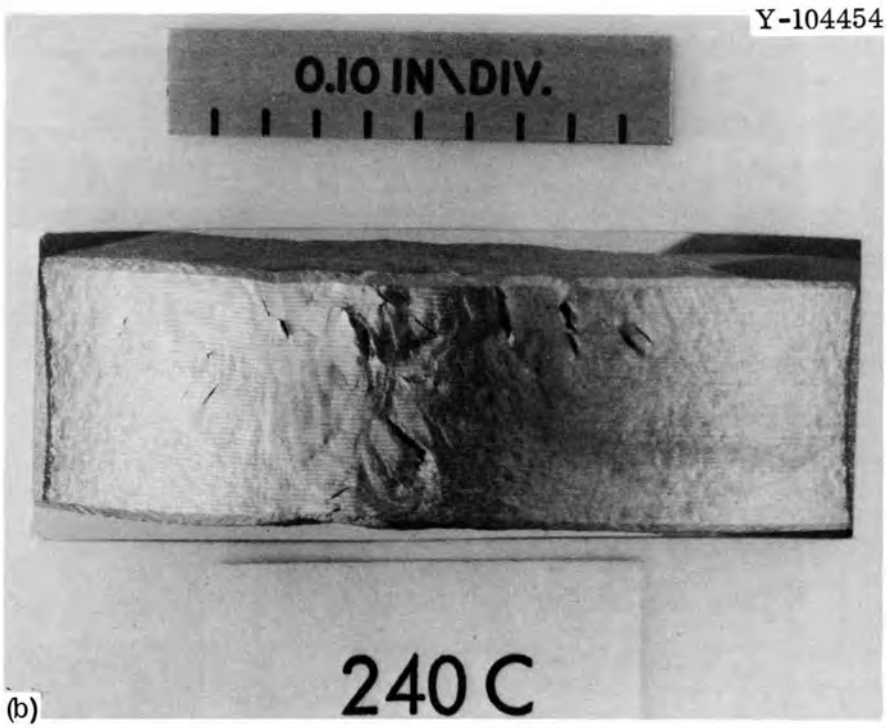

(b)

Fig. 18.2. Photographs of Weldments that Failed the Bend Test. (a) Alloy 800-18 filler metal, rich in sulfur and phosphorus. (b) Alloy 800-24 filler metal, rich in carbon.

The metallographic specimens were electrolytically etched (2 1/2 V) in a solution of 81.5 wt % acetic acid, 14.5 wt % chromic acid (CrO_3), and 4 wt % H_2O to reveal the presence of martensite induced by strain. This etchant also revealed the ferrite in the microstructure. The low-magnification photomicrographs of Figs. 18.3 and 18.4 are typical of the results with this etchant. Note the dark band in the heat-affected zone of the cold-worked specimen from heat 5415. This appears to be a good example of tempered martensite. This coupon had at least 15% martensite induced by strain after cold working as determined by the Magne-Gage. This band is not visible in the cold-worked specimen from heat 5420 (Fig. 18.4), and the Magne-Gage indicated that this coupon contained less than 2% martensite.

The specimens were repolished and etched with boiling Murakami's reagent (8.3 wt % potassium hydroxide, 8.3 wt % potassium ferricyanide, 83.4 wt % water) to better reveal the ferrite in the microstructure. The photomicrographs in Fig. 18.5 are typical of the results obtained. Some of these specimens were difficult to etch with this reagent, but there was no readily apparent reason for this anomaly. The most interesting feature of these microstructures appears in the heat-affected zone. Note that some sort of transformation evidently occurred in the ferrite phase in this zone. The particles no longer have smooth contours, but, instead, there is an indication that melting occurred and that there was flow along the austenite grain boundaries. This appears to be in direct contrast to the opinion that ferrite is the first phase to solidify and, thus, has a higher melting point than austenite. This is an important area of contention, and further study by hot-stage metallography is planned.

We found the interpretation of the complex cold-worked structures very difficult by optical microscopy with oil immersion and phase contrast techniques. Accordingly, we began a study with the electron microscope. This investigation indicates that these microstructures consist of austenite with a rather high density of dislocations, bands of ϵ phase, and martensite needles within these bands. A typical electron micrograph of one of the cold-rolled structures is shown in Fig. 18.6.

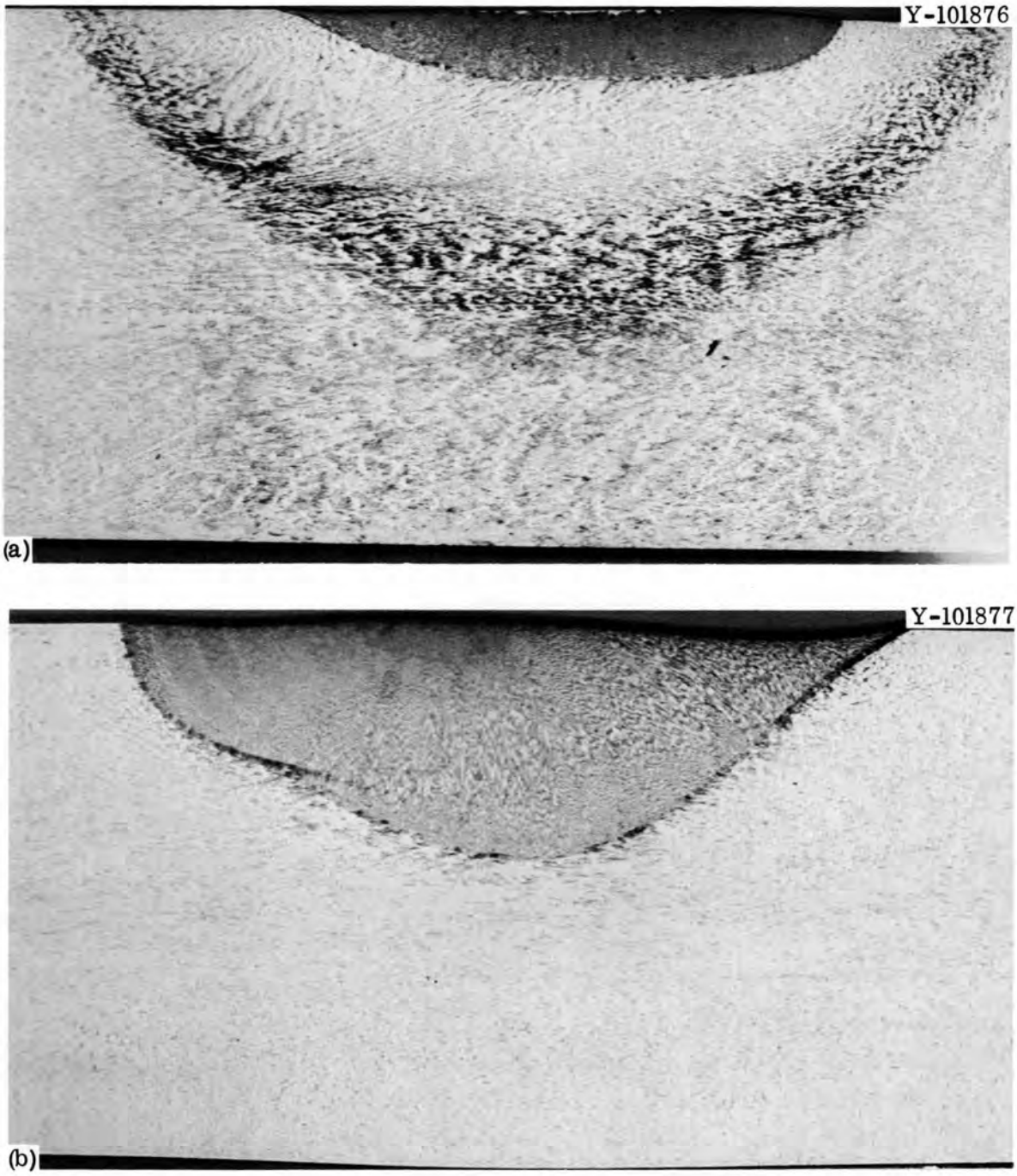

Fig. 18.3. Gas Tungsten-Arc Welds in Coupons from Heat 5415 (Fe–11.8% Ni–20.3% Cr). Special etchant to reveal martensite. 25×. (a) Base metal cold worked 50% at 0°C. (b) Base metal annealed 60 min at 1150°C after cold working.

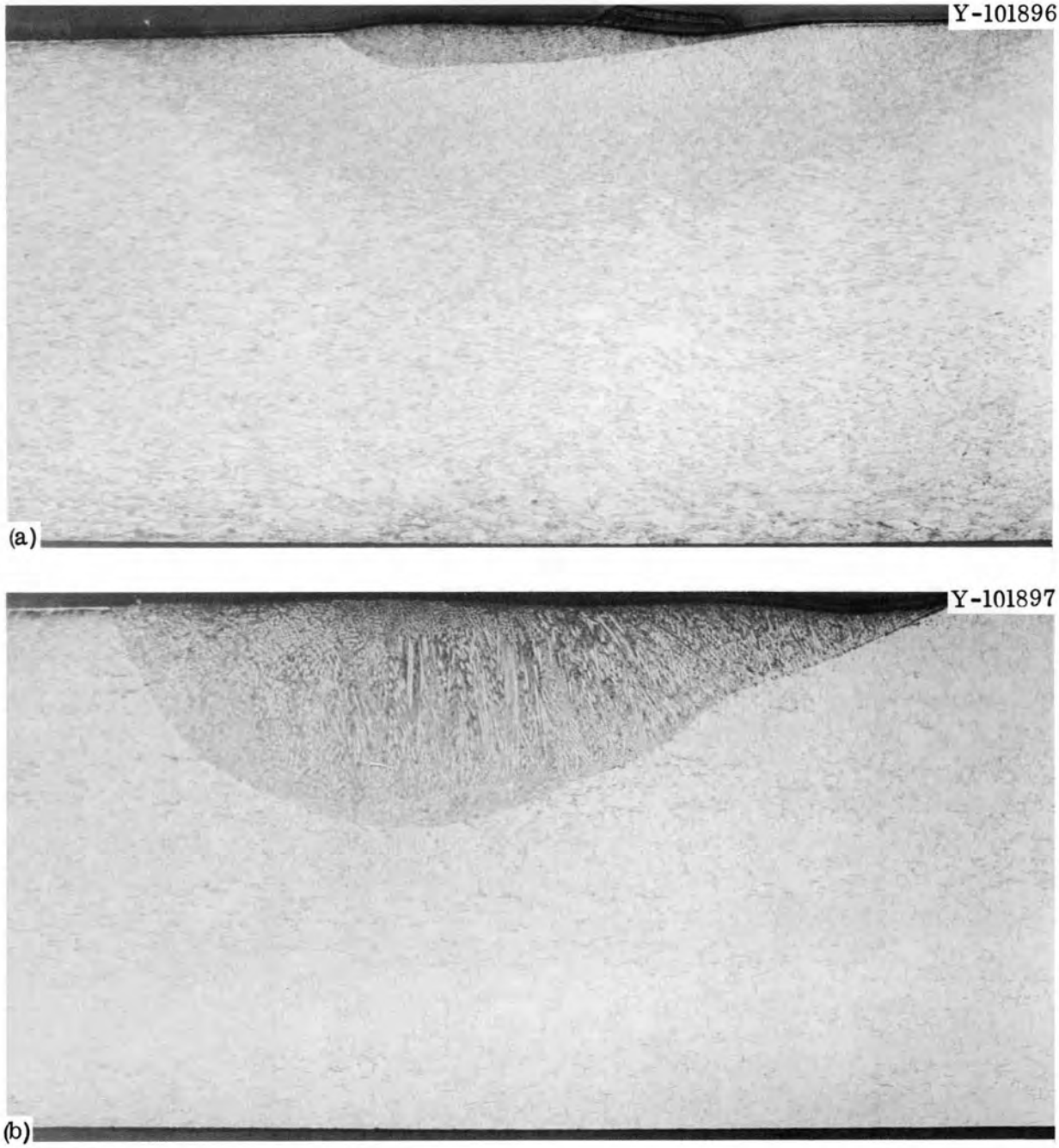

Fig. 18.4. Gas Tungsten-Arc Welds in Coupons from Heat 5420 (Fe–15.3% Ni–23.3% Cr). Special etchant to reveal martensite. 25×. (a) Base metal cold worked 50% at 0°C. (b) Base metal annealed 60 min at 1150°C after cold working.

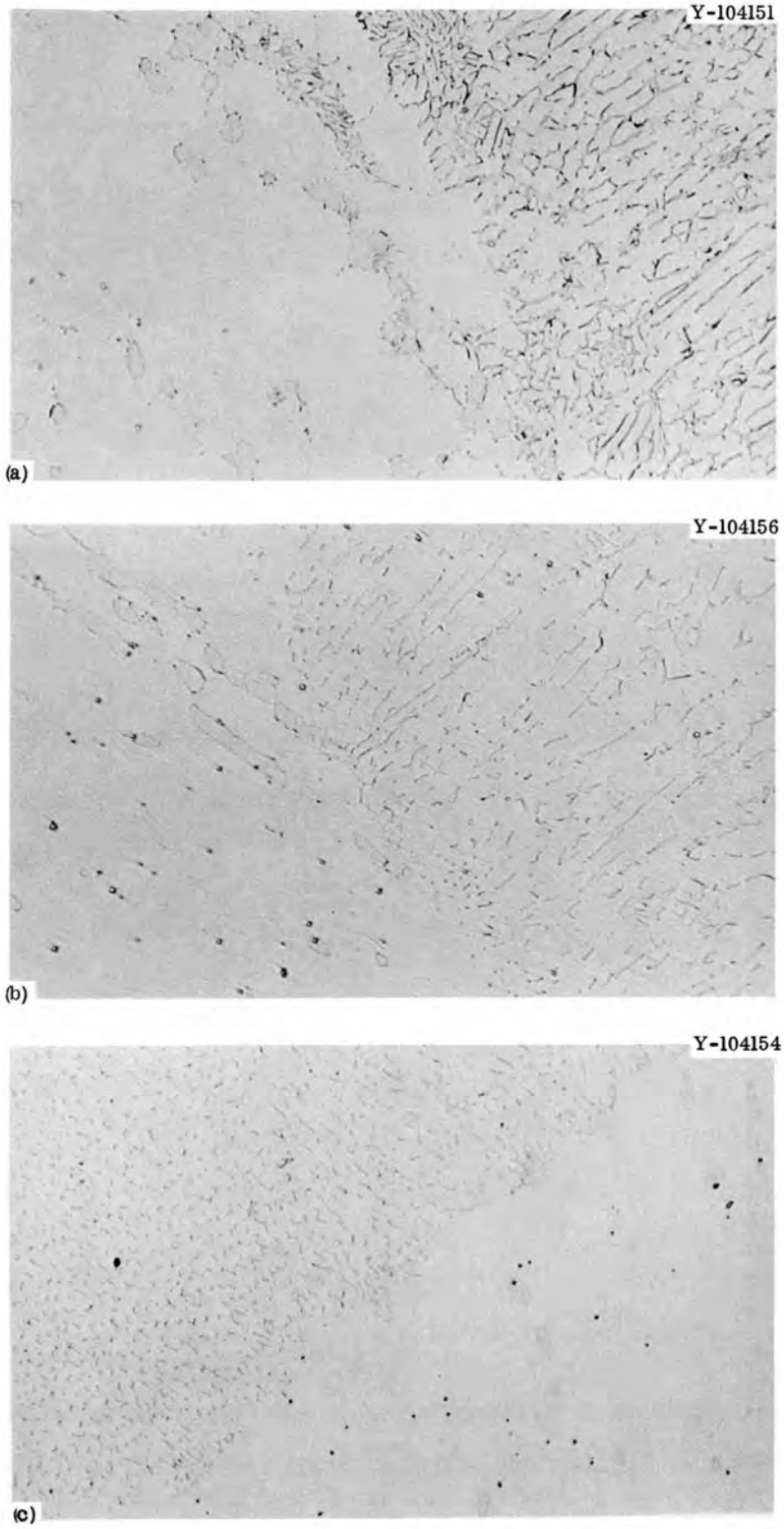

Fig. 18.5. Cross Sections of Weldments Etched with Boiling Murakami's Reagent to Reveal Ferrite. 500×. Reduced 28%. (a) Gas tungsten-arc weld in annealed coupon from heat 5415. (b) Gas tungsten-arc weld in annealed coupon from heat 5420. (c) Electron-beam weld in annealed coupon from heat 5416.

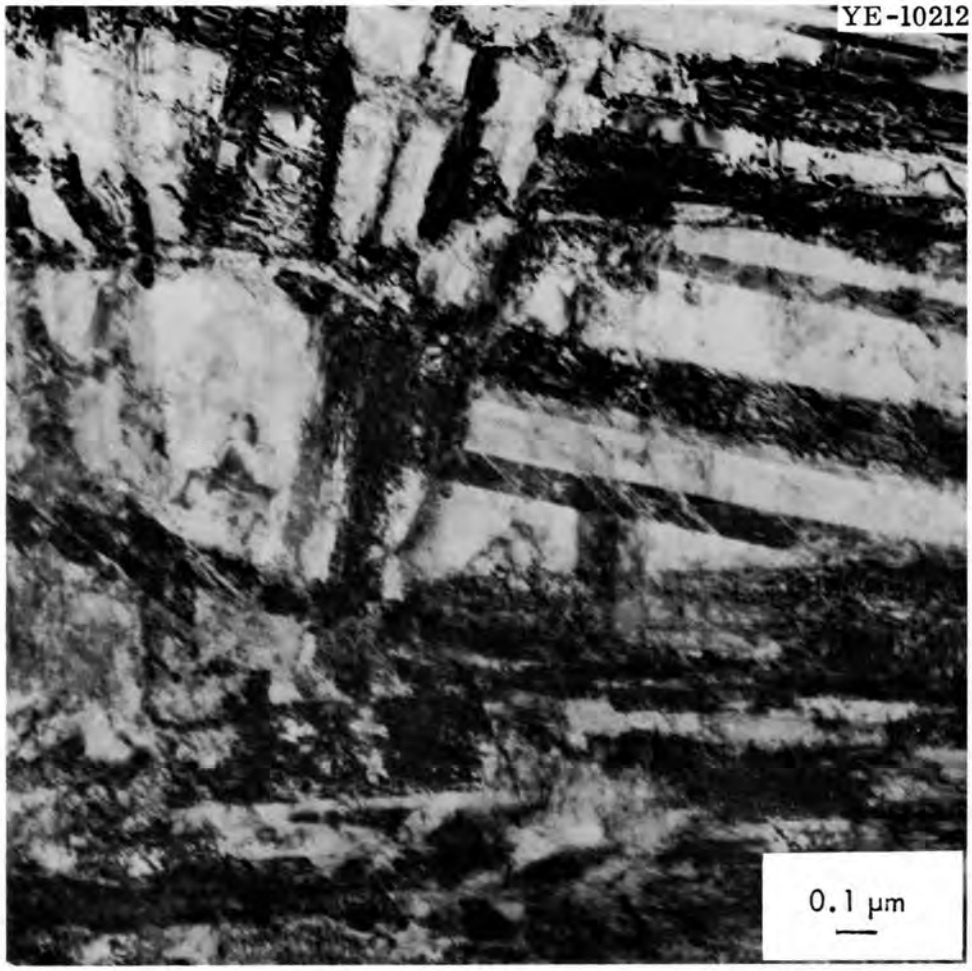

Fig. 18.6. Transmission Electron Micrograph of a Specimen from Heat 5410 (Fe–9.8% Ni–18.3% Cr) That Had Been Deformed 25% Reduction in Thickness by Rolling at 0°C.

Notes

1. D. A. Canonico and W. J. Werner, Fuels and Materials Development Program Quart. Progr. Rept. Sept. 30, 1970, ORNL-4630, p. 261.

19. NONDESTRUCTIVE TESTING

W. O. Harms R. W. McClung

Our task is to develop new and improved methods of nondestructively testing reactor materials and components. We are studying various physical phenomena, developing instruments and other equipment, devising techniques, and designing and fabricating reference standards. Among the methods being studied for both normal and remote inspection are electromagnetics (with major emphasis on eddy currents), ultrasonics, and penetrating radiation.

Electromagnetic Inspection Methods (Eddy Currents)

Solutions for Electromagnetic Induction Problems (C. V. Dodd, W. A. Simpson, C. C. Lu,[1] W. E. Deeds[2])

We are refining and extending an earlier relaxation program. The program will allow the magnetic permeability to vary with field strength and the conductor to move relative to the coil.

We are also attempting to calculate the variations caused by a number of second-order effects. In our most accurate measurements of impedance, the calculated impedance is several tenths of a percent different from the measured impedance. While this disagreement is relatively small in itself, if we try to make an absolute measurement of an electromagnetic property of a sample, such as electrical conductivity, without the use of reference standards, the error in conductivity will be several percent. Thus, we concluded that these second-order effects are quite important and represent the present limit in making absolute eddy-current measurements with alternating current. These second-order effects could be due to the lack of complete axial symmetry, small dimensional variation, imperfections in the winding technique, and interaction between the windings in the coil (most likely, it is a combination of these). We are using both analytical and empirical techniques to determine the causes of these effects.

We wrote a computer program that calculates the conductivity and lift-off needed to give a particular normalized coil impedance. Thus, we are now able to measure the normalized coil impedance, using a Wayne Kerr impedance bridge, and to determine the electrical conductivity and lift-off directly. The calculated lift-off agrees with the measured lift-off to within 0.0001 in. (the accuracy of the shims used to set the lift-off mechanically), although there is some ambiguity about the exact position of "zero lift-off." The electrical resistivity calculated from impedance values that were measured by alternating current was about 7% higher than the resistivity measured by the direct current method. We are preparing a new batch of conductivity standards, consisting of 12 different alloys. We shall machine about 20 standards from each alloy for measurements by alternating and direct current and shall attempt to get a more accurate set of conductivity standards for measurements by alternating current.

We applied our computer programs to improve the accuracy of measurements of thickness by means of the phase-sensitive eddy-current instrument and reflection-type coils, as shown in Fig. 19.1. The solid line represents the phase shift for a 10% change in thickness for various values of the parameter $\bar{r}^2\omega\mu\sigma$. The dashed line represents the percentage of error in the measurement of thickness due to a variation in lift-off of 0.2 $\bar{r}$. By varying the shape of the coil, we can vary the value of $\bar{r}^2\omega\mu\sigma$ to a position at which we will obtain the minimum phase shift due to a given variation in lift-off. If we make this point of minimum phase shift occur at the same value of $\bar{r}^2\omega\mu\sigma$ as the maximum phase shift due to a variation in thickness, the error due to lift-off will approach a very small value. We constructed a coil and verified that we can attain this small phase shift with a rather large variation in lift-off. The dotted line represents the error that would be produced in measurements of thickness by a variation in conductivity of 1% (this points out the need for good calibration standards). We are also using our computer programs to study the measurement of cladding thickness. The results are very similar to those for measurements of plate thickness, although the shape of the coil is different.

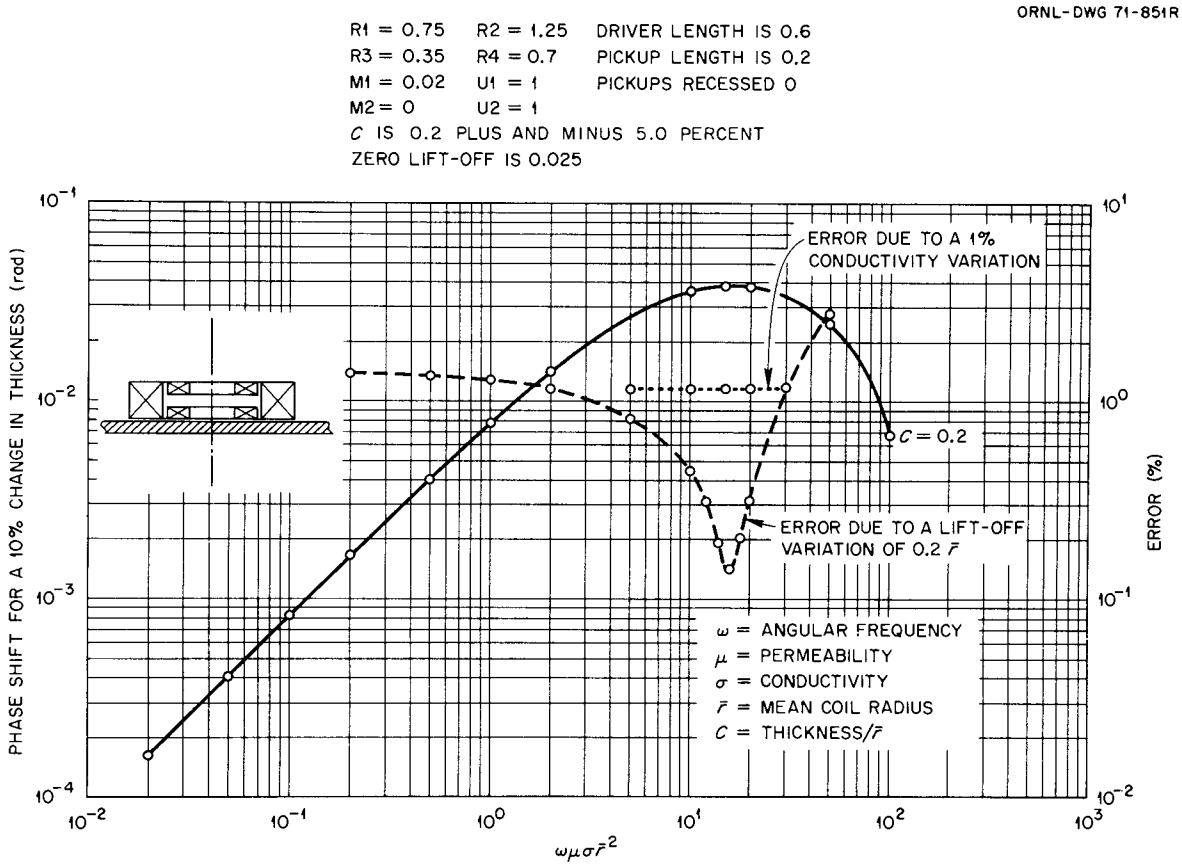

Fig. 19.1. Phase Shift for a 10% Thickness Change and Percent Error Due to Lift-Off Versus $\omega\mu\sigma\bar{r}^2$.

Ultrasonic Inspection Methods

Ultrasonic Frequency Analysis (H. L. Whaley, K. V. Cook, Laszlo Adler[2])

We continued our basic studies of frequency effects in ultrasonic testing by means of spectral analysis. We are employing a special electronic system developed for these studies to learn more about the effects of frequency on conventional ultrasonic techniques. This will enable us to develop new test techniques based upon principles derived from these studies.

We are studying the spectral variations in broadbanded ultrasonic pulses as a function of the acoustical discontinuity with which they have interacted. Such a study can lead to improvements in the characterization of hidden flaws by means of ultrasonic inspection. Spectral analysis of ultrasonic pulses returned from reflection of various types of flaws in

various orientations revealed systematic variations that were functions of the size, shape, orientation, and position of the reflector. We derived analytical expressions that successfully account theoretically for these variations.

We applied the principles developed from these reflection experiments to demonstrate the feasibility of determining the size and orientation (or the size in spite of the orientation) of flaws within a metal specimen by frequency analysis. The sample used was an 8.5 × 7.5 × 2.8 in. plate of steel with smooth, but not polished, surfaces. Flat-bottomed holes of various sizes were drilled at a variety of angles in planes randomly oriented with respect to the sides of the plate. The bottoms of these holes simulated planar flaws with varying depth, size, and angular orientation with respect to the top surface of the plate. Figure 19.2 shows the specimen beside a rubber replica of the flat-bottomed holes drilled in it. One hole was improperly drilled and, therefore, not used. The ultrasonic examination is performed from the surface opposite that containing the drilled holes.

Photo 99784

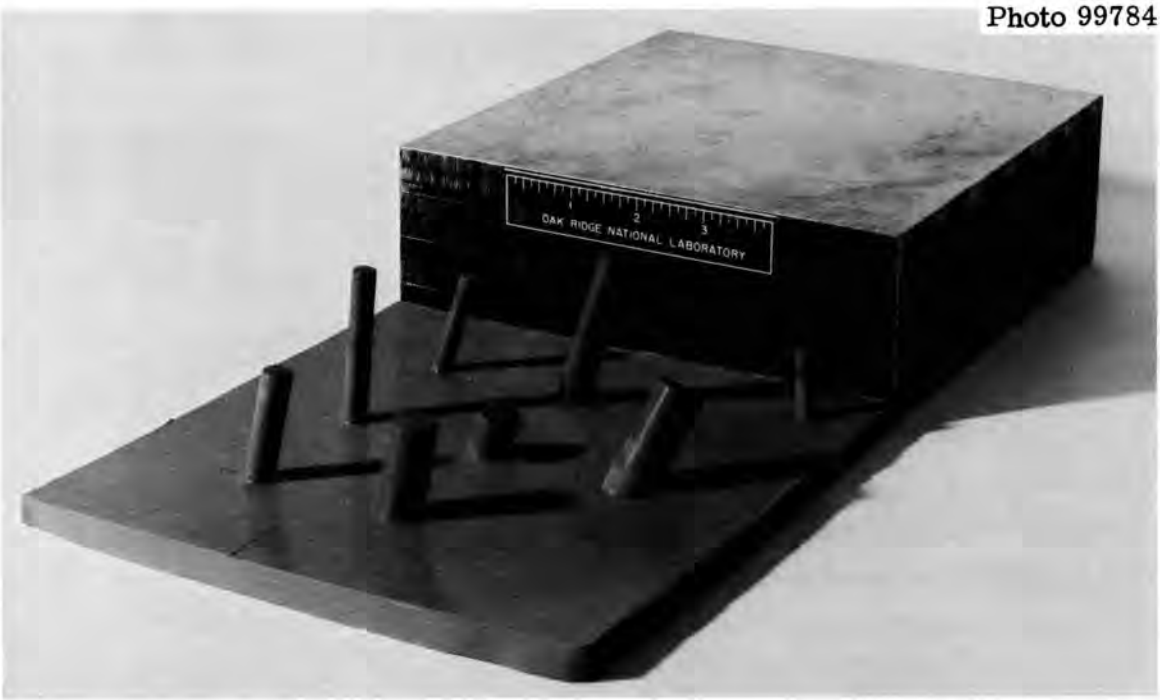

Fig. 19.2. Steel Plate Specimen and Rubber Replica of Drilled Holes.

An experimental procedure to extract the spectral information needed to characterize each flaw was reported.[3] Basically, three separate measurements were taken, the first with the ultrasonic beam perpendicularly incident to the surface of the plate and the second and third at known angles of incidence with respect to the surface in each of two orthogonal planes randomly oriented with respect to the sides of the plate. Figure 19.3 shows representative data obtained in this analysis. In the left-hand column are shown the frequency spectra (for the three cases of incidence described) for the 0.250-in.-diam flaw at an 18° angle (hole 1). The corresponding signal waveforms in the right-hand column are the waveforms of the reflected ultrasonic pulses that were analyzed. The primary numerical information extracted from the frequency spectra is the average spacing between the interference maxima in the spectrum. The size and orientation of each flaw as determined by spectral analysis are compared with the actual value in Table 19.1.

For comparison, a conventional test using only the amplitude of the signal was also used to determine the size of the discontinuities in the plate. Hole 8 was used as a reference for the amplitude test, since its flat bottom was parallel to the surface. With perpendicular incidence to the plate, we inferred the size of each hole from the amplitude of the reflection from each hole bottom as compared to that from the reference hole. With the amplitude technique, one cannot tell that a flaw lies at an angle, so the size of the signal is taken to estimate the size of the reflection as though it were lying parallel to the surface of the plate. Figure 19.4 demonstrates the relative success of the two methods. The experimental points are numbered to indicate the particular hole involved. It can be seen that the results from the frequency analysis fit well about the ideal line while no response at all to flaw size is evident for the determination based on the amplitude. The reference hole for the amplitude case (hole 7) was not plotted, of course, since its size must be known in order to determine the others.

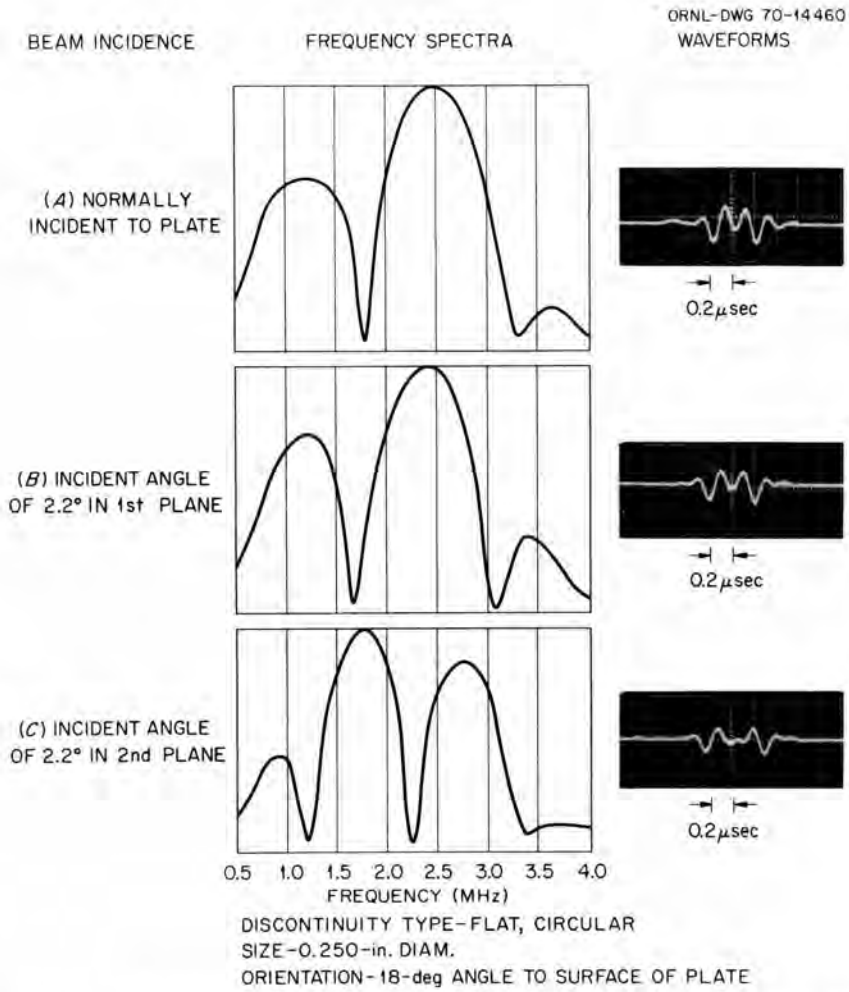

Fig. 19.3. Frequency Spectra and Signal Waveforms for the 0.250-in.-diam Flaw at an 18° Angle.

Table 19.1. A Comparison of the Actual Size and Angle of Each Artificial Flaw in a Steel Plate Specimen with the Experimental Values Determined from Frequency Analysis

Hole Number	Actual		Experimental	
	Hole Size (in.)	Angle (deg)	Hole Size (in.)	Angle (deg)
1	0.250	18	0.241	22.4
2	0.313	31	0.361	30.1
3	0.375	9.7	0.347	13
4	0.438	18	0.468	18
5	0.563	9.5	0.626	7
6	0.625	28.8	0.621	27
7	0.250	0	0.253	~ 0

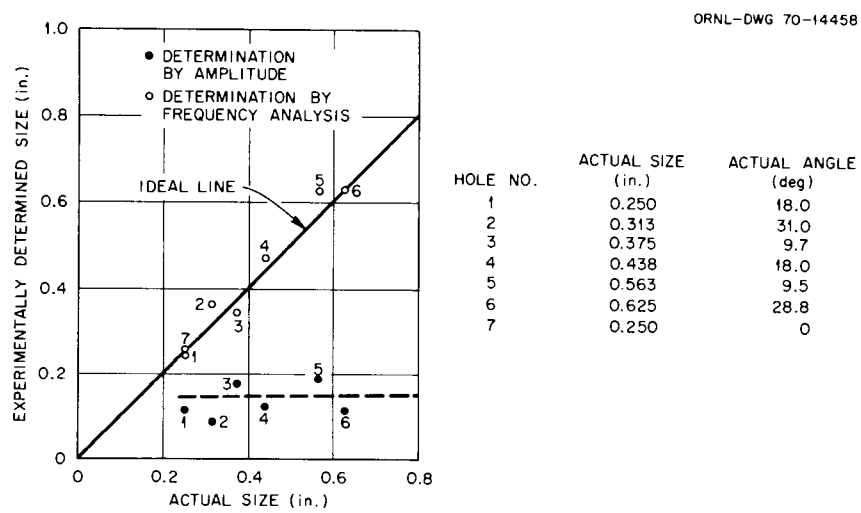

Fig. 19.4. Comparison of Sizes Determined for Artificial Flaws in a Steel Plate by Amplitude and Frequency Analysis Techniques.

Penetrating Radiation

Radiation Scattering (B. E. Foster, S. D. Snyder)

We continued our studies of the use of scattered and fluorescent radiation for measuring the thickness of coatings or claddings on reactor components.

We used a section of a HFIR fuel plate to determine the present capability of the system. Successive points at 1/4-in. intervals were monitored across the width of the plate on both the flat-core side and the contoured-core side. The 16-keV fluorescent x ray from U was monitored. The outline of the contour core (related to the thickness of Al over the fuel) was clearly discernible in the data from that side of the plate. On the flat-core side of the plate, the indication of cladding thickness was relatively uniform except at the edges of the plate. However, this curvature was probably caused by the thin fuel section at the core edges being less than an infinite thickness to the radiation beam. A piece of Al 0.00025 in. thick inserted on the flat-core side caused a change in total integrated counts of 4000, which represents a 2% change in count rate, well above the noise level.

The moisture seal on the NaI(Tl) crystal was damaged. We repaired the pinhole, but the repair slightly decreased resolution at the ^{55}Fe energy of 6 keV. The input amplifiers of the analyzer also became erratic and caused a nonlinear output in the low-number channels. Each difficulty was corrected, and we are recalibrating the system to assure consistency with data obtained previously.

Closed-Circuit Television for Radiographic Evaluation (B. E. Foster, S. D. Snyder)

We are continuing our study of the use of a closed-circuit television system as a rapid densitometer for reading radiographs. The preliminary equipment arrangement consists of a film viewer as a source of illumination, an RCA 525-line closed-circuit television system with a scan rate of 9623 in./sec, and an oscilloscope to delay and view any one of the 525 active lines of video. The radiograph is viewed by means of a zoom lens with a 20- to 88-mm focal distance. We are still working on the reduction of noise and drift.[4] A portion of the noise problem is related to repetition rate. Sampling oscilloscopes are designed to handle fast pulses or frequencies up to 1000 MHz or 1 GHz. However, at lower frequencies (i.e., 60 Hz, which is the frame rate of television systems) such oscilloscopes seem to have excessive vertical jitter or noise. In addition, the recording system that we are now using is rather slow;

this requires a slow readout of the scan and the slow readout adds to the problem of jitter.

In an attempt to overcome the problem of jitter, we modified the camera so that a selected line of video could be scanned repeatedly at a repetition rate of 15,750 times per second rather than the normal rate of 30 times per second. We thought that this increased repetition rate would not only decrease the effective dead time of the system, which would improve the ratio of signal to noise, but would also allow vertical magnification of the single line of video from the camera so that it would fill the entire television screen. However, the "recovery time" of the photosensitive detector in the Vidicon was longer than the time period of one line of video. As a result, the photosensitive surface became very insensitive to changes in light intensity.

We found that the sampling unit was a useful but not optimum replacement for the Lumatron. We are now evaluating a Biomation Transient Recorder sampling unit.

The neutral density filters were received. They will reduce the increments to 0.1 between successive density points during calibration. Previous data and calibration were based on a density wedge with increments of density of 0.2 between steps.

Notes

1. Mathematics Division.

2. Consultant from the University of Tennessee.

3. H. L. Whaley and L. Adler, A New Technique for Ultrasonic Flaw Determination by Spectral Analysis, ORNL-TM-3056 (September 1970).

4. B. E. Foster and S. D. Snyder, Fuels and Materials Development Program Quart. Progr. Rept. Sept. 30, 1970, ORNL-4630, pp. 277–279.

20. ADVANCED MATERIALS FOR STEAM GENERATORS

P. Patriarca G. M. Slaughter

The purpose of this program is to determine the corrosion resistance of welds in several high-temperature alloys being considered for use in steam generators for advanced high-temperature reactors. We need to know how well these weldments will resist both general and preferential corrosion in steam at 540 to 760°C.

The program currently includes two areas of investigation: (1) general corrosion (uniform scale, including pitting and knife-edge attack at fusion lines) at 595 and 650°C together with an evaluation of the general weldability of various combinations of base and filler metals, and (2) stress corrosion cracking (induced by contaminants) at 540°C or higher.

General Corrosion at 595 and 650°C

Studies of Weldments Between Similar and Dissimilar Metals (J. P. Hammond)

The general corrosion specimens recently accumulated a total exposure of 16,000 hr (about 2 years) in superheated steam at 595 and 650°C (1100 and 1200°F) and were permanently removed from their autoclaves for evaluation. The details on the preparation of specimens, which were finished in the belt-ground condition, were given previously.[1] The weldments involved are listed in Table 20.1.

Corrosion results in terms of weight gained for the weldments between similar metals at 595 and 650°C are shown in Figs. 20.1 and 20.2; those for weldments between dissimilar metals are shown in Figs. 20.3 and 20.4. The units are in milligrams gained per specimen (20 cm^2). The linear portion of the curves was established from corrosion data by the least-squares method; extrapolations were made to the coordinate to establish intercepts.

Numerical values for the intercepts and slopes of the curves for weldments between similar metals (Figs. 20.1 and 20.2) are given in Table 20.2 along with data calculated from these slopes and intercepts for penetration of base metal in 20 years. Penetration established from

Table 20.1. Alloy Combinations Under Investigation

Identification Code	Base Metal	Base Metal	Filler Metal
A9	Inconel 625	Inconel 625	Inconel 625
A13	Inconel 625	Incoloy 800	Inconel 625
A12	Inconel 625	Incoloy 800	Inconel 82
A18	IN 102	IN 102	IN 102
A19	IN 102	Incoloy 800	IN 102
A20	IN 102	Incoloy 800	Inconel 82
A5	Hastelloy X	Hastelloy X	Hastelloy X
A6	Hastelloy X	Incoloy 800	Hastelloy X
A8	Hastelloy X	Incoloy 800	Hastelloy W
A7	Hastelloy X	Incoloy 800	Inconel 82
A2	Incoloy 800	Incoloy 800	Inconel 82
A3	Inconel 600	Inconel 600	Inconel 82
A4	Type 304 stainless steel	Type 304 stainless steel	Type 304 stainless steel

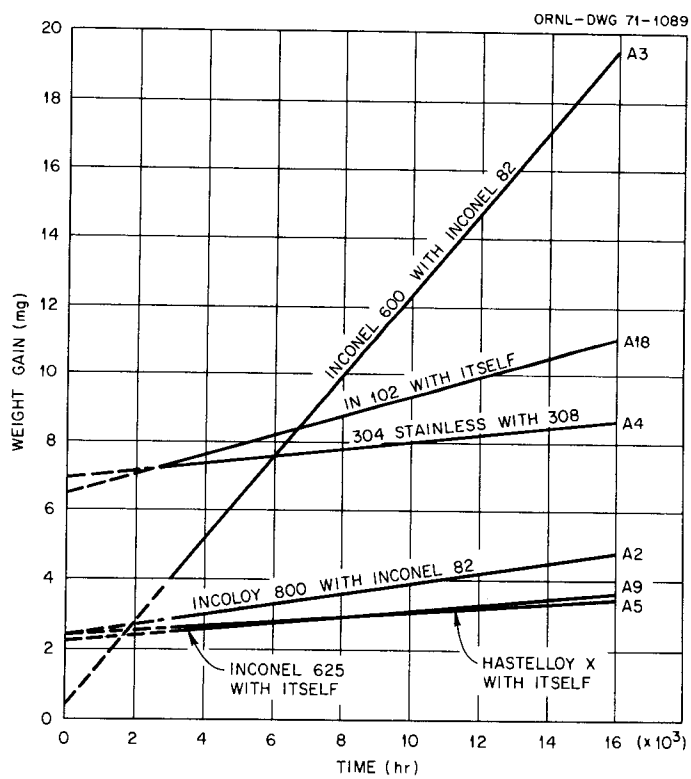

Fig. 20.1. Corrosion of Similar-Metal Weldments in 595°C (1100°F) Superheated Steam. The curves are a best fit to a linear rate law. Specimen surface area was 20 cm^2.

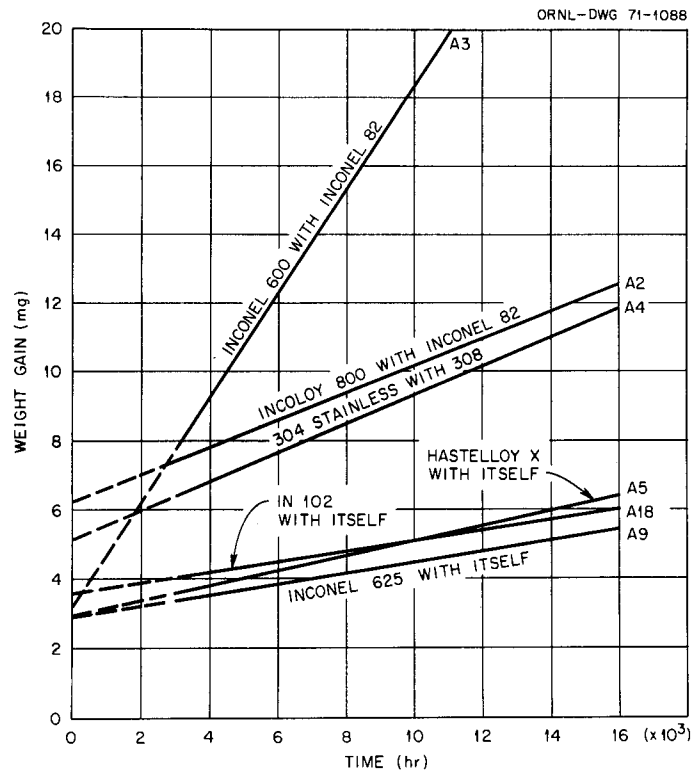

Fig. 20.2. Corrosion of Similar-Metal Weldments in 650°C (1200°F) Superheated Steam. The curves are a best fit to a linear rate law. Specimen surface area was 20 cm^2.

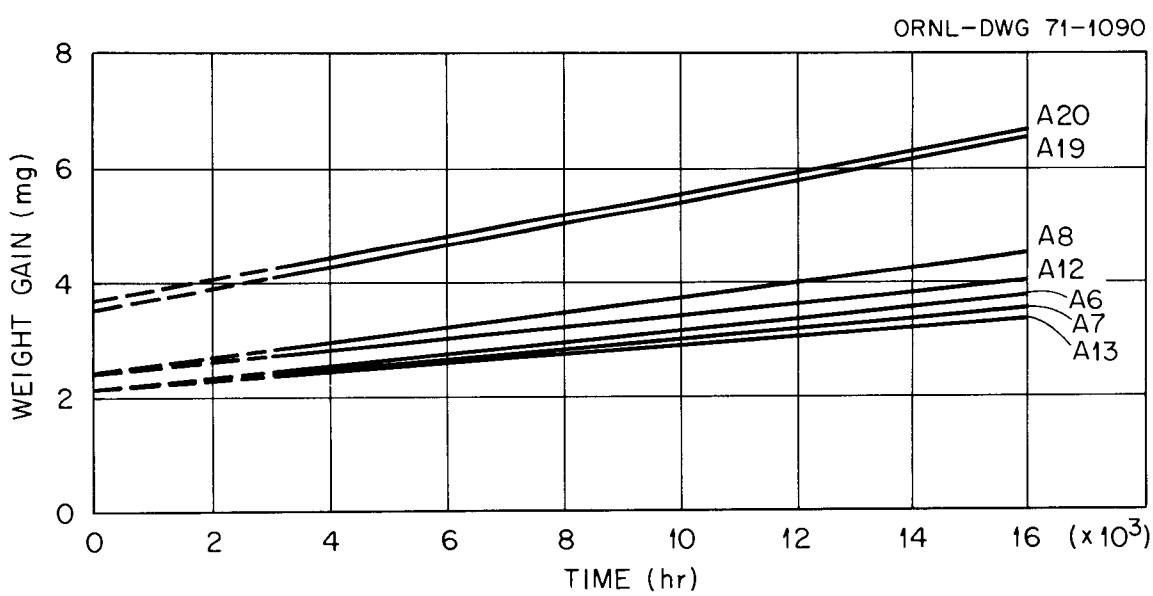

Fig. 20.3. Corrosion of Dissimilar-Metal Weldments in 595°C (1100°F) Superheated Steam. The curves are a best fit to a linear rate law. Specimen surface area was 20 cm^2.

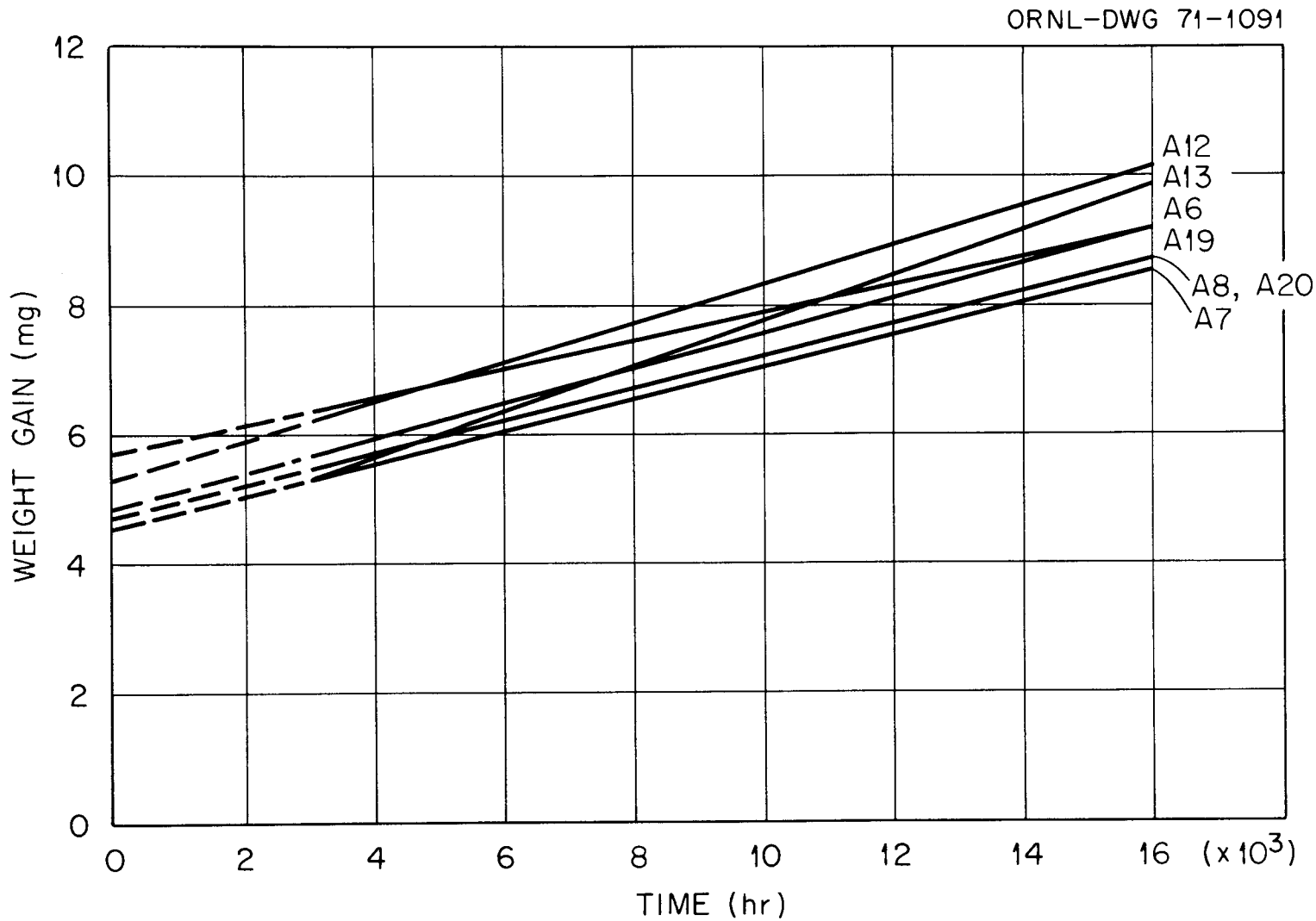

Fig. 20.4. Corrosion of Dissimilar-Metal Weldments in 650°C (1200°F) Superheated Steam. The curves are a best fit to a linear rate law. Specimen surface area was 20 cm^2.

Table 20.2. Metal Penetration of Similar-Metal Weldments Calculated from Weight-Gain Data[a]

Identification Code	Weldments	Intercepts and Slopes of 16,000 hr Weight-Gain Curves[b] With Standard Errors[c]		Penetration in 20 years	
		ΔW_o (mg/dm^2)	K_ℓ (mg/dm^2 – 1000 hr)	Based on 8000-hr Curves (in.)	Based on 16,000-hr Curve (in.)
		Exposed at 595°C (1100°F)			
A9	Inconel 625 with itself	11.0±0.23	0.42±0.03	0.0014	0.0012
A5	Hastelloy X with itself	12.1±0.29	0.31±0.04	0.0013	0.0009
A18	IN 102 with itself	20.8±0.90	1.41±0.10	0.0050	0.0041
A2	Incoloy 800 with Inconel 82	12.4±0.37	0.68±0.05	0.0023	0.0018
A3	Inconel 600 with Inconel 82	2.2±1.42	5.93±0.19	0.0189	0.0156
A4	Type 304 stainless steel with type 308 stainless steel	34.8±0.28	0.50±0.04	0.0018	0.0015
		Exposed at 650°C (1200°F)			
A9	Inconel 625 with itself	14.4±0.51	0.80±0.07	0.0034	0.0023
A5	Hastelloy X with itself	14.5±0.81	1.08±0.11	0.0039	0.0028
A18	IN 102 with itself	17.7±0.45	0.84±0.06	0.0023	0.0025
A2	Incoloy 800 with Inconel 82	31.1±1.02	2.02±0.14	0.0081	0.0052
A3	Inconel 600 with Inconel 82	16.5±3.82	7.57±0.52	0.0287	0.0205
A4	Type 304 stainless steel with type 308 stainless steel	25.4±0.86	2.12±0.12	0.0043	0.0049

[a]Amounts of corrosion do not allow for oxide flaking during test and are based on the following calculated concentrations of metal in the scales of the respective weldments: A9 – 76.1%, A5 – 74.1%, A18 – 76.7%, A2 – 73.5%, A3 – 76.2%, and A4 – 71.3%.

[b]ΔW (mg/dm^2) = ΔW_o (mg/dm^2) + K_ℓ (mg/dm^2 – 1000 hr) T(1000 hr), where ΔW is weight gain, ΔW_o is intercept, K_ℓ is slope, and T is time.

[c]The standard error of the intercept is for an individual specimen.

the former corrosion curves representing 1 year of exposure[2] are included for comparison. The methods for calculating penetration data were given previously.[3]

Observe that the penetrations calculated for 20 years from the data for 16,000 hr are generally somewhat less than those for 8000 hr, reflecting shallower curve slopes for the former. Since, except for the stainless steel specimens, specimens of the respective weldments showed no physical evidence of scale flaking, we view the trend toward shallower curve slopes with the longer exposure as favorable. The penetrations calculated for 20 years for the Inconel 625, Hastelloy X, IN 102, and Incoloy 800 similar-metal weldments at 595 and 650°C were all below 0.0005 in. except for Incoloy 800 exposed to 650°F, which was exactly 0.0005 in. Inconel 600 welded to itself with Inconel 82 was penetrated about 0.0015 in. after exposure at 595°C and about 0.002 in. after exposure at 650°C. The data on the stainless steel weldments are suspect since these spalled.[3]

The corrosion of the dissimilar-metal weldments in Figs. 20.3 and 20.4 also reflects only modest penetration in 20 years. The trends of the curves for the similar-metal weldments (Figs. 20.1 and 20.2) correlate with the results for the dissimilar-metal weldments (Figs. 20.3 and 20.4) and can be used to explain the close bracketing of curves for weldments in dissimilar metals when exposed at 650°C and their separation into two groups when exposed at 595°C.

A metallographic examination of the scales formed on the base metals and weld deposits of the respective alloy weldments after 2 years of exposure revealed no significant changes in the structural characteristics of the scales. Neither were indications of any aggravated forms of attack noted at the fusion lines of the welds.

Studies on Simulated Root Pass Compositions (J. P. Hammond)

The total exposures accumulated by the corrosion specimens synthesized to simulate the root passes of weldments in composition and structure[4] now have reached times ranging from 2000 to 9000 hr. The root passes of welds are receiving special attention because they generally are more highly alloyed (from dilution with base metal) than subsequent

passes, and it is the root pass that is exposed to steam in service. These synthetic root pass compositions were designed to match the compositions corresponding to the 50% dilution factor that we obtained in welds of the general corrosion specimens.

The synthetic specimens represent root passes of weldments between both similar and dissimilar metals, weldments of Incoloy 800 and Inconel 600 welded to themselves with Inconel 82 filler metal (A2 and A3), and weldments of Inconel 625, Hastelloy X, and IN 102 welded to Incoloy 800 with themselves (A13, A6, and A19) and with Inconel 82 (A12, A7, and A20) as filler metal. All are being studied in the as-welded, electropolished, belt-ground, and sandblasted surface conditions.

Although we shall wait until the specimens recently introduced have received longer exposures before making quantitative evaluations on this group of specimens, some observations are noteworthy at this point.

All of the specimens of this group, with the exception of those that were sandblasted, appeared to have retained their scales well. The sandblasted specimens almost invariably lost substantial weight for the first 1000 hr of exposure at both 595 and 650°C; this suggests scale spallation during early stages of scaling. With additional exposure, they gained weight, giving rates that were quite steady with time and often comparatively high. The cause of this phenomenon is not yet clear.

But for few exceptions, the order of the amounts of corrosion that occurred for the respective surface conditions of the individual alloys was (1) as welded, (2) electropolished, (3) belt ground, and (4) sandblasted.

Whereas the amounts and rates of corrosion usually were significantly higher at 650°C than at 595°C for the respective alloys and conditions, temperature did not appear to be nearly so important an experimental variable as surface condition. There were isolated instances in which corrosion at 595°C appeared to be significantly higher than at 650°C. These included the alloys corresponding to IN 102 welded to Incoloy 800 with both IN 102 and Inconel 82 as filler metal (weldments A19 and A20) both in the as-welded and electropolished conditions.

The amounts and rates of corrosion observed for simulated root pass specimens in the ground condition appeared to fall within the same general ranges observed earlier for the similar- and dissimilar-metal weld specimens (Figs. 20.1–20.4).

A root pass alloy that showed especially good resistance to corrosion in all four surface conditions was one corresponding to Hastelloy X welded to Incoloy 800 with Inconel 82 (weldment A7). Alloys that indicated corrosion one to two orders of magnitude higher than this include Inconel 600 welded to itself with Inconel 82 (A3) and IN 102 welded to Incoloy 800 with itself and Inconel 82 (A19 and A20), both for the as-welded and electropolished conditions (for synthesized alloys A19 and A20, this applies to the 595°C exposure only).

Stress-Corrosion Cracking in a Chloride Environment (J. P. Hammond)

The first three stress-corrosion test runs[5] were completed, but no specimens have failed yet.

In the third test run, which consisted of cycling between 540 and 280°C (1000 and 540°F) to expose specimens alternately to superheated and saturated steam, the NaCl injection level was altered from the 1 ppm level planned earlier to 0.25 ppm while the O level was maintained at 20 ppm to duplicate the contaminant concentration levels that actually existed in the superheated steam of the first two runs. These runs showed a NaCl content of about 0.25 ppm for the superheated steam, even though chloride was being injected into the loop at a level of 1 ppm. The excess chloride, corresponding to that which could not be dissolved into the steam, was deposited on the walls of the loop.

The fourth run, which was just begun, will consist of alternately cycling between superheated steam at 480°C (900°F) and saturated steam (280°C or 540°F) with 0.25 ppm NaCl and 20 ppm O for the dry phase of the cycling and 10 ppm NaCl and 20 ppm O for the wet phase. The temperature for the dry phase was reduced from 540 to 480°C (1000 to 900°F) to further reduce stress relaxation of specimens during testing. Hopefully, these conditions of test will begin to produce failures in the more crack-prone specimens. The specimens involved in run 4 were given in the last report.

Notes

1. J. P. Hammond, GCRP Semiann. Progr. Rept. March 31, 1969, ORNL-4424, pp. 63–72.

2. P. Patriarca and J. P. Hammond, GCRP Semiann. Progr. Rept. March 31, 1970, ORNL-4589, pp. 66–76.

3. J. P. Hammond, P. Patriarca, and G. M. Slaughter, "Corrosion of Advanced Steam Generator Alloy Weldments in 1100 and 1200°F (595 and 650°C) Steam," paper presented at 26th Annual Conference, National Association of Corrosion Engineers March 9–13, 1970, Philadelphia, Pa. To be published in the proceedings.

4. P. Patriarca and J. P. Hammond, GCRP Semiann. Progr. Rept. Sept. 30, 1970, ORNL-4508, pp. 68–70.

5. J. P. Hammond, Fuels and Materials Development Program Quart. Progr. Rept. Sept. 30, 1970, ORNL-4630, pp. 280–286.

Previous reports in this series:

ORNL-4330	Period Ending June 30, 1968
ORNL-4350	Period Ending September 30, 1968
ORNL-4390	Period Ending December 31, 1968
ORNL-4420	Period Ending March 31, 1969
ORNL-4440	Period Ending June 30, 1969
ORNL-4480	Period Ending September 30, 1969
ORNL-4520	Period Ending December 31, 1969
ORNL-4560	Period Ending March 31, 1970
ORNL-4600	Period Ending June 30, 1970
ORNL-4630	Period Ending September 30, 1970

INTERNAL DISTRIBUTION

1–3. Central Research Library
4. ORNL – Y-12 Technical Library
Document Reference Section
5–34. Laboratory Records Department
35. Laboratory Records, ORNL RC
36. ORNL Patent Office
37. G. M. Adamson, Jr.
38. S. E. Beall
39. J. A. Conlin
40. W. B. Cottrell
41–42. C. M. Cox
43. J. A. Cox
44. R. S. Crouse
45. F. L. Culler
46. J. E. Cunningham
47–48. J. H. DeVan
49. R. G. Donnelly
50. W. P. Eatherly
51. J. I. Federer
52. D. E. Ferguson
53. J. H Frye, Jr.
54. R. J. Gray
55. B. L. Greenstreet
56. W. R. Grimes
57. W. O. Harms
58–60. M. R. Hill
61. H. Inouye
62–94. P. R. Kasten
95. G. W. Keilholtz
96. J. M. Leitnaker
97. H. R. Livesey
98. E. L. Long, Jr.
99. A. L. Lotts
100. W. R. Martin
101. R. W. McClung
102–104. H. E. McCoy, Jr.
105. H. C. McCurdy
106. W. T. McDuffee
107. D. L. McElroy
108. J. R. McGuffey
109. C. J. McHargue
110. L. C. Oakes
111. R. E. Oakes
112. P. Patriarca
113. S. Peterson
114. P. L. Rittenhouse
115. M. W. Rosenthal
116. D. J. Rucker
117. A. W. Savolainen
118. A. C. Schaffhauser
119. J. L. Scott
120. J. D. Sease
121–122. G. M. Slaughter
123. J. O. Stiegler
124. D. A. Sundberg
125. V. J. Tennery
126. D. B. Trauger
127. J. E. Van Cleve
128. T. N. Washburn
129. J. R. Weir, Jr.
130. G. D. Whitman
131. R. G. Wymer
132. H. L. Yakel

EXTERNAL DISTRIBUTION

AEC-RDT SITE REPRESENTATIVES

133. R. H. Ball, Gulf General Atomic
134. D. F. Cope, Oak Ridge National Laboratory
135. Theodore Iltis, Westinghouse Advanced Reactor Division
136. M. E. Jackson, Argonne National Laboratory
137. C. L. Matthews, Oak Ridge National Laboratory
138. R. L. Morgan, Atomics International
139. D. A. Moss, Idaho
140. J. Sako, WADCO
141. Atomic Energy Commission Library, Washington

AIR FORCE MATERIALS LABORATORY, Wright-Patterson Air Force Base

142. C. H. Armbruster
143. H. M. Burte
144. I. Perlmutter

AMES LABORATORY, USAEC, Iowa State University, Ames, Iowa 50010

145. M. S. Wechsler

ARGONNE NATIONAL LABORATORY

146. B.R.T. Frost
147. J. H. Kittel
148. M. V. Nevitt
149. D. R. O'Boyle
150. P. G. Shewmon
151. R. C. Vogel

ATOMIC POWER DEVELOPMENT ASSOCIATES

152. A. A. Shoudy, Jr.

ATOMICS INTERNATIONAL

153. J. G. Asquith
154. T. A. Moss
155. H. Pearlman
156. S. Siegel

BABCOCK & WILCOX COMPANY, Beaver Falls, Pennsylvania 15010

157. William Buley

BABCOCK & WILCOX COMPANY, Lynchburg, Virginia 24505

158. C. J. Baroch
159. S. P. Grant
160. C. R. Johnson
161. L. R. Weissert

BATTELLE MEMORIAL INSTITUTE, Columbus, Ohio

162. D. Keller
163. S. J. Paprocki
164. Defense Materials Information Center

BROOKHAVEN NATIONAL LABORATORY

165. D. H. Gurinsky
166. C. Klamut

BUREAU OF MINES

167. Haruo Kato, Albany Metallurgy Research Center, P.O. Box 70, Albany, Oregon 97321
168. T. A. Sullivan, Bureau of Mines, Boulder City, Nevada 89005

COMBUSTION ENGINEERING

169. M. Andrews
170. W. P. Chernock

DIVISION OF NAVAL REACTORS, AEC, Washington

171. R. H. Steele

DIVISION OF REACTOR DEVELOPMENT AND TECHNOLOGY, AEC, Washington

172. J. C. Crawford, Jr.
173. G. W. Cunningham
174. R. P. Denise
175. K. E. Horton
176. J. R. Hunter
177. E. E. Kintner
178. W. H. Layman
179. W. H. McVey
180. J. J. Morabito
181. E. C. Norman
182. R. E. Pahler
183. A. J. Pressesky
184. M. A. Rosen
185. S. Rosen
186. J. M. Simmons
187. E. E. Sinclair
188. B. Singer
189. A. Taboada
190. A. N. Tardiff
191. A. Van Echo
192. C. E. Weber
193. M. J. Whitman

DIVISION OF RESEARCH, AEC, Washington

194. L. C. Ianniello
195. P. W. McDaniel
196. D. K. Stevens

GENERAL ELECTRIC, Cincinnati

197. H. C. Brassfield

GENERAL ELECTRIC, Nuclear Systems Programs, Cincinnati

198. E. E. Hoffman

GENERAL ELECTRIC, Pleasanton

199. H. W. Alter

GENERAL ELECTRIC, San Jose

200. R. Duncan
201. J. L. Krankota

GENERAL ELECTRIC, Sunnyvale

202. R. E. Skavdahl
203. C. N. Spalaris
204. E. L. Zebroski
205. Technical Library

GEORGE C. MARSHALL SPACE FLIGHT CENTER, Huntsville, Alabama

206. R. J. Schwinghamer

GULF GENERAL ATOMIC

207. L. J. Colby
208. A. J. Goodjohn
209. J. P. Howe
210. J. N. Lindgren
211. J. F. Watson
212. L. Yang

IDAHO NUCLEAR CORPORATION

213. W. C. Francis
214. W. A. Yuill

KNOLLS ATOMIC POWER LABORATORY

215. R. F. Wojciescak

LMFBR PROGRAM OFFICE, Argonne National Laboratory

216. G. A. Bennet
217. P. F. Gast
218. J. M. McKee

LOS ALAMOS SCIENTIFIC LABORATORY

219. R. D. Baker

MOUND LABORATORY

220. W. T. Cave
221. R. E. Vallée

NASA HEADQUARTERS

222. J. J. Lynch

NASA, LEWIS RESEARCH CENTER

223. G. M. Ault
224. J.W.R. Creagh
225. J. J. Lombardo
226. F. E. Rom
227. L. Rosenblum
228. N. T. Saunders
229. C. M. Scheuermann

NAVAL RESEARCH LABORATORY

230. J. R. Hawthorne

NUCLEAR MATERIALS AND EQUIPMENT CORPORATION

231. K. H. Puechl

OAK RIDGE OPERATIONS OFFICE

232. Laboratory and University Division

OHIO STATE UNIVERSITY, Columbus, Ohio 43212

233. R. W. Staehle

RENSSELAER POLYTECHNIC INSTITUTE

234. D. W. Dickinson
235. W. F. Savage

SANDIA CORPORATION

236. J. R. Holland
237. P. D. O'Brian

SPACE NUCLEAR SYSTEMS OFFICE, AEC, Washington

238. R. E. Anderson
239. D. Beard
240. J. F. Griffo
241. H. Jaffe
242. C. E. Johnson
243. A. P. Litman
244. J. A. Powers
245. F. C. Schwenk

UNION CARBIDE CORPORATION, New York

246. J. A. Swartout

UNION CARBIDE CORPORATION, Carbon Products Division, Cleveland, Ohio 44101

247. C. F. Leitten, Jr.

UNITED NUCLEAR CORPORATION

248. A. A. Strasser

UNIVERSITY OF CALIFORNIA, Lawrence Radiation Laboratory, Livermore

249. W. R. Holman
250. L. W. Roberts
251. A. J. Rothman

U.S. NAVAL AIR SYSTEM COMMAND (AIR-52031B)

252. I. Machlin

USAEC Scientific Representative, American Embassy, Box 40, FPO, N.Y. 09510

253. W.L.R. Rice

WADCO, P.O. Box 1970, Richland, Washington 99352

254. T. T. Claudson
255. D. L. Condotta
256. E. A. Evans
257. J. W. Finnigan
258. J. E. Hanson
259. B. R. Hayward
260. B. M. Johnson
261. H. N. Pederson
262. W. E. Roake
263. W. F. Sheely
264. J. C. Tobin

WESTINGHOUSE, Advanced Reactor Division, Waltz Mill Site

265. E. C. Bishop
266. A. Boltax
267. P. J. Levine
268. P. Murray
269. W. E. Ray
270. J. J. Taylor
271. G. A. Whitlow

WESTINGHOUSE, Astronuclear Laboratory

272. R. T. Begley
273. D. C. Goldberg

WESTINGHOUSE, Atomic Power Division

274. Library

WESTINGHOUSE, Bettis

275. R. H. Fillnow
276. P. N. Gustafson
277. Westinghouse Bettis Laboratory Library

WESTINGHOUSE, Nuclear Energy Systems, Tampa Division

278. M. E. Eilbeck

279–280. Division of Technical Information Extension
281–283. Director, Division of Reactor Licensing, AEC, Washington, D.C. 20545
284–285. Director, Division of Reactor Standards, AEC, Washington, D.C. 20545